Proceedings of Surgetica'2014

Jocelyne Troccaz

Proceedings of

SURGETICA'2014

Computer-Assisted Medical Interventions: scientific problems, tools and clinical applications

Editor : Jocelyne TROCCAZ

Chambéry, France, December, 2014

COMPUTER ASSISTED MEDICAL INTERVENTIONS

ANR

“Surgetica” conference series aims at gathering clinicians, scientists and industrial actors in order to present and to discuss new computerized guidance tools and their clinical applications. The 2014 conference has gathered French actors of Computer Assisted Medical Interventions (CAMI) and three international invited speakers Pr Alberto Arezzo (Department of Surgical Sciences, University of Torino, Italy), Pr Nassir Navab (Technische Universität München, Germany) and Pr Russell H. Taylor (Johns Hopkins University, Baltimore, USA) to discuss the recent progress and the remaining clinical and scientific challenges of the field.

Surgetica is a single-track conference mixing scientific and clinical presentations (oral and poster). The conference language was English. An industrial exhibit was proposed for complementary exchange about existing tools and clinical practice. Digital proceedings contain the accepted extended abstracts. The papers can be separately uploaded from http://surgetica2014-papers.imag.fr/ website.

The last morning of the conference was dedicated to the presentation of activities developed in the CAMI excellence laboratory (cf. http://cami-labex.fr).

Scientific topics include among others: image processing and registration, modeling and simulation, medical robotics and navigation systems, sensors and instrumentation, specific man-machine interfaces and augmented reality, protocol encoding and recognition, clinical evaluation of systems.

All clinical specialties are concerned among which: orthopedics and trauma, urology, cardiac, vascular, digestive surgery, endoscopic surgery, interventional imaging and radiology, neurosurgery, ENT, craniofacial surgery, radiation therapy.

Jocelyne TROCCAZ, Research Director CNRS
TIMC Laboratory, Grenoble, France

Organizing committee :
Chair : Jocelyne TROCCAZ, CNRS, TIMC-IMAG Laboratory

Pr Philippe MERLOZ, Grenoble University Hospital, TIMC-IMAG
Pr Eric STINDEL, Brest University Hospital, LATIM Laboratory
Jérôme SZEWCZYK, UPMC, ISIR Laboratory
Nabil ZEMITI, Montpellier II University, LIRMM Laboratory
Florent NAGEOTTE, Strasbourg University, ICUBE Laboratory
Antoine SIMON, Rennes I University, LTSI Laboratory

Program committee :
Chair : Jocelyne Troccaz, TIMC-IMAG, Grenoble

Bernard Bayle, ICube, Strasbourg
Georges Bettega, Cranio-facial surgery, Grenoble university hospital
Ivan Bricault, TIMC-IMAG, Radiology, Grenoble university hospital
Philippe Cinquin, TIMC-IMAG, CIC-IT Grenoble university hospital
Jean-Luc Descotes, TIMC-IMAG, Urologie, Grenoble university hospital
Jean-Yves Gauvrit, Radiology, Brest university hospital
Pascal Haigron, LTSI, Rennes
Julien Leboucher, LATIM, Brest
Antoine Lucas, vascular surgery, Rennes university hospital
Michel de Mathelin, ICube, Strasbourg
Philippe Merloz, TIMC-IMAG, Orthopedics-trauma, Grenoble university hospital
Guillaume Morel, ISIR, Paris
Pierre Mozer, ISIR, La Pitié Salpétrière Hospital, Paris
Florent Nageotte, ICube , Strasbourg
Yohan Payan, TIMC-IMAG, Grenoble
Philippe Poignet, LIRMM, Montpellier
Pierre Renaud, ICube, Strasbourg
Lotfi Senhadji, LTSI, Rennes
Antoine Simon, LTSI, Rennes
Eric Stindel, LATIM, Orthopedics-trauma, Brest university hospital
Jérôme Szewczyk, ISIR, Paris
Jean-Philippe Verhoye, Cardiac and vascular surgery, Rennes university hospital
Nabil Zemiti, LIRMM, Montpellier

Conference organization:
MCO Congrès, Marseille, France

WEDNESDAY 3RD, DECEMBER

08:45 OPENING SESSION (J.Troccaz)

09:00-10:15 ORTHOPEDICS
Chairman: E.Stindel

09:00 Mid-term results of 29 computer-assisted osteotomies for genu valgum deformity.
D. Saragaglia, B. Chedal-Bornu
Grenoble University Hospital

09:15 Functional hip center detection using only a tibial tracker for computer assisted tibial osteotomy:in vitro evaluation.
Z. Dib, G. Dardenne, N. Poirier, P-Y Huet, C.Lefevre, E. Stindel
LATIM, B-com, OSTESYS SAS, Brest University Hospital

09:30 Three dimension fluoroscopy-based navigation for dorsal percutaneous instrumentation in traumatic vertebral fractures.
S. Ruatti G. Kerschbaumer, A. Moreau Gaudry, E. Chipon, C. Dubois, J. Tonetti, M. Milaire, P.Merloz
Grenoble University Hospital, CIC-IT Grenoble, TIMC-IMAG

09:45 Multi-modal Intra-articular Device for Virtual Biopsies of Cartilage.
A.Moreau-Gaudry, A. Meneses, F. Billet, D. Girardeau-Montaut, G. Custillon, B.Vettier, R. Adler, D. Saragaglia, P. Gaudin, P. Merloz, P. Cinquin
TIMC-IMAG, CIC-IT Grenoble, Grenoble University Hospital, NYU Langone Medical Center

10:00 Vector field interpolation for scapular position estimation from noisy acromial motion capture.
S. Bouvel, A. Roby-Brami, G. Morel, V. Pasqui
ISIR

10:15-10:45 COFFEE BREAK

10:45-11H45 ORGAN DETECTION AND TRACKING
Chairman: P.Haigron

10:45 Assistance to High Intensity Focused Ultrasound (HIFU) therapy: Real-time motion compensation using ultrafast ultrasound imaging.
L-A. Chanel, F. Nageotte, J. Vappou, J. Luo, L. Cuvillon, M. de Mathelin
ICube, Department of Biomedical Engineering of Tsinghua University

11:00 Interactive Tracking of Soft Tissues in 2D Ultrasound Images.
L. Royer, M. Marchal, A. Le Bras, G. Dardenne, A. Krupa
B-com, INRIA Rennes, Rennes University Hospital

11:15 Fully Automatic Organ Localization of Medical Images Using Improved Random Regression Forests.
P. Samarakoon, E. Promayon, C. Fouard
TIMC-IMAG

11:30 Kidney 3D dynamic modeling and tumor tracking for therapeutic transcutaneous treatment.
V. Leonardi, M. Daniel, N. Olofsson, P. Souteyrand, V. Vidal, J-L. Mari
LSIS, LIIE, Upssala University

11:45-12:30 POSTER TEASER (22x2mn)

12:30-14:00 LUNCH

14:00-15:00 INVITED SPEAKER 1
Chairman: Y.Payan

Robotic imaging for patient and process specific, multi-modal intra-operative, imaging and Visualization.
Pr Nassir NAVAB
TUM University, Munich

15:00-16:30 REGISTRATION
Chairwoman: C.Fouard

15:00 Fluorescence imaging of prostate cancer: when the surgeon looks beyond the visible.
R. Heus, M-P. Montmasson , A. Moreau-Gaudry, M. Hamel, F. Giroud, E. Chipon, O. Gaiffe , C.Pieralli ,M. Kassem, J-A. Long, J-L. Descotes, P. Cinquin, S. Voros
CIC-IT Grenoble, Grenoble University Hospital, TIMC-IMAG, FEMTO-ST

15:15 Registration of Preoperative Liver Model for Laparoscopic Surgery with Intraoperative 3D acquisition.
J. Bano , A. Hostettler, S. Nicolau, C. Doignon, L. Soler, J. Marescaux
IRCAD, ICube, IHU Strasbourg

15:30 Video Synchronization: An Approach to Biopsy Site Re-localization.
A.S. Vemuri, A. Sportes, S. Nicolau, J. Marescaux, N. Ayache, L. Soler
IHU Strasbourg,IRCAD, INRIA Sophia-Antipolis, NHC, Strasbourg University Hospital

15:45 Phantom study of fiducial-free 3D-3D registration procedures for electromagnetic endovascular navigation.
LH.N'Guyen-Duc, A. de Lambert, S. Esneault, M. Castro, C. Göksu, J-L. Magne, P. Haigron
LTSI, Therenva, Grenoble University Hospital, CIC-IT Grenoble

16:00 Percutaneous procedures with CT-Ultrasound fusion guiding imaging system: evaluation of the accuracy.
F. Bing, J. Garnon, I. Enescu, G. Tsoumakidou, M-A. Thenint, E. Breton, M. de Mathelin, M. Cardoso Saldanhas, M. Schaeffer, E. Sauleau, A. Gangi
Strasbourg University Hospital, ICube, Barretos Cancer Hospital

16:15 Evaluation of Human Factors in Neuronavigated Transcranial Magnetic Stimulation (TMS).
H. Chauvat, R. Ginhoux, B. Maurin
ECE Paris, Axilum Robotics

16:30-17:00 COFFEE BREAK

17:00-17:45 POSTER SESSION

17:45-18:30 INSTRUMENT DETECTION AND TRACKING
Chairman: J.Leboucher

17:45 Online registration applied to multi-modal tracking for real-time scan plane alignment in interventional MRI.
M. *Neumann, L. Cuvillon, E. Breton, M. de Mathelin, L. Pan, A. Hengerer*
ICube, Siemens Research Corporate

18:00 Automatic detection of endoscope in intraoperative CT image : application to AR guidance in laparoscopic surgery .
S. Bernhardt , S. Nicolau, V. Agnus, L. Soler, C. Doignon, J. Marescaux
IHU Strasbourg, ICube, IRCAD

18:15 3D Pose Estimation of Actuated Instruments in Flexible Endoscopic Surgery.

P. Cabras, D. Goyard, F. Nageotte,P. Zanne, C. Doignon
ICube

THURSDAY, 4TH, DECEMBER

09:00-10:00 BIOMECHANICS
Chairman: M.Rochette

09:00 Biomechanical modeling to prevent soft tissues pressure ulcers.
V. Luboz, A. Perrier, M. Bucki, N. Vuillerme, F. Cannard, B. Diot, Y. Payan
TIMC-IMAG, Texisense SAS, AGIM, IDS SAS

09:15 Predicting the consequences of tongue cancer surgery: design of a 3D patient-specific biomechanical model and evaluation.
P-Y. Rohan, A. Bijar, G. Bettega, P. Perrier, Y. Payan
TIMC-IMAG, Gipsa-lab, Grenoble University Hospital

09:30 Biomechanical model of the fetal head for interactive childbirth simulation.
M. Bailet, F. Zara, E. Promayon
LIRIS, TIMC-IMAG

09:45 An augmented reality approach integrating deformation simulation to assist EVAR procedures.
A.Duménil, A. Kaladji, J. Gindre, M. Rochette, C. Göksu, A. Lucas, P. Haigron
LTSI, Therenva, CIC-IT Rennes, ANSYS France

10:00-10:45 CLINICAL DEVELOPMENTS
Chairman: P.Poignet

10:00 Laparoscopic gastric bypass and gastric electrical stimulation with a robotically controlled needle holder (JaimyTM).
F. Reche, B. Trilling, T. Olshefski, P-A. Waroquet, C. Arvieux, J-L. Faucheron
Grenoble University Hospital, Endocontrol Medical

10:15 Computer assisted transcatheter valve implantation for valve-in-valve procedures.
R. Belhaj, DLH. N'Guyen, M. Castro, S. Cadet, V. Auffret, VG. Ruggieri, J-P. Verhoye, P. Haigron
LTSI, Rennes University Hospital, Therenva

10:30 Small pulmonary nodule localization with intraoperative CBCT during video-assisted thoracic surgery.
S. Rouzé, M. Castro, P. Haigron, J-P. Verhoye, B. de Latour
LTSI, Rennes University Hospital

10:45-11:15 COFFEE BREAK

11:15-11:45 POSTER SESSION

11:45-12:45 COMPUTER-HUMAN INTERACTION
Chairman: N.Zemiti

11:45 Haptic and visuo-haptic feedback for guiding laparoscopic surgery gestures.
T. Howard, J. Szewczyk
ISIR

12:00 A novel contactless human-machine interface for laparoscopic telesurgery.
F. Despinoy, A. Sanchez, N. Zemiti, P. Jannin, P. Poignet
LIRMM, LTSI

12:15 Evaluation of a new robotized needle holder on ergonomics and skills.
T. Bensignor, B. Gayet, G. Morel

ISIR, Paris Montsouris Institute

12:45-14:00 LUNCH

14:00-15:00 INVITED SPEAKER 2
Chairman: P.Merloz

State of the art mini-robotic technology, clinician's perspectives and barriers.
Pr Alberto AREZZO, MD
Torino University

15:00-16:00 ROBOTICS
Chairman: P.Renaud

15:00 Endonasal Endoscopic Approach for Deep Brain Tumors Using Concentric Tube Robot.
M.N. Boushaki, C. Liu, V. Trevillot, P. Poignet
LIRMM, Montpellier University Hospital

15:15 Towards clinical application of continuum active micro-endoscope robot based on EAP actuation.
M.T. Chikhaoui, K. Rabenorosoa, N. Andreff
FEMTO-ST

15:30 Real-time FEM based control of soft surgical robots.
F. Largillière, E. Coevoet, L. Grisoni, C. Duriez
LIFL, INRIA Lille

15:45 Achieving high precision in prostate biopsy thanks to robot closed loop control based on 3D ultrasound imaging.
C. Poquet, M-A. Vitrani, P. Mozer, G. Morel
ISIR, La Pitié Salpétrière Hospital

16:00-16:30 TASK MODELLING OR MONITORING
Chairwoman: S.Voros

16:00 OntoSPM: a core ontology of surgical procedure models.
B. Gibaud, C.Penet, P.Jannin
LTSI

16:15 Analysis of dose monitoring uncertainties for prostate adaptive radiation therapy.
M. Nassef, A. Simon, G. Cazoulat, C. Lafond, O. Acosta, J. Balosso, R.d de Crevoisier, P. Haigron
LTSI, Centre Eugène Marquis Rennes, Grenoble University Hospital

16:30-17:00 COFFEE BREAK

17:00-18:00 DEVICES
Chairman: J.Szewczyk

17:00 Bidimensional Localization of Active Ultrasound Markers.
G. Custillon, S. Voros, P. Cinquin, A. Nguyen-Dinh, A. Moreau-Gaudry
CIC-IT Grenoble, TIMC-IMAG, Grenoble University Hospital, Vermon

17:15 Dental implant stability assessment using quantitative ultrasound.
R. Vayron, G. Haiat
MSME

17:30 An innovative NiTi based stent as an emergency treatment for acute urinary retention in case of benign prostatic hyperplasia.

G. Anthérieu, Y. Payan, D. Favier, N. Connesson, P. Mozer
TIMC-IMAG, ISIR, La Pitié Salpétrière Hospital

17:45-18:30 VIDEO SESSION

FRIDAY, 5TH DECEMBER

09:00-10:00 INVITED SPEAKER 3:
Chairman: G.Morel

Medical robotics and computer-integrated, interventional medicine.
Pr Russell H. TAYLOR
Johns Hopkins University, Baltimore

10:00-10:30 CAMI labex presentation
P. Cinquin (CAMI labex coordinator)

10:30-11:00 COFFEE BREAK

11:00-12:00 CAMI ACTIVITIES

11:00 CamiTK framework.
V. Leal, C. Fouard, E. Promayon (TIMC-IMAG)

11:15 Virtual Observatory.
A. Moreau-Gaudry (CIC-IT, Grenoble University Hospital)

11:30-12:00 Round table "CAMI interactions with other groups and initiatives"
Moderator: L. Senhadji (LTSI)

12:00 Closing session surgetica

12:15-13:00 Lunch

13:00-16:00 ANNUAL LABEX OFFICIAL MEETING
Labex members only

POSTERS

Patient specific guides for total knee arthroplasty. A cadaveric study.
S. Dao-Lena, P.Merloz
Grenoble University Hospital, TIMC-IMAG, CIC-IT Grenoble

3D MRI/CT non-rigid registration for image-guided prostate brachytherapy.
I.Hamdan, J. Bert, C. Hamitouche, G. Dardenne, D. Visvikis
B-com, LATIM

Robust point matching and outlier handling for minimally invasive Computer Aided Orthopedic Surgery (CAOS).
O. Haddad, J. Leboucher, J. Troccaz, E. Stindel
LATIM, TIMC-IMAG, Brest University Hospital

Registration using wavelet coefficients in spectral domain.
M. Ourak, B. Tamadazte, N. Andreff
FEMTO-ST

TRUS/T2 MRI 3D prostate elastic registration for HIFU thermal therapy.

K. Wu, C. Garnier, H. Shu, J-L. Dillenseger
LTSI, South University of Nanjing

Real-time simulation of soft tissue deformations for the childbirth related models using HEML.
Z-W. Chen, F.Mourette
Mines Paris Tech

Biopsym : a virtual reality simulator integrating a learning environment for image-guided prostate biopsy.
S-Y. Selmi, G. Fiard, E. Promayon, L. Vadcard, J. Troccaz
TIMC-IMAG, Grenoble University Hospital, LSE

Toward an MR-compatible needle holder with adaptive using an active tensegrity mechanism compliance.
Q. Boehler, M. Vedrines, S. Abdelaziz, P. Poignet,P. Renaud
ICube, LIRMM

Robotized needle steering with 3D echographic feedback for prostate brachytherapy.
P. Mignon, P. Poignet, J. Troccaz
TIMC-IMAG, LIRMM

3D Ultrasound Probe Calibration Using Robotic Arm and Image Registration.
J. Sarrazin, E. Promayon, M. Baumann, J. Troccaz
TIMC-IMAG, Koelis SAS

Feature Comparison for Unsupervised Laparoscopic Video Retrieval.
A.P. Twinanda, M. de Mathelin, N. Padoy
ICube, IHU Strasbourg

Surgical Process Model of laparoscopic rectopexy. (download paper
A.Huaulmé , S. Voros, F. Reche, J-L. Faucheron, P. Jannin, A. Moreau-Gaudry
TIMC-IMAG, LTSI, Grenoble University Hospital, CIC-IT Grenoble

An Ontology-based Software Suite for the Analysis of Surgical Process Model.
C. Garraud, B. Gibaud, C. Penet, G. Cazuguel, G. Dardenne, P. Jannin
B-Com, LTSI,LATIM

Reconstruction of 3D dose distribution in external beam radiotherapy using portal imaging.
L. Autret, J. Bert, S. Benhalouche, L. Desbat, D. Visvikis
LATIM, TIMC-IMAG

Observations of Semi-rigid Needle Deflection in 3D CT/MRI.
E. Dorileo, N. Zemiti, P. Poignet, N. Hungr, I. Bricault, C. Fouard
LIRMM, TIMC-IMAG, Grenoble University Hospital

Calibration with DCC in tomography.
L. Desbat, B. Spencer
TIMC-IMAG

Direct model based needle trajectory generation for ultrasound-guided regional anaesthesia.
N. Morette, C. Novales, A. Housni, P. Vieyres, O. Hadjerci, A. Hafiane
PRISME

Fusion on multi-modal data for Cardiac Resynchronization Therapy planification and guidance.
S. Bruge, A. Simon, A. Hernandez, C. Leclercq, M. Garreau
LTSI, Rennes University Hospital

Virtual fracture reduction of the acetabulum using a rigid body biomechanical model.
M. Boudissa, M. Chabanas, H. Oliveri, J. Tonetti
TIMC-IMAG, Grenoble University Hospital

Towards a computer assisted system for dosimetry optimisation of intrapleural photodynamic therapy for malignant pleural mesothelomia.
C. Munck, S. Mordon, A, Scherpereel, H. Porte, X. Dhalluin, N. Betrouni
INSERM U703, Calmette Hospital Lille

Evaluation of two Computed Assisted Medical Intervention (CAMI) systems in Forensic investigation.
F. Grenier, S. Voros, J. Boutonnat, V. Scolan, F. Paysant, A. Moreau-Gaudry
TIMC-IMAG, Grenoble University Hospital

The CATANE project: a SMA-based approach of mini-invasive surgery.
J-B. Cazeneuve, R. Blanc, J. Szewczyk
ISIR, Paris Rothschild Foundation Hospital

INVITED SPEAKERS

Pr Nassir NAVAB – Surgetica'2014 invited talk

Robotic imaging for patient and process specific, multi-modal intra-operative, imaging and Visualization.

Abstract:

In this talk, I will first discuss the needs for developing novel intra-operative personalized imaging solutions. I will present my views on the future of intra-operative imaging and in particular on the important role robotics and control need to play. I will then focus on some of our latest results in patient and process specific multi-modal robotic imaging. I will introduce the novel concept of "desired view" control for intra-operative X-ray, SPECT and Ultrasound imaging. I will introduce: 1) the first intra-operative SPECT/CT imaging solution, 2) An MR-based desired view control for Robotic Ultrasound imaging, and 3) the deployment of desired view control concept for clinical applications in X-ray angiography. In terms of visualization after presenting a quick overview of the development of Medical Augmented Reality since early 90s, I will summarize our efforts in the last decade not only in improving depth perception and user interaction within augmented environments, but also in introducing such visualization techniques into real operating rooms. Finally, I will show some of our latest results in relevance-based augmented reality visualization and advance UI for computer assisted Interventions.

Short bio:

Nassir Navab is a Professor of Computer Science and founder and director of the Computer Aided Medical Procedures (CAMP) Laboratories at TU Munich and Johns Hopkins University. He is a fellow and member of board of directors of the MICCAI society. He is an associated editor for IEEE transactions on Medical Imaging and member of the editorial board of Medical Image Analysis and International Journal of Computer Vision. He received the Siemens Inventor of the Year award in 2001 and the SMIT medical Innovation award in 2010. He is the inventor for 44 US and over 50 European patents. He has published hundreds of papers and has co-authored over twenty papers awarded in most prestigious international conferences. Nassir acts as Area Chair for ECCV 2014, Program Board for IPCAI 2014 and General Chair for IEEE ISMAR 2014. He is the General Chair for MICCAI 2015, which will be held in Munich, October 5-9. His current fields of interest include Patient and Process Specific Robotic Imaging, Medical Augmented Reality and Computer Vision. (For more details please visit: http://campar.in.tum.de and http://camp.lcsr.jhu.edu/)

Pr Alberto AREZZO – Surgetica'2014 invited talk

State of the art mini-robotic technology, clinician's perspectives and barriers.

Abstract:

There are at least three good reasons to use robotics in surgery:

- to do better, things already done by standard laparoscopy
- to do more often procedures in a laparoscopic way, that require lots of skills under standard condition, as they become easier.
- to enable procedures of evident benefit for the patient which are not possible today with existing endoscopic technology

This last one is the case of mini-robotic technology.
Many prototypes have been proposed in the past decade.
We do have a novel idea, called RED - Robot for Endoscopic Dissection which should overcome current limitations, and allow full compatibility with existing technologies currently available world-wide.
We look forward to a robotic system which should be:

1. user friendly
2. force feed-back
3. miniaturization for NOTES applications

Short bio:

Professor Alberto Arezzo is Associate Professor of Surgery in the Department of Surgical Sciences of the University of Torino.
General Surgeon and Digestive Endoscopists for operative procedures
Coordinator of several research projects sponsored by the European Commission and private companies.
Former Scientist at the Section for Minimally Invasive Surgery at the Eberhart Karls University of Tuebingen, Germany, Dir. Prof. Med. Gerhard Buess, pioneer of endoscopic surgery.
Currently Associate Professor of Surgery at the Dept. of Surgical Sciences, Dir. Prof. Mario Morino, pioneer of endoscopic surgery, he is covering a special role for Endoscopic Surgery.
He performed thousands of procedures, mainly colorectal surgery, open, laparoscopic and transanal, including emergencies.
Expert in the field of proctology, particularly Transanal Endoscopic Microsurgery and Operative procedures under Flexible Digestive Endoscopy, such as difficult polypectomies, mucosectomies (EMR), endoscopic submucosal dissections (ESD).
Main interest are New Technologies for Endoscopic Surgery and Flexible Endoscopy.

Pr Russell H. TAYLOR – Surgetica'2014 invited talk

Medical robotics and computer-integrated, interventional medicine.

Abstract:

This talk will discuss ongoing research at the JHU Engineering Research Center for Computer-Integrated Surgical Systems and Technology (CISST ERC) to develop CIIS systems that combine innovative algorithms, robotic devices, imaging systems, sensors, and human-machine interfaces to work cooperatively with surgeons in the planning and execution of surgery and other interventional procedures. This talk will describe past and emerging research themes and illustrate them with examples drawn from our current research activities in medical robotics and computer-integrated interventional systems.

Short bio:

Russell H. Taylor received his Ph.D. in Computer Science from Stanford in 1976. He joined IBM Research in 1976, where he developed the AML robot language and managed the Automation Technology Department and (later) the Computer-Assisted Surgery Group before moving in 1995 to Johns Hopkins, where he is the John C. Malone Professor of Computer Science with joint appointments in Mechanical Engineering, Radiology, and Surgery and is also Director of the Engineering Research Center for Computer-Integrated Surgical Systems and Technology (CISST ERC) and of the Laboratory for Computational Sensing and Robotics (LCSR). He is the author of over 350 peer-reviewed publications, a Fellow of the IEEE, of the AIMBE, of the MICCAI Society, and of the Engineering School of the University of Tokyo. He is also a recipient of numerous awards, including the IEEE Robotics Pioneer Award, the MICCAI Society Enduring Impact Award, and the Maurice Müller Award for Excellence in Computer-Assisted Orthopaedic Surgery.

ORTHOPEDICS

Mid-term results of 29 computer-assisted osteotomies for genu valgum deformity.

D. Saragaglia*, B. Chedal-Bornu*

*Department of Orthopaedic Surgery and Sport Traumatology. Grenoble South Teaching hospital. Avenue de Kimberley, 38130, Échirolles, France.

Introduction: Osteotomies for valgus deformity are much less frequent than those for varus deformity as evidenced by published series which are, on one hand, less numerous and on the other hand, based on far fewer cases. The principle of realignment osteotomy of the lower limb is to discharge the injured compartment by transferring the load on the opposite compartment, that must obviously be healthy. For genu varum deformity, it has been proved that navigation allows to reach easier the preoperative correction goal (1,2,3,4). Our hypothesis was that navigation for genu valgum could be as accurate as for genu varum deformity. The aim of this paper was to present the mid-term results of 29 computer-assisted osteotomies for genu valgum deformity performed between September 2001 and March 2013.

Material and methods: the series was composed of 27 patients (29 knees), 20 females and 7 males, aged from 15 to 63 years (mean age: 42.4+/-14.3 years). The preoperative functional status was evaluated according to the Lyshölm-Tegner score. The mean score was of 64+/-20.5 points (18-100). The stages of osteoarthritis were evaluated according to modified Ahlbäck's criteria. We operated on 12 stage 1, 9 stage 2, 5 stage 3 and 1 stage 4. 2 female patients had no osteoarthritis but a particularly unesthetic deformity (of which one was related to an overcorrected tibial osteotomy). The pre and postoperative HKA angle was measured according to Ramadier's protocol. We measured also the medial tibial mechanical angle (MTMA) and the medial femoral mechanical angle (MFMA). The mean preoperative HKA angle was 189.3°+/-3.9° (181° to 198°); the

mean MFMA was 97.2° +/- 2.6° (93° to 105°) and the mean MTMA was 90.1° +/- 2.8° (86° to 95°). The goal of the osteotomies was to obtain an HKA angle of 179° +/- 2° and a MTMA of 90°+/2° in order to avoid an oblique joint line. We performed 24 femoral osteotomies (14 medial opening wedge and 10 lateral closing wedge) and 5 double osteotomies (medial tibial closing wedge + lateral opening wedge osteotomy).

The functional results were evaluated according to Lyshölm-Tegner, IKS and KOO Scores, which were obtained after revision or telephone call.

Results: We did not found any complication except a transient paralysis of the common fibular nerve. 23 patients (4 lost to follow-up) were reviewed at a mean follow-up of 50.9+/-38.8 months (6-144). The mean Lyshölm-Tegner score was 92.9+/-4 points (86-100), the mean KOO score 89.7+/-9.3 (68-100), the mean IKS « knee» score 88.7 +/-11.4 points (60 à 100) and the mean « function » score 90.6 +/-13.3 points (55-100). 22 of the 23 reviewed patients (25 knees) were very satisfied or satisfied of the result. Regarding the radiological results, the mean HKA angle was of 180.1°+/-1.9° (176° to 185°), the mean MFMA of 90.7°+/-2.5° (86°-95°) and the mean MTMA of 89.1°+/-1.9° (86°-92°). The preoperative goal was reached in 86.2% (25/29) of the cases for HKA angle and in 100% of the cases for MTMA when performing double level osteotomy (5 cases). At this follow-up, no patient was revised to TKA.

Conclusion: computer-assisted osteotomies for genu valgum deformity lead to excellent results a mid-term follow-up. Navigation is very useful to reach the preoperative goal.

References

1- Saragaglia D, Pradel P, Picard F. L'ostéotomie de valgisation assistée par ordinateur dans le genu varum arthrosique : résultats radiologiques d'une étude cas-témoin de 56 cas. E-mémoires de l'Académie Nationale de Chirurgie 2004 ; 3 : 21-25. Disponible à : http://www.bium.univ-paris5.fr/acad-chirurgie

2- Saragaglia D, Roberts J. Navigated osteotomies around the knee in 170 patients with osteoarthritis secondary to genu varum. Orthopaedics 2005; 28, Suppl. n°10: S1269-S1274.

3- Saragaglia D, Blaysat M, Mercier N, Grimaldi M. Results of forty two computer-assisted double level osteotomies for severe genu varum deformity. Int Orthop 2012; 36:999-1003.

4- Saragaglia D, Mercier N, Colle PE. Computer-assisted osteotomies for genu varum deformity: which osteotomy for which varus? Int Orthop 2010; 34:185-190.

5- Ramadier JO, Buard JE, Lortat-jacob A, Benoit J. Mesure radiologique des déformations frontales du genou. Procédé du profil vrai radiologique. Rev Chir Orthop 1982 ; 68 : 75-78.

Functional hip center detection using only a tibial tracker for computer assisted tibial osteotomy: in vitro evaluation.

Zoheir DIB [1, 5], Guillaume DARDENNE [2], Nicolas POIRIER [4, 5], Pierre-Yves HUET [3],

Christian LEFEVRE [1, 3, 4, 5], Eric STINDEL [1, 3, 4, 5]

[1]Laboratoire de Traitement de l'Information Médicale, (LaTIM - INSERM UMR 1101), Brest, France ;
[2]B<>com, Rennes, France ;
[3]OSTESYS SAS, Plouzané, France ;
[4]Centre Hospitalier Régional et Universitaire de Brest, Service Orthopédie Traumatologie, Brest, France ;
[5] Université de Bretagne Occidentale, Brest, France.

Introduction:

In orthopedic surgery, the lower limb alignment defined by the HKA parameter i.e. the angle between the hip, the knee and the ankle centers, is a crucial clinical criterion used for the achievement of several surgeries such as tibial osteotomy.

The hip center used for the HKA computation is defined by the experts as the anatomical center of the femoral head. The methods used in the CAOS systems allow the determination of the hip center without any direct access to the femur head anatomy by using functional methods [1, 2]. Therefore, the functional hip center can be computed with specific algorithms; the most common ones are the *Least Moving Point* (LMP) [1] and The *Pivoting* (PIV) [3].

Usually, the acquisition of the functional hip center requires a femoral tracker [1, 2, 3]. This practice introduces additional invasivity to navigated tibial osteotomy comparing to the conventional surgery which is performed only on the proximal tibia [4]. The use of only tibial tracker may overcome this limit and reduce the invasivity during navigated tibial osteotomies; however, the accuracy of the functional hip center acquisition with only one tibial tracker has not been studied before.

This study shows in-vitro results concerning the difference between the HKA angle obtained with the anatomical hip center (HC_{ANAT}) and those obtained with the functional hip centers coming from the LMP ($HC_{LMP\text{-}T}$) and the PIV ($HC_{PIV\text{-}T}$) algorithms and acquired using only a tibial tracker.

Materials and Methods:

Measurements have been performed by a surgeon at the anatomy lab of the University of Brest on six lower limbs. An ATRACSYS® camera (RMS precision = 0.3 mm) was used to acquire 3D positions of:

- two trackers: one attached on the femur and the other on the tibia,
- a digitizer allowing us to acquire 3D anatomical points.

A software was implemented in C++, it allows the surgeon to acquire:

1. The medial and the lateral points of the femur condyles with the digitizer to compute the knee center.
2. The medial and the lateral points of the ankle with the digitizer to compute the ankle center.
3. The rotation motion of the lower limb around the pelvis with the tibial and the femoral trackers, for the computation of the functional hip centers HC_{LMP} and HC_{PIV} using both femoral and tibial trackers independently. 500 positions of the trackers have been recorded by acquisition.
4. 1000 points with a digitizer on the femoral head. A sphere is then fitted to these points to compute the sphere center corresponding to the anatomical hip center HC_{ANAT}.

All acquisitions have been repeated five times per lower limb. To give a better scan of the acquisitions, each acquisition is clipped into 10 frames with: 400 successive positions by frame and 10 positions between each frame.

The acquisition of the functional hip center has been performed in full extension of the lower limb and in different range of degrees of flexion between 0° and 45°, to assess the impact of flexion on the HKA. The differences D_{LMP-T} and D_{PIV-T} and the differences D_{LMP-F} and D_{PIV-F} have been computed for all specimens *i* (0 < i < 6), all acquisitions j(0<j<5) and all frames f(0<f<10).

$$D_{LMP-T}(i,j,f) = \left|HKA_{LMP-T}(i,j,f) - HKA_{ANAT\_AVERAGE}(i)\right|$$

$$D_{PIV-T}(i,j,f) = \left|HKA_{PIV-T}(i,j,f) - HKA_{ANAT\_AVERAGE}(i)\right|$$

And

$$D_{LMP-F}(i,j,f) = \left|HKA_{LMP-F}(i,j,f) - HKA_{ANAT\_AVERAGE}(i)\right|$$

$$D_{PIV-F}(i,j,f) = \left|HKA_{PIV-F}(i,j,f) - HKA_{ANAT\_AVERAGE}(i)\right|$$

Where:

- $HKA_{ANAT\_AVERAGE}(i)$ is the HKA obtained with $HC_{ANAT\_AVERAGE}(i)$,
- $HC_{ANAT\_AVERAGE}(i)$ is the average of all $HC_{ANAT}(i,j)$ obtained for a given lower limb ;
- $HKA_{LMP-T}(i,j,f)$ is the HKA computed with $HC_{LMP-T}(i,j,f)$.
- $HKA_{PIV-T}(i,j,f)$ is the HKA computed with $HC_{PIV-T}(i,j,f)$.
- $HC_{LMP-T}(i,j,f)$ is the HC_{LMP-T} obtained with the f^{th} frame of the j^{th} *acquisition* of the i^{th} lower limb, from the tibial tracker;
- $HC_{PIV-T}(i,j,f)$ is the HC_{PIV-T} obtained with the f^{th} frame of the j^{th} *acquisition* of the i^{th} lower limb, from the tibial trakcer.

According to [1], the functional hip center acquisition had better results with a rotation motion, therefore, only this motion has been investigated in our paper to study the accuracy of the functional hip center acquisition.

Results:

Figure 1 shows the results concerning the HKA differences in degrees as defined by D_{LMP-T} and D_{PIV-T} for all range of tibial flexion.

The average and standard deviation for the acquisitions with tibial flexion range between 35° and 45° are respectively 2.1° ± 1.4° and 2.3° ± 2.1° for LMP and PIV.

Figure 2 shows the results concerning the impact on the HKA in degrees for the hip center acquisition with tibial flexion <5° vs. the impact on the HKA for the hip center acquisition with the femoral tracker.

The average HKA differences and standard deviation are respectively for the LMP and the PIV 1.3° ± 1.0° and 1.0° ± 0.8° using the tibial tracker and there are 1.2± 0.9° and 1.1°± 0.9°using the femoral tracker.

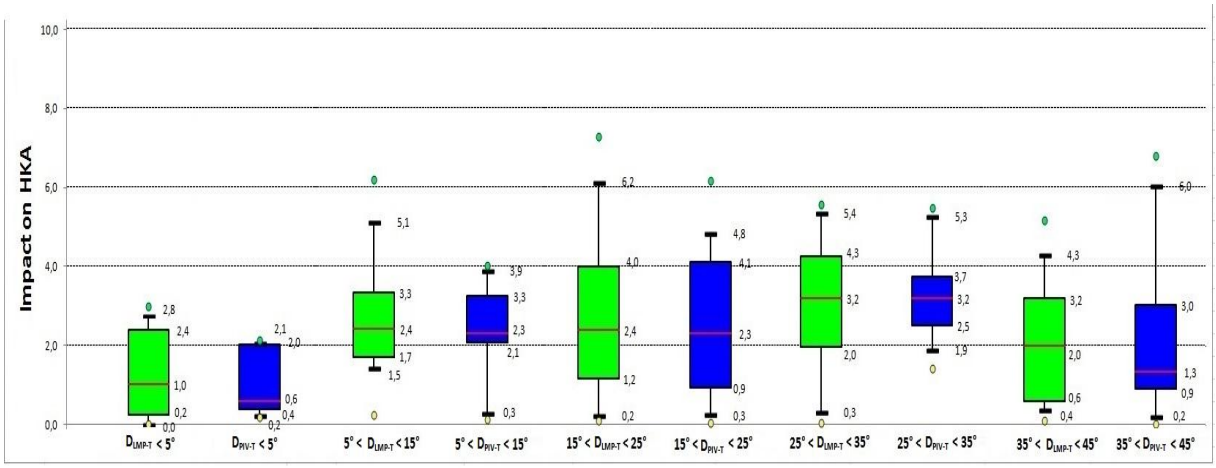

Figure 1: impact of flexion on HKA for the functional hip center detection with only tibial tracker

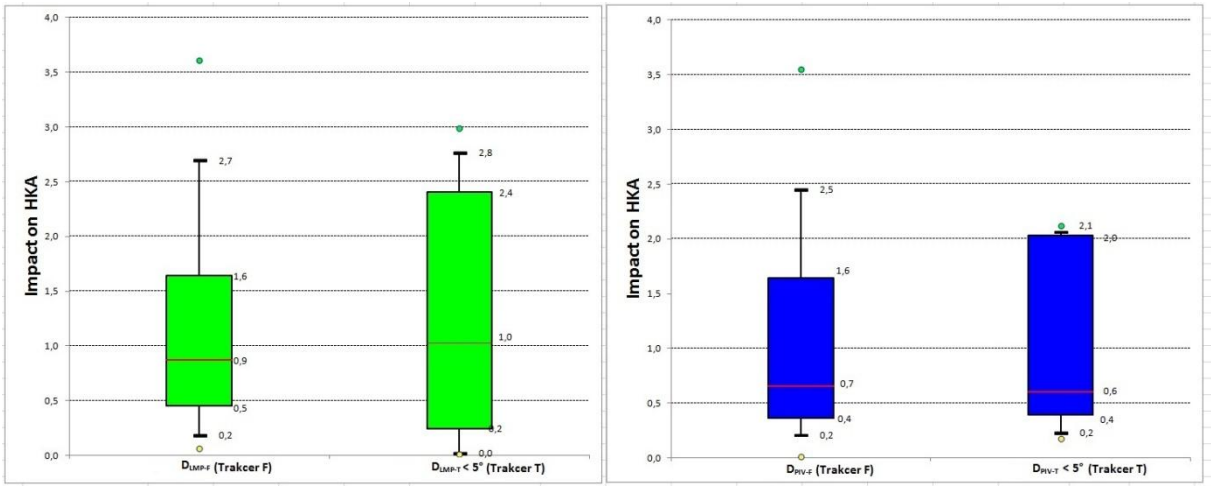

Figure 2: impact on the HKA of the HJC acquisition with tibial tracker (T) and femoral tracker (F).

Discussion:

Several papers in the literature have studied the accuracy and the robustness of methods allowing CAOS systems to determine the functional hip center [1, 2, 3] with a femoral tracker. This study shows results coming from in-vitro data using only a tibial tracker for an application to a mini invasive navigated tibial osteotomy surgery.

We have therefore compared the HKA obtained with HC_{ANAT} with those obtained with HC_{LMP} and HC_{PIV} in the presence of various degrees of tibial flexion around the femur, where the HC_{ANAT} average (standard deviation) variations was 0.89(0.63) mm. We had found a direct relationship between the errors on HKA and the tibia flexion since the errors on the HKA computation increased by increasing the range of tibia flexion. Respectively for the LMP and the PIV methods, the errors increased from an average (SD) of 1.3(1.0)° and 1.0(0.8)° in flexions less than 5° to 3.1(1.8)° and 3.4(1.2)° in flexions between 25° and 35°, until 6.2(4.2)° and 7.5(5.3)° in flexions superior than 50°.

Given these results, the impact on the HKA of the hip center acquisition with the tibial tracker in flexion < 3° was compared to those with the femoral tracker acquisition. The functional hip center accuracy with the femoral tracker for the LMP method is better than those with the tibial trakcer, LMP and PIV errors were respectively 1.1(0.9)° and 1.2(0.9)° with femoral tracker and 1.3(1.0)° and 1.0(0.8)° with tibia tracker. However the differences in HKA are small for both the LMP and the PIV methods.

The results are extremely encouraging since, for all acquisition with flexion less than 5°, the impact on HKAs are less than 3° which is the gool of tibial osteotomy.

Acknowledgment: This work was partly supported by the French ANR within the Investissements d'Avenir program (Labex CAMI) under reference ANR-11-LABX-0004.

References:

[1] Stindel E. et al., Detection of the center of hip joint in computer-assisted surgery: An evaluation study of the Surgetics algorithm. Computer Aided Surgery 10(3): 133-139, 2005.

[2] Zoheir D. et al., In Vitro comparison of two methods of detection of the functional hip center Vs. anatomical hip center in computer assisted. Bone & Joint Surgery Journal 95-B(SUPP 28): 19,2013.

[3] Ehrig, R.M. et al., A survey of formal methods for determining the center of rotation of ball joints. Journal Of Biomechanics, 39(15):2798-2809, 2006.

[4] Natasha E. P. et al., Computer-Assisted Navigation in High Tibial Osteotomy: A Systematic Review of the Literature. The Open Orthopedics Journal 6(SUPP 2 M8): 305-312, 2012.

Three Dimension Fluoroscopy-Based Navigation For Dorsal Percutaneous Instrumentation In Traumatic Vertebral Fractures.

Sebastien Ruatti, *Gael Kerschbaumer, Alexandre Moreau Gaudry, Emilie Chipon, Caroline Dubois, Jerome Tonetti, Michel Milaire, Philippe Merloz*.

Univ Dept Orthopaedic Surgery; CIC-IT, Grenoble; Lab TIMC – IMAG, (Univ. Joseph Fourier - CNRS UMR 5525), Pavillon Taillefer - Faculté de Médecine - 38706 La Tronche cedex - France

Introduction: In recent years internal fixation of the spine by using posterior approach with minimal-invasive and percutaneous technique were increasingly used in trauma. The percutaneous surgery lose information and navigation is supposed to provide better data because the lost information is found again. We hypothesize that a percutaneous minimal invasive dorsal procedure by using 3D intra-operative imaging for vertebral fractures allows short operating times with correct screw positioning and does not increase radiation exposure.

Objectives: The aim of this study was to perform a prospective, monocentric, randomized, comparative and controlled trial study between three dimension (3D) fluoroscopy-based navigation (3D fluo) and conventional 2D fluoroscopy surgical procedure (CP) in order to check the effectiveness of 3D fluoroscopy-based navigation in terms of accuracy, radiation exposure and operative running time.

Methods: 59 patients were included in this study. 29 patients (108 implants) were operated on by using conventional surgical procedure (CP) and 30 patients (72 implants) were operated on by using a 3D fluoroscopy-based navigation system (3D fluo). In the two groups, a percutaneous approach was performed for transpedicular vertebroplasty or percutaneous pedicle screws insertion. In the two groups surgery was done from T4 level to L5 levels. Patients (54 years old on average) suffered trauma fractures, fragility fractures or degenerative instabilities. Evaluation of screw placement was done by using post-operative CT scan with two independent radiologists that used Youkilis criteria. Operative and radiation running time were also evaluated.

Results: With percutaneous surgery, the 3D fluo technique was less accurate with 13.88% of misplaced pedicle screws (10/72) compared with 11.11% (12/108) observed with CP. The radiation running time for each vertebra level (two screws) reached on average 0,56 mSv with 3D fluo group compared to 1,57 mSv with the CP group. The time required for instrumentation (one vertebra, two screws) with 3D fluo was 19,75 minutes compared with CP group 9,19 minutes. The results were statistically significant in terms of radiation dose and operative running time ($p < 0,05$), but not in terms of accuracy ($p=0,24$).

Discussion and Conclusion: The operative running time with 3D fluo group is much longer than with CP procedure. This fact can be explained by navigation tools set up, calibration and image acquisition. The low radiation dose observed with 3D fluo group (as compared with CP group) can be explained by the fact that image acquisition allows for implantation of three vertebral levels. The difference in terms of precision is not significant. With percutaneous procedures, 3D fluoroscopy-based navigation system has no superiority in terms of operative running time and to a lesser degree in terms of accuracy, as compared to 2D conventional procedure, but the benefit in terms of radiation dose is important. Other advantages of the 3D fluo system are twofold: up-to-date image data of patient anatomy and immediate availability to assess the anatomical position of the implanted screws. On a clinical point of view, the advantages of dorsal percutaneous pedicle screw insertion for the patient are the chances of early mobilization and reduction of postoperative pain. With the development of new percutaneous instrument systems short mono- segmental or bi-segmental instrumentations can be performed in addition to long percutaneous instrumentations.

Multi-modal Intra-articular Device for Virtual Biopsies of Cartilage

A. Moreau-Gaudry[1,2], A. Meneses[3], F. Billet[1], D. Girardeau-Montaut[1], G. Custillon[1], B.Vettier[1], R. Adler[4], D. Saragaglia[5], P. Gaudin[3], P. Merloz[6], and P. Cinquin[1,2]

[1] TIMC-IMAG Laboratory, GMCAO team, Grenoble, France
[2] CIC-IT, *Centre d'Investigation Clinique - Innovation Technologique*
[3] Grenoble Hospital - Rheumatology
[4] NYU Langone Medical Center, New York, USA
[5] Grenoble Hospital - Orthopedy and Sports Traumatology Surgery - South
[6] Grenoble Hospital - Orthopedy and Traumatology - North

Introduction

Different kinds of imaging techniques are currently used to evaluate osteoarthritis (OA): plain radiographs, MRI, arthroscopy, ultrasonography. Each of them shows its own advantages and drawbacks. OA is traditionally diagnosed on standard radiographs, as a joint space narrowing that testifies of the chondrolysis, with associated lesions like geodes and osteophytes. Nevertheless, all these radiological signs are only visible at advanced stages of the disease [1].

Qualitative MR scanning techniques (*dGEMRIC*, T2 mapping, T1rho mapping, and sodium imaging) that evaluate deterioration of biochemical components of articular cartilage are being accepted into clinical routine. Less-validated methods for quantifying cartilage composition (Ultrashort Echo Time, diffusion-Weighted Imaging, and *gagCEST*) are also emerging. Each technique correlates with biochemical cartilage components, with advantages and limitations for clinical and research use [2]. Articular cartilage can also be evaluated during arthroscopy. In arthroscopic classifications, parameters like lesion location, depth, and size can be visually and then subjectively estimated [3]. The classifications of Collins, Outerbridge and the French Society of Arthroscopy all seem to suffer from a lack of inter and intra-observers reliability [4]. In the case of knee cartilage assessment, reliability has been improved by dividing the knee into sectors. This allows localization of the area of damage. The depth of the lesion can be evaluated with the International Cartilage Repair Society classification. However, arthroscopy limitations have also been reported. Among these, very early osteoarthritis cannot be detected and cartilage evaluation is limited to its surface only. The diagnosis of deep cartilage defects has a high validity but the diagnosis of low grade lesions is often inaccurate [5, 6]. Ultrasonography (US) has been increasingly used these past decades in routine, especially in case of musculoskeletal diseases. The international OMERACT group (Outcome Measures in Rheumatoid Arthritis Clinical Trials) is interested in outcome measurement and technical standardization. Its Ultrasound group has developed

scoring systems to assess diagnosis and therapy responses in inflammatory arthritis, particularly rheumatoid arthritis and ankylosing spondylitis. Furthermore, ultrasound-detected cartilage pathology has recently been summarized in a systematic review: cartilage thickness, sharpness and clarity are the items that are most frequently used to define cartilage pathology [7]. However, ultrasonography is infrequently used in everyday clinical practice for osteoarthritis because of the lack of well accepted ultrasound parameters in this pathology. Therefore, numerous challenges have to be addressed to improve not only the early diagnosis of cartilage alterations but also the monitoring of the cartilage disease evolution.

Focusing on the US research field, new leads are currently investigated. Quantitative ultrasound parameters are currently described to qualify cartilage lesions: thickness, speed of sound, ultrasound reflection coefficient, integrated reflection coefficient, or ultrasound roughness index. These parameters seem sensitive enough to detect mechanical degradation, or fibrillation of cartilage surface. Intra-articular probes are now developed to perform such quantitative ultrasound evaluation in arthroscopic conditions [8]. Neverteless, to the best of our knowledge, no 3D cartilage evaluation has ever been considered with such intra-articular approaches, although mature 3D navigation technologies are available and daily used in clinical practice.

A new medical device

We introduce a new, multimodal and navigated imaging device, usable during a standard arthroscopic procedure. This device enables the realization of on-the-fly virtual biopsies (non-destructive, without sample extraction), thanks to two innovations: the ability to register the instruments' position with regards to pre-operative quantitative imaging, and the ability to enhance the evaluation of cartilage tissue by taking new imaging modes into account. Registration with pre-operative images (MRI with various sequences, arthroscanner) is performed through a two-step, non-rigid deformation process based on the relative position of some key anatomical landmarks, recorded thanks to a 3D-localizer pointer.

Three-dimensional localization (using a stereoscopic camera, with active LED markers on each tracked item, supplied by the French company BlueOrtho) allows to acquire a patient-specific bone volume model, which is key to integrating a user-friendly (automated parameter setup), intra-articular ultrasonic transducer in this arthroscopic setup. It is then possible to precisely measure not only the shape of a defect (area, depth, ICRS grading) but also other features of the cartilage tissue (roughness, stiffness) using real-time data fusion. The addition of other imaging modes (including, but not limited to, Optical Coherence Tomography) will further enhance this evaluation.

The imaging devices' shape and size are similar to arthroscopes (diameter, length) and 3D-localized in the reference space of the patient's anatomy, on a unique screen. This display consists in a 3D anatomic volume (see Figure 1), mapping multiple criteria, both pre-operative (GAG content for example) and per-operative (ICRS score, roughness index). Each per-operative criterion has

the advantage of being updated on-the-fly. Considering the example of defect debridement, it will allow the surgeon to visualize the amount to damaged tissue to remove, check on his progress, and precisely tailor a potential scaffold or implant.

First evaluation

First proofs of concept were obtained during pre-clinical trials on cadaver specimens, at the Grenoble Hospital's anatomopathology laboratory and at the *Laboratoire dAnatomie des Alpes Françaises*. These trials' goal was to show on one hand that compared to histology (see Figure 1) and MRI (see Figure 2) the US data are correct, and on the other hand that such a new device can be used in an arthroscopic setup, its usage validated by surgeons.

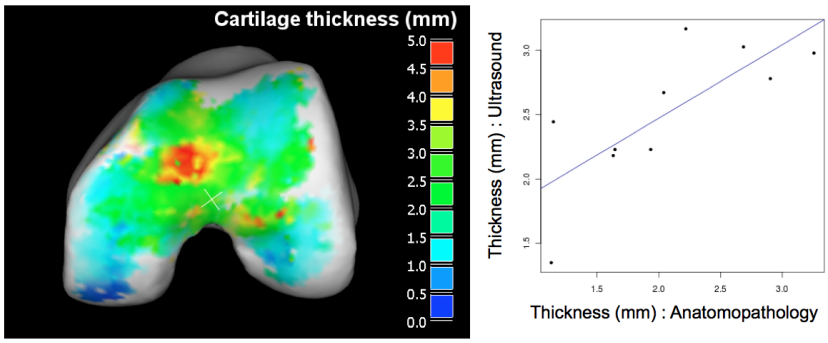

Fig. 1. A cartilage thickness map was computed from the 2.5D US images (gathered under arthroscopic conditions), here on femoral condyles (left). A comparison between histology and ultrasound shows a statistically significant correlation (Kendall: $p = 0.016$) on tibial plateau samples. This comparison is made possible by the fact that the US images are spatially localized with submillimeter precision.

Conclusion

The feasibility of using a navigated, intra-articular ultrasonic transducer in an arthroscopic setup is demonstrated. A first *in-vivo* clinical trial is the next step.

This work was supported by French state funds managed by the *Agence Nationale de la Recherche* within the *Investissements d'Avenir* programme (Labex CAMI), under reference *ANR-11-LABX-0004*.

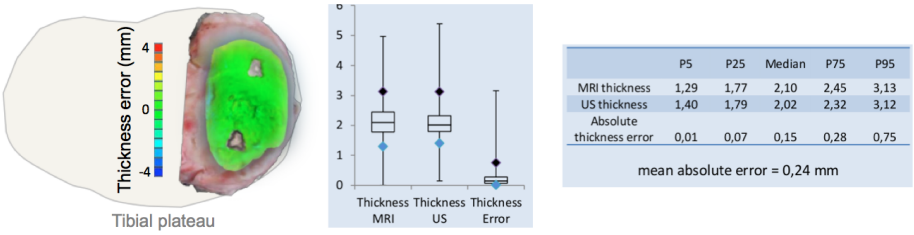

	P5	P25	Median	P75	P95
MRI thickness	1,29	1,77	2,10	2,45	3,13
US thickness	1,40	1,79	2,02	2,32	3,12
Absolute thickness error	0,01	0,07	0,15	0,28	0,75

mean absolute error = 0,24 mm

Fig. 2. Nine tibial plateaus were scanned using both MRI and US. A low mean absolute error between imaging modes validates the use of US for the measurement of cartilage thickness, and the evenly distributed difference (here, the example of plateau n7 from the set) validates the hypothesis made regarding the ultrasound speed in cartilage.

References

1. Chan, W.P., P. Lang, M.P. Stevens, K. Sack, S. Majumdar, D.W. Stoller, et al., Osteoarthritis of the knee: comparison of radiography, CT, and MR imaging to assess extent and severity, in AJR Am J Roentgenol. 1991. p. 799-806.
2. Matzat SJ, van Tiel J, Gold GE, Oei EH.Quantitative MRI techniques of cartilage composition. Quant Imaging Med Surg. 2013 Jun;3(3):162-74.
3. Brittberg, M. and C.S. Winalski, Evaluation of cartilage injuries and repair. J Bone Joint Surg Am, 2003. 85-A Suppl 2: p. 58-69.
4. Brismar, B.H., T. Wredmark, T. Movin, J. Leandersson and O. Svensson. Observer reliability in the arthroscopic classification of osteoarthritis of the knee. J Bone Joint Surg Br, 2002. 84(1): p. 42-7
5. Ayral, X., A. Gueguen, R.W. Ike, J.P. Bonvarlet, L. Frizziero, K. Kalunian, et al., Inter-observer reliability of the arthroscopic quantification of chondropathy of the knee. Osteoarthritis Cartilage, 1998. 6(3): p. 160-6.
6. Oakley, S.P., I. Portek, Z. Szomor, A. Turnbull, G.A. Murrell, B.W. Kirkham, et al., Poor accuracy and interobserver reliability of knee arthroscopy measurements are improved by the use of variable angle elongated probes. Ann Rheum Dis, 2002. 61(6): p. 540-3.
7. Keen, H.I., R.J. Wakefield and P.G. Conaghan. A systematic review of ultrasonography in osteoarthritis. Ann Rheum Dis, 2009. 68(5): p. 611-9.
8. Podlipska J, Koski JM, Pulkkinen P, Saarakkala S. In vivo quantitative ultrasound image analysis of femoral subchondral bone in knee osteoarthritis. ScientificWorldJournal. 2013.

Vector field interpolation for scapular position and orientation estimation from noisy acromial motion capture.

BOUVEL Simon (1,2,3), ROBY-BRAMI Agnès (1,2,3), MOREL Guillaume (1,2,3), PASQUI Viviane (1,2,3)
1- Sorbonne Universités, UPMC Univ Paris 06, UMR 7222, ISIR, F-75005, Paris, France
2- CNRS, UMR 7222, ISIR, F-75005, Paris, France
3- INSERM, U1150, Agathe-ISIR, F-75005, Paris France

1. Introduction

Several shoulder pathologies, such as impingement syndrome or rotator cuff tear, affect a large group of the population. Being able to prevent them or being able to design efficient shoulder prosthesis requires a good understanding of the shoulder mechanics, and therefore being able to measure the shoulder position and orientation accurately during motion. Measurement techniques all have a degree of invasivity and accuracy. An ideal measurement method would be accurate and non-invasive.

This study focuses on the estimation of the motion of the scapula using optoelectronic motion capture, therefore completely non-invasive. The main method for recording the scapular motion is to use a physical cluster of motion capture markers on the acromion (a flat part of the scapula). Yet, due to important skin tissue artifact, the measurement is not accurate after a certain degree of elevation of the arm [1,2]. However, another system usable with non-invasive motion capture is the scapula locator. It is more precise than the acromial cluster but can only be used as the subject remains motionless [1,2,3].

In this study, we separate the data acquisition in two parts: a first set of so-called prerecorded data is acquired, as the subject remains motionless, using both an acromial cluster (inaccurate) and a scapula locator (gold standard). This data is not sufficient for a motion analysis as there is no guarantee that the subject will go through the same trajectory during motion. A second set of data is acquired as the subject performs a motion, using only the acromial cluster.
From the prerecorded data, a set of transformations between the acromial cluster and the scapula locator can be computed. Our goal is to find an estimate of this transformation at every available configuration of the second set of data (during motion). Then, applying the estimated transformation to the measured acromial cluster during motion would give a better estimation of the scapula position and orientation during motion.

1. Methods

a. Problem formulation

This is a case of spatial interpolation of transformation problem. Knowing a set of transformations at certain points in space from the prerecorded data, the objective is to find an estimation of this transformation at other points. Due to complications induced by the orientations not being elements of a vector space, we focused on interpolating points from the acromion to points on the scapula, the resulting estimation of the scapular point being the mean of all estimations.

This is a problem of multivariate interpolation. After trying simple algorithms such as the inverse distance method or nearest neighbor method that turned out ineffective, the natural neighbors interpolation was used. This method is known for providing a smooth interpolation, so seems well suited for the problem.

b. Description of the algorithm

Consider $P^i, i \in [1,n]$, n elements of R^m, on which are associated $f^i, i \in [1,n]$ n functions(Fig. 1a). Our goal is to estimate this function at another point P_e. The natural neighbors algorithm is a weighted averaging method. Computing the weights is performed in three steps :

- The Voronoï tessellation of $\{P^i, i \in [1,n]\}$ is computed (Fig. 1b). This provides for each P^i an associated Voronoï cell c_i
- The Voronoï tessellation of $\{P^i, i \in [1,n]\} \cup \{P_e\}$ is computed (Fig. 1c). Only the cell $c_e$associated to P_e will be used.
- The weights $w_i, i \in [1,n]$ can be computed by : $w_i = \frac{Volume\ of\ c_e \cap c^i}{Volume\ of\ c^i}$ (Fig. 1d)

Then, the estimated function f_e associated to P_e is computed by : $f_e = \frac{\sum_{i=1}^{n} w_i f^i}{\sum_{i=1}^{n} w_i}$.

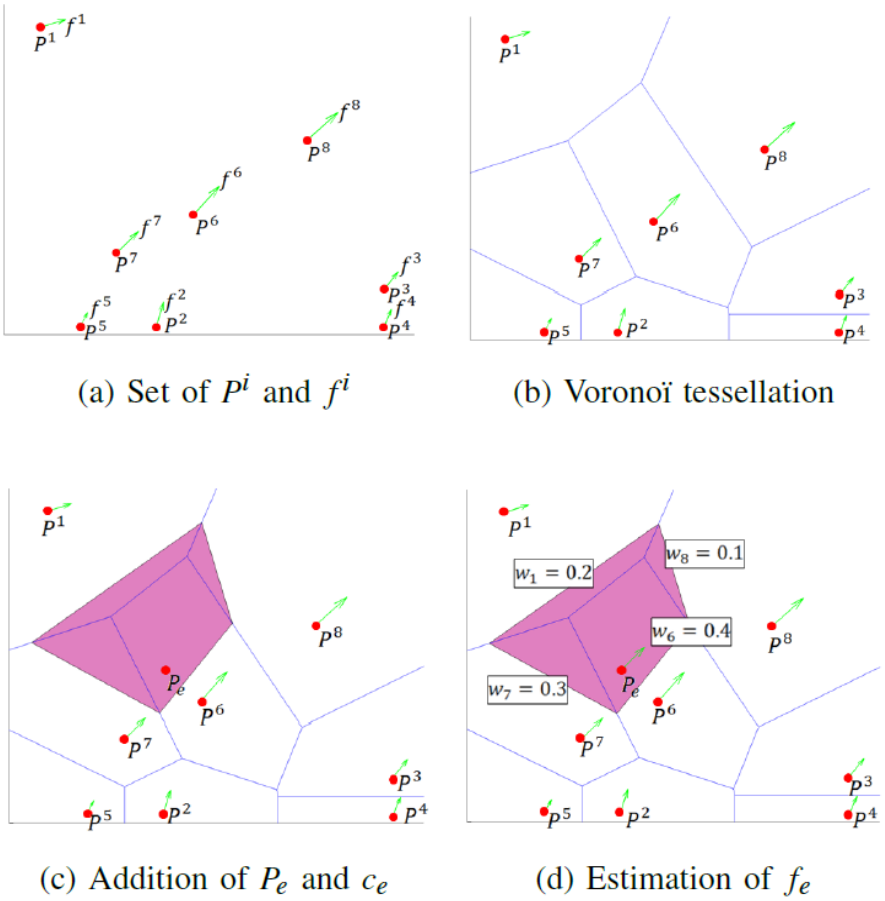

Figure 1 : Description of natural neighbors interpolation.

Practically, the points P^i are the positions of the points of the acromial cluster from the prerecorded data, the points P_e are the positions of the points of the acromial cluster from data

during motion, and the functions f^i are the vectors pointing from one point of the acromial cluster to another point of the scapula.

c. Experimental setup

For the validation of this method, we did not set up an experiment on human subjects. This is due to the absence of ground truth regarding the position of the scapula during motion. Instead, we tested the method on a 7 degrees on freedom WAM manipulator robot, on which we attached a piece of flexible material (Fig. 2). We used the optoelectronic CODAMOTION motion capture device to acquire data. We placed markers both on the acromial cluster placed on the soft material and on the arm of the robot (Fig. 2).

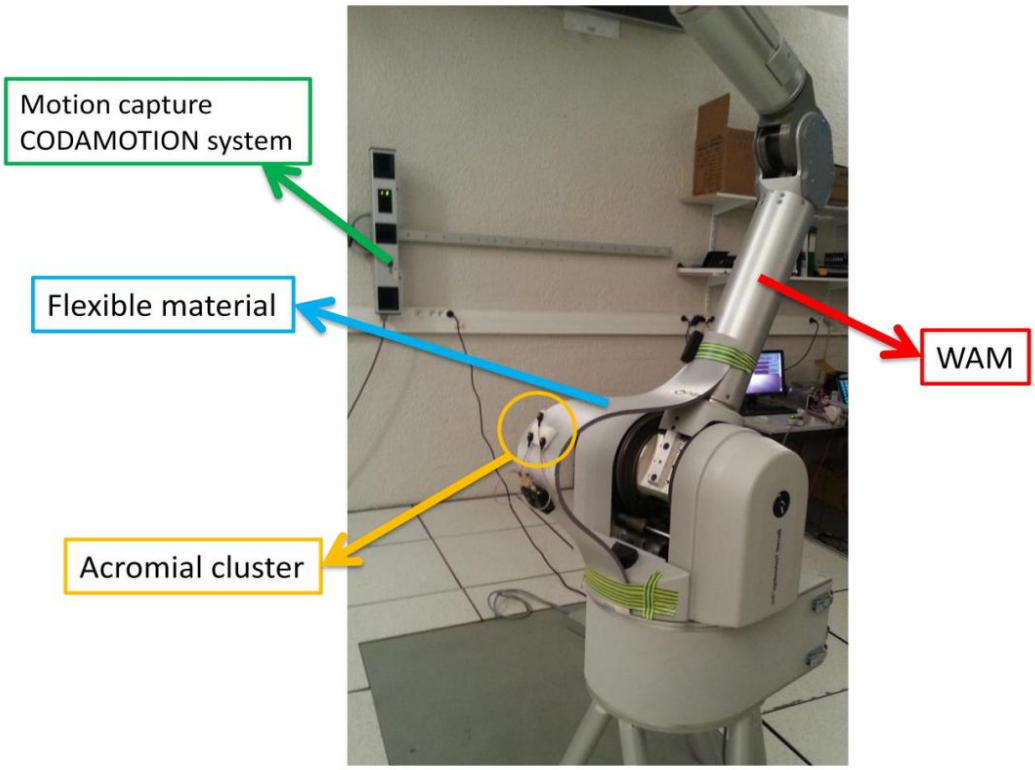

Figure 2 : experimental setup

A set of prerecorded data was setup, the markers on the soft tissue playing the role of the acromial cluster, and the ones on the arm of the robot play the role of the scapula locator. From there, the transformations between the markers on the soft tissue and the ones on the robot can be computed. Then, the robot is controlled to do a simple motion. From this second set of data, only the positions of the points on the soft tissue were considered. The algorithm was then applied on these points, with knowledge of the prerecorded data, to estimate the position of the points on the arm of the robot. An error can be computed between the estimated points positions and the measured ones.

There are large deformations of the soft tissue as the robot performs its movement. This ensures that the soft tissue displacement is greater than what it would be in the case of a scapular study. Note that the motion of the robot does not accurately match the motion of the shoulder, but the induced deformations with the robot are greater. So any error reduction with this experimental setup will be increased with a scapular study.

2. Experimental results

The mean position error between the estimated points and the measured points was 7.1mm (std 6.6mm), with a maximum value of 35mm and a minimum value of 0.1mm. Note that the deformation induced displacement was around 150mm, so the estimation seems efficient. Compared to what the error would be in case of rigid transformation between the markers on the soft tissue and the ones on the robot, there is up to 90% error reduction.

For an improvement on this method, we need not only to consider the interpolation of the positions, but also orientation, which brings its lot of problems. We could integrate in the position/orientation of all the other joints available, such as the elbow, which probably gives valuable information. A priori knowledge of the joints kinematics could also be integrated in the algorithm in future works.

This work was supported by French state funds managed by the ANR within the Investissements d'Avenir programme (Labex CAMI) under reference ANR-11-LABX-0004

References

[1] S. Brochard, M. Lempereur, and O. Rémy-Néris, "Double calibration: an accurate, reliable and easy-to-use method for 3D scapular motion analysis." Journal of biomechanics, vol. 44, no. 4, pp. 751–4, Feb. 2011.

[2] A. R. Karduna, P. W. McClure, L. a. Michener, and B. Sennett, "Dynamic Measurements of Three-Dimensional Scapular Kinematics: A Validation Study," Journal of Biomechanical Engineering, vol. 123, no. 2, p. 184, 2001.

[3] J. a. I. Prinold, A. F. Shaheen, and A. M. J. Bull, "Skin-fixed scapula trackers: a comparison of two dynamic methods across a range of calibration positions." Journal of biomechanics, vol. 44, no. 10, pp. 2004–7, July 2011

ORGAN DETECTION AND TRACKING

Assistance to High Intensity Focused Ultrasound (HIFU) therapy: Real-time motion compensation using ultrafast ultrasound imaging

Laure-Anaïs Chanel[1], Florent Nageotte[1], Jonathan Vappou[1], Jianwen Luo[2], Loïc Cuvillon[1], Michel de Mathelin[1]

1: ICube, UMR 7357 Université de Strasbourg-CNRS
2: Department of Biomedical Engineering, School of Medicine, Tsinghua University, Beijing, China

Background:

HIFU therapy is a very promising non-invasive and non-ionizing method for ablation of solid tumors[1]. HIFU therapy relies on the absorption of the acoustic energy at the focal region, leading to localized tissue heating and necrosis subsequently. Some applications of this therapy such as ablation of prostate tumors and of uterine fibroids are already used in clinical routine. Other applications such as tumor ablation in intra-abdominal organs (liver, kidney, pancreas etc.) are still under research. One of the major challenges in intra-abdominal HIFU therapy is the need to find an adequate acoustic window, which is particularly complex due to the presence of bone (e.g. ribs) and air (e.g. intestine, lungs). Another major problem of HIFU therapy in intra-abdominal organs is their physiological motion, which is principally due to breathing[2], thus preventing the focused ultrasound beam from targeting correctly the tumor. The main solution to overcome this limitation is to perform HIFU sonication only during the patient apnea periods. However, this solution is associated with substantially longer treatment times and decreased efficiency. In this context, we are developing an all-in one robotized HIFU solution for active motion compensation in real-time using ultrafast ultrasound imaging. Motion compensation using standard US probes has already been proposed (see [3] for instance). In this study, we aim at (1) Improving the accuracy and spatial resolution of displacement estimates by working directly on raw radiofrequency (RF) ultrasonic signal, and (2) Coupling our ultrasound imaging system with a HIFU transducer for simultaneous displacement estimation during HIFU treatment.

Methods:

An ultrasound visual servoing system was developed in order to keep the distance between the HIFU transducer and the tumor constant during the whole treatment. An ultrasound probe is inserted into the spherical HIFU transducer through its central hole so that the position of the HIFU focal point is fixed in the conventional US image. The ultrasound probe is attached to the effector of a robot (Sinters) in an eye-in-hand configuration. A fast ultrasonic speckle tracking method was used to estimate motion in real time. This method consists in cross correlating ultrasound RF signal between the initial image and the current image. It does not require B-mode reconstruction and can be applied in any subregion of the image. An ultrafast displacement estimation method that relies on pre-calculated sum-tables, avoiding redundancy in cross-correlation calculations is used [4] . Ultrasound RF signals are acquired using a research ultrasound imaging system (Verasonics, WA, USA). A phased array ultrasound probe (f=2.5 MHz) was used in this study.

The central frequency of the HIFU transducer was 2 MHz and was driven at an electrical power equal to 40 W, which corresponds to an acoustic power of approximately 20 W. In order to avoid any interference between the HIFU and the imaging ultrasound signals, an interleaved sequence was used (8 ms imaging / 42 ms HIFU heating for a 50 ms cycle)

The position of the HIFU transducer is controlled in real-time by the robotic arm. A Position-Based Visual Servoing loop working at 20 Hz is used, where the position error is given by the displacement corresponding to the "residual motion" measured by the speckle tracking algorithm. A proportional controller computes the velocity input sent to the robot, which has a 500 Hz internal control loop with a PID and a trajectory generator. The image acquisition and processing steps (reconstruction and motion estimation) introduce a delay estimated to 12 ms approximately.

The visual servoing scheme was simulated on Simulink and then tested on a phantom made of silicon with cellulose particles for backscattering of the imaging ultrasound beams (see Figure 1). For a good transmission of ultrasound, this phantom was immersed in degased and demineralized water. The phantom was positioned on a motorized x-table to simulate the organ motion.

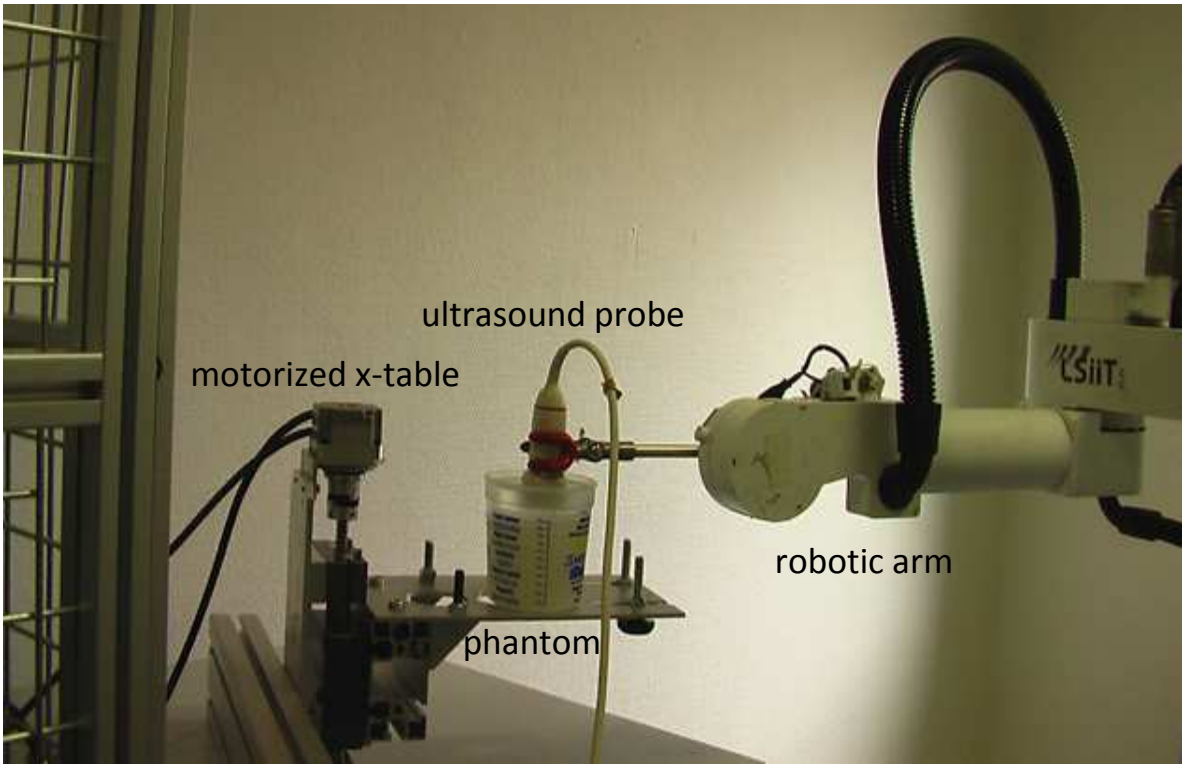

Figure 1: Experimental set up

Results:

For a 1D motion of 2.3 mm of amplitude and 0.25 Hz of frequency and a controller gain of 12, simulation results on Simulink showed a residual motion of 0.3 mm in amplitude which corresponds to a reduction of 87 % of the object motion. As for the result of the experiment on the phantom, the mean residual motion was 0.33 mm in amplitude (maximum amplitude of 0.42 mm), which corresponds to a reduction of 86% of the phantom motion (see Figure 2).

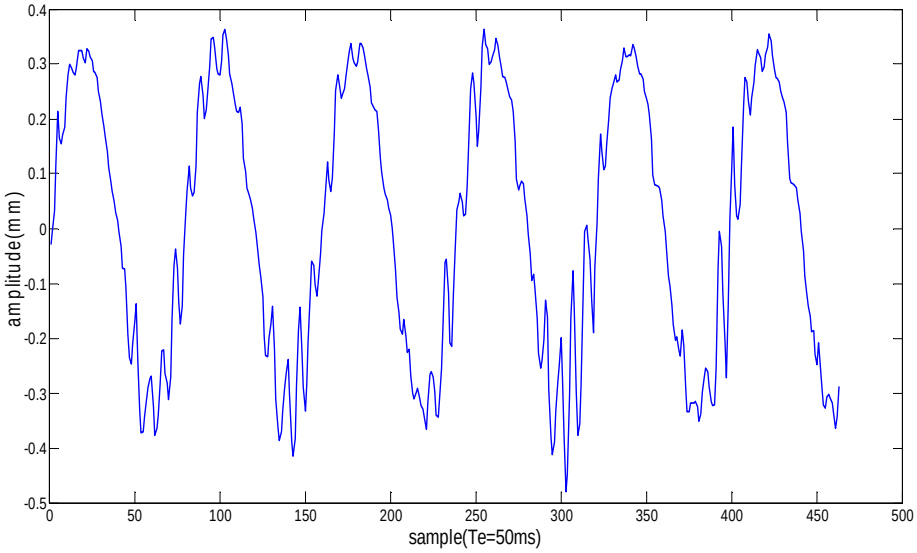

Figure 2: residual motion estimated by ultrasound imaging for a 1D motion of 2.3 mm of amplitude

The actual amplitude of breathing motion is larger than the one used here (typically 1 to 2.5 cm for liver, 1 to 1.5 cm for kidney and less than 2 cm for pancreas peak to peak) [2]. We can however estimate that for a typical breathing motion of 2 cm of amplitude peak to peak, the residual motion would be 1.4 mm. This is deemed to be negligible in most of the clinical cases except for in the case of very small tumor (<1cm in diameter). Though breathing motion is predominant in the superior-inferior axis, motion in antero-posterior axis reaching a maximum of 10 mm and motion in lateral axis reaching a maximum of 5 mm peak to peak need to be taken into account.

Conclusion:

The experimental results show that the visual servoing allows for a significant reduction of the apparent motion. The robotized system is thus proved to be efficient for motion compensation. Optimizing this system is needed for a larger reduction of the motion, for instance by using a more advanced controller. For further studies, HIFU sonications will be performed in order to assess differences in terms of thermal lesion. First, sonication will be performed without any motion, then with motion but without motion compensation and finally with both motion and visual servoing.

Acknowledgment:

This work was partly supported by the French ANR within the Investissements d'Avenir program (Labex CAMI) under reference ANR-11-LABX-0004

References:

[1] J. W. Jenne, T. Preusser, and M. Günther, "High-intensity focused ultrasound: Principles, therapy guidance, simulations and applications", *Zeitschrift für Medizinische Physik*, vol. 22, no. 4, pp. 311–322, Dec. 2012.

[2] A. Muller, L. Petrusca, V. Auboiroux, P. J. Valette, R. Salomir, and F. Cotton, "Management of Respiratory Motion in Extracorporeal High-Intensity Focused Ultrasound Treatment in Upper Abdominal Organs: Current Status and Perspectives", *Cardiovasc Intervent Radiol*, vol. 36, no. 6, pp. 1464–1476, Dec. 2013.

[3] A. Krupa, G. Fichtinger, and G. D. Hager, "Real-time motion stabilization with B-mode ultrasound using image speckle information and visual servoing", *The International Journal of Robotics Research*, vol. 28, no. 10, pp. 1334–1354, 2009.

[4] J. Luo and E. E Konofagou, "A fast normalized cross-correlation calculation method for motion estimation", *Ultrasonics, Ferroelectrics and Frequency Control, IEEE Transactions on*, vol. 57, no. 6, pp. 1347–1357, 2010.

Interactive Tracking of Soft Tissues in 2D Ultrasound Images

Lucas Royer[1,2,3], Maud Marchal[1,3], Anthony Le Bras[4], Guillaume Dardenne[1], and Alexandre Krupa[1,2]

[1]Institut de Recherche Technologique b-com, Rennes, France
[2]Inria Rennes - Bretagne Atlantique, France
[3]INSA de Rennes, France
[4]CHU de Rennes, France

June 12, 2014

1 Introduction

In several medical applications such as liver or kidney biopsies, an anatomical region needs to be continuously tracked during the intervention. When using ultrasound (US) image modality, tracking soft tissues remains challenging due to the deformations caused by physiological motions or medical instruments, combined with the generally weak quality of the images. In order to overcome the previous limitation, different techniques based on physical model have been proposed in the literature. [SMSM06] proposed a registration method based on the mass-spring system in order to constrain the deformation, and Zhang *et al* [ZW13] introduced an other registration technique based on finite element model where the extraction of the scale invariant features is needed. However, their model are built from features which are difficult to extract in US images due to the speckle noise. Finally, Marami *et al* [MSFC14] presented very recently an elastic registration method applicable to multi-modality image registration where the deformation is computed from modality independent neighborhood descriptor. In this paper, we propose an approach for tracking deformable target within 2D US images based on a physical model driven by smooth displacement field obtained from dense information. This allows to take into account highly localized deformation in the US images. Section 2 presents our method based on a combination of an intensity-based approach and a physically-based model. Section 3 describes the performances of our approach and comparisons on real data. Section 4 concludes the paper.

2 Method

2.1 Definition of the Tracking Region

The target is defined by a region of interest composed of N_p pixels. A grid of N_c control points is superimposed on it such that $N_c << N_p$. The grid is composed of a set of blocks where each corner represents a control point. Each block includes a constant number of pixels N_b and four controls points. A pixel position P is related to the associated control points by using a bi-linear interpolation. Thus, for the vector $\mathbf{P}$ containing all the pixel positions, and the vector $\mathbf{P_c}$ containing the control points positions, we have the following relation:

$$\mathbf{P} = \mathbf{C}.\mathbf{P_c} \tag{1}$$

where $\mathbf{C}$ is a matrix $N_p \times N_c$ which contains all the bi-linear coefficient of each pixel position in function of its control points. The equation 1 allows to estimate the N_p pixels positions from the control points coordinates. In this paper, our objective is to interactively find the positions of the control points such that the region of interest keeps being tracked at any time thanks to the intensity variation of each pixel.

2.2 Intensity-based Approach

Let us define $\mathbf{I}$ the vector composed of the intensity values of the N_p pixels. The objective is to define the optimal displacement of the control points such that the error difference on the pixel intensities between the initial image

and the current image is minimized. We propose to use an approach which relates the intensity time variation to the displacements of the control points by using a Jacobian $\mathbf{J}$:

$$\dot{\mathbf{I}} = \mathbf{J}.\dot{\mathbf{P_c}} \tag{2}$$

where $\dot{\mathbf{I}}$ is the time variation of the pixel intensities and $\dot{\mathbf{P_c}}$ the displacements of the control points. Combining equations 1 and 2, the Jacobian can be expressed as:

$$\mathbf{J} = \nabla\mathbf{I}.\mathbf{C} \tag{3}$$

where $\nabla\mathbf{I}$ represents the gradient of the pixel intensities regarding the x and y. As it was shown in [NK13], if we want to ensure an exponential decrease of the error between the reference and current template, we can express the variation of the control points $\widehat{\dot{\mathbf{P_c}}}$ between the initial and current states as :

$$\widehat{\dot{\mathbf{P_c}}} = -\lambda.\mathbf{J}^{+}.(\mathbf{I_{current}} - \mathbf{I_{ref}}) \tag{4}$$

where $\lambda > 0$ is the proportional coefficient involved in the exponential convergence decrease of the difference between the current intensities $\mathbf{I_{current}}$ and the initial ones $\mathbf{I_{ref}}$. $\mathbf{J}^{+}$ represents the pseudo-inverse matrix of the Jacobian $\mathbf{J}$. In this work, we chose to constrain the deformation by integrating a physically-based model of the expected deformation.

2.3 Deformable Component

In order to take into account the deformations of the region of interest, a deformable model is superimposed to it. Our deformable model consists of a mass-spring-damper system where the nodes are the controls points of the grid. Thus, the force F_{ij} exerted on a control point P_c^i from a neighbor point P_c^j is:

$$F_{ij} = (K_{ij}(d_{ij} - d_{ij}^{init}) + D_{ij}(\dot{P_c^i} - \dot{P_c^j}))(P_c^i - P_c^j) \tag{5}$$

where d_{ij} represents the distance between the two control points in their current position. d_{ij}^{init} represents the initial distance value. K_{ij} is the stiffness of the spring while D_{ij} is the damping coefficient. The values of these coefficients can be different, depending on the homogeneities of the tissues. The forces applied on each control point P_c^i of the deformable system could be summarized in F_i:

$$F_i = \sum_{j^{neighbors}} F_{ij} + G_i\dot{P_c^i} + F_{ext} \tag{6}$$

where G_i is the velocity damping coefficient and F_{ext} corresponds to the external forces. We chose to use a semi-implicit Euler integration scheme for simulating our system. The external forces are computed from the control points displacements $\widehat{\dot{\mathbf{P_c}}}$ from equation 4. We integrate at each time step this displacement to obtain the external force representing the intensity variation. Once the external forces have been applied to the mass-spring-damper system, the simulation is performed in order to obtain the resulting displacements of the control points.

3 Results

We evaluated the performances of our method on real sequences of acquired 2D US images. The deformable targets were chosen in human liver US images acquired thanks to a 2D convex US probe of 2-5 MHz frequency bandwidth (C60, Sonosite). The tracking system is built from ViSP C++ library, and its computation time is estimated to 1.4 second per frame with non-optimized code. In order to test the robustness of both method on real data, we performed our test on a real sequence containing 173 images of 640 × 480 pixels. In this sequence, the target represents an hyper-echogenic area. Moreover, we added an extra rigid motion which translates and rotates the original sequence. We also launched the tracking without mass-spring based only on the intensity image variation. The results are presented in figure 1 from which we can see that the presence of dynamic noise results to the mis-estimation of the deformation which makes the target tracking fails without the mass-spring system. With our approach the deformable target is well tracked (fig. 1).

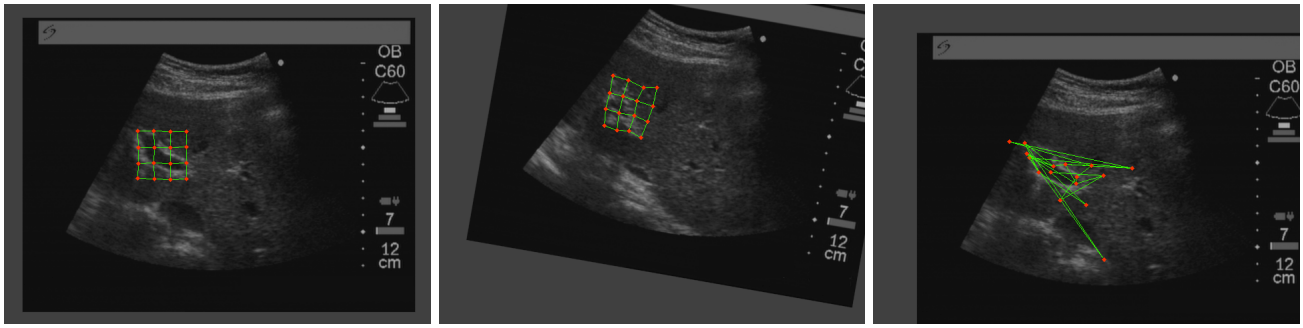

Figure 1: Results estimated on real data. (Left) Template tracking with mass-spring system at initialization (frame 1). The grid (size of each block 8×8 pixels) is with its initial shape due to low amount of deformation. (Middle) Template tracking with mass-spring system after deformation (frame 65). We can observe that the grid is deformed due to low similarity between reference template and current template. (Right) Template tracking without mass-spring system at frame 13. For the last case, we observe tracking failure due to the speckle noise presence.

4 Conclusion

We proposed an interactive approach for tracking deformable target within 2D US images based only on dense information and a physically-based model. In order to estimate both the rigid and the elastic motions of the soft tissues, we included in our approach a physically-based model superimposed to the region of interest. This deformable model is controlled by the intensity variation of the image and allows to take into account highly localized deformations in the US images. It opens novel perspectives in computer-assisted interventions based on US imaging and where deformable organs are involved, such as image-guided needle biopsy.

References

[MSFC14] Bahram Marami, Shahin Sirouspour, Aaron Fenster, and David W. Capson. Dynamic tracking of a deformable tissue based on 3d-2d mr-us image registration. In *Proceedings of SPIE Medical Imaging*, 2014.

[NK13] C. Nadeau and A. Krupa. Intensity-based ultrasound visual servoing: Modeling and validation with 2-d and 3-d probes. *IEEE Transactions on Robotics*, 29(4):1003–1015, 2013.

[SMSM06] Jian-Kun Shen, Bogdan J. Matuszewski, Lik-Kwan Shark, and Christopher J. Moore. Deformable image registration using spring mass system. In Mike J. Chantler, Robert B. Fisher, and Emanuele Trucco, editors, *BMVC*, pages 1199–1208. British Machine Vision Association, 2006.

[ZW13] Jingya Zhang and Jiajun Wang. Model-based nonrigid image registration using scale-invariant features. In *Signal Processing, Communication and Computing (ICSPCC), 2013 IEEE International Conference on*, pages 1–5, Aug 2013.

Fully Automatic Organ Localization in Medical Images Using Improved Random Regression Forests

Prasad Samarakoon, Emmanuel Promayon and Céline Fouard
TIMC-IMAG Laboratory, CNRS UMR 5525 , University of Joseph Fourier, Grenoble, France
{*Prasad.Samarakoon, Emmanuel.Promayon, Celine.Fouard*} *@imag.fr*

***Index Terms*—localization, random regression forests, medical image analysis**

The article presents the use of an improved random regression forest method to localize multiple organs in Computed Tomography (CT) images. The method was trained using 50 CT images and tested on 25 CT images yielding 15.66% improvement on the localization with respect to the bounding wall prediction error compared to the state of the art results.

I. Introduction

RANDOM Regression Forests (RRF) were first used in the field of medical image analysis by Criminisi et al.[1] to automatically localize multiple organs in CT images. The organ localization problem was solved as a continuous parameterization regression problem in which the image voxels were directly mapped to a localized organ bounding box.

II. Methodology

RRF consists of a collection of Random Regression Trees (RRT). Each RRT comprises of split and leaf nodes (Figure 1). At each split node j the following binary split function (whose sole purpose is binarily dividing the incoming voxels) is defined:

$$\xi_j > f\left(\mathbf{v}, \theta_j\right) > \tau_j \tag{1}$$

where $\xi_j, \tau_j \in \mathbb{R}$ are upper and lower thresholds and $f\left(\mathbf{v}; \theta_j\right)$ is the weak learner response computed at the voxel $\mathbf{v}$ and θ_j is the weak learner (inspired by [1], [2], [3]). Each leaf node (l) predicts the a posteriori probability of an organ's bounding box with respect to the position of the leaf:

$$\Pr\left(\mathbf{d}_c|l\right) = \mathcal{N}\left(\mathbf{d}_c, \bar{\mathbf{d}}_c, \Lambda\right) \tag{2}$$

where $\mathbf{d}_c$ is the bounding box vector of organ C; $\bar{\mathbf{d}}_c$,$\Lambda$are mean and covariance of $\mathbf{d}_c$.

RRF has two main phases. 01.) Training phase: building RRF using training images where the target organ's bounding boxes are manually delineated. 02.) Testing phase: using the trained RRF on a new image to predict the localization of target organs.

At the training phase each split node is given a collection of different split configurations consisting of a lower and upper threshold and a weak learner. The split function is applied to all voxels reaching that particular split node across all available split configurations. Then the split configuration that best discriminates the incoming voxels is found using an information gain measure (Eq. 3). The lower and upper thresholds and weak learner of the selected split configuration are saved as the values of the corresponding split node.

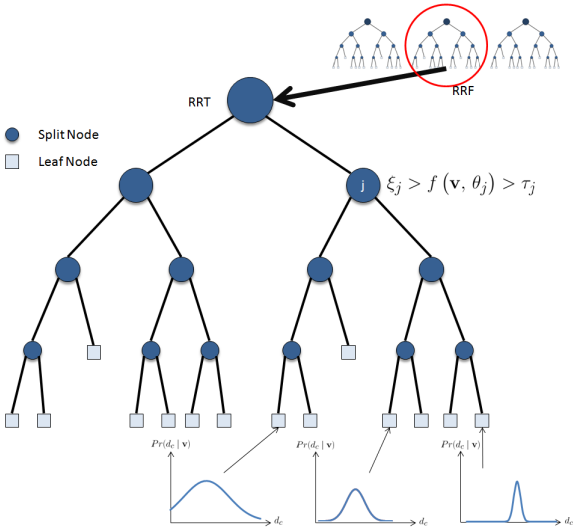

Figure 1. **Random Regression Forest** is a collection of regression trees. Each regression tree consists of split nodes (including root) and leaf nodes. Split nodes have the responsibility of dividing the incoming voxels into two parts depending on the response of the split function. Ultimately, the leaf nodes define the a posteriori probabilities of the organ bounding boxes with respect to the position of the leaf.

$$IG(\mathcal{S}, \theta) = H(\mathcal{S}) - \sum_{i=\{L,R\}} w_i H(\mathcal{S}_i) \tag{3}$$

where *H*: entropy; $\mathcal{S}$: set of voxels reaching the split node; *L,R*: left and right children resulted from the parameters defined by ξ_j, τ_j, θ_j and $\omega_i = \frac{\mathcal{S}_i}{\mathcal{S}}$: the relative portion of voxels reaching the child. Eq. 3 can be approximated by:

$$IG(\mathcal{S}, \theta) = \log\left(|\Gamma\left(\mathcal{S}\right)|\right) - \sum_{i=\{L,R\}} w_i \log\left(|\Gamma\left(\mathcal{S}_i\right)|\right) \tag{4}$$

where $\Gamma\left(\mathcal{S}\right)$: $\Gamma = \mathrm{diag}\left(\Lambda_{ld}, \Lambda_{rd}\right)$.

Growing of RRT is stopped when the depth of RRT has reached a predefined maximum decision level or when the

number of voxels reaching the node is below a certain predefined threshold or when there is no positive information gain. Leaf nodes of a trained RRT will store $\bar{\mathbf{d}}_c$ and Λ_c of $\mathbf{d}_c$s of all the voxels aggregated at the particular leaf. Hence at leaf nodes, $\Pr(\mathbf{d}_c|l)$ is known.

At the testing phase, every voxel $\mathbf{v}$ of an unseen image volume $\mathcal{V}$, is pushed through each RRT where the split function is applied at each split node and is eventually aggregated at a leaf node per RRT of RRF. Once all the voxels are treated, the absolute position of each leaf node $\hat{\mathbf{v}}$ is found by calculating the mean of all voxels aggregated at that leaf node contrary to using the mode as in [1] and [4].

Then absolute position of the bounding box vector $\Pr(\bar{\mathbf{b}}_c|l)$ can be known since $\mathbf{b}_c = \hat{\mathbf{v}} - \mathbf{d}_c$. Finally, the absolute position of the organ's bounding box ($\mathbf{b}_c$) is found by taking the total probability summation:

$$\Pr(\mathbf{b}_c) = \sum_{t=0}^{T} \sum_{l \in \mathcal{L}_t} \Pr(\mathbf{b}_c|l) \Pr(l) \tag{5}$$

where $\mathcal{L}_t$: subset of leaf nodes used for calculation; $\Pr(l)$: proportion of voxels at leaf l with respect to all voxels of $\mathcal{L}_t$. $\mathcal{L}_t$ is determined by choosing the best discriminating leaf nodes of RRF having the highest confidence in their predictions.

III. Results and Discussion

RRF method was implemented to localize left and right kidneys of 75 CT images belonging to 75 patients randomly selected from the CHU Grenoble database without considering any specific pathology. From which, 50 and 25 images were randomly selected for training and testing respectively. RRF consisted of 3 RRTs using 9 maximum decision levels (parameters were influenced by [1]). Results were produced within 1.62 seconds on average for an image of average size of 30 cm x 30 cm x 40 cm (100 x 100 x 245 voxels).[1]

Our method produced better results in comparison to the literature with respect to the bounding wall prediction error BWPE[2] (Table Ia) and centroid hit error CHE[3] (Table Ib). The use of a predictive determination of Lt using the input image instead of a hardcorded percentage of voxels (1% in [1] and 75% in [4]) contributes to the amelioration. In addition, using mean instead of mode when calculating the leaf node position seems to better preserves the probabilistic impact and to counter some ill effects of the outliers.

[1]Results were generated on an Intel® Xeon® @ 3.00 GHz machine with 32 GB of RAM using sequential programming.

[2]BWPE is the absolute error between the automatically predicted bounding box wall and the manually segmented bounding box wall [5].

[3]CHE occurs when the centroid of the automatically predicted bounding box falls outside the bounding box drawn manually [5]. In the case of a CHE, it is further investigated in which direction/directions the Centroid has overflown with respect to the manually drawn bounding box. In 3D image volumes, three directions; namely, left to right, anterior to posterior and feet to head are present.

	Our Method			*Criminisi [4]*			*Pathak[5]*		
	M	Sd	Md	M	Sd	Md	M	Sd	Md
RK	13.2	12.2	10.3	16.1	15.5	-	18.5	18.0	12.3
LK	11.9	11.9	9.2	13.6	12.5	-	17.3	16.5	12.8

(a)

	Our Method		*Pathak [5]*	
Direction	RK	LK	RK	LK
All	8%	8%	26%	20%
Left to right	0%	0%	8%	10%
Anterior to posterior	0%	4%	10%	12%
Inferior to superior	8%	4%	22%	16%

(b)

Table I. **(a) Bounding wall prediction error comparison with *Criminisi et al.* [1], [4] and *Pathak et al.* [5]** in mm**.** RK, LK: Right and left kidney, M: mean, Sd: standard deviation, Md: median. **(b) Centroid-hit error comparison with *Pathak et al.*** [5] (where 100 testing images were used).

IV. Conclusion

Random Regression Forests method with the intuitive testing mechanisms proposed is quite efficient in localizing organs fully automatically producing results within 1.62 seconds. With the proposed improvements, mean BWPE was reduced by 15.66% with respect to the previous state of the art results.

Our future work will focus on reducing the training time by using parallel programming and applying RRF to other image modalities such as MRI.

Acknowledgements: This work was supported by the French ANR within TECS project Robacus (ANR-11-TECS-020-01) and within the Investissements d'Avenir programme - Labex CAMI (ANR-11-LABX-0004). The authors are grateful to Prof. Ivan Bricault of CHU Grenoble for providing the CT images.

References

[1] A. Criminisi, J. Shotton, D. Robertson, and E. Konukoglu, "Regression forests for efficient anatomy detection and localization in CT studies," in *Medical Computer Vision. Recognition Techniques and Applications in Medical Imaging*, no. 6533 in Lecture Notes in Computer Science, pp. 106–117, Springer Berlin Heidelberg, Jan. 2011.

[2] A. Criminisi, J. Shotton, and S. Bucciarelli, "Decision forests with long-range spatial context for organ localization in CT volumes," in *MICCAI Workshop on Probabilistic Models for Medical Image Analysis*, 2009.

[3] R. Cuingnet, R. Prevost, D. Lesage, L. D. Cohen, B. Mory, and R. Ardon, "Automatic detection and segmentation of kidneys in 3D CT images using random forests," in *Medical Image Computing and Computer Assisted Intervention MICCAI 2012*, no. 7512 in Lecture Notes in Computer Science, pp. 66–74, Springer Berlin Heidelberg, Jan. 2012.

[4] A. Criminisi, D. Robertson, E. Konukoglu, J. Shotton, S. Pathak, S. White, and K. Siddiqui, "Regression forests for efficient anatomy detection and localization in computed tomography scans," *Medical Image Analysis*, vol. 17, no. 8, pp. 1293–1303, 2013.

[5] S. D. Pathak, A. Criminisi, J. Shotton, S. White, D. Robertson, B. Sparks, I. Munasinghe, and K. Siddiqui, "Validating automatic semantic annotation of anatomy in DICOM CT images," in *SPIE Medical Imaging 2011: Advanced PACS-based Imaging Informatics and Therapeutic Applications*, vol. 7967, pp. 796704–796704, Mar. 2011.

Surgetica 2014, Chambéry

Kidney 3D dynamic modeling and tumor tracking for therapeutic transcutaneous treatment

Valentin Leonardi[1,2], Marc Daniel[1], Nils Olofsson[1,3], Philippe Souteyrand[2], Vincent Vidal[2], Jean-Luc Mari[1]

[1] Aix-Marseille Université, LSIS UMR CNRS 7296, Marseille, France
[2] Aix-Marseille Université, LIIE EA 4264, Marseille, France
[3] Uppsala Universitet, Sweden

Abstract

We present a new method of 3D kidney dynamic modeling used in the context of organ and tumor motion tracking. This work is in line with the *KiTT* project (Kidney Tumor Tracking) which gathers researchers from different fields: geometric modeling, radiology and urology. It arose from the tendency of nowadays surgical gestures to be less and less invasive (HIFU, coelioscopy). The goal is to develop a totally non-invasive protocol of kidney tumors eradication by transmitting ultrasound waves through the skin without breaking in it. As the kidney presents motions and deformations during the breathing cycle, the main issue is to know the tumor position at any time in order to adjust the waves accordingly. Moreover, it is primordial for the practitioner to have a realistic simulation of the kidney motion during the therapeutic protocol. Indeed, the treatment could eventually induce modifications in the organ behavior. Therefore, a kidney tracking would allow the practitioner to have a total control during the treatment.

The method we present is composed of four different steps and follows a logical workflow from three abdominal acquisitions to kidney and tumor tracking.

First, we use a semi-automatic region growing approach to extract the contour of the kidney in a set of MRI or CT-scan acquisition slices. Let N be the number of slices where the kidney is present, the segmentation of the entire organ only needs one seed for the slice $\frac{N}{2}$. It is then automatically propagated from slice to slice; the barycenter of the points defining the contour of kidney on slice k defines the seed for the slice $k+1$. As organs (especially the spleen) can be adjacent to the kidney, the segmented regions could tend to overflow into them and falsify the results. Thus, the segmentation is refined by analyzing the histogram of the segmented regions and defining a threshold of number of appearances. This way, the less frequent grey values that correspond to the errors are eliminated.

The second step deals with the reconstruction of the point cloud coming from the segmentation. A recent and efficient algorithm is used, the *Poisson surface reconstruction*. The principle of this method is to find a function which equals 1 inside the point cloud and 0 outside. It is deduced from a Poisson equation based on the point cloud, considered as the gradient of the function. This method is very robust to noise and, therefore, can eliminate segmentation errors that may remain. Thus, a triangulated surface static model of the kidney is computed.

These two first steps are done three times for the inhale, mid-cycle and exhale phases. In this way, the third stage consists in generating a dynamic model of the kidney from these three static models. We use an automatic *mesh morphing* approach to merge the topologies of the three models. As this principle is only based on geometric data, it is the opposite stance of the existing work in the domain. The models are divided into two parts (called *patches*) along their main axis. Every *patch* is then projected onto the unit disk in order to superimpose both projections of the same part of the kidney. This way, these *patches* are morphed into each other by creating a correspondence map between their vertices and faces. The underlying goal is to obtain a *metamesh* which comprises the topologies of the models and allows a smooth transformation between them. Thus, the vertices defining the *metamesh* have an initial and a final position directly deduced from the correspondence map. The interpolation between these two positions creates intermediate models, which offers the smooth transition from one mesh to another. These intermediate models correspond to the kidney for the intermediate breathing phases between the three initial ones. A parameter t is defined to deal with the transitions. For $t = 0$, the resulting intermediate model correspond to the inhale phase. For $t = 1$, it corresponds to the mid-cycle phase and for $t = 2$ to the exhale phase. Then, it is possible to compute accurately any intermediate model for any phase of the cycle by setting t to any value between 0 and 2. Thus, the motion and the deformation of the organ are known throughout the respiratory cycle.

Interpolating methods induce local approximations, especially for the tumor growth. Therefore, the fourth step focuses on reducing these approximations by introducing constraints in the mesh morphing stage. They force two tumor growths of two different models to morph into each other. Thus, we use a tumor detection method to identify these regions. It is based on discrete curvature information and exploits the presence of concave areas at the base of the growth; these areas are iteratively expanded using mathematical morphology tools to confine the growth from the rest of the kidney. For each iteration, all regions are distinguished from each other and must match a criterion of relative size and global convex curvature to be identified as the tumor growth. This way, the dynamic model presents accurate local transformations and is suitable to be used as kidney tracking. Finally, another interest of detecting the tumor growth is to retrieve the tumor position and size using a *Best Fit Sphere* algorithm. Its application on all intermediate models allows knowing the tumor position for the whole breathing phase, which consists in its tracking.

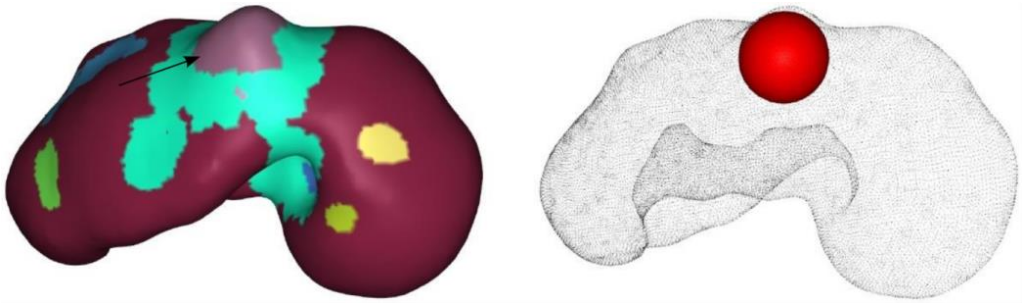

Figure 1. *Kidney model for which several regions have been detected. The one indicated by the arrow has been identified as the tumor growth (left) – The tumor size and position are retrieved by applying a BFS algorithm on this region (right).*

Our method is validated using two extra kidney static models corresponding to two phases of the cycle (respectively around 25% and 75%). The images from which these models are reconstructed are acquired using an abdominal belt. This device is used concurrently with a classic MRI machine to track the motion of the diaphragm, from which the breathing cycle can be directly deduced. Thus,

the phases at which the acquisitions are performed are known accurately. Each acquisition is about 50 seconds long and needs an apnea of 10 seconds. Therefore, we create two intermediate models corresponding to the same breathing phases of the extra static models. Then, we estimate the error inherent to our dynamic model by computing the *Euclidian, Hausdorff* and *Root Mean Square* distances between the intermediate and static models. We show the mean precision of our models are on the order of 1 millimeter for both the kidney and tumor tracking. Therefore, our work is suitable for a medical use where the margin of error practitioners use is about 5 millimeters.

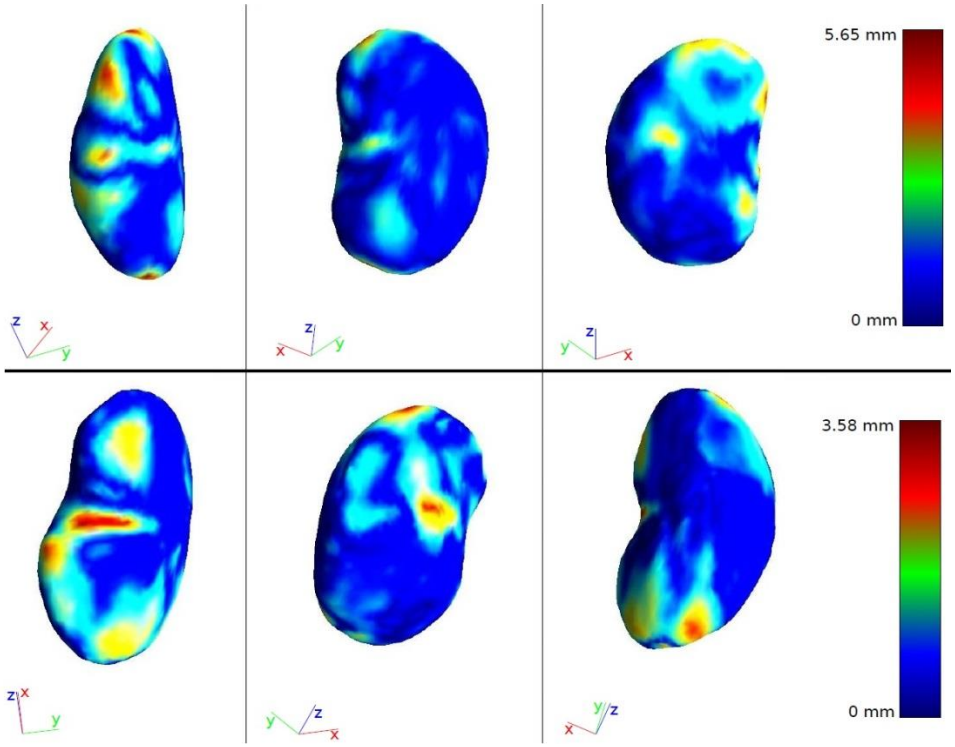

Figure 2. *Distance map of two intermediate kidney models obtained by mesh morphing for two given breathing phases. The evaluated accuracy validates the use of our method in a medical context.*

Acknowledgements

This work is granted by the group Novartis and by the Foundation “Santé, Sport et Développement Durable”, presided over Pr. Yvon Berland. The authors would like to thank the persons involved in the *Kidney Tumor Tracking* (KiTT) project : Christian Coulange for his precious help, Marc André, Frédéric Cohen, Philippe Souteyrand and Julien Frandon for their wise advice and for providing CT scan and MRI data, and Pierre-Henri Rolland for his support.

REGISTRATION

“Fluorescence imaging of prostate cancer”: when the surgeon looks beyond the visible

Redha Heus Ph.D.[1], Marie-Paule Montmasson I.E.[2], , Alexandre Moreau-Gaudry Ph.D. M.D.[1], Malika Hamel[2], Françoise Giroud Ph.D.[2], Emilie Chipon Ph.D.[1], Olivier Gaiffe Ph.D.[3], Christian Pieralli Ph.D.[3], Maysoun Kassem M.D.[5], Jean-Alexandre Long Ph.D. M.D.[1,4], Jean-Luc Descotes Ph.D. M.D.[4], Philippe Cinquin Ph.D. M.D.[2], Sandrinr VorosPh.D.[2].

Corresponding Author’s contact information:
Redha Heus, bureau B126, Pavillon Taillefer, Faculté de Médecine, 38706 La Tronche Cedex, Redha.Heus@imag.fr, +33 4 56 52 00 73

(1) : Centre d‟Investigation Clinique - Innovation Technologique, INSERM, CHU de Grenoble, UJF-Grenoble 1, CIT803, Grenoble, F-38041, France; UJF-Grenoble 1 / CNRS, TIMC-IMAG UMR 5525, Grenoble, F-38041, France;

(2): UJF-Grenoble 1 / CNRS / INSERM, TIMC-IMAG UMR 5525, Grenoble, F-38041, France;

(3): FEMTO-ST, UMR CNRS 6174, Université de Franche-Comté F-25030 Besançon cedex, France;

(4): Urology Department, Grenoble University Hospital;

(5): anatomic pathology Department, Grenoble University Hospital;

In developed countries, prostate cancer (PC) is the most frequent male diagnosed cancer and the third leading cause of cancer death in men [Inca2013]. In 75% of the cases, PC is diagnosed at a localized stage within the prostate (T1 or T2), this localized PC is generally treated with surgery "*prostatectomy"*. In this operation, the surgeon removes the entire prostate gland within its capsule and some of the tissue around it. A non-complete removal of cancer tissue may lead to positive surgical margins which are associated to a higher risk of biochemical recurrence (15-20% of the patients) [Pfitzenmaier08].

The major possible complications of prostatectomy are urinary problems (removing the bladder sphincter) and erectile dysfunction (damage bundles of nerves). In light of these considerations, the surgeon must determine the best compromise between a complete removal of tumor tissues and conservation of sensitive structures mentioned above. The last decade has seen the emergence of several imaging approaches to assist the surgeon to find this compromise [Xing2008, Bouchelouche2010].

Fluorescence imaging is a very active field of researches for imaging of prostate tumor tissues. The prostate specific membrane antigen (PSMA) is the main target to image the tumor sites by fluorescence. PSMA is not fluorescent by itself but, antibodies anti-PSMA labelled with a fluorescent marker can make it visible Its expression levels increases with disease progression suggesting that PSMA could be an interesting marker of PC [Tagawa2010]. In current works such as [Nakajima2011], the experiments are performed on animal models which does not guarantee success on human tissues.

Intraoperative fluorescence imaging of PC could be also done using tissue auto-fluorescence. Protoporphyrin IX (PpIX) auto-fluorescence was widely studied to target various types of cancer [Moonen2006, Widhalm2013, Mellisi2014]. PpIX is an intracellular protein which accumulates in malignant cells. This marker is not specific to PC but could be exploited to highlight cancerous lesions during a prostatectomy.

Based on these recent research progresses, we have developed a bimodal fluorescence fibered testbench for the classification of tissue during a radical prostatectomy [Voros2013]. This medical device prototype can detect the fluorescence signals of the two markers mentioned above: PpIX and PSMA labelled with Alexa Fluor 488 tracer. This testbench is equipped with two laser diodes:

- Blue laser: emitting at 405nm to excite the auto fluorescence of PpIX (peak of emission at 630nm) (Figure 1.A).
- Green laser: emitting at 488nm to excite PSMA-AlexaFluor® 488(peak of emission at 520nm).

  The choice of the AlexaFluor®488-marker allows us to exploit jointly the fluorescences without any intersection between their spectra (Figure 1.A).

In summary, our testbench is able to deliver us from the spectral parameters measured (Figure 1.A+B+C):

- Tissues status: pathologic vs. healthy (PpIX fluorescence).
- Tissues nature: prostatic vs. non prostatic (PSMA-AlexaFluor® 488 fluorescence).

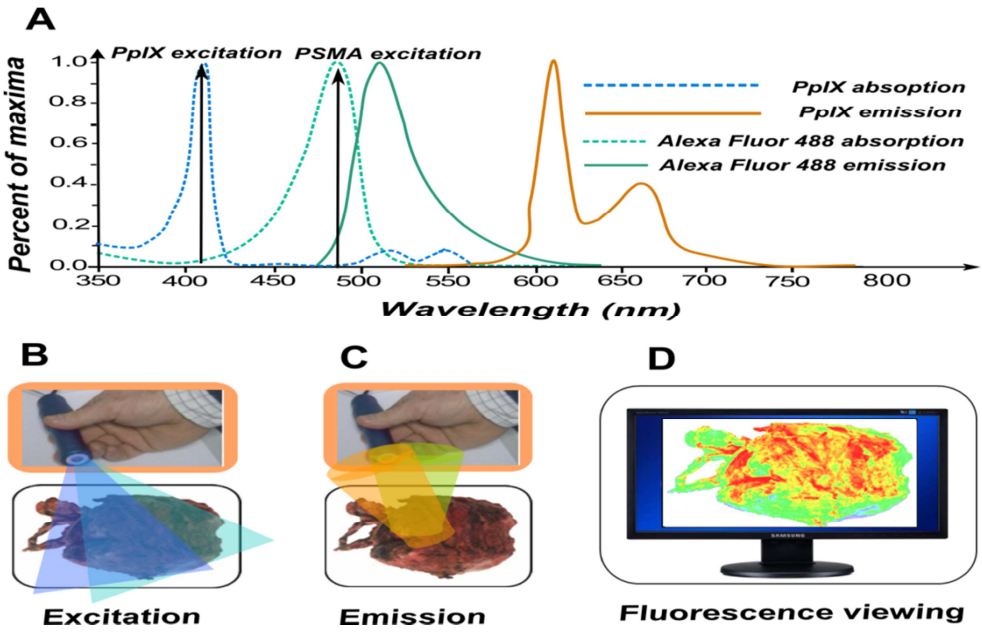

Figure 1: Bimodal fluorescence probe (illustration). A: PpIX and PSMA-AlexaFluor488 spectra. B: multiwavelength excitation (405 and 488 nm). C: Collection of PpIX and PSMA-AlexaFluor488 fluorescence's. D: Display fluorescence according to a color code.

These spectral measures (displayed as a fluorescence spectrum or in color code) could in term allow the surgeon to know in near real-time the nature and status of the surgical margin (Figure 1.D).

Preliminary experiments were performed in the frame of a biomedical research called COPROST. This protocol, already accepted by the ethical instances and just started in 2014, allows us to obtain healthy and cancerous fresh prostate chips from 35 patients during transurethral resections.

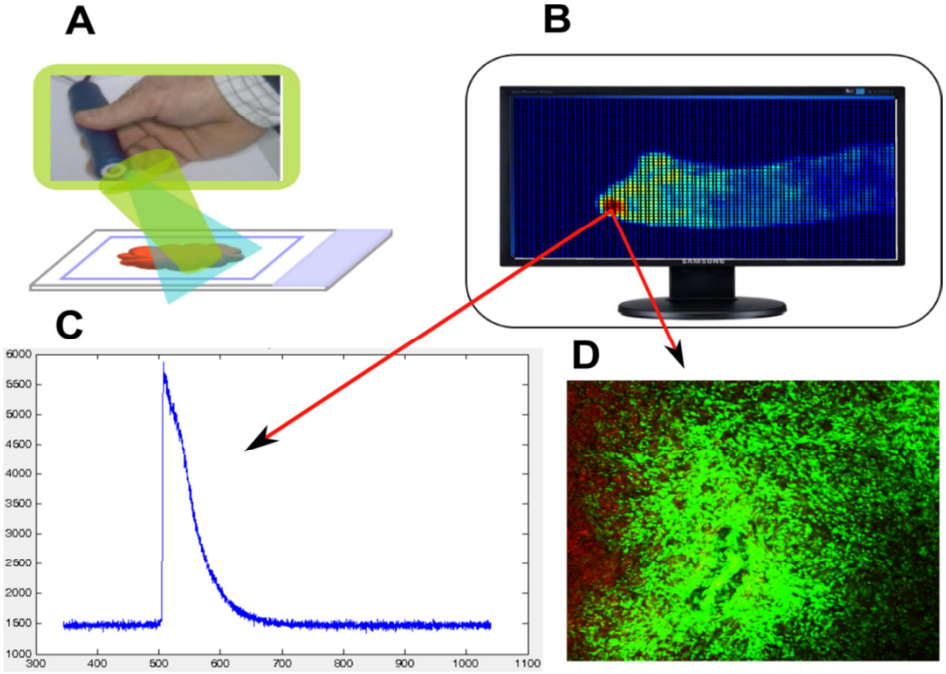

Figure 2: Prostate tissue (PSMA) fluorescence. A: fluorescence measure with bimodal probe (Illustration). B: Display measures according to fluorescence intensity. C: Fluorescence spectrum of one field of the fluorescence image (intense fluorescence area: red); it's clearly the fluorescence of PSMA-AlexaFluor488 (peak at 520nm). D: The same field was scanned with a confocal microscope (zoom x10).

First measures conducted on a small cohort of healthy samples (more than twenty prostate chips obtained from 4 patients) were very promising. The prostatic tissue was well detected with PSMA-AlexaFluor®488 signal (figure 2). The results were confirmed by confocal microscope measures. We will now focus on cancerous prostate chips to validate the detection of Ppix fluorescence. However, our prototype was successfully used on leaves to detect chlorophyll, which has fluorescence properties very similar to PpIX.

These initial results are very encouraging; they allow us to validate both: our bimodal probe prototype and our approach to target PSMA. These advances encourage us to build a miniaturized bimodal laparoscopic-compliant fluorescence probe to ultimately help the surgeon to see the real contours of cancerous tissue in abdomen cavity during prostatectomy.

Acknowledgments

This work has been supported by French National Research Agency (ANR) through TecSan program (project DEPORRA n°ANR-09-TECS-006).

This work was also supported by the French ANR within the Investissements d'Avenir program (Labex CAMI) under reference ANR-11-LABX-0004.

References:

[Bouchelouche2010] K. Bouchelouche, P.L. Choyke and J. Capala. **Prostate specific membrane antigen- a target for imaging and therapy with radionuclides**; *Discov Med.* 2010 Jan;9(44):55-61.

[INCa2013] INCa (www.e-cancer.fr). **Les-cancers-en-France-edition-2013_v2.pdf**. 2013.

[Millesi2014] M. Millesi, B. Kiesel, A. Woehrer, J.A. Hainfellner et al. **Analysis of 5-aminolevulinic acid-induced fluorescence in 55 different spinal tumors**; *Neurosurg Focus.* 2014 Feb;36(2):E11.

[Moonen2005] P.M.J. Moonen and J.A. Witjes. **Diagnosis of Bladder Cancer – Fluorescence Cystoscopy and Urinary Markers**; *European Urological Review*, 2005:1-5.

[Nakajima2011] T. Nakajima, M. Mitsunaga, N.H. Bander, W.D. Heston et al. **Targeted, Activatable, In Vivo Fluorescence Imaging of Prostate-Specific Membrane Antigen (PSMA) Positive Tumors Using the Quenched Humanized J591 Antibody-Indocyanine Green (ICG) Conjugate**; *Bioconjugate Chem.* 2011, 22, 1700–1705.

[Pfitzenmaier2008] J. Pfitzenmaier, S. Pahernik, T. Tremmel, A. Haferkamp et al.: **Positive surgical margins after radical prostatectomy: do they have an impact on biochemical or clinical progression?**, *BJU International*, Vol. 102(10), pp. 1413-1418, 2008.

[Tagawa2010] S.T. Tagawa, H. Beltran, S. Vallabhajosula, S.J. Goldsmith et al. **Anti-Prostate Specific Membrane Antigen-based Radioimmunotherapy for Prostate Cancer**; *Cancer.* 2010 February 15; 116(4 Suppl): 1075–1083.

[Voros2013] S. Voros, A. Moreau-Gaudry, B. Tamadazte, G. Custillon et al.: **Devices and systems targeted towards augmented robotic radical prostatectomy**; *IRBM*, Volume 34, Issue 2, Pages 139-146.

[Widhalm2013] G. Widhalm, B. Kiesel, A. Woehrer, T. Traub-Weidinger et al. **5-Aminolevulinic acid induced fluorescence is a powerful intraoperative marker for precise histopathological grading of gliomas with non-significant contrast-enhancement**; *PLoS One*. 2013 Oct 18;8(10).

[Xing2008] Y. Xing and J. Rao. **Quantum dot bioconjugates for in vitro diagnostics & in vivo imaging**; *Cancer Biomark*. 2008;4(6):307-19.

Registration of Preoperative Liver Model for Laparoscopic Surgery with Intraoperative 3D Acquisition

J. Bano[1,2,3] , A. Hostettler[1], S.A. Nicolau[1], C. Doignon[2], L. Soler[1,3], J. Marescaux[1,3]

[1] IRCAD-France, Virtual-Surg, Place de l'Hopital 1, 67091 Strasbourg Cedex, FRANCE
[2] ICube (UMR 7357 CNRS), University of Strasbourg, FRANCE
[3] IHU, Institut Hospitalo-Universitaire, Strasbourg, FRANCE

Keywords: registration, liver, laparoscopy, intraoperative, augmented reality

I. Purpose

Laparoscopic surgery is a well-known surgical technique that can replace open surgery to improve patient healthcare. However, this kind of surgery is difficult to achieve due to the loss of 3D depth and tactile perceptions during intervention. Augmented reality has been proposed to display structures like liver vessels or tumours that are usually hidden on the video. This information is usually coming from an image acquired before the intervention and thus without pneumoperitoneum. This gas injection, used to create a working space, highly modifies viscera shape and particularly the liver which undergoes deformations over several centimeters [1] (cf. Fig. 1). Therefore, it is mandatory to update the preoperative model shape for augmented reality based guidance applications. Obviously, this update can be done only if intraoperative information of the critical structures is available. Practically, such information can be provided by a surface acquisition (using an optical technique) or by intraoperative 3D acquisition (using a rotational C-arm). Although rotational C-arms are currently not routinely integrated in surgical rooms, such a set-up begins to be more and more available in hospitals.

Vagvolgyi et al. [2] proposed to register a preoperative model of the kidney on an intraoperative surface reconstruction computed from a stereo endoscope. Firstly, a rigid alignment is performed using interactively selected landmarks refined by an ICP registration. Secondly, a deformation is applied so that the preoperative model fits the reconstructed surface using a mass spring model. The same kind of method is applied for open surgery based on a two-step registration (rigid and non-rigid) using surface information acquired from an optical system [3]. Despite realistic results, no quantitative evaluation was provided on patient data.

In our context, all these methods cannot provide satisfactory global accuracy. Indeed, the liver undergoes significant motion and compression in the antero-posterior direction but, even if the position of the anterior intraoperative part of the liver could be known, the posterior part position remains unknown. One can clearly see in the Figure 1 that an alignment of anterior faces of preoperative and intraoperative liver cannot guarantee a proper registration of the posterior liver part, mainly because of the compression, which makes anterior and posterior parts closer. Without intraoperative information of the anterior part, it seems extremely difficult to foresee the liver shape.

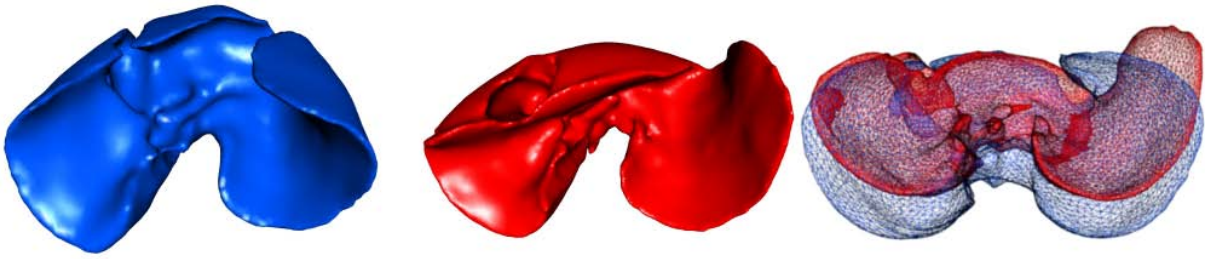

(a) **(b)** **(c)**

Fig. 1. Porcine liver surface meshes before (left column) and after pneumoperitoneum (middle column). The two meshes in wireframe (on the right) outline the important deformations that porcine

liver undergoes due to pneumoperitoneum: the anterior part shifts down and the left lobe moves toward the left in the abdominal cavity.

II. Method

The liver and critical structures (vessels and tumours) are segmented on a preoperative CT by experts using semi-automatic tools. The anterior part of the liver is the only data segmented on an intraoperative 3D C-arm acquisition as it is in contact with the pneumoperitoneum gas and thus easily identifiable. Afterwards, the preoperative data have to be registered in the same frame than the intraoperative one. This first global and rigid registration is achieved by computing the geometric transformation between the spine on the preoperative image and the intraoperative one. Moreover, we propose to use the position of the portal vein entry to refine the translation accounting for the cranio-caudal sliding of the liver into the abdominal cavity.

As a preliminary step, the preoperative model is first rigidly registered on the intraoperative one so that when superimposed, their posterior part is on top of each other. Then, the preoperative model is deformed according to a matching field. This field is performed by matching the vertices of both meshes according to a minimization step with a criterion based on the geodesic distance to relevant anatomical landmarks (that have to be selected manually). This means that the geodesic distance of a vertex to a landmark on the preoperative model is assumed to be approximately the same as the distance between the corresponding vertex and the matched landmark on the intraoperative model (cf. Fig. 2).

Finally, this surface matching is used to update the preoperative model shape from the biomechanical simulation engine SOFA [4]. During this step, a finite element model is used to interpolate this field on the liver inner part and its vessels. The biomechanical parameters used for this model are Young's modulus (15 kPa found in [5]) and Poisson ratio (0.35 to allow slight volume compression). The deformation is finally performed by adding springs between the matched points. During this step, the matching field is also regularized depending on the spring stiffness value. This value is selected empirically so that the preoperative anterior part overlaps the intraoperative one.

III. Result

Our validation is performed on data measurement from two pigs (cf. Fig. 1): a pair of 3D volume data sets has been acquired before and after pneumoperitoneum for both pigs.

We obtain a mean error less than 4 mm for the whole liver surface in both cases. As a reference we compute the distance between the two input meshes just after the rigid registration process for which the mean error is 6 mm.

The evaluation of the vessel registration accuracy is performed by computing the Euclidean distance between some vein bifurcations which have been manually selected. We obtain for the first case (resp. the second case) an average error of 17.5 mm$\pm$9.0mm and maximum value 37.4 mm (resp. 14.8 mm$\pm$10.7mm and maximum value 38.2 mm) without our registration and 10.3 mm$\pm$2.7mm and maximum value 15.8 mm (resp. 10.8 mm$\pm$8.3mm and maximum value of 28.9 mm) after the non-rigid registration.

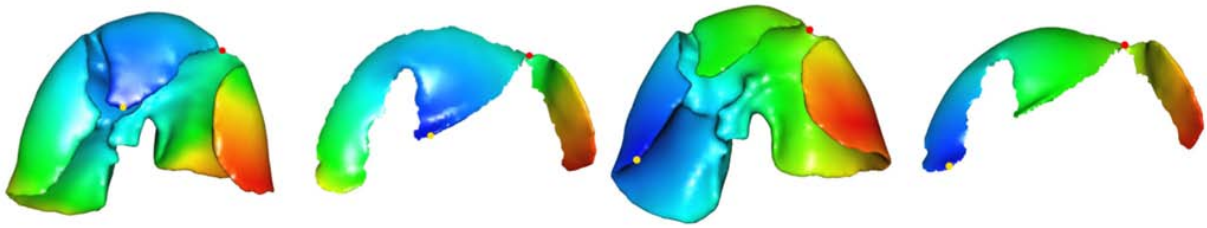

(1a) **(1b)** **(2a)** **(2b)**

Fig. 2. Two examples of the geodesic distance on the preoperative liver mesh (a) and the liver anterior part after pneumoperitoneum (b). Colours on each mesh illustrate the geodesic distance of each vertex

to a landmark (the yellow point). Blue vertices are close to the landmarks and red ones are far. The red dots correspond to anatomically matched vertices between the preoperative and intraoperative models. One can see that the colour surrounding the red dot is approximately the same on both examples (a,b).

IV. Conclusion

In this paper, we have presented a new and efficient technique for updating a preoperative shape model using intraoperative data from a 3D C-arm acquisition. Firstly, we have shown that a registration based on the anterior surface information only is not sufficient to provide good accuracy for the liver. To tackle this issue, we have proposed to rigidly register the posterior part of the liver. The deformation of the anterior part is performed with a non-rigid registration corresponding to the anatomical area in the intraoperative image. Results show the feasibility of our approach. We are aware that our method requires some manual steps (portal vein entry identification and landmark matching) but it seems acceptable for our clinicians.

References

[1] F M Sanchez-Margallo, J L Moyano-Cuevas, R Latorre, J Maestre, L Correa, J B Pagador, L F Sanchez-Peralta, J A Sanchez-Margallo, and J Usan-Gargallo. Anatomical changes due to pneumoperitoneum analyzed by mri: an experimental study in pigs. Surg Radiol Anat, 33(5):389–96, 2011.

[2] Balazs Vagvolgyi, Li-Ming Su, Russell Taylor, and G Hager. Video to ct registration for image overlay on solid organs. Proc. Augmented Reality in Medical Imaging and Augmented Reality in Computer-Aided Surgery (AMIARCS), pages 78–86, 2008.

[3] D Caleb Rucker, Yifei Wu, Janet E Ondrake, Thomas S Pheiffer, Amber L Simpson, and Michael I Miga. Nonrigid liver registration for image-guided surgery using partial surface data: a novel iterative approach. In SPIE Medical Imaging, pages 86710B–86710B. International Society for Optics and Photonics, 2013.

[4] http://www.sofa-framework.org/

[5] E. Samur, M. Sedef, C. Basdogan, L. Avtan, and O. Duzgun. A robotic indenter for minimally invasive characterization of soft tissues. In Int'l Congress Series, volume 1281, pages 713–718. Elsevier, 2005.

Video Synchronization: An Approach to Biopsy Site Re-localization

Anant S. Vemuri[1,3], Adrien Sportes[4,2], Stephane Nicolau[2], Jacques Marescaux[2], Nicholas Ayache[3,1] and Luc Soler[2,1]
[1]IHU, Strasbourg; [2]IRCAD, Virtual-Surg, Strasbourg; [3]INRIA, Sophia Antipolis; [4]NHC, CHU, Strasbourg.

Introduction:

Barrett's esophagus (Barrett's esophagus) is the pre-malignant lesion for the majority of patients with esophageal adenocarcinoma. The sequence of events from Barrett's esophagus to adenocarcinoma has several steps, encompassing low grade intra-epithelial Neoplasia (LGIN), and high grade intra-epithelial neoplasia (HGIN). As it seems that this evolution spans many years, endoscopic surveillance for patients with Barrett's esophagus has been advocated, to detect neoplasia at early and curable stages. In recent years endoscopic imaging techniques have improved greatly. However, even using sophisticated imaging techniques, the standard approach of comprehensive endoscopic biopsy protocol includes direct sampling from suspicious areas in combination with systematic random four quadrant biopsies (4QBs) every 1±2 cm along the length of the Barrett's segment, according to the Seattle protocol, is recommended as the gold standard for surveillance. The approach is labor-intensive but is currently considered to be the state of the art. However, the primary problem is the inter-operative re-localization of these biopsy sites to guide the treatment. Often re-localization is performed using the markings made on the endoscope which are highly unreliable and prevent targeted treatments.

Related Work:

Several approaches to track the biopsy points "*intra-operatively"* exist [2,3]; each of them relying on the recovery of the 3D structure of the anatomy, to map and track the biopsy sites as they move in and out of the field-of-view of the endoscope frame. Atasoy et al. [3] propose to formulate the re-localization as image-manifold learning process for re-localization of the biopsy sites. However, they do not provide any spatial relations of the extracted segments inter-operatively, and so have not sufficiently clarified the application of their result in a clinical context for re-localization. We believe that, relying only on image based information for information extraction, that has to be mapped across multiple interventions can be highly unreliable; especially, due to temporal changes in tissue texture over multiple procedures, coupled with a highly deformable endoscopic scene, where repeatability of feature extraction, matching and tracking poses a significant challenge.

In an earlier work [1] we had proposed a general framework for inter-operative biopsy site re-localization framework by introducing an Electro-magnetic tracking system (EMTS) into the loop and providing a way to inter-operatively register video sequences to provide a guided navigation in the esophagus. In this work, we present a few modifications to our earlier approach to fit more closely with the work-flow in the clinical setting. Here we also present a qualitative evaluation of our approach.

System Setup:

The system consists of an electromagnetic tracking system (EMTS), which includes an electromagnetic field emitter (EMFE), a tracking interface, a titanium arm to mount the EMFE, EM sensors, a dual channel Karl Storz flexible endoscope. EMFE has a working volume of $50 \times 50 \times 50$cm3. It has a blind zone of about 5cm in front of it, so it is positioned ~ 6cm above the patient's chest and fixed in position using a titanium arm. The EMTS and the endoscope video output are connected to a computer. In our previous work, [1], we used a single sensor inserted into the endoscope channel. We discuss in the next few sections why this approach poses some practical issues. As a modification to our approach in [1], we propose an alternative using three sensors. One sensor attached at the Suprasternal (or Jugular) notch. It is the anatomical landmark located at the superior border of the manubrium of the sternum, between the clavicular notches. Externally it is a large dip, visible just below the neck. It is a

stable landmark that stays stationary during a breathing cycle or when the patient position is changed. The second sensor is attached along the sternum about 10-15cms below the Jugular notch. The third sensor is inserted in one of the channels of the endoscope, such that the sensor is placed at the opening of the channel.

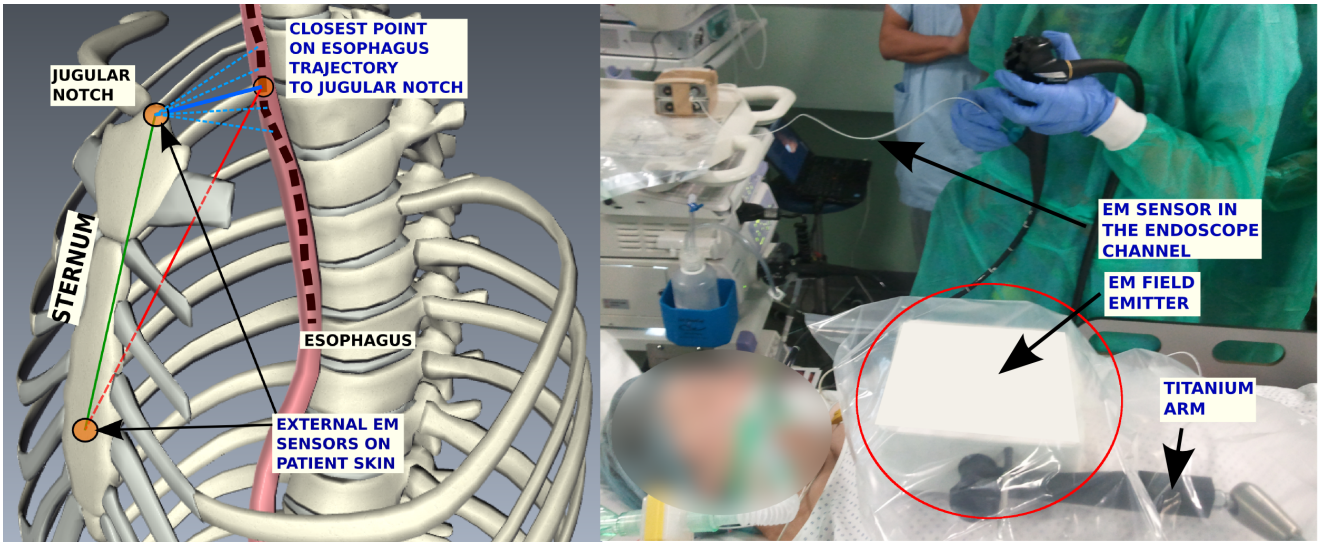

Fig. 1: Placement of sensors (left) and System setup (right)

The above figure shows the placement of the sensors on the patient.

Data acquisition: The process of acquiring data during an intervention involves a synchronized capture of video from the endoscope and tracking data from the EMTS. For each corresponding position of the endoscope in the esophagus, the corresponding position of (all three) sensors is recorded.

Inter-operative registration: To synchronize a previously performed recording with a live procedure, the reference frames of the EMTS have to be registered. We use the sensors attached to the sternum as our anatomical landmarks. More specifically, we use the sensor attached to the Jugular notch as the reference point. From this reference point, we define two vectors. The first in the direction of the second sensor placed on the sternum, $\hat{n}_1$. The second point is computed online as the centroid of a cluster of points in the spherical region closest to the jugular notch in the esophagus trajectory. It defines the second vector at the Jugular notch $\hat{AC}$. Using these vectors we define a reference frame at the jugular notch as shown in the figure below. We register the live intervention and recorded interventions using these reference frames that are centered at the Jugular notch. We use the Jugular notch as our reference frame since it is easily identifiable externally and is very stable upon repeated sensor placement.

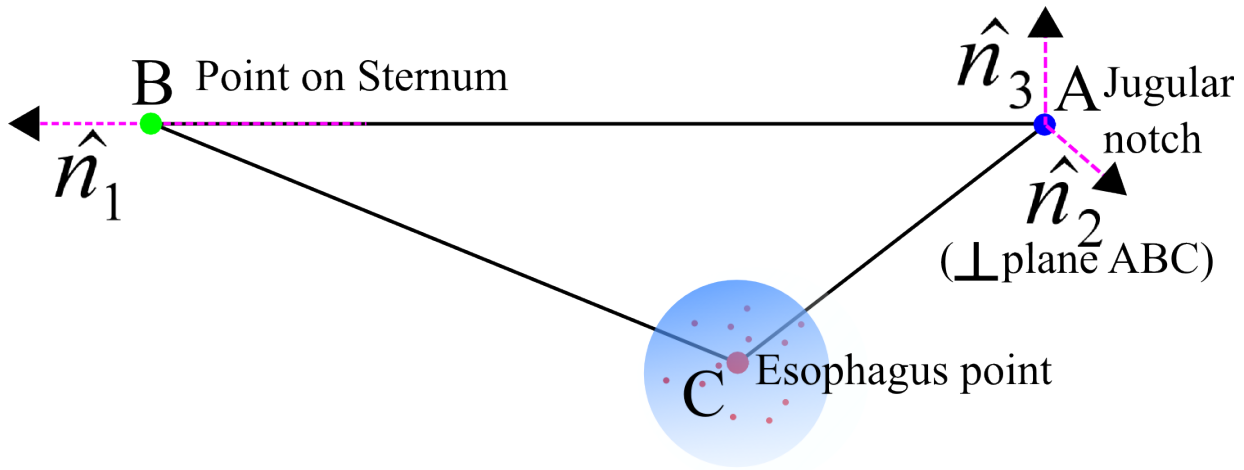

Fig. 2: Forming the reference frame for inter-operative registration.

The registration is performed online during the procedure so, there are no additional steps are necessary to initialize the video synchronization.

Evaluation:

Here we present a more detailed qualitative evaluation of our approach with experts and young gastroenterologists. We make two recordings of a pig's esophagus. The first with no markings made and the second with markings made using a coagulation device. Between the two recordings all the sensors were removed and replaced. Our experts tagged the regions in all the images of the first recording where the coagulation markings were made by reviewing the images from the second recording. This corresponds to the ground truth. The experiments were presented in two phases. The first using a classical approach where the evaluator had access to a printed picture of the marking and the distance inside the esophagus where the picture was taken. As the expert reviews the recorded images, he is also presented with an approximate distance inside the esophagus of each of the recorded images. In the second phase, the evaluator used our software which providing a synchronization between the two recordings. The evaluator had to locate and tag the markings on to the first recording using the information provided to him. The table below shows the result from eight evaluations. It values are the number of markings found out by the evaluator out of 12.

#	Classical Approach	Synchronization Approach
1	6	10
2	9	11
3	3	12
4	6	12
5	0	10
6	7	12
7	8	12
8	3	12

Our initial evaluation results are quite promising. We are performing more experiments and expect to provide a more detailed evaluation of our work soon.

References:

1. Vemuri et. al. “Inter-Operative Trajectory Registration for Endoluminal Video Synchronization: Application to Biopsy Site Re-localization” , MICCAI 2013.
2. Allain et. al. “Biopsy site re-localization based on the computation of epipolar lines from two previous endoscopic images”, MICCAI 2009.
3. Atasoy et. al. “Endoscope video manifolds for targeted optical biopsy”, IEEE, TMI 2012.

Phantom study of fiducial-free 3D-3D registration procedures for electromagnetic endovascular navigation

LH Nguyen-Duc[1,2], A de Lambert[4], S Esneault[3], M Castro[1,2], C Göksu[3], J-L Magne[4], P Haigron[1,2]

[1] INSERM, U1099, Rennes, France
[2] LTSI, Université de Rennes 1, Rennes, France
[3] Therenva, Rennes, France
[4] CIC-IT, CHU de Grenoble, Grenoble, France

This work was partly supported by the French ANR within the Investissements d'Avenir program (Labex CAMI) under reference ANR-11-LABX-0004. This work has been partially conducted in the experimental platform TherA-Image (Rennes, France) supported by Europe FEDER.

Introduction

Nowadays, the minimally invasive endovascular approach plays a major role in the therapeutic arsenal of vascular practitioners. It is increasingly indicated and constitutes the standard treatment for a number of vascular pathologies. It is especially the case in Abdominal Aortic Aneurism repair (EVAR) where a complex endoprosthesis (modular, branched, fenestrated stent-grafts) is endovascularly inserted and deployed at the anchoring site in order to repair the aneurysm. Because the intervention is commonly performed under fluoroscopic control, endovascular positioning and navigation is based on a 2D visual feedback at the cost of an exposure to X-rays and contrast medium.

Some works on electromagnetic tracking (EMT) navigation have been reported [1] with the aim to limit in the long run the use of X-rays and contrast agent in the course of endovascular interventions. However, issues related to the integration of these approaches into clinical workflow and to the demonstration of the medical benefit have not yet been addressed. Besides accuracy, a current limitation of reported studies is that fiducials linked to anatomical structures of interest have to be observable both in pre- and intra-operative spaces.

The main issue we address in this work deals with registration between the 3D EMT coordinate system and the 3D patient coordinate system in order to localize the tip of a specific catheter in relation to vascular structures of interest. The aim of this work is to study and implement an operational 3D-3D registration approach that does not require fiducial landmarks placed into the patient (neither pre-operatively nor intra-operatively).

Method

The first implemented method can be deployed in a standard operating room. It is based on a 3D-3D intrinsic registration using the tracking of the catheter tip inside the vasculature. The basics of this approach have been presented in [2]. It makes use of a set of 3D positions obtained in the EMT space by moving a modified catheter freely inside the vascular lumen. In addition to lumen constrained positions we also consider in our study a scenario with path constrained positions. The 3D-3D registration is performed by iteratively minimizing the distance between the transformed EMT 3D positions and the pre-operative 3D description of the vasculature. This distance is defined as the distance map computed from the segmentation of the vasculature in the pre-operative CT. Inside the vasculature the distances are set to zero, while outside they take positive values.

The second implemented method can be deployed in a hybrid operating room with 3D rotational X-ray imaging (3DRX). It is based on the 3D-3D extrinsic registration from a set of external magnetic sensors arranged on the operating table (prior to installation of the imaging subject). The 3DRX intra-operative image is segmented to obtain the 3D description of the vasculature and to determine the 3D positions of the sensors in the 3DRX coordinate system. The rigid transformation between the two corresponding point sets expressed in both the 3DRX and the EMT coordinate systems is computed with the direct linear transformation algorithm.

In vitro experiments were performed in the operating environment, using a soft silicone abdominal aortic aneurysm model (ELASTRAT® *in vitro* model, Shelley Medical) and the Aurora® magnetic tracking system (Northern Digital). The registration procedure software was developed in C++ based on the open source Computer Assisted Medical Intervention toolkit (CamiTK) [3]. The tests described below were performed in order to study the localization accuracies according to different acquisition configurations or parameters: positions of the field generator (FG), constraint on catheter tip trajectories for intrinsic registration, number of sensors for extrinsic registration.

The localization procedure was repeated five times with two different positions A and B of the FG with respect to the phantom (Fig. 1a, Fig. 1b). In the purpose of evaluation, the 3DRX volume was used to describe the vasculature for the intrinsic registration.

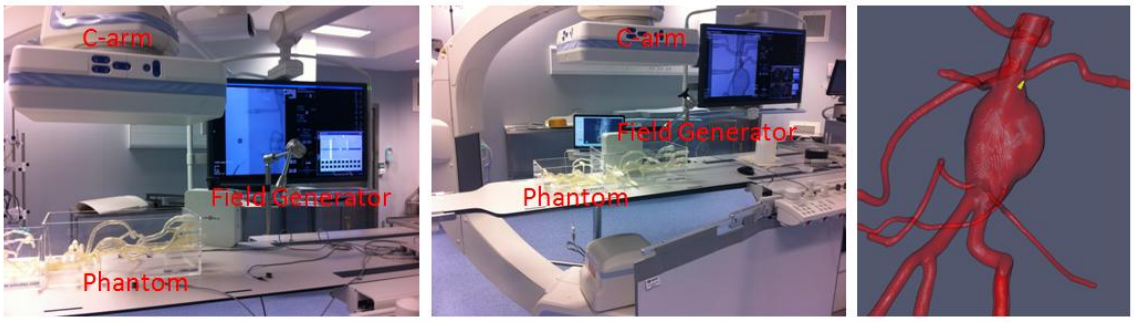

(a) (b) (c)

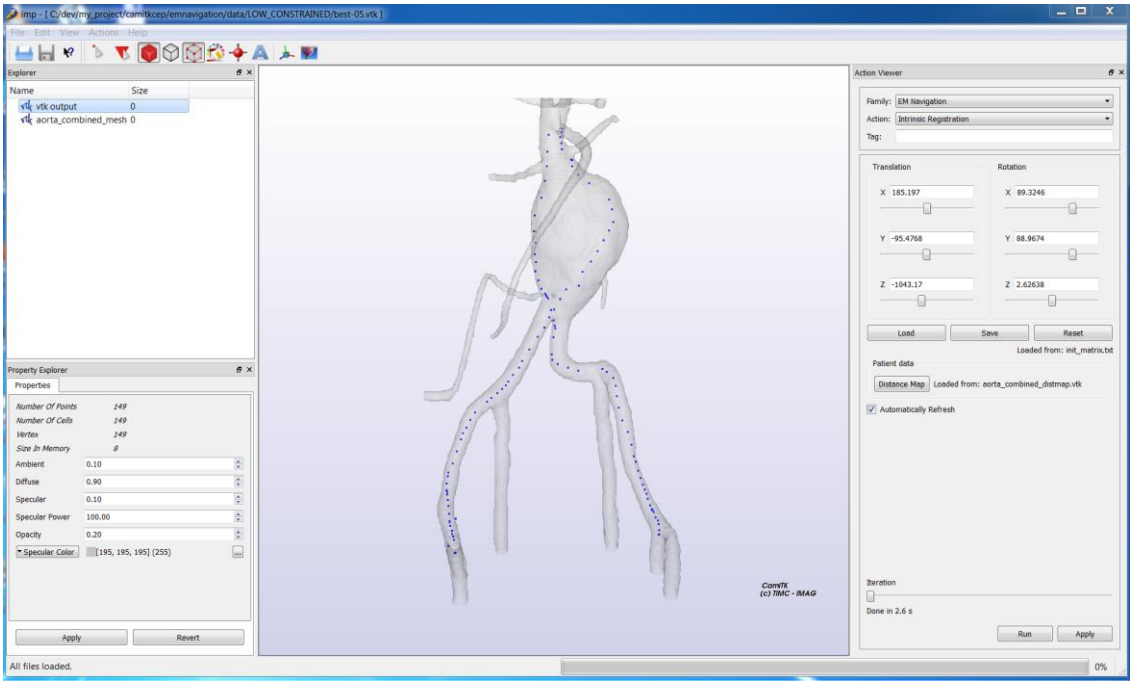

(d)

Figure 1. Field Generator positions next to the operating table: (a) Position A (b) Position B. (c) Navigation interface: the green arrow corresponds to the catheter tip position and orientation. (d) Registration procedure software: the blue dots depict the transformed 3D positions of the catheter tip to the 3D description of the vasculature space.

We used the modified catheter with a five degrees of freedom sensor coil placed in its tip. For the low constrained trajectories, the modified catheter was successively inserted into each iliac artery, and was positioned in the coeliac aorta. The modified catheter was withdrawn freely with different speeds inside the aorto-iliac lumen to obtain 5 low constrained trajectories in the EMT coordinate system. The modified catheter was also inserted and displaced with different speeds inside another catheter already in place in the aorta to obtain 5 high constrained trajectories. In the case of extrinsic registration approach, two configurations of external sensors (3, 4 sensors) were considered. They were observed both with EMT and 3DRX (Artis ZeeGo, Siemens).

Results

Table 1 shows the localization errors obtained with the different registration approaches. For the different configurations, the localization error is given by the distance between the 3DRX position and the transformed EMT position of the catheter tip. The mean and standard deviation (SD) of the localization errors for each configuration was computed on 9 arbitrary positions (not used for the registration) of the catheter tip inside the aorta.

Table 1. Localization errors expressed in *mm*.

			FG Positions			
			Position A		Position B	
			Mean	SD	Mean	SD
Intrinsic registration (Catheter tip trajectories)	Low constrained trajectories (LCT)	LCT 1	2.811	0.815	2.191	0.549
		LCT 2	2.655	0.559	1.747	0.717
		LCT 3	2.819	0.660	1.749	0.553
		LCT 4	2.738	1.109	2.336	0.263
		LCT 5	2.638	0.843	2.849	1.025
		All LCT	*2.732*	*0.742*	*2.174*	*0.762*
	High constrained trajectories (HCT)	HCT 1	2.307	0.528	2.155	0.524
		HCT 2	1.851	0.682	2.519	0.641
		HCT 3	2.815	0.607	1.463	0.495
		HCT 4	1.907	0.580	2.195	0.527
		HCT 5	2.359	0.552	1.219	0.641
		All HCT	*2.248*	*0.666*	*1.910*	*0.733*
Extrinsic registration (External sensors)	3		0.800	0.486	0.787	0.212
	4		0.793	0.553	0.727	0.268

As shown in Tab. 1, the localization error are related to the distance between the FG and the tracked catheter and to the constraint on the trajectory inside the vascular structure. The localization error obtained with the intrinsic registration approach decreases from low constrained to high constrained trajectories for both of the FG positions. We obtained better results when the FG is closer to the tracked catheter (position B). For the extrinsic registration approach we did not notice differences of localization error with higher number of sensors.

Considering the intrinsic registration approach with the FG in position B and high constrained trajectory, we tested the capability of navigating to a specific target. Using the 3D navigation

interface (Fig. 1c), two operators successfully reached a target sphere of 2.5mm radius placed at the entrance of each renal artery. For the operator 1 and 2 respectively, the average time was 47s and 43s to access left artery and 76s and 65s to access right artery.

Conclusion

We studied two 3D-3D registration approaches. They do not require external landmarks placed on the patient and thus could be more easily integrated in the clinical workflow. Due to the limited localization accuracy, it is still difficult to consider the EMT solution for precise positioning of the endovascular devices. However, the EMT system could be used to assist the navigation toward locations which are difficult to access, *e.g.* for the catheterization of collateral arteries in the context of endovascular aneurysm repair. Additional *in-vivo* experiments are required to confirm the navigation capability of the EMT system.

References

[1] Manstad-Hulaas F, Ommedal S, Tangen GA, Aadahl P, Hernes TN. Side-branched AAA stent graft insertion using navigation technology: a phantom study. *Eur Surg Res* 2007;**39**(6):364-71.

[2] de Lambert A, Esneault S, Lucas A, Haigron P, Cinquin Ph, Magne J-L, Electromagnetic Tracking for Registration and Navigation in Endovascular Aneurysm Repair: A Phantom Study. *European journal of vascular and endovascular surgery*. 2012. (43)6:684-9.

[3] C. Fouard, A. Deram, Y. Keraval, E. Promayon. CamiTK: a Modular Framework Integrating Visualization, Image Processing and Biomechanical Modeling. In Soft Tissue Biomechanical Modeling for Computer Assisted Surgery, Y. Payan (ed.), pp. 323-354, 2012.

Percutaneous procedures with CT-Ultrasound fusion guiding imaging system: evaluation of the accuracy

Fabrice Bing[1,2];Julien Garnon[1];Iulian Enescu[1];Georgia Tsoumakidou[1];Marie-Aude Thenint[1];Elodie Breton[2];Michel de Mathelin[2];Mateus Cardoso Saldanha[3];Mickael Schaeffer[4];Eric Sauleau[4];Afshin Gangi[1,2]

1 Interventional Radiology Unit, Nouvel Hôpital Civil, Hôpitaux Universitaires de Strasbourg, 67100 Strasbourg, France

2 ICube laboratory, UMR 7357, Strasbourg University, boulevard Sébastien-Brant, BP 10413, 67412 Illkirch cedex, France

3 Radiology Unit, Cancer Hospital de Barretos, Brazilia

4 Groupe de méthode en recherche clinique, Service de santé publique, Hôpitaux universitaires de Strasbourg, 67100 Strasbourg, France

Percutaneous interventional procedures need precise device positioning, using imaging guidance such as ultrasound (US), Computed Tomography (CT), fluoroscopy or Magnetic Resonance Imaging (MRI). Fusion imaging guidance may be an interesting solution when the interventional radiologist needs information belonging to different imaging volume. Virtual navigation systems in pre-operative 3D MRI or CT datasets bring the possibility to improve real-time lesion targeting. These systems can be used alone with optical or electromagnetic tracking platforms, or associated with US guidance.[1] For this last solution, the operator has the opportunity to navigate in the CT or MRI 3D volume loaded when performing the US exploration. Hence fusion systems bring the possibility to navigate in an enhanced 3D volume, as the CT or MRI volume loaded can be injected (arterial or portal time for the liver for example). The operators can beneficiate from dynamic information of contrast injection without loosing it during the procedure. However, the operator has to be sure that when looking at the lesion in the virtual volume, it corresponds to the reality. This is even more important in case of hard-to-find lesions with ultrasound.[2-4]

Evaluation of accuracy of fusion imaging guidance system using US as real-time imaging modality for positioning a needle *in vitro*[5] or in a mobile organ[6] has been poorly reported. In this study, we wanted to investigate the accuracy of this system, in measuring the distance between virtual and real locations of a 22G needle put in contact of a hepatic lesion.

Materials and methods

Informed consent was signed by all patients who accepted to participate to this study, validated by the clinical research center of our institution. Eight needles in eight patients

treated by radiofrequency thermal ablation (RFA) for hepatic tumors were evaluated. The insertion of a 22G spinal needle in the liver was performed using the CT–ultrasound fusion imaging system (Toshiba, TUS-A500, SmartFusion application). The aim was to put the needle just at the contact of the lesion, without penetrating it.

Shortly, a magnetic position sensor was attached to the ultrasound transducer shaft. A CT scanner was performed just before the procedure and 3D DICOM data sets were used for fusion. A general anesthesia was performed before the CT scan acquisition and the patient remained in the same position on the CT table during the whole procedure. Rigid coregistration was performed using one to three anatomical points (portal vein, coeliac artery, hepatic veins) to match the two imaging data sets spatially to each other. To calculate the real coordinates of the needle, CT scanner was repeated once the spinal needle in its final position.The accuracy of the fusion system was evaluated with the 22 Gauge needle tip position and did not concern the insertion of the final needle used for thermal ablation. Once the procedure finished, differences between real (x, y, z) and virtual (x', y,' z') coordinates of the tip of the needle (D for distal point) and of a needle point located 3cm proximally to the tip (P for proximal) were calculated (Figure 1). X, y and z coordinates correspond to the left-right, antero-posterior and cranio-caudal axis respectively.

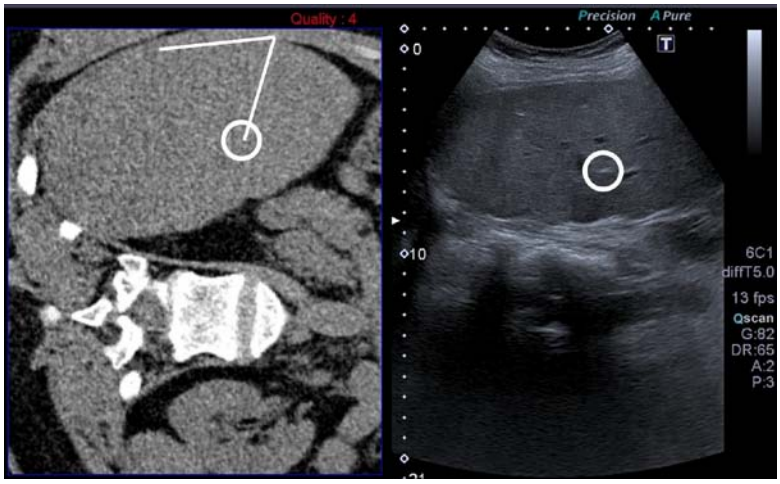

Figure 1. Virtual CT image (left side) and corresponding real-time US image (right side) used for the insertion of the 22G needle in the liver. Distance between the tip of the needle (white point in the circle on US image) and the liver capsula and angulation between the needle and the tangent of the capsula are calculated on the US image and reported on the CT image.

Real coordinates were easily calculated on the control scanner. To obtain virtual coordinates, the CT plane seen on the US fusion had to be exactly reproduced using the initial

3D CT volume. Virtual location of the tip of the needle was then reported on the CT volume and coordinates (x',y',z') of points P and D calculated (Figure 2).

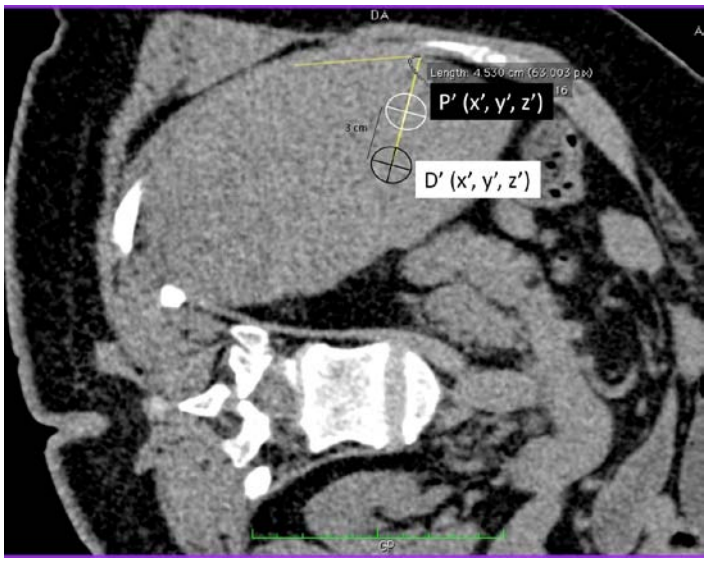

Figure 2. Reconstruction of the virtual CT plane with the initial CT volume to get virtual coordinates of the tip of the needle (D'(x', y', z')) and a point on the needle 3cm proximally from the tip (P'(x', y', z')). All of the organs seen on the picture have to present the same aspect as on the virtual CT plane (figure 1, left side). Once the good plane obtained, same angulation and distance of the needle in the liver as seen on real US image are reported on the plane and virtual coordinates calculated.

Statistical analysis

A baysian analysis of the data was performed to know the probability of the error to be less or more than 7 mm: this value was considered to be acceptable for an ablation of a hepatic tumor. It was not possible to obtain p values as the number of patient included was too small.

Results

Absolute value of mean differences of the three coordinates (|x'-x|,|y'-y|,|z'-z|, mean±SD) were 2.7±2, 6.2±4.6 and 5.2±4.7 mm for the distal (D) point. Results were 2.5±2.5, 5.7±2.9 and 5.6±4.7 mm for the proximal (P) point. Global mean difference was 4.7mm±4.1mm and 4.6mm±3.7mm for D and P respectively. Those differences were compared to 7 mm by using gamma distributions and bayesian methods. X coordinates could be considered less than 7 with probabibility close to 1. Y and Z were not considered bigger or smaller (Prob > 7 close to 50%). No difference was observed when comparing coordinates of P to D.

Discussion

In this preliminary study, we evaluated the accuracy of a fusion imaging guidance system for the insertion of a 22G needle in the liver. The aim was not to report the clinical error, as we did not try to put the tip of the needle in the lesion. The measured error corresponds firstly to the registration error, secondly to the error due to the localized deformation of the organ and thirdly to liver motion during breathing. Mean registration error reported was 3.0±0.1mm using calf livers.[5] In a study using CT imaging alone with electromagnetic needle tracking, image registration error averaged 1.4 mm in the phantom but was 19 mm in the animal.[7] Accuracy of CT–US image system was evaluated in pigs: from 6 mm for muscle and kidney, the accuracy dropped to 14 mm in the liver.[8] This discrepancy emphasizes the problem of respiratory error. For an optimal navigation in the US 3D volume, the operator needs to exert an abdominal pressure with the probe that may stretch the liver in the three dimensions. This deformation is not taken into account in the CT volume and the operator has to adapt this pressure to understand the location of the needle in the virtual 3D CT volume. The liver motion during breathing results in a modification of the real position of the target, not reported in the virtual CT volume. Initial, final CT scanner and procedure were performed in an ideal situation as the patient was exactly in the same position on the table.

This study presents several limitations. First the reconstruction of the virtual CT plane added a supplementary error, as it may be difficult to have exactly the same planes. This step was sometimes laborious and very long. It is difficult to know how imprecise the reproducibility of the virtual plane was. Secondly the needle is not visible on the virtual CT scanner and we made an extrapolation of the tip and angulation of the needle from the US image to the CT scanner. However, this extrapolation is mentally used by the operator when performing the punction and we tried to reproduce the same for the measurement. Thirdly, the error is measured in ideal conditions as the CT scan recorded has just been performed before the procedure in the exact position of the punction. It will be interesting to evaluate the accuracy of the system when a CT scan or MRI preformed days before the punction is loaded.

We found that CT–ultrasound fusion allows navigation in both ultrasound and pre-operatively acquired CT volume with a mean difference of coordinates of 4.7mm±4.1mm and 4.6mm±3.7mm for the tip of the needle and a needle point located 3 cm proximally respectively. This error is acceptable in comparison to the mean registration error of 3.0 mm reported in a in vitro study.[5] This error has to be reevaluated with the insertion of the final needle that will further modify the anatomy and when the prior MRI or CT 3D volume is

performed away from the procedure: these conditions of working are closer to real everyday examinations.

Acknowledgments

This work was partly supported by the French ANR within the Investissements d'Avenir program (Labex CAMI) under reference ANR-11-LABX-0004 and by the PRI (Projet de Recherche Interne) of the University Hospital of Strasbourg (CHRU).

The authors do not present any conflict of interest in relation with this article.

References

1. Krucker J, Xu S, Venkatesan A, et al. Clinical utility of real-time fusion guidance for biopsy and ablation. J Vasc Interv Radiol 2011; 22:515-24.
2. Hirooka M, Iuchi H, Kumagi T, et al. Virtual sonographic radiofrequency ablation of hepatocellular carcinoma visualized on CT but not on conventional sonography. AJR Am J Roentgenol 2006; 186:S255-60.
3. Nakai M, Sato M, Sahara S, et al. Radiofrequency ablation assisted by real-time virtual sonography and CT for hepatocellular carcinoma undetectable by conventional sonography. Cardiovasc Intervent Radiol 2009; 32:62-9.
4. Lee MW, Rhim H, Cha DI, et al. Percutaneous radiofrequency ablation of hepatocellular carcinoma: fusion imaging guidance for management of lesions with poor conspicuity at conventional sonography. AJR Am J Roentgenol 2012; 198:1438-44.
5. Crocetti L, Lencioni R, Debeni S, See TC, Pina CD, Bartolozzi C. Targeting liver lesions for radiofrequency ablation: an experimental feasibility study using a CT-US fusion imaging system. Invest Radiol 2008; 43:33-9.
6. Hakime A, Deschamps F, De Carvalho EG, Teriitehau C, Auperin A, De Baere T. Clinical evaluation of spatial accuracy of a fusion imaging technique combining previously acquired computed tomography and real-time ultrasound for imaging of liver metastases. Cardiovasc Intervent Radiol 2010; 34:338-44.
7. Banovac F, Wilson E, Zhang H, Cleary K. Needle biopsy of anatomically unfavorable liver lesions with an electromagnetic navigation assist device in a computed tomography environment. J Vasc Interv Radiol 2006; 17:1671-5.
8. Appelbaum L, Solbiati L, Sosna J, Nissenbaum Y, Greenbaum N, Goldberg SN. Evaluation of an electromagnetic image-fusion navigation system for biopsy of small lesions: assessment of accuracy in an in vivo swine model. Acad Radiol 2013; 20:209-17.

Evaluation of Human Factors in Neuronavigated Transcranial Magnetic Stimulation (TMS)

Hubert Chauvat[1,2], Romuald Ginhoux[2], Benjamin Maurin[2]

(1) ECE Paris, 37 quai de Grenelle, Immeuble Pollux, 75015 Paris
(2) Axilum Robotics, 1 place de l'hôpital, 67000 Strasbourg

Introduction

Transcranial Magnetic Stimulation (TMS) is a non-invasive brain stimulation technique where a coil delivering focal, short and high-intensity magnetic pulses is applied to the head [1]. Depending on the targeted cortical area, effects of the locally induced electrical currents have shown to have therapeutic applications for the treatment of drug-resistant depression, auditory hallucinations of schizophrenia or neuropathic pain [2]. The coil being held by hand, TMS is affected by the experience and attention of the operator manipulating it. Human errors in targeting the appropriate area therefore alter the accuracy and repeatability of the delivery of transcranial stimuli. Human factors are of a particular relevance in clinical applications of TMS where current treatment protocols, for instance in depression, involve several thousands repeated stimulations during a session of several tens of minutes, where sessions have to be repeated every day for a few weeks [2].

Computer and robot assistance tools have been developed with the objective to improve the accuracy of the targeting of the stimulations: Neuronavigation allowed to personalize the targeted cortical area based on MR images of the head, improving the accuracy of the transcranial stimulations [4, 5]. Robotic manipulators were introduced taking advantage of neuro-navigation tracking tools to further cancel the head motion during a session, repeat a TMS protocol at the desired positions and make sure the maximal amount of energy is transmitted to the brain by keeping the coil applied to the head [6, 7, 8].

If neuronavigation and robotics contribute to suppress a part of human factors in TMS, however, the human operator still has a key impact on accuracy and repeatability. Indeed, performing the necessary head registration at the beginning of a TMS session requires training and attention from the operator. Head registration is the prerequisite step to any neuronavigated or robotic TMS session and has to be repeated from scratch at any session once the patient is equipped with optical tracking markers. The objective is to put in correspondence the brain in the MR images with the brain of the real patient. Limited data are currently available to understand the influence of human factors on the quality of head registration although it directly affects the quality of coil positioning. In [3], authors evaluated the mean error of head registration in a commercial Nexstim neuronavigation device to 2.5 mm in an overall mean error of their entire system evaluated to 5.7 mm but did not describe the evaluation method. The goal of the paper is to study the influence of human factors on the

repeatability of head registration. We propose a systematic framework applicable to commercial neuro-navigation devices and give early results.

Materials

We used a commercial neuronavigation device (Localite TMS Navigator v2.8, Localite, St Augustin, Germany) where head registration consists in 3 main steps: First, as a pre-registration step, the positions of a few anatomical landmarks highlighted on a 3D reconstruction of the skull have to be recorded on the corresponding parts of the real head. For that purpose, the operator equips the patient with optical tracking markers and uses a specific pointing tool (see Fig. 1), containing 3 optical markers, all being in the field of view of a NDI Polaris Spectra camera (NDI, Ontario, Canada). Second, an arbitrary number of additional points have to be recorded freely over the surface of the skin, allowing for a precise surface fitting of the real head. Third, the software computes the final registration and allows to measure offsets between the pointing tool and the 3D head model.

We used a dummy plastic head which went into a CT scanner (Siemens Somatom) to create reference images in DICOM format for loading into neuronavigation devices. The head surface is spanned by about hundred holes, including holes on ears and nose (see Fig. 1). As holes are easily visible in the images, they allow for a precise pointing during registration and provide ground-truth references.

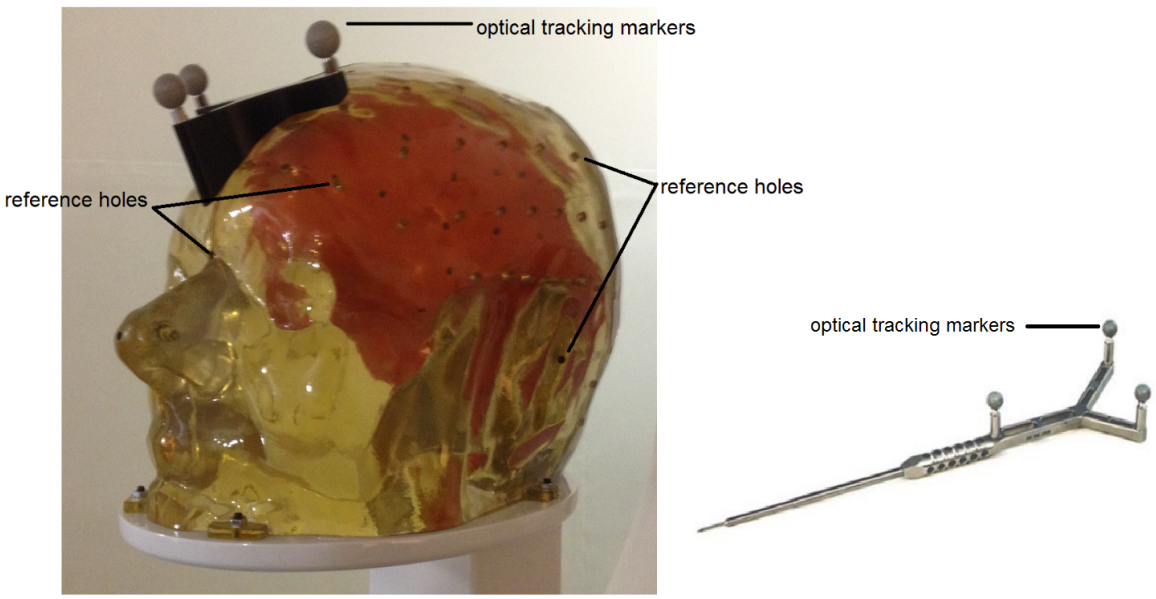

Figure 1 - Dummy plastic head equipped with optical tracking markers (left) and pointing tool (right)

Methods

Three holes of the dummy head were defined as landmarks for the pre-registration step: there were 2 holes in left and right preauricular areas and 1 hole on the nasion. About 100

surface points were recorded during the second registration step. 1 additional hole was used during the final registration step as a verification point: the pointing tool was inserted in the hole and the distance between the tip of the tool and the center of the hole was measured using the neuronavigation software. Head registration is supposed to be perfect when that distance is 0.

Seven operators (male, 23-52 years old) received a training. Each operator had to realize 3 different head registrations: the first one (T1) was designed to be the most accurate. The operator took time to position the pointing tool as precisely as possible and to turn its tracking markers towards the optical axis of the camera to optimize marker detection (the camera's optical axis and the plane formed by the three markers are orthogonal). The goal was to obtain a reference offset for each operator.

Then, we designed two tests to simulate typical error scenarii in order to evaluate how human factors can induce errors at the final step of the registration process. For the second test (T2), the operator kept the pointing tool in the planned holes, but this time, he had to turn it along its axis in order to reach an orientation of its three optical markers where the camera can barely see them: the camera's optical axis and the plane formed by the three markers are almost coplanar. The final test (T3) focused on good orientation of the tool but a bad positioning: the operator voluntarily missed the expected holes by 2 millimeters.

Results & Discussion

Results are shown in Fig. 2. In ideal conditions (T1) where one would expect the reference offset to be close to 0, we measured a mean error of 1.43 mm (min: 0.40 mm, max: 3.00 mm). This shows that head registration is not repeatable from one operator to another, shifting the position of the coil up to 3 mm during a TMS session. The second test (T2) proves that if the pointing tool is not properly oriented towards the camera, the offset error can be multiplied by a factor of 2 (min: 0.80 mm, mean: 2.90, max: 7.00). The third test (T3) shows that if the landmarks are not accurately pointed at during the first registration step, it becomes difficult to reach an error below 2 mm whereas 100 surface points have been recorded (min: 1.40 mm, mean: 3.20, max: 6.20).

These results show that training and attention of the operator affect the repeatability of head registration. T2 and T3 show common human errors which may combine on real patients, leading to large registration offsets. By shifting the coil position on the real head they may weaken the repeatability of TMS.

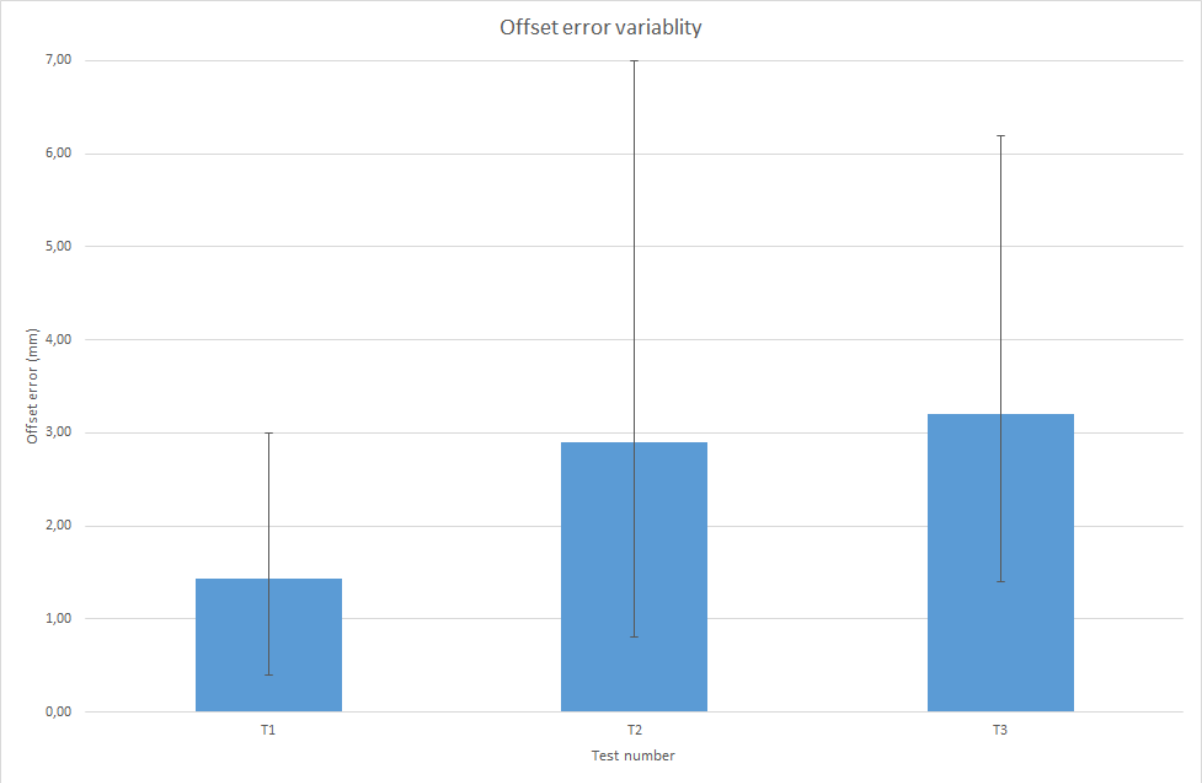

Figure 2 - Offsets measured with the verification point in the 3 head registration tests.

References

[1] A. T. Barker, R. Jalinous, and I. L. Freeston, Non-invasive magnetic stimulation of human motor cortex, The Lancet, vol. 325, no. 8437, pp. 1106–1107, 1985.

[2] J.-P. Lefaucheur et al., French guidelines on the use of repetitive transcranial magnetic stimulation (rTMS): Safety and therapeutic indications, Clinical Neurophysiology (2011), vol 41, num 5-6, p221-295.

[3] J. Ruohonen, J. Karhu, Navigated Transcranial Magnetic Stimulation, Clinical Neurophysiology (2010), vol 40, p7-17.

[4] R. Sparing, M.D. Hesse and G.R. Fink, Neuronavigation for transcranial magnetic stimulation (TMS): Where we are and where we are going, Cortex 46 (2010), p118-120.

[5] R. Ahdab, S.S. Ayache, P. Brugières, C. Goujon, J.-P. Lefaucheur, Comparison of “standard’’ and navigated procedures of TMS coil positioning over motor, premotor and prefrontal targets in patients with chronic pain and depression, Clinical Neurophysiology (2010), vol 40, p27-36

[6] Lars Richter, Robotized Transcranial Magnetic Stimulation, Springer, 2013.

[7] R. Ginhoux, P. Renaud, L. Zorn, L. Goffin, B. Bayle, J. Foucher, J.P. Armspach and M. de Mathelin, A Custom Robot for Transcranial Magnetic Stimulation: First Assessment on Healthy Subjects, IEEE Conference on Engineering in Medicine and Biology, July 2013.

[8] G. Pennimpede, Hot Spot Hound: a novel robot-assisted platform for enhancing TMS performance, IEEE Conference on Engineering in Medicine and Biology, July 2013.

INSTRUMENT DETECTION AND TRACKING

Online registration applied to multi-modal tracking for real-time scan plane alignment in interventional MRI

M. Neumann[1], L. Cuvillon[1], E. Breton[1], M. de Mathelin[1], L. Pan[2], A. Hengerer[2]

[1]ICube, Université de Strasbourg, CNRS, IHU Strasbourg; Strasbourg, France
[2]Center for Applied Medical Imaging, Siemens Corporate Research, Baltimore, MD, United States

1 Introduction

Magnetic resonance imaging (MRI) is used for guiding minimally invasive percutaneous interventions, such as tumor ablations and biopsies, owing to the high soft-tissue contrast and to the possibility of free image plane orientation and positioning of MRI. In order to monitor the procedure in real-time, the acquired image planes are aligned to the instrument (needle) axis. This real-time image plane orientation and positioning is usually performed manually, by a technologist at the MRI console, and its time efficiency strongly relies on the experience of the team, as well as on available communication means with the physician standing inside the MRI room. The previously developed tracking approaches for automatic scan plane alignment can be divided in active (wired components measuring tracking gradients [1] or optical systems for marker tracking [2]) and passive systems (image-based detection of instruments or markers [3] [4]). Advantages of active approaches are the tracking precision, the small size of the sensors, or the high imaging frequency when camera systems are used. Passive approaches allow for tracking within the MR images, without heavy additional instrumentation. Combining active and passive approaches allows to join their individual advantages.
In this work, the evaluation of an online registration approach for a multi-modal tracking workflow is presented, combining MR image tracking of a passive marker and RGB-D sensor images for real-time automatic scan plane alignment.

2 Materials and Methods

All experiments are performed in a 1.5T magnet (MAGNETOM Aera, Siemens) using an interactive, real-time, multi-slice SSFP sequence [5] (Field of View 450mm, TE/TR 2.2/4.1ms, Flip Angle 50°, Slice Thickness 5mm, refresh rate 900ms). The proposed workflow (both MR and RGB-D image reception and processing, scan plane control) is performed on an external PC connected to the MRI console PC and to the RGB-D sensor. The RGB-D sensor is positioned in the back of the MRI scanner capturing the scene inside the MRI tunnel. The tracked target consists in an MRI contrast-agent filled cylinder with 2 colored balls attached at its distal ends in order to be simultaneously

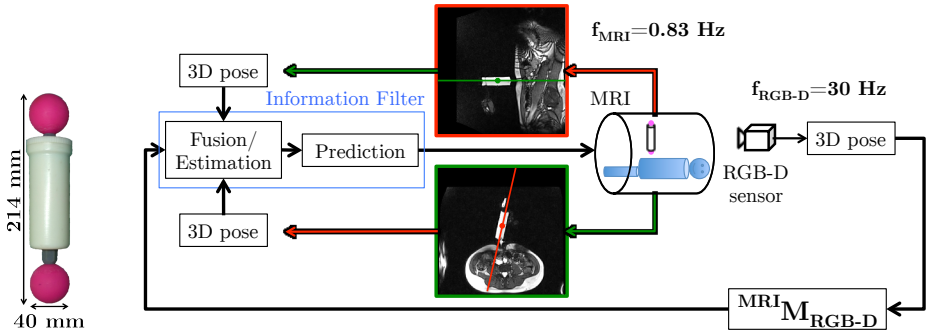

(a) (b)

Fig. 1: a: Multi-modal tracking marker composed of a passive MRI marker and 2 colored balls. b: Multi-modal tracking workflow: sagittal (red) and transversal (green) oblique MR image planes are alternately acquired. Detection results from RGB-D sensor and from MR images are fused and the MR image planes are aligned accordingly.

detectable in MR and RGB-D sensor images (Fig.1a). The proposed workflow controls 2 alternately acquired orthogonal real-time MR scan planes aligned to the marker axis. For this purpose, the 3D marker pose is detected in both modalities and then fused using an Information Filter (IF). Based on the predicted marker pose from the IF, a marker-aligned scan plane is calculated and the corresponding command is sent to the MRI console PC (Fig.1b).

A dynamic online registration procedure is performed in the beginning of the workflow in order to determine the rigid transformation between the RGB-D sensor frame and the MRI frame of reference ($^{MRI}M_{RGB-D}$). For this purpose, up to 20 marker positions are detected in both modalities (matched points) and the acquired point clouds are then used for determination of the optimal rigid transformation between RGB-D and MRI frames. In the beginning of the workflow, tracking is performed based on MR images only [6], as this transformation is unknown. As soon as a valid transformation has been found, the workflow switches to hybrid mode, where tracking is performed by fusing measurements of both modalities. At least 3 matched points are necessary for determination of a first rigid transformation between the modalities. The quality of the registration increases with the quantity of the matched points and depends also heavily on their spatial distribution. Therefore, during the entire intervention, current matched points are evaluated against newly acquired points and replaced if registration quality is improved.

3 Results

Registration quality is assessed with the root mean square error (RMSE) between the point set acquired in the MRI frame and the corresponding one in the RGB-D

sensor frame, back projected to the MRI frame with the current rigid transformation. In a series of 14 workflows (mean duration 1.5 min; 20 matched points per workflow) performed by a user displacing the tracked target in a free-hand motion, a mean RMSE of 7 mm was obtained, that is on the order of slice thickness and in-plane resolution, as expected.
One strength of the workflow is that when detection fails in one modality, the IF uses the available measurements from the other modality. Furthermore, the IF allows the flexible fusion of the MRI and RGB-D measurement data, acquired with different measurement frequencies.

4 Conclusion

The proposed multi-modal workflow combines the high imaging rate of an RGB-D sensor with a slower MR image based tracking approach that allows for online registration and can function independently in case of camera obstruction. This workflow could be easily integrated in the clinical workflow as only little additional instrumentation is needed (RGB-D sensor and wireless marker) and no explicit calibration step has to be performed. Dynamic registration (thanks to MRI tracking alone) would allow to displace the RGB-D sensor during the procedures, for instance to improve the line-of-sight.

5 Acknowledgment

This work was partly supported by the French ANR within the Investissements d'Avenir program (Labex CAMI) under reference ANR-11-LABX-0004 and the IHU Strasbourg (ANR-10-IAHU-02).

References

1. K. Qing et al. "A multi-slice interactive real-time sequence integrated with the EndoScout tracking system for interventional MR guidance," in Proceedings of the 18th Annual Meeting of ISMRM, 2010, p. 1860.
2. R. Viard et al., "Needle positioning in interventional MRI procedure: real time optical localisation and accordance with the roadmap," in EMBS 2007. 29th Annual International Conference of the IEEE, 2007, pp. 2748-2751.
3. A. de Oliveira et al., "A new system for passive tracking of a prostate biopsy device with automatic 3D needle position estimation," in Proceedings of the 16th Annual Meeting of ISMRM, 2008, p. 3003.
4. F. Maier et al., "3D passive marker tracking for MR-Guided interventions," in Proceedings of the 19th Annual Meeting of ISMRM, 2011, p. 3749.
5. L. Pan et al., "An integrated system for catheter tracking and visualization in MR-Guided cardiovascular interventions," in Proceedings of the 19th Annual Meeting of ISMRM, 2011, p. 195.
6. M. Neumann et al., "Evaluation of an image-based tracking work ow with kalman Filtering for automatic image plane alignment in interventional MRI," in EMBS 2013. 35th Annual International Conference of the IEEE , 2013, pp. 2968-2971.

AUTOMATIC DETECTION OF ENDOSCOPE IN INTRAOPERATIVE CT IMAGE: APPLICATION TO AR GUIDANCE IN LAPAROSCOPIC SURGERY

Sylvain Bernhardt[*†‡], Stéphane A. Nicolau[‡], Vincent Agnus[‡], Luc Soler[*‡],
Christophe Doignon[†] and Jacques Marescaux[*‡]

[*]IHU, Institut Hospitalo-Universitaire, Strasbourg, FRANCE
[†]ICube (UMR 7357 CNRS), Université de Strasbourg, Strasbourg, FRANCE
[‡]IRCAD, Virtual Surg, Strasbourg, FRANCE
sylvain.bernhardt@ihu-strasbourg.eu

I. Introduction

Augmented reality (AR) in minimally invasive surgery has rapidly grown over the recent years [1]. Commonly, the surgical scene is augmented through the endoscopic view with a 3D model extracted from a preoperative acquisition. Nevertheless, due to the probable pneumoperitoneum and the patient displacement, the organs of interest often drastically change in shape and place [2]. Methods exist that attempt to recover or simulate the distortion between the pre- and intraoperative states. For example; surface reconstruction can be used to recover the organ surface from the endoscopic image, but the registration is reliable only for the visible part of the organ. Also, methods have been designed to recover the organ distortion through simulation using biomechanical models or through successive intraoperative 3D acquisitions but these still require yet another calibration process to locate the endoscope. The most popular solution is to resort to optical tracking; however this technique is costly, cumbersome and prohibits the surgeon from occluding the line of sight between the tracking cameras and the endoscope. This also requires many calibration steps that can slow down the surgical workflow.

The 3D rotational C-arm is one piece of equipment getting more and more popular as its relatively small bulkiness makes reasonable the use of intraoperative imaging. In this context, we propose a new paradigm to automatically register the referential frame of the intraoperative 3D imaging system with the one of the endoscopic camera, without any external tracking system or analysis of the endoscopic image. We propose to include the distal part of the endoscope in the C-arm acquisition (as shown in Fig.1) and estimate the position of the optical center from the scope position and orientation in the reconstructed volume.

Depending on the intervention stage, the camera is brought to move or remain still. For example, during the surgical stages of segmentectomy or thermal ablation, the endoscope may remain static. Then, our method allows an automatic registration that requires no additional equipment in the hybrid operating room or on the patient. If endoscopic navigation is required, we then could resort to a classic tracking technique but our approach would still remove any need of calibration for these systems.

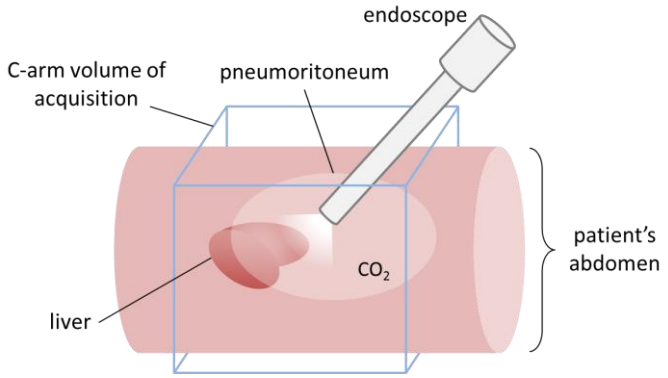

Figure 1: Illustration of the laparoscope placement in the abdomen and through the C-arm imaging volume.

II. Methodology

In order to carry out AR, one needs to merge accurately the model rendering and the image from the endoscope. To achieve this, we must determine what is the exact view of the model that is corresponding to the endoscopic image content. This can be done by determining all the intrinsic and extrinsic parameters of the camera that are subject to varying from one intervention to another. Among the intrinsic parameters, we consider the position of the optical center, the (radial) distortion of the lens and the field of view. The extrinsic parameters are essentially the location and orientation of the camera in the model space (i.e. the 3D image space).

The intrinsic parameters are obtained through a classical camera calibration based on Zhang's method [3] with filming of a chessboard, once the surgeon has fixed the zoom and optics as desired. Thereby, we can notably determine the focal length, the position of the optical center in the image plane, as well as the radial distortion of the lens, allowing to warp (undistort) the image. During experiments we have led, we usually got reprojection errors below 0.7 pixel.

To determine the extrinsic parameters, we use the video information about the endoscope tip included in the volume image. The metallic composition of the endoscope makes it highly reflective to x-rays and yields very large values in the CT image – much larger than surrounding artifacts or what any human tissue would produce. Thus, it is trivial to threshold the voxels representing the endoscope tip. Afterwards, knowing the tubular (right cylinder-shaped) shape of the endoscope, we retrieve the orientation and tip location of the endoscope in the volume image. It is worth observing that the resulting tip location does not necessarily correspond to the position of the optical center on the cylinder axis, as it depends on the zoom factor. Nonetheless, calibration experiments have shown that, with the FOV often set to a minimum value during interventions, the optical center is very close to the actual tip of the endoscope. In case of a zoom change, we could resort to a solution similar to [4,5] i.e. inferring the FOV from the size of the circular outline in the endoscopic image. So, we are able to determine all the extrinsic parameters but one; the tubular shape of the endoscope prevents from determining the actual roll angle around the axis of revolution. This estimation is fully automatic by using a camera-mounted high-end accelerometer which measures the angular position (pitch and roll) with respect to the gravity field.

III. Experiments

A dedicated chessboard has been made to assert our method's accuracy. It has been painted with a mix of black paint and baryum sulfate, a common radio-opaque component used in radiology, which makes it visible from both the CT machine and the camera. Once the camera has been calibrated and the tiny chessboard has been acquired by both modes of imaging following the protocol previously described, the endoscope position in the CT volume has been estimated with our method. Then, we independently extract the chessboard corners from both the CT volume and the endoscopic image with OpenCV and VTK. Thus, once the image from the volume rendering is blended with the camera view, the registration error (in pixels) can be computed between the two sets of image points across the 1080*p* image. We performed this experiment three times with different positions for the chessboard and the camera and got no more than 7 pixels of average registration error. The largest registration error corresponds to approximately no more than 0.70mm in the scene. Therefore, these errors are significantly small enough to fulfill AR purposes for surgical procedures.

We also performed our method on *in vivo* pig data, as shown by Fig.2.

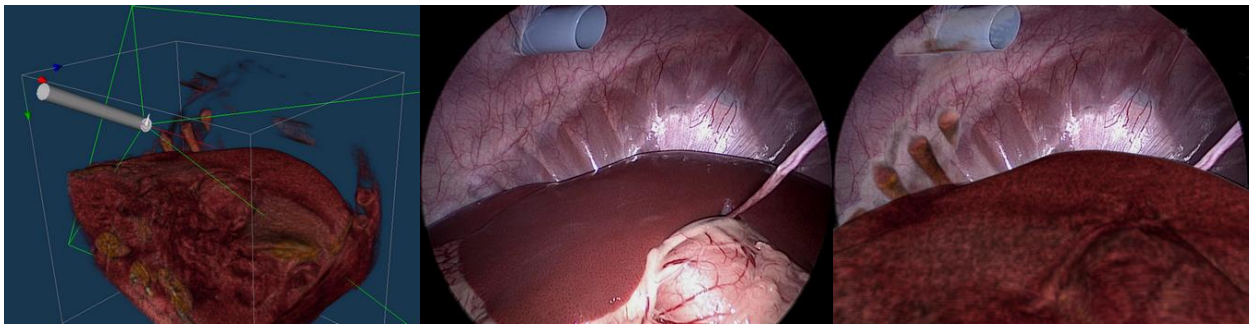

Figure 2: The volume rendering is displayed both with the endoscope represented by a white cylinder and a green frustum (left). The corresponding endoscopic image (middle) is then augmented with these volume renderings as per our method (right).

IV. Conclusion

In this article, we presented a novel way of registering the intraoperative model with the endoscopic camera, enabling AR without any external tracking device. The inclusion and analysis of the endoscope tip inside the C-arm field of acquisition allows a precise determination of almost all the camera extrinsic parameters. Rigorous evaluations with a calibration object and in vivo showed both quantitatively and qualitatively the benefits of our method. In the near future, more testing ought to be done to fully validate the technique and an integration to an operation room should also be achieved in order to experiment fully intraoperatively.

Acknowledgments

The authors would like to thank the IHU of Strasbourg for making the experiments possible, as well as P. Mewes and J. Fallert from Siemens and Storz for lending the necessary equipment. This work is part of the LASAR projet funded by IHU.

References

[1] T. Sielhorst, M. Feuerstein, and N. Navab, "Advanced Medical Displays : A Literature Review of Augmented Reality," *Journal of Display Technology*, vol. 4, no. 4, pp. 451–467, 2008.

[2] F. M. S´anchez-Margallo et al., "Anatomical changes due to pneumoperitoneum analyzed by MRI: an experimental study in pigs," *Surgical and radiologic anatomy : SRA*, vol. 33, no. 5, pp. 389–396, 2011.

[3] Z. Zhang, "A Flexible New Technique for Camera Calibration," *IEEE Transac. on Pattern Analysis and Machine Intelligence*, vol. 22, no. 11, pp. 1330–1334, 2000.

[4] T.-Y. Lee, T.-S. Chang, C.-H. Wei, S.-H. Lai, K.-C. Liu, and H.-S. Wu, "Automatic Distortion Correction of Endoscopic Images Captured With Wide-Angle Zoom Lens," *IEEE Transac. on Biomedical Engineering*, vol. 60, no. 9, pp. 2603–2613, 2013.

[5] C. Doignon et M. de Mathelin, A Degenerate Conic-Based Method for a Direct Fitting and 3-D Pose of Cylinders with a Single Perspective View, IEEE Int'l Conf. on Robotics and Automation, **ICRA'07**, Roma, Italy.

3D Pose Estimation of Actuated Instruments in Flexible Endoscopic Surgery

Paolo Cabras, David Goyard, Florent Nageotte
Philippe Zanne and Christophe Doignon*†

October 22, 2014

1 Introduction

With the advent of new minimally invasive surgery (MIS) techniques, flexible and continuum systems, which in the past were only used for minor tasks, are now making inroads in surgical interventions. In flexible surgical endoscopy, instruments are long, thin, usually cable-driven bendable systems. Their manipulation is complex and robotic assistance is of high interest for using them during surgical tasks [1]. However, the accurate robotic control of continually bending instruments is difficult. Indeed, proximal information from encoders is not reliable because of complex mechanical interactions involving cables and sheaths. For implementing efficient control modes the loop should be closed using external sensors. This is critical for allowing automatic gestures and improving telemanipulation.

Due to issues related to size, compatibility with the surgical environment and resistance to deformation, there are no standard sensors which can be directly used *in-vivo* for flexible instruments. Therefore, using the embedded endoscopic camera seems to be an interesting way to measure the positions of the instruments while providing information relative to the environment. This approach has been previously attempted in [2]. However, the described method only works properly if the system geometric model is perfectly known and constant, which is not the case in practice.

In this context, we propose two different solutions to the problem in the case of the STRAS / Anubis (ICube / Karl Storz) robotic system (see Fig. 1)[3].

*This work was supported by French state funds managed by the ANR within the Investissements d'Avenir programme (Labex CAMI) under reference ANR-11-LABX-0004. Authors thank Karl Storz for providing the Anubis platform and the flexible instruments

†Authors are with ICUBE, University of Strasbourg, CNRS, France. cabras@unistra.fr

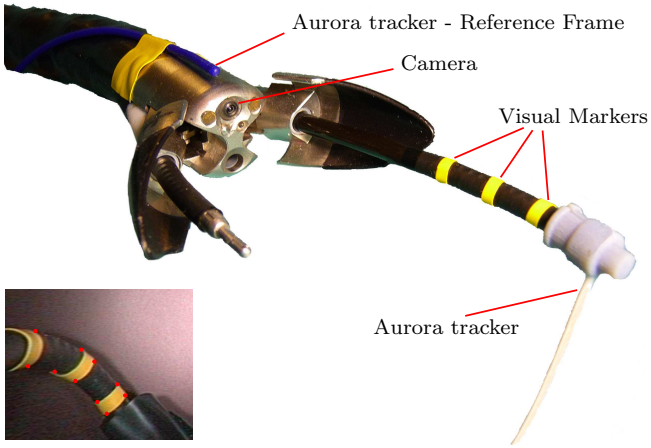

(a)

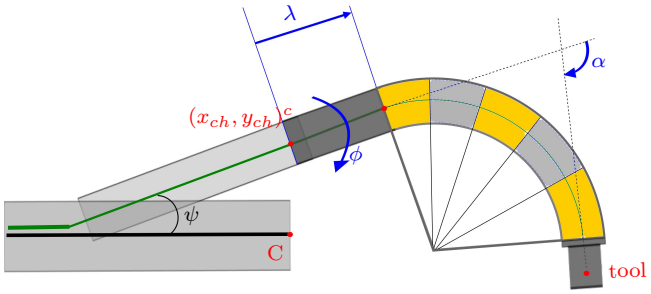

(b)

Figure 1: Flexible system for surgery and its modeling. (a) The tip of the Anubis platform with the camera, the flexible surgical instruments and their markers and the Aurora magnetic tracker. Middle: a typical endoscopic image. (b) Modeling of the instrument by its DOF (λ, ϕ, α) and its mechanical parameters (the ouptut of the instrument channel ($[x_{ch}, y_{ch}]$) and the orientation of the channel wrt the camera (ψ)).

2 Experimental Setup and Materials

The distal part of the Anubis platform is composed of an endoscopic camera and two instruments coming out from two channels included in the body of the endoscope (Fig. 1). These instruments have three degrees of freedom (DOF): translation and rotation with respect to the channel axis and deflection (indicated respectively as λ, ϕ and α in Fig. 1). To entirely describe the system, other *mechanical* parameters have to be taken into account: the position of the instrument channel (x_{ch}, y_{ch}) and its inclination wrt to the camera axis (ψ).

In-vivo environments present many different structures and, during the operation, smoke or water can decrease the quality of the image and make the detection of the instrument difficult. For this reason, three yellow markers were attached on the bending section of the surgical instruments as shown in Fig. 1: two markers in correspondence with the beginning and the end of the bending section and one in a median position.

The segmentation of the markers is realized by detecting the yellow regions in the CMY color space. Two kind of features are used. For each of the 6 sections defined by the limits between the colored markers and the black instrument, two characteristic points, called "corners" can be individuated (red spots in Fig. 1). One can also extract the "centroids" of each projection of the markers.

Electromagnetic trackers (Aurora, NDI) were attached onto the Anubis head (Fig. 1), providing ground truth measurements for the position of the tip of the instrument with respect to the camera.

3 Model-based Pose Estimation

Assuming that the camera and the system geometrical models are known, a synthetic (virtual) image of the scene can be computed for a given instrument configuration. Then, the problem of the 3D pose estimation can be formalized as an optimization problem whose aim is to find the best instrument configuration in terms of a "cost function" based on image features [4].

Approaches developed in [2] consider that the position of image features are influenced by the variation of the three DOF of the flexible instruments only. However, a complete precise model is difficult to obtain and parts of it may even vary during the operation for example due to play between the instruments and the channels. Therefore, a tolerance on the *mechanical* parameters should be considered. It is reasonable to assume that the actual values of the *mechanical* parameters are close to the nominal values. Hence, we developed a new cost function including terms that constrain the estimation of these parameters close to their nominal values.

4 Learning-based Solution

The basic idea in this second approach is to *learn* the function relating the 3D position of the instrument tip to the image features. This avoids relying onto a

parametric (potentially incomplete) model of the system.

We have chosen to use a network of radial basis functions (RBF) with Gaussian kernels for this data fitting problem, which allows to fit local variations while avoiding noise overfitting [5]. The input space is composed of the three centroids of the images of the markers. Centroids allow to execute the approximation function in a low dimensionality space. The output data are provided by the EM tracker. Once the centroids are obtained, the training data set (composed by centroids coordinates and 3D position) is enriched, taking into account possible segmentation errors.

The training set consists of 180 samples and is created by automatically covering the instrument workspace with a pre-defined robotic motion. The parameters and hyper-parameters (number of basis functions) of the RBF network are obtained by cross-validation onto this training set.

5 Results

A test sequence consisting of 116 images has been acquired. Three methods have been compared: (1) the model-based approach proposed in [2], (2) our improved method taking into account *mechanical* parameters variation and (3) the learning-based approach. For limiting the effect of image processing errors, the image features have been selected manually for the model-based techniques, but a random uniform noise of amplitude 5 pixels has been added. For the learning-based approach, image processing is automatic and identical in the training and test stages (see section 2). Results are shown in Fig. 2. RMS errors along x, y and z directions are respectively 2.75, 3.61 and 5.2 mm for method (1) (not shown in the figure), 1.96, 1.3 and 3.6 mm for method (2) and 1.64, 1.52 and 2.71 mm for method (3). Hence both proposed methods allow to significantly reduce the position measurement error with respect to the standard approach.

6 Conclusions

In this paper, two original techniques for estimating the 3D position of a flexible surgical tool used in flexible endoscopic surgery have been presented.

Both methods are demonstrated to be superior to the standard approach. Comparison is still difficult because, on one hand image processing required for the model-based approach is critical and no robust solution have been identified yet. On the other hand the workflow for the learning approach is more demanding, since it requires a specific sensor for generating the training set.

So far, results have been obtained using images only and considering them individually. Temporal filtering and fusion with information from proximal encoders are currently under investigation to improve the accuracy of measurement.

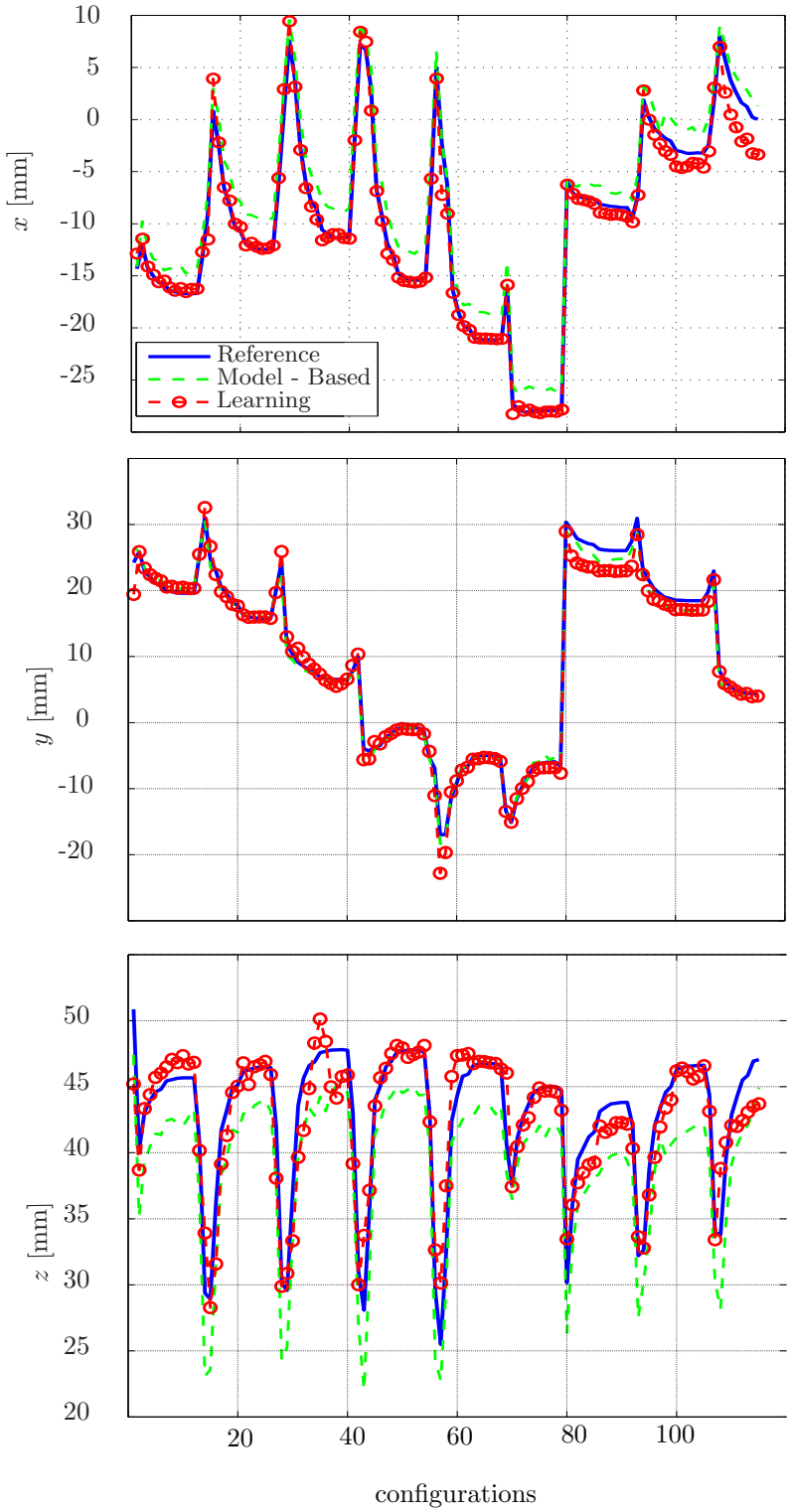

Figure 2: Comparison between the reference given by the EM trackers (blue), the estimation by the learning (red) and the improved model-based method (green) for x, y and z coordinates of the instrument tip during a test trajectory.

References

[1] G. Dogangil, B. Davies, and F. Rodriguez y Baena, "A review of medical robotics for minimally invasive soft tissue surgery," in *Proc. of the Institution of Mechanical Engineers*, vol. 224, no. 5, May 2010, pp. 653–679.

[2] R. Reilink, S. Stramigioli, and S. Misra, "Pose reconstruction of flexible instruments from endoscopic images using markers," in *IEEE International Conference on Robotics and Automation (ICRA)*, 2012, pp. 2938–2943.

[3] A. De Donno, L. Zorn, P. Zanne, F. Nageotte, and M. de Mathelin, "Introducing STRAS: a new flexible robotic system for minimally invasive surgery," in *IEEE International Conference on Robotics and Automation (ICRA)*, 2013, pp. 1213–1220.

[4] E. Marchand and F. Chaumette, "Virtual visual servoing: a framework for real-time augmented reality." *Eurographics*, vol. 21, no. 3, 2002.

[5] D. Broomhead and D. Lowe, "Multivariable functional interpolation and adaptive networks," *Complex Systems*, vol. 2, pp. 321–355, 1988.

BIOMECHANICS

Biomechanical modeling to prevent soft tissues pressure ulcers

V. Luboz[1], A. Perrier[1,2,3], M. Bucki[2], N. Vuillerme[3,5], F. Cannard[2], B. Diot[3,4] and Y. Payan[1]

(1) TIMC-IMAG Laboratory, CNRS & University Joseph Fourier, France

(2) Texisense S.A.S, Montceau-les-Mines, France

(3) AGIM Laboratory, CNRS & University Joseph Fourier, France

(4) IDS S.A.S, Montceau-les-Mines, France

(5) Institut Universitaire de France, Paris, France

INTRODUCTION

Pressure ulcers (PU) affect almost half of the patients in reanimation or geriatric units. They are localized injuries that affect the skin and underlying soft tissues, usually below a bony prominence. The main suspected causes are the excessive pressure intensity (internal tissue strains above 50 % for about 10 minutes) or prolonged compression (internal strains above 20 % for about two hours) [1]. Specific forms of PU, termed Deep Tissue Injuries (DTI), are defined as pressure-related injury to subcutaneous tissues such as skeletal muscles [2]. DTI start in deep tissues underneath an intact skin and progress outward rapidly, causing substantial subcutaneous damages before being visible. Prevention through daily examination lacks efficiency because of the nature of DTI: when visual symptoms appear, it is often too late to prevent dramatic injuries. Measuring surface pressures is believed to be effective in alerting patients at risk against focal pressures that may cause soft tissues injury [3], but these measurements cannot predict dangerous internal tissue loading [4]. For example, similar pressures may be observed under the buttocks of a heavy paraplegic person with sharp ischial tuberosity (IT) and a thin person with blunt ITs; however, their susceptibility to DTI depends on the IT curvature as well as the thickness of the soft tissues which lead to different internal strains creating the injuries [5]. It is consequently crucial to monitor these internal strains. The only way to estimate these strains from the skin surface pressures is to build a patient-specific biomechanical model of the soft tissues and the bony prominences. PU are frequent in reanimation and geriatric patients, especially at two locations: the buttocks (below the ischial tuberosities and the sacrum) and the foot (below the heel). In this study, we therefore introduce two generic models of the buttocks and of the foot that can be used as a foundation to create patient-specific biomechanical models with the objective of personalized PU prevention.

METHODS

Our foot and buttocks models have been developed using the 3D biomechanical simulation platform, Artisynth [6]. The models are composed of bones and soft tissues, including skin, muscles and fat. On top of these, the foot model includes ligaments and joints. The surfaces of these structures (skin, muscles and bones) are inspired by the surfaces from the zygote database (www.zygote.com) for the foot and segmented from a young healthy subject for the buttocks. Using an automatic Finite Element (FE) mesh generator [7], the surfaces were filled with elements based on a hexahedral grid,

completed with wedges and tetrahedrons to maximize the accuracy and to ensure continuity between structures. The bones are modeled as rigid solids. Figures 1 and 2 plot the corresponding FE meshes.

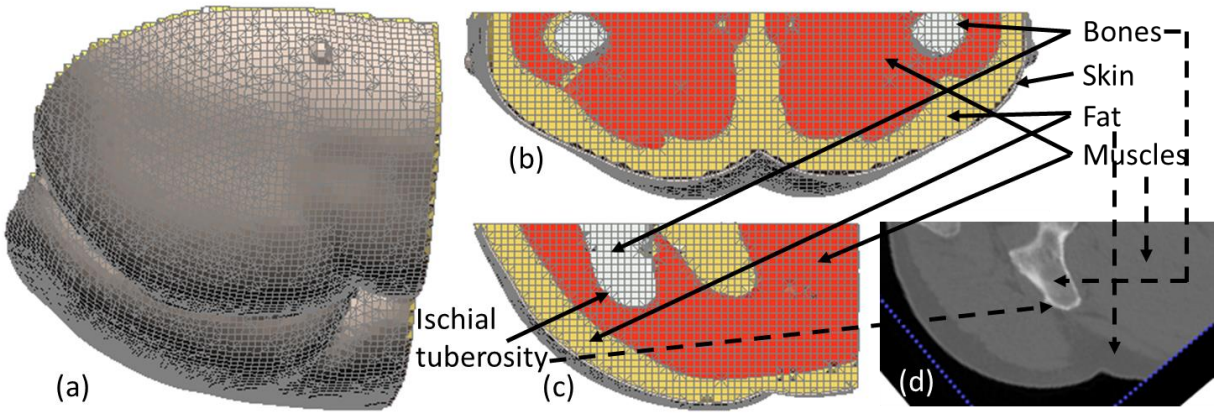

Figure 1. (a) Finite element model of the buttocks; (b) frontal and (c) and sagittal cross sections showing the three layers of materials defining the buttocks model: skin (in grey), fat (in yellow) and muscles (in red); the bones are represented in white and are simulated as fixed nodes; (d) CT scan slice showing the ischial tuberosity surrounded by muscles and fat tissues.

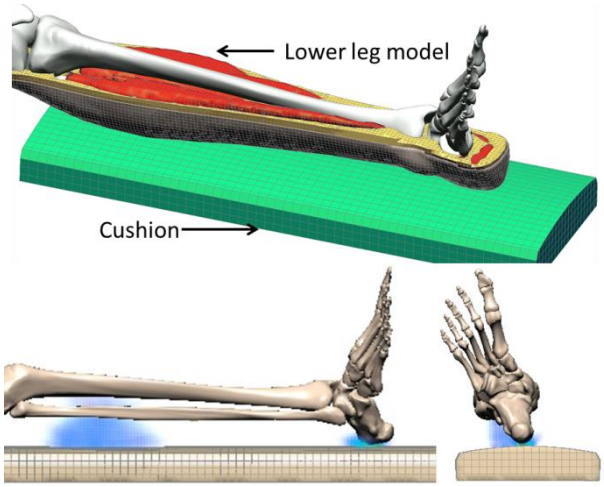

Figure 2. Top: the four types of materials defining the lower leg FE model: skin (only one layer of elements around the leg), muscles (in red), fat (in yellow), and Achilles tendon. Bottom: clusters of the nodes with VM strains above 20 %. The maximum VM strain (57 %, in red) is located under the heel, at the interface between fat and calcaneus.

The buttocks FE mesh (Fig. 1) models the soft tissues representing the skin, muscles and fat using three different Neo Hookean materials, as those tissues undergo large deformations following an hyper elastic behavior, with Young moduli set to 200 kPa for the skin, 100 kPa for the muscles, and 30 kPa for the fat. All materials have a Poisson ratio of 0.49.

For the foot FE mesh (Fig. 2), the soft tissues are modeled as four different Neo Hookean materials with Young moduli set to 200 kPa for the skin, 100 kPa for the muscles, 1 GPa for the tendon, and 30 kPa for the fat. All materials have a Poisson ratio of 0.495, except for the fat with a value of 0.49 [5]. The 26 foot bones are modeled as rigid body surfaces coupled to the nearby FE nodes. The 33 foot joints are simulated by pivots connecting each bone with its neighbors.

RESULTS

Biomechanical models can be used to simulate the behavior of the buttocks or the foot under different constraints. They can compute the internal strains and stresses in the subcutaneous tissues under various external patterns of pressures applied at the skin surface, and therefore predict the risks for DTI development. For example, the bottom panel of figure 2 plots the levels of internal strains due to the contact of the lower leg on a soft cushion. This kind of simulations could allow specifically assessing the influence of the calcaneus bone geometry on the risk of PU creation, or the influence of the cushion stiffness. In this case, a cushion with a soft stiffness seems to limit the risk in terms of short term PU creation, while cushions mildly inflated under one of the sections of the leg leads to a risk of PU creation in a time period around two hours (since the 20 % VM strain threshold is reached in all cases [1]). The same kind of behavior can be observed for the buttocks. Thanks to these biomechanical models, it is consequently possible to define a time threshold, a pressure threshold, or a cushion stiffness threshold, that should prevent PU.

DISCUSSION

Our biomechanical models allow simulating the foot and buttocks with a realistic behavior in terms of surface and internal pressures. These constraint analyses resulting from a prescribed load could consequently determine if and when pressure ulcers may appear. Our future works will aim at automatically creating patient-specific models from these generic models and to couple them interactively with data provided by the "TexiSense Smart Sensor" that could provide a daily personalized PU prevention [8].

ACKNOWLEDGEMENTS

This work was carried out with the financial support of IDS Company, Carnot LSI Institute, the Labex CAMI (ANR-11-LABX-0004), the Institut Universitaire de France and the French national research project ANR/TecSan 2010 IDSocks.

REFERENCES

[1] Loerakker, S. et al. (2011). *Journal of Applied Physiology*, Vol. 111(4), pp. 1168-1177.

[2] Ankrom M.A. et al. (2005). *Advances in Skin and Wound Care*, Vol. 18(1), pp. 35–42.

[3] Pipkin L., & Sprigle S. (2008). *Journal of Rehabilitation Research and Development*, Vol. 45, pp. 875–882.

[4] Linder-Ganz E. et al. (2008). *Journal of Biomechanics*, Vol. 41, pp. 567–580.

[5] Sopher R. et al. (2010). *Journal of Biomechanics*, Vol. 43, pp. 280–286.

[6] Lloyd J.E. et al. (2012). *Soft Tissue Biomechanical Modeling for Computer Assisted Surgery*, Studies in Mechanobiology, Tissue Engineering Biomaterials, Vol.11. Springer Verlag, pp. 355–394.

[7] Lobos C. et al. (2010). *Informatics in Oral Medicine: Advanced Techniques in Clinical and Diagnostic Technologies*. Hershey, PA: Medical Information Science Reference, pp. 126-158.

[8] Perrier A. et al. (2014). *Innovation and Research in BioMedical Engineering*, Vol 32(2), pp. 72-76. *Special issue Technologies for Health and Autonomy*.

Predicting the consequences of tongue cancer surgery: design of a 3D patient-specific biomechanical model and evaluation

Pierre-Yves Rohan[1], Ahmad Bijar[1,2], Georges Bettega[3], Pascal Perrier[2] and Yohan Payan *[1]

[1]TIMC-IMAG, UMR CNRS 5525, Université Joseph Fourier, La Tronche, France
[2]Gipsa-lab, UMR CNRS 5216, Grenoble-INP, Grenoble, France
[3]Department of Maxillo-facial Surgery, University Hospital, Grenoble

1 Introduction

The preoperative prediction of the consequences of tongue cancer surgery on tongue mobility is a topic of paramount interest for maxillo-facial surgeons. Loss of tongue mobility is associated with an impairment of basic functions such as speech articulation and deglutition which can, in some cases, induce a substantial decrease in the quality of life of patients [1]. Significant variability has been observed across patients in the recovery of these functions, which are linked with tumor location and reconstruction techniques, but also, strongly, with patient-specific characteristics, such as vocal-tract morphology and idiosyncratic motor control strategies and which call for the development of tools to predict the functional consequences of tongue cancer surgery.

Recent advances in our group on the development of a three-dimensional (3D) finite-element biomechanical model of the oral cavity [2, 3] and on the design of automatic adaptation of finite-element meshes to subject-specific morphology [4] constitute encouraging steps towards the development of pre-operative planning tongue surgery systems. In particular, Buchaillard et al. [5] showed the potential of such models to qualitatively predict the impact of oral cancer ablative surgery and reconstruction on tongue mobility. Building upon this work, our objective is to perform a clinical evaluation of the proposed biomechanical model by comparing between the acoustic signal predicted by our model after tongue cancer surgery and the acoustic data collected in post-surgery conditions. In the present work, we focus on the design of a 3D patient-specific biomechanical model.

2 Materials and methods

2.1 Materials

Pre-operative Magnetic Resonance Images are acquired on the head of a 50 year old patient undergoing tongue cancer using a 3-T clinical scanner and pixel resolution 1 x 1 x 1 mm^3. Acoustic data of the patient in both pre-surgery and post-surgery conditions were also collected following the procedure developped by Acher et al. [6].

2.2 Methods

An improved version of the 3D Finite Element (FE) model of the oral cavity developed in ANSYS at the laboratory [3] is used. It consists of a soft deformable tongue and the surrounding hard tissues with which the tongue interacts (jaw, teeth, palate and hyoid bone). The improvements relate, primarily, with the tongue mesh as described in [7]. The identification of each muscle group in the tongue mesh is performed

*yohan.payan@imag.fr

automatically. Muscle activation is modelled using the FE formulation of the Hill muscle model proposed by Blemker et al. [8, 9] that includes both the active stress stiffening effect and the passive transversal isotropy of muscles. Passive tissues (inactive muscles) are modelled using a 5-parameter Mooney-Rivlin model.

The patient-specific model is automatically set up using pre-operative MR data coming from a patient undergoing tongue cancer surgery. A volume image registration-based approach is used, in which an atlas FE mesh is deformed using a 3D transform derived from patient-to-atlas volume (MR) image registration [10]. The volume image registration includes rigid/affine registration (as global alignment) and non-rigid registration (as local alignment). The global transformation removes the scale and position differences between the atlas and patient (MR) image volumes. Accordingly, the local transformation compensates the inter-patient morphological differences. Finally, the obtained 3D deformation field (derived from registration) is used to deform the tongue atlas mesh to fit the patient's tongue morphology. As the deformed mesh may possess irregular or low quality elements, an automatic mesh repair algorithm is used [4].

Tongue cancer surgery was accounted for in the model by modifying the biomechanical properties of the tongue tissues that were excised and reconstructed during the surgical procedure. This was done in collaboration with a maxillo-facial surgeon. First, the zone that was resected was identified and the corresponding elements in the biomechanical model were removed. In our case, the hemi-glossectomy performed by the surgeon consisted in resecting partially or totally the styloglossus, the tranversalis, the hyoglossus and the genio-glossus muscles. Then, the tongue model was reconstructed with flaps having passive elastic properties. In practice, the surgeon used an anterolateral thigh cutaneaous flap. The flap is totally inactive during tongue activation.

The response of the tongue to the activation of muscles, responsible for the production of cardinal vowels /i/, /a/, /u/, after tongue surgery, is simulated. The deformed tongue surface is then used as input for the acoustic model of sound synthesis which, in turn, is used to compute the predicted spectral characteristics of vowels in post-surgery condition.

3 Results

The patient-specific tongue geometry and mesh reconstructed from the Pre-operative Magnetic Resonance Images is represented in figure 1 below.

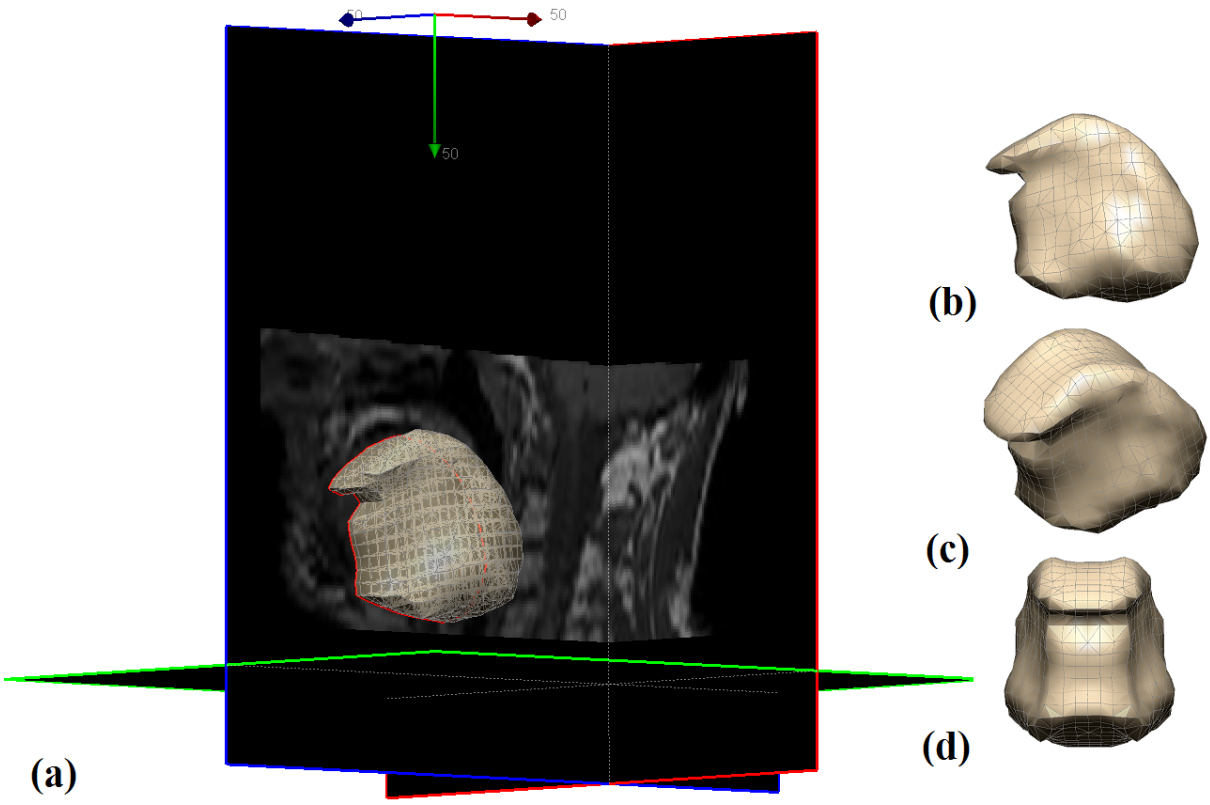

Figure 1: (a) Pre-operative MR data of the patient undergoing tongue cancer surgery superimposed with the 3D patient-specific tongue mesh set-up. (b) Side, (c) isometric and (d) front views respectively of the 3D FE tongue mesh.

4 Perspectives

Comparison between the acoustic signal predicted by our model and the acoustic data collected in post-surgery conditions (6 months after surgery) is currently being performed and will serve as basis for the evaluation of the prediction of the impact of the surgery.

5 Conclusion

A patient-specific biomechanical model is set up in this study to predict the impact of surgery on tongue mobility. Evaluation of the model is done by comparing the simulated acoustic signal with the acoustic data collected in both pre-surgery and post-surgery conditions. Further work is required to (i) develop appropriate numerical strategies that allow to accurately handle and account for the resection and reconstruction procedure and (ii) reduce computation time.

Acknowledgments

This work was supported by French state funds managed by the Grenoble University AGIR projects (CLAM) and by the ANR within the Investissements d'Avenir programme (Labex CAMI) under reference ANR-11-LABX-0004.

References

[1] H. Schliephake, R. Schmelzeisen, R. Schönweiler, T. Schneller, and C. Altenbernd, "Speech, deglutition and life quality after intraoral tumour resection: A prospective study," *International Journal of Oral and Maxillofacial Surgery*, vol. 27, no. 2, pp. 99–105, 1998.

[2] J.-M. Gérard, P. Perrier, and Y. Payan, "3D biomechanical tongue modeling to study speech production," in *Speech Production: Models, Phonetic Processes, and Techniques* (J. H. \. M. Tabain, ed.), Chapter 6, pp. 85–102, Psychology Press, New York, 2006.

[3] S. Buchaillard, P. Perrier, and Y. Payan, "A biomechanical model of cardinal vowel production: muscle activations and the impact of gravity on tongue positioning," *The Journal of the Acoustical Society of America*, vol. 126, no. 4, pp. 2033–2051, 2009.

[4] M. Bucki, C. Lobos, and Y. Payan, "A fast and robust patient specific finite element mesh registration technique: application to 60 clinical cases," *Medical Image Analysis*, vol. 14, no. 3, pp. 303–317, 2010.

[5] S. Buchaillard, M. Brix, P. Perrier, and Y. Payan, "Simulations of the consequences of tongue surgery on tongue mobility: implications for speech production in post-surgery conditions," *The International Journal of Medical Robotics and Computer Assisted Surgery*, vol. 3, no. 3, pp. 252–261, 2007.

[6] A. Acher, P. Perrier, C. Savariaux, and C. Fougeron, "Speech production after glossectomy: Methodological aspects," *Clinical Linguistics & Phonetics*, vol. 28, no. 4, pp. 241–256, 2013.

[7] P.-Y. Rohan, C. Lobos, M. Nazari, P. Perrier, and Y. Payan, "Finite element modelling of nearly incompressible materials and volumetric locking: a case study," *Computer Methods in Biomechanics and Biomedical Engineering*, Accepted.

[8] S. S. Blemker, P. M. Pinsky, and S. L. Delp, "A 3D model of muscle reveals the causes of nonuniform strains in the biceps brachii," *Journal of Biomechanics*, vol. 38, no. 4, pp. 657–665, 2005.

[9] M. A. Nazari, P. Perrier, and Y. Payan, "The distributed lambda (λ) model (DLM): a 3-d, finite-element muscle model based on feldman's λ model; assessment of orofacial gestures," *Journal of speech, language, and hearing research*, vol. 56, no. 6, pp. S1909–1923, 2013.

[10] C. Tong, *Generation of patient-specific Finite-Element mesh from 3D medical images*. PhD thesis, National University of Singapore, 2014.

Biomechanical model of the fetal head for interactive childbirth simulation

M. Bailet*[1,2], F. Zara[1], and E. Promayon[2]

[1]Université de Lyon, CNRS, Université Lyon 1, LIRIS, SAARA team, UMR5205, F-69622, France
[2]UJF-Grenoble 1, CNRS, TIMC-IMAG, UMR5525, F-3804, France

1 Introduction

Obstetricians and midwives practical training is mostly done through an apprenticeship on real parturient. In addition to the risks for the parturient and the fetus, this approach does not allow the student to see a large variety of cases and acquire related dexterity, especially for the least performed interventions such as forceps or vacuum delivery. For these reasons, the use of simulators appears to be a practical and safe approach to acquire task-oriented skills in obstetrics [3] as well as confidence.

There is a large variety of obstetrics simulators from the simple passive manikin to complex actuated device with graphic feedback. These simulator give a qualitative information on the user gesture. On the other side, [2] have proposed a finite element based biomechanical simulation of the fetal descent that gives quantitative information on the effort undergoing by the pelvic organs and related potential tissue injuries during childbirth. But finite element based simulation are computational expensive and could not be run in interactive time needed for training. The goal of this work is to provide a 3d biomechanical model of the fetal head that could be coupled with haptic simulator [5]. Precision and computation time aspects have to be taken into account to provide an interactive simulation focused on the possible damages undergoing by the fetal head.

2 Method

The fetal head is the part of the fetus where the largest deformations (fetal head molding) and potential injuries can occur. To simulate the its deformation

*Corresponding author : mathieu.bailet@imag.fr

during childbirth, we propose a triangular shell model combined with a volume constraint that guarantees the incompressibility of the fetal head.

Shell models of the cranial bones have already been used to statically simulate the fetal head molding during the first stage of labor [4]. However, this simulation is static and do not take into account the intra-cranial matter since it model only the fetal skull. The shell mechanical model proposed integrates a membrane behavior using CST elements (Constant Strain Triangle) as well as bending behavior with DKT (Discrete Kirchhoff Triangle) elements [1]. The CST membrane element is a two dimensional triangular element used for plane stress problem. It has six Degrees of Freedom (DOF), to model the plane displacements at each node. The DKT bending element is based on the well-known Kirchhoff thin plate theory where transverse shear deformations are neglected. This element has nine DOF to model the out-of-plane displacements and the rotations around x and y axis.

Our formulation use an element-based co-rotational formulation where the element stiffness matrices are expressed in their respective local frame. Combined with a linear material, this formulation models a small-strain and large rotation behavior. The mesh model was reconstructed from a medical manikin. It has 8928 triangular elements divided in two material zones : one corresponding to cranial bones and one corresponding to fontanelles and sutures (see Fig. 1a). The isotropic linear material properties for these two areas were taken from Lapeer and Prager [4]. The cranial bones area has a Young Modulus of 2.65 GPa, a Poisson Coefficient of 0.22, a density of 1800 $kg.m^{-3}$ and a thickness of 0.8 mm. The fontanelles and sutures area has a Young Modulus of 7.23 MPa, a Poisson Coefficient of 0.49, a density of 1000 $kg.m^{-3}$ and a thickness of 0.6 mm.

To approximate the effect of the biological matter inside the fetal head, an incompressibility constraint is enforced on the volume defined by the shell element mesh.

Both the shell model and the volume constraint codes are implemented in GPGPU using a parallelization on elements. We use an implicit backward euler scheme for time integration with a matrix-free conjugate gradient as linear solver.

Three fetal head diameters were monitored during the simulation : the maxillo-vertical diameter (MaVD), the orbito-vertical diameter (OrVD) and the suboccipito-bregmatic diameter (SOBD) (see Fig. 1c).

3 Results

We present in Fig. 1 a simulation of the fetal head in the first stage of labor when it undergoes intra-uterine and cervix pressure (see Fig. 1b). The geometric model chosen results from the scan of the head of a generic manikin used in the haptic simulator of Silveira et al. [5]. The pressure load were computed using the Bell idealized model with a maximal pressure of 45 kPa. Our results were coherent with the in-vivo experiments from Sorbe and Dahlgren [6] and static fetal skull simulation from Lapeer and Prager [4] (see Table 1). We notice an

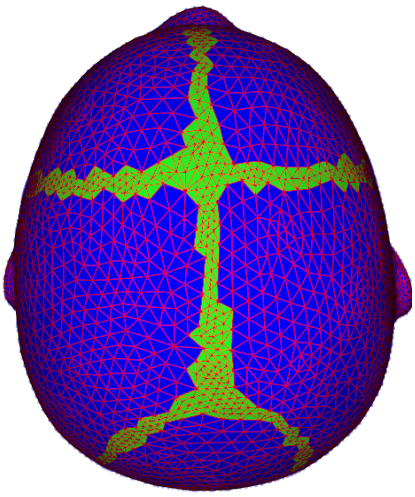

(a) The two material areas (cranial bones and fontanelles/sutures)

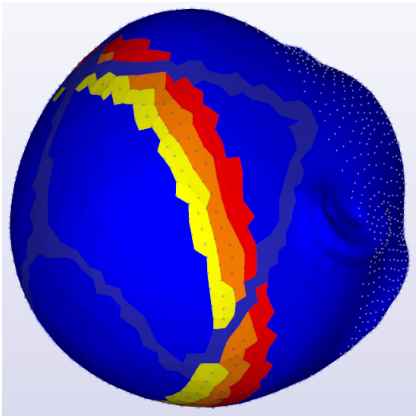

(b) Pressures load

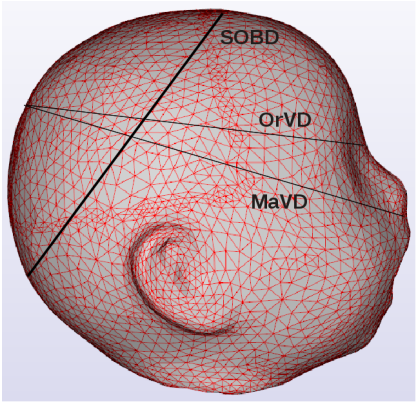

(c) Tracked diameters

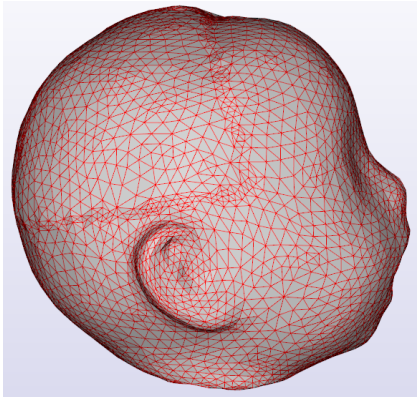

(d) Deformed fetal head

Figure 1: Fetal head undergoing intra-uterine and cervix pressure. Model and simulation results.

overlapping of the two parietal bones (see Fig. 1d).

This simulation was run with a time step 0.01 seconds and a frame rate of 21 frames per seconds on an NVIDIA Quadro 600 with 96 cores.

4 Conclusion

The biomechanical model presented in this paper offers precise dynamic simulation of the fetal head molding in a reasonable computational time making it suitable for use with haptic training simulators such as the one presented in

	Sorbe 1983		Lapeer 2001		Ours	
Measures	ø	disp	ø	disp	ø	disp
MaVD	140.5	+1.90	129.3	+1.43	124.6	+1.29
OrVD	126.9	+2.20	119.3	+1.24	110.9	+1.13
SOBD	117.1	-1.70	88.7	-2.52	107.4	-3.57

Table 1: Fetal head diameter (ø) and its variation (disp) in mm.

Silveira et al. [5]. The conjunction of an haptic device providing qualitative information of the gesture and biomechanical simulation providing quantitative information will improve the training experience of the student. Nevertheless, the biomechanical model can be improved by considering anisotropic material for the cranial bones. In future work, we plan to use our model with more complex scenarios involving the fetal head such as forceps and vacuum delivery. It could also be noticed that at this stage, a patient specific approach is not considered because the simulation is focused on training.

5 Acknowledgments

This work is financed by a grant from the French Région Rhône-Alpes. It was supported by French state funds managed by the ANR within the Investissements d'Avenir program (Labex CAMI) under reference ANR-11-LABX-0004 and within the MN program under reference ANR-12-MONU-0006.

References

[1] Jean-Louis Batoz, Klaus-JÜRgen Bathe, and Lee-Wing Ho. A study of three-node triangular plate bending elements. *International Journal for Numerical Methods in Engineering*, 15(12):1771–1812, 1980. ISSN 1097-0207. doi: 10.1002/nme.1620151205. URL `http://dx.doi.org/10.1002/nme.1620151205`.

[2] Romain Buttin, Florence Zara, Behzad Shariat, Tanneguy Redarce, and Gilles Grangé. Biomechanical simulation of the fetal descent without imposed theoretical trajectory. *Computer methods and programs in biomedicine*, 2013.

[3] Roxanne Gardner and Daniel B. Raemer. Simulation in obstetrics and gynecology. *Obstetrics And Gynecology Clinics Of North America*, pages 97–127, 2008.

[4] R.J. Lapeer and R.W. Prager. Fetal head moulding: finite element analysis of a fetal skull subjected to uterine pressures during the first stage of labour. *Journal of Biomechanics*, 34(9):1125 – 1133, 2001. ISSN

0021-9290. doi: http://dx.doi.org/10.1016/S0021-9290(01)00070-7. URL http://www.sciencedirect.com/science/article/pii/S0021929001000707.

[5] R. Silveira, Minh Tu Pham, T. Redarce, M. Betemps, and O. Dupuis. A new mechanical birth simulator: Birthsim. In *Intelligent Robots and Systems, 2004. (IROS 2004). Proceedings. 2004 IEEE/RSJ International Conference on*, volume 4, pages 3948–353. vol.4, Sept 2004. doi: 10.1109/IROS.2004.1390031.

[6] B. Sorbe and S. Dahlgren. Some important factors in the molding of the fetal head during vaginal delivery - a photographic study. *International Journal of Gynecology & Obstetrics*, 21(3):205 – 212, 1983. ISSN 0020-7292. doi: http://dx.doi.org/10.1016/0020-7292(83)90081-4. URL http://www.sciencedirect.com/science/article/pii/0020729283900814.

An augmented reality approach integrating deformation simulation to assist EVAR procedures

Aurélien Duménil[1,2,3], Adrien Kaladji[1,2,4], Juliette Gindre[1,2], Michel Rochette[5], Cemil Göksu[3], Antoine Lucas[1,2,4], Pascal Haigron[1,2]

[1] INSERM, U1099, Rennes, F-35000, France
[2] Université de Rennes 1, LTSI, Rennes, F-35000, France
[3] Therenva, Rennes, F-35000
[4] CIC-IT 804, Rennes, F-35000, France
[5] ANSYS France, Villeurbanne, F-69100, France

1. Introduction

The EndoVascular Aneurysm Repair (EVAR) for abdominal aortic aneurysms consists in intravascularly inserting a delivery system and deploying stent-grafts at the aneurysm site in order to re-channel the blood flow. As this procedure has a high success rate in the short term and benefits in terms of blood losses, intraoperative morbidity and length of hospital stay, its indication is constantly increasing, compared to open surgery.

However, this technique has some intrinsic limitations, notably due to the nature of the intraoperative imaging system (2D fluoroscopy). One of its drawbacks is a limited visual feedback about location of endovascular devices regarding the vascular structure. This limitation can increase x-ray exposure time and quantity of contrast agent injected to visualize the vascular structure. Image-guided interventions based on an augmented reality system can propose a solution to limit these drawbacks by superimposing preoperative CT-scan onto the intraoperative images. Nevertheless, introduction of stiff endovascular devices naturally deforms and straightens arteries, especially iliac arteries. These deformations may therefore cause a mismatching between preoperative data and intraoperative data [1]. In clinical routine, practitioners usually estimate deformations thanks to their experience and by analyzing the shape of stiff devices which can appear to be located outside the superimposed preoperative vascular structure. In this context, patient-specific simulation could provide a more objective tool to assist intraoperative navigation by estimating arterial deformations and improving localization of structures of interest. Simulation from preoperative patient CT-scan could be used to update and enrich intraoperative images. Such an augmented reality process aimed at improving 3D/2D data matching and reducing effort of abstraction that clinicians have to do during the intervention.

We propose an approach oriented towards an approximate solution consistent with the clinical workflow in order to assist endovascular navigation during EVAR procedure. Our method consists in a data matching between preoperative data (CT-scan, deformation simulation, stent-graft geometry) and intraoperative images. It involves a registration process to align preoperative and intraoperative data, a FEM-based simulation to estimate arterial deformations and a geometrical simulation to visualize stent-graft into the estimated deformed vascular structure.

2. Methods

FEM-based simulation of the deformations of the vascular structure

Previously, we proposed a FEM-based patient-specific simulation to estimate the intraoperative deformations of the vascular structure due to the introduction of a stiff guidewire [2] and a delivery system. This method involves a biomechanical model created from patient preoperative CT-scan and tuned by comparing the simulated guidewire with intraoperative images showing the real guidewire from a training patient group. The simulation consists in initializing the device into the vascular structure, activating contact between the device and the vascular structure and relaxing progressively initial constraints in order to obtain an equilibrium state.

Geometrical placement of stent-grafts

We introduced also a geometrical simulation to visualize stent-grafts into the estimated deformed vascular structure [3]. Our method consists in representing stent-grafts (bifurcated main body and iliac extensions) by surface meshes and positioning them into the vascular structure. First, a main body is placed along the aorta centerline. The centerlines of iliac arteries are then extrapolated to the limbs of the main body and iliac extensions are positioned on these centerlines. Position and orientation of each stent-graft can be modified interactively and overlap between stent-grafts can be adjusted.

Preoperative and intraoperative data matching

Matching between preoperative and intraoperative coordinate systems was done through a 3D/2D rigid registration process based on the centerline of the undeformed vascular structure. The 3D centerline was extracted from the preoperative CT-scan with the sizing software EndoSize® (Therenva). The 2D centerline was derived from standard angiography, with a contrast medium injected so as to visualize the undeformed vascular structure at the beginning of the intervention. The registration process consists in minimizing the Euclidean 2D distance between the projected 3D centerlines and the 2D centerlines in order to align the preoperative and intraoperative coordinate systems.

Augmented reality system

Using this data matching, results of the FEM-based simulation (undeformed and deformed vascular structures, simulated device) and results of the geometrical stent-graft placement (stent-graft meshes) were projected onto fluoroscopic images (fig.1).

In order to quantify the accuracy of the FEM-based simulation results, the simulated devices (stiff guidewire and delivery system) were projected onto intraoperative images on which the real devices are visible. The simulation error was thus defined by the mean distance between the real device and the projected simulated device.

It seemed to be interesting to compare this simulation error with the magnitude of the deformations. A way to estimate it was to project the undeformed vasculature onto the same intraoperative images in order to observe the distance between the projected vasculature and the real devices. The magnitude of deformation was thus quantified by the mean distance between the real device and a minimum-curvature path of the projected vasculature (fig.2).

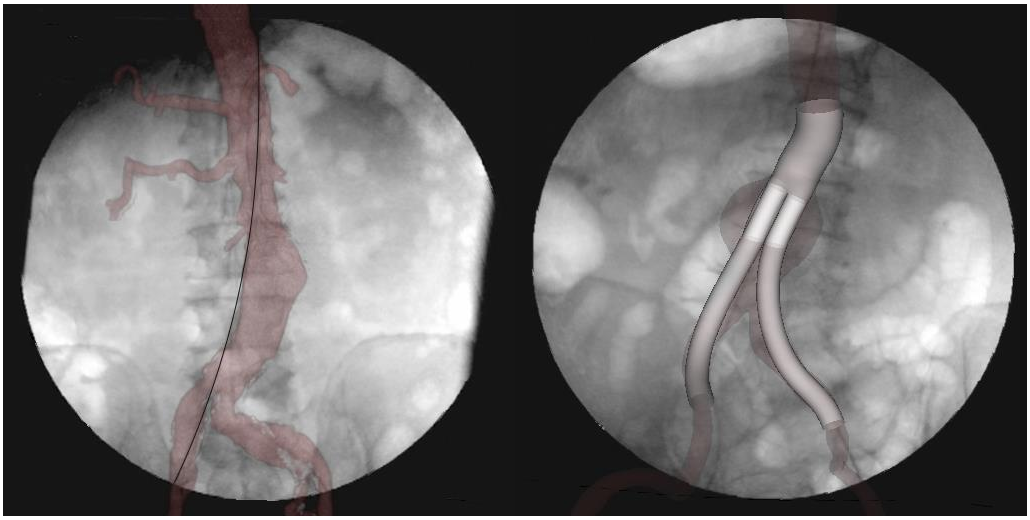

a) *b)*

Figure 1:
a) Projection of a deformed CT-scan obtained by applying estimated deformation field to the original CT-scan onto an intraoperative image on which the real guidewire is visible (black).
b) Projection of simulated stent-graft placement onto an intraoperative image before the real stent-graft deployment.

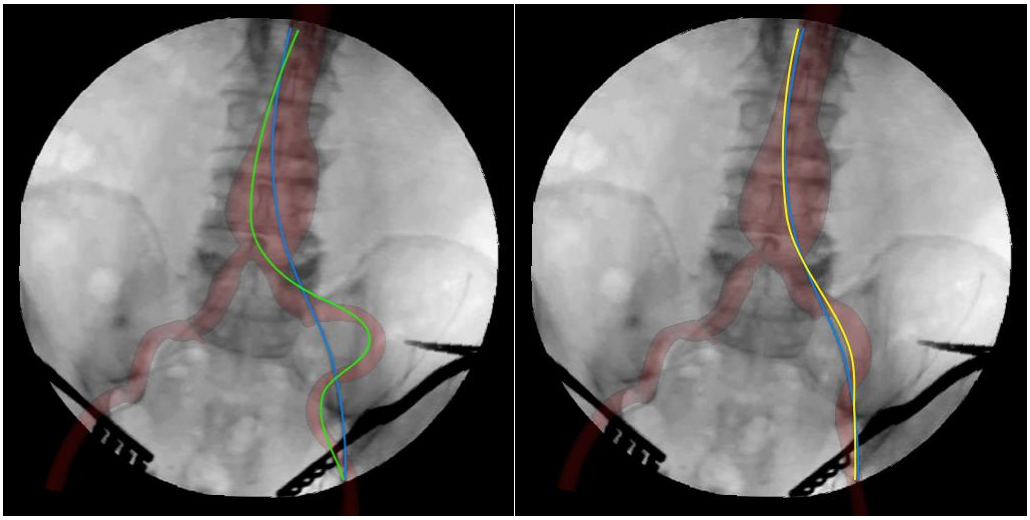

a) *b)*

Figure 2:
a) Projection of the undeformed vasculature (red) and the minimum-curvature path (green) onto an intraoperative image on which the real guidewire is visible (blue).
b) Projection of the estimated deformed vasculature (red) and the simulated guidewire (yellow).

3. Results

CT-scan data and intraoperative images were obtained for 5 patients who underwent EVAR in the Department of vascular surgery of the University Hospital of Rennes, France. FEM-based simulations were carried out using Ansys Mechanical implicit finite element solver. Placement of stent-grafts chosen during the sizing of the 5 patients was also simulated.

The registration process between preoperative and intraoperative coordinate systems was done with a mean error of 1.5 ± 1.1 mm. Simulation results (deformed vascular structures, simulated devices, stent-graft meshes) were then projected onto the intraoperative images.
The mean simulation error was 2.2 ± 1.0 mm (mean maximum: 4.6 mm) for the guidewire simulation and 3.0 ± 2.0 mm (mean maximum: 7.8 mm) for the delivery system simulation. The mean magnitude of deformation was 5.2 ± 3.3 mm (mean maximum: 12.3 mm) for the guidewire and 7.6 ± 4.4 mm (mean maximum: 16.6 mm) for the delivery system.
The simulation of the resulting deformation caused by the guidewire and the delivery system gives acceptable results. The simulation error is higher for the delivery system than for the guidewire. This can be explained by the fact that the tuning of the model parameters was performed only for the guidewire. Even if the simulation results could be improved, the simulation error is always lower than the magnitude of deformation, especially when the mean maximum simulation error is compared with the mean maximum magnitude of deformation. The simulation can be considered as sufficiently accurate to use the estimated deformed vasculature in an augmented reality system. Indeed, the matching between the vasculature and the observed devices is largely improved by projecting the deformed vasculature instead of the undeformed vasculature.

4. Conclusion

We presented an original augmented reality approach for the matching of 3D preoperative data and 2D intraoperative images in the context of EVAR procedures. Patient-specific simulations were used to estimate anatomical deformations of the vasculature at different procedure steps. The superimposition of the vasculature model and the real devices is thus improved by taking into account these deformations. Moreover, the geometrical placement of stent-grafts can also be projected onto intraoperative images in order to bring additional data to assist the endovascular navigation.

Acknowledgement

This work was partly supported by the French ANR within the Investissements d'Avenir program (Labex CAMI) under reference ANR-11-LABX-0004.

References

[1] G. Penney, A. Varnavas, N. Dastur, et T. Carrell, « An Image-Guided Surgery System to Aid Endovascular Treatment of Complex Aortic Aneurysms: Description and Initial Clinical Experience », in Information Processing in Computer-Assisted Interventions, vol. 6689, R. Taylor et G.-Z. Yang, Éd. Springer Berlin / Heidelberg, 2011, p. 13-24.
[2] Dumenil, A.; Kaladji, A.; Castro, M.; Esneault, S.; Lucas, A.; Rochette, M.; Goksu, C.; Haigron, P., "Finite-Element-Based Matching of Pre- and In-traoperative Data for Image-Guided Endovascular Aneurysm Repair," IEEE Transactions on Biomedical Engineering, vol.60, no.5, pp.1353,1362, May 2013
[3] A. Dumenil, A. Kaladji, J. Gindre, M. Castro, M. Rochette, C. Goksu, P. Haigron, « Visualization of stent-graft placement in deformed vascular structure in EVAR procedure », Proceedings of MICCAI - Stent'13, 2nd MICCAI Workshop on Computer Assisted Stenting
22 September 2013

CLINICAL DEVELOPMENTS

Title

LAPAROSCOPIC GASTRIC BYPASS AND GASTRIC ELECTRICAL STIMULATION WITH A ROBOTICALLY CONTROLLED NEEDLE HOLDER (JAiMY™)

Fabian RECHE*, MD - Bertrand TRILLING*, MD - Terri OLSHEFSKI** - Pierre Alexandre WAROQUET*, MD - Catherine ARVIEUX* MD, PhD - Jean Luc FAUCHERON* MD, PhD

*Department of Digestive and Emergency Surgery
University Hospital of Grenoble - FRANCE

**EndoControl, Grenoble, FRANCE

Aims

Minimally invasive surgery creates new challenges for the surgeon, particularly during bariatric procedures. The use of long rigid instruments through rigid ports limits intra-abdominal degrees of freedom and also triangulation, making it difficult to reach certain structures and position the needle appropriately for various suturing tasks.

Laparoscopic suturing and knot tying in minimal access surgery is an advanced skill. Mastering this skill is a difficult process, especially when the needle holder is not parallel to the suture line and triangulation is limited.

We present data from 2 interventions performed using a robotic needle holder.

Methods

In the first case, we present the patient, a 35 year old female with a history of stage 3 morbid obesity with a BMI of 47 and a comorbidity of type 2 diabetes.

The intervention started with the creation of a small proximal gastric pouch. The dissection was realized with thermofusion tissue sealers and the transection with the 45mm Endo GIA endocutter with purple staples.

This dissection was continued until the left diaphragmatic crus to complete the proximal gastric pouch.

We identified the premier jejunal limb at the level of the root of the transverse mesocolon and we created an omega limb, (en pré-colique) and we restored the gastric continuity with a mechanic latero-lateral gastro-jejunal anastomosis, using the 45 mm Endo GIA endocutter with purple staples.

To realize the closure of the gastro-jejunostomy, we used the robotic needle holder (JAiMY™, EndoControl, Grenoble, France). The instrument has a 5mm outer diameter and offers 2 motorized distal degrees of freedom: deflection of the shaft, to adjust needle positioning in the appropriate plane, and unlimited axial rotation of the end effector, to drive the needle holder through the tissue.

The surgeon can manipulate the instrument's ring control to operate the 2 motorized movements. Pushing the ring control deflects the instrument tip, while turning the ring control rotates the distal end of the instrument.

This closure was performed with a subcuticular continuous suture using a 2/0 absorbable suture.

We made an alimentary limb of 150 cm and then we performed a latero-lateral anastomosis between the biliopancreatic limb and the alimentary limb. The closure was performed usinga subcuticular continuous suture using a 2/0 suture with the robotic needle holder. Transection of the biliopancreatic limb to the left of the gastro-jejunal anastomosis to transform the omega limb into the Roux-en-Y form.

We used the robotic needle holder to close the mesenteric defect and also Petersen's defect with 2 nonabsorbable 2/0 sutures. Petersen's defect must be closed using a non-absorbable suture in order to avoid internal hernias and to prevent the duodenal jejunal limb from becoming occluded or strangulated. The combination of distal shaft deflection and rotation of the end effector off the robotic needle holder offers a fully articulated tip for easy maneuverability and unparalleled access. We performed a waterproofness test using Methylene blue.

In the second case, we present the patient, a 32 year old female with a diabetic nephropathy and a gastric emptying data of 1143 minutes.

The instrument was used during a laparoscopic gastric electrical stimulation procedure to place the electrodes.

Results

The first procedure was completed without complication in 190 minutes. The 2 anastomoses were performed in 30 minutes and the closure of the 2 defects was completed in 13 minutes using the evaluated robotic needle holder (Photo 1). A classic defect closure with a standard needle holder would take between 19- 22 minutes.

Laparoscopic suturing to create the conduit and the closure of mesenteric defects are an advanced skill and mastering this skill is a difficult process, especially because the angle between the needle holder and suture line is unparallel and triangulation is limited.

In the second procedure, it is important that the ski needles attached to the electrodes are parallel to and tunneled into the seromuscular anterior gastric wall for approximately 2 cm. The combination of distal shaft bending and rotation of the end effector of the robotic instrument enables an ideal positioning of the electrodes (Photo 2).

Furthermore, the robotic needle holder facilitates the placement of sutures to anchor electrodes in the gastric wall by passing the ski needles through the anchoring disc.

The combination of distal shaft bending and rotation of the end effector of the robotic needle holder offers fully articulating tip for easy maneuverability and unparallel access.

Conclusion

The use of this robotic instrument is a great help to suture during many different interventions by facilitating and improving surgeon gesture. The instrument has been used many times by the surgical team during various digestive procedures (hiatal hernia repair, fundoplication, gastric stimulation and gastric bypass).

This robotic instrument brings together the advantages of minimally invasive surgery with the surgical control required to perform delicate operations.

Due to various factors, including medical economic constraints, the features and reusability of the evaluated instrument make it a feasible alternative to the current MIS robotic systems while performing laparoscopic digestive procedures. The instrument helps surgeons to

perform suturing steps quicker which reduces the total duration of interventions and consequently lowers occupation time in the operating room.

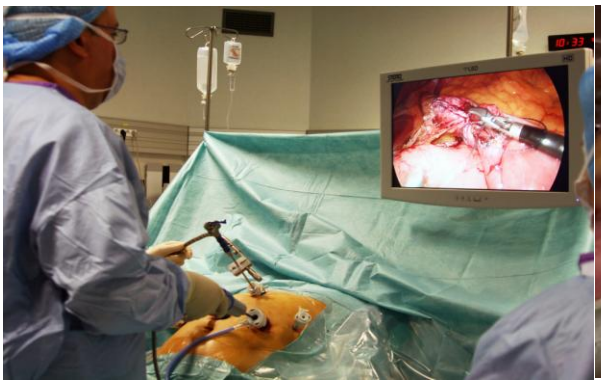

Photo 1: Gastric Bypass with JAiMY.

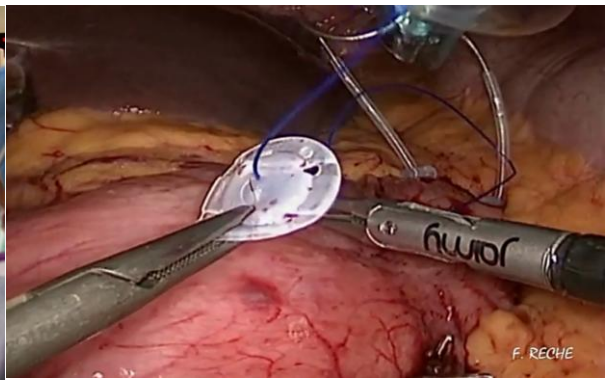

Photo 2: Gastric Electrical Stimulation with JAiMY.

Computer assisted transcatheter valve implantation for valve-in-valve procedures.

R. Belhaj[1,2,3], D.L.H. Nguyen[1,2], M. Castro[1,2], S. Cadet[4], V. Auffret[1,2,3],V.G. Ruggieri[1,2,3], J.P. Verhoye[1,2,3], P. Haigron[1,2]

[1] Université de Rennes 1, LTSI, Rennes, F-35000, France

[2] INSERM, U1099, F-35000, France

[3] CHU Hopital Pontchaillou, Rennes, F-35000, France

[4] Therenva, Rennes, F-35000, France

In adult cardiac surgery, bioprosthetic heart valves are increasingly being used instead of mechanical valves in younger adult patients, and have been associated with comparable long-term survival [1]. However, the trade-off is an increased risk of late reoperation, due to structural valve degeneration, which progressively increases with time. It is inevitable that, as younger patients are treated with bioprosthetic heart valves, and as their life expectancy continues to increase, we will face a growing number of patients with degenerated tissue valves requiring reoperation. Nonetheless, redo valvular surgery is considered high-risk, a risk further increased by older age and the associated comorbidities in these elderly patients [2].

In the native aortic valve, TAVI (*Transcatheter Aortic Valve Implantation*) has emerged over the last decade as a reproducible and efficient technique in the treatment of Aortic Stenosis (AS) in symptomatic high-risk patients [3]. As TAVI evolved and clinical outcomes improved, valve-in-valve (ViV) procedures emerged as a new therapeutic option in the treatment of degenerated bioprosthetic heart valves.

Despite some core similarities with TAVI, ViV procedures pose new technical challenges. From pre-operative planning to Transcatheter Heart Valve (THV) positioning and deployment inside the degenerated tissue valve, critical steps determine the technical and clinical results: choosing the right THV size, assessment of the bioprosthesis failure mechanism [4] as well as achieving the optimal position for deployment of the THV inside the bioprosthesis.

Live two-dimensional (2D) X- ray fluoroscopy guidance is mostly used during the intervention, in order to visualize the degenerated bioprosthesis and guide the progression and deployment of the THV. Medical imaging technology, including computed tomography (CT) and echocardiography is a key asset in both planning the procedure and delivering the THV.

As our experience grows, we have learned that the patient's degenerated bioprosthesis can be helpful in both sizing and positioning the THV, by providing a radio-opaque reference plane (Figure 2). Nonetheless, ViV procedures are still technically demanding, and THV positioning remains a critical challenge for short and long-term technical and clinical success: a suboptimal position may lead to complications such as THV embolization, intervalvular regurgitation, suboptimal function, mitral valve conflict, and coronary ostial occlusion. Moreover, reducing contrast injection and radiation exposure is a constant preoccupation for the physician.

The issue addressed by this work was to study the feasibility of designing an operational tool enhancing perception and endovascular navigation during ViV procedures, in order to position and deploy precisely the THV with respect to an optimal target location inside the degenerated bioprosthesis.

In order to potentially overcome the current challenges associated with ViV procedures under 2D fluoroscopy guidance, we present the basis of an augmented reality approach to intra-operatively guide the navigation of the THV in the aortic root and the degenerated bioprosthesis, that represent moving targets for the deployment.

In the proposed approach, a 3D mesh model of aortic root and the bioprosthetic valve's stent is obtained in the planning phase from the pre-operative CT. These data are further combined with the 2D intra-operative live fluoroscopic images, and visualized through the augmented reality navigation interface by considering the transformation determined in the 3D/2D registration process, and the moving 2D intra-operative position of the existing bioprothesis tracked in real-time.

More precisely, the aortic root, the ascending aorta and the bioprosthesis stent are first segmented from the pre-operative CT-scan, using Endosize® software (Therenva, Rennes, France) (Figure 1). The extracted data is then used to design a 3D mesh model. Afterwards, we also determine the 3D location of radiopaque feature points (3 at least) on the existing bioprosthesis (Figure 1), the optimal X-rays view to consider during the intervention, as well as the 3D target plane for the deployment of the THV. The definition of the target area of implantation is based on the bioprosthesis design (supra or intra-annular), and the THV model (Figure 2).

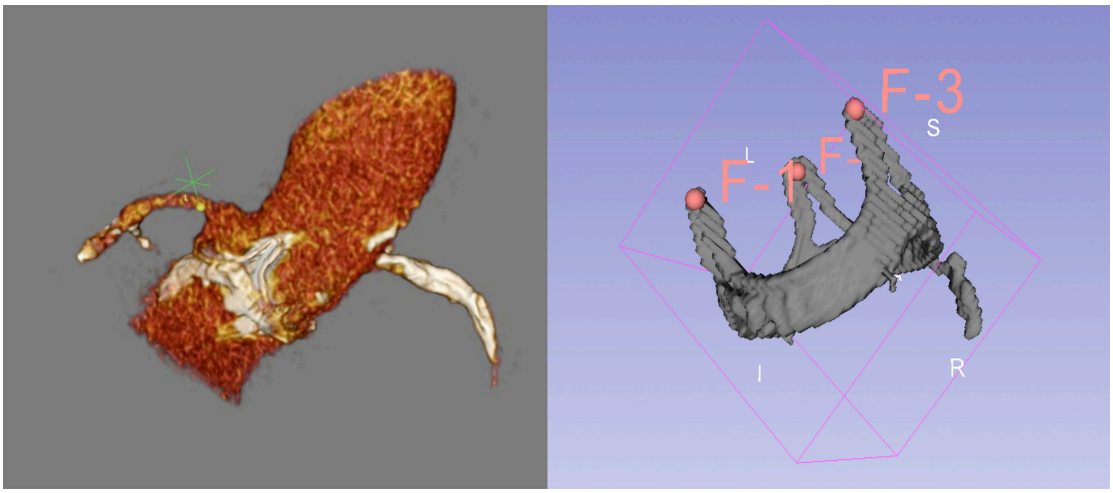

Figure 1. Mesh model of the segmented Aortic root with the coronary arteries. On the second picture, mesh model of the bioprosthetic valve's stent, with 3 landmarks used for the feature based registration (F-1, F-2 and F-3).

When a single intra-operative X-rays view is used to observe the endovascular device during THV placement, the 3D/2D registration process can constitute a critical component impacting the fusion and tracking processes involved in the navigation system. In the ViV case, the existing bioprosthesis landmarks (radiopaque feature points) are observable both in the 3D pre-operative CT image and in the 2D intra-operative X-rays image. A classical feature based registration process was used to determine the rigid 3D-2D transformation by minimizing the distance between the corresponding 3D preoperative and 2D intra-operative feature points. The 3D-2D transformation was used to project the pre-operative 3D aortic root mesh model and additional landmarks for decision making (Coronary artery ostia, target plan) onto live fluoroscopic images from CT images (figure 2). The data overlay was updated onto live fluoroscopic images according to the aortic root motion via the tracking of the degenerated bioprosthesis. A robust Tracking-Learning-Detection approach [5] was used with reduced interaction to a temporal sequence of fluoroscopic images acquired under a single view with the intra-operative imaging device (C-arm). During the implantation procedure, the THV is navigated and placed in order to align it with the tracked target plane (Figure 1) and subsequently implanted.

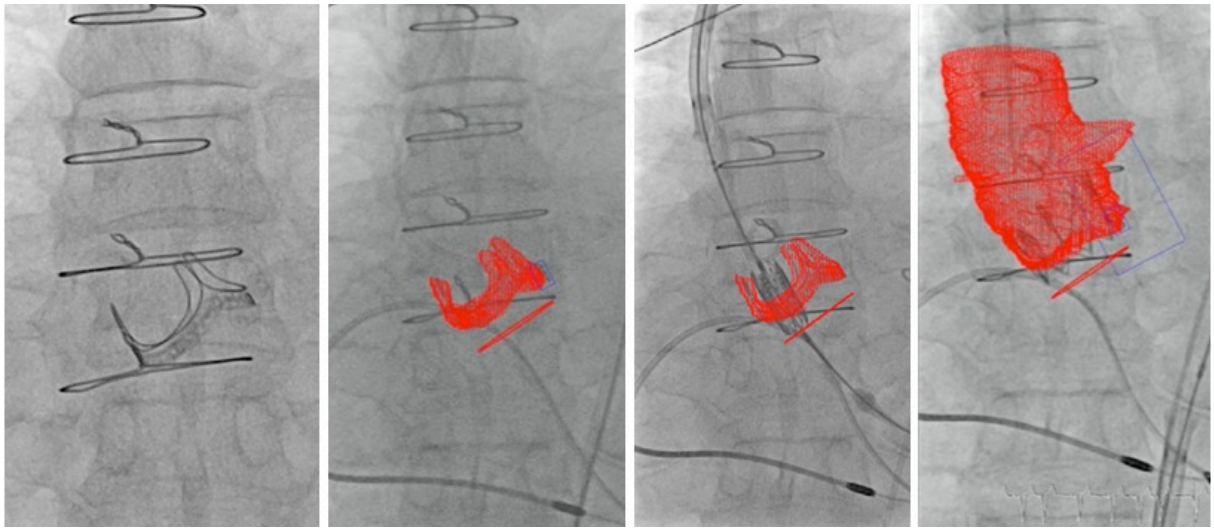

Figure 2. Fluoroscopic aspect of a bioprosthetic heart valve. On the second picture, augmented reality interface with overlaid mesh of the bioprosthesis stent, with the target plan of implantation. On the third picture, the THV is aligned with the target plan before deployment. Additional projection of the aortic root with the coronary ostia on the fourth picture, after THV implantation.

This approach combines medical imaging and computer assistance technologies, and provides additional objective data in real-time to support intra-operative decision. The feasibility the proposed approach has been successfully tested during two live ViV cases. This first experiment showed that augmented reality could allow the physician to secure an optimal THV placement, reducing therefore the risks, as well as providing reproducibility in these challenging procedures.

In conclusion, we presented the basis of an augmented reality approach that combines live fluoroscopy and 3D/2D registration of pre-operative CT scan to assist with procedure planning and navigation in Valve-in-Valve procedures.

References

1 - Hammermeister K, Sethi GK, Henderson WG, Grover FL, Oprian C, Rahimtoola SH. Outcomes 15 years after valve replace- ment with a mechanical versus a bioprosthetic valve: final report of the Veterans Affairs randomized trial. *J Am Coll Cardiol.* 2000; 36:1152-1158.

2 - Maganti M, Rao V, Armstrong S, Feindel CM, Scully HE, David TE. Redo valvular surgery in elderly patients. *Ann Thorac Surg*. 2009;87: 521–525.

3 - Webb J, Wood D. Current Status of Transcatheter Aortic Valve Replacement. Journal of the American College of Cardiology 2012:483–92

4 - Ruggieri VG, Anselmi A, Wang Q, Esneault S, Haigron P, Verhoye J-P. Computed Tomography Image Processing to Detect the Real Mechanism of Bioprosthesis Failure: Implication for Valve-In-Valve Implantation. Journal of Heart Valve Disease. 2013 Mar;22(2):236-8.

5 - Nguyen DLH, Garreau M, Auffret V, Le Breton H, Verhoye J, Haigron P. Intra-operative tracking of aortic valve plane. IEEE Engineering in Medicine and Biology Society Conference (EMBC); 2013; p. 4378-81

6 - Fluoroscopic Guide to an Ideal Implant Position for Sapien XT and CoreValve During a Valve-in-Valve Procedure Vinnie N. Bapat et al. Jacc : cardiovascularinterventions vol. 6, no.11, 2013

Acknowledgment

This work was partly supported by the French ANR within the Investissements d'Avenir program (Labex CAMI) under reference ANR-11-LABX-0004.

This work has been partially conducted in the experimental platform TherA-Image (Rennes, France) supported by Europe FEDER.

Small pulmonary nodule localization with intraoperative Cone Beam Computed Tomography during video-assisted thoracic surgery

Authors :

Simon Rouzé[1,2,3], Miguel Castro[1,2], Pascal Haigron[1,2], Jean-Philippe Verhoye[1,2,3], Bertrand de Latour[1,2,3]

1 : Université de Rennes 1, LTSI, Rennes, F-35000, France

2 : INSERM, U1099, Rennes, F-35000, France

3 : Cardiothoracic and cardiovascular Unit, Rennes University Health center, Rennes, F-35033, France

Introduction

Five-year survival of lung cancer in Europe remains limited: 10% only [1]. In opposition, small and limited pulmonary lesions fully resected by surgery are associated with survivals of more than 80% [2]. Consequently, to detect lung lesions as soon as possible, several screening programs have been developed. Recently, the National Lung Screening Trial established the interest of low dose computed tomography (CT) to detect lung lesions [3]. Therefore, the diagnosis of lung lesions increased significantly [4]. Nevertheless, the histological patterns of those lesions need to be explored. Regarding the usual small size of those lesions and their localisations, most of time a surgical biopsy needs to be performed. Video assisted thoracic surgery (VATS) is the best approach for those biopsies. Sometimes, the localization of those lesions can represent a real challenge. Several guidance systems have been developed. The more accurate ones are invasive and need a preoperative procedure (i.e. hooks, coils) [5]. In this work we describe a non-invasive guidance procedure, using intraoperative Cone Beam Computed Tomography (CBCT) and augmented fluoroscopy to guide the resection during the VATS.

Materials and Methods

Patients with isolated lesion of the lung were included. They had to be aged of more than 18 year old and consented to the procedure. The size of lesion was less than 35 millimetres. The localisation of the lesion was not an inclusion criteria.

The procedure was happening in the operating theatre under general anaesthesia, intubated selectively and installed in lateral decubitus position.

The VATS procedure was performed using 3 thoracic incisions allowing a triangulation. We used 30° - 10mm optics, HD camera and imaging system (Stryker corporate).

The DynaCT acquisitions were performed by a C-arm system with an intraoperative CBCT functionality (Artis zeego system, Siemens Healthcare, with a flat-panel detector and a 2048 × 1538 element). Acquisitions were performed after exclusion and limited deflation of the operated lung: after the incisions, a creation of a limited pneumothorax was performed under control of the thoracoscopy. In fact, the size of pneumothorax was controlled to be big enough to allow us to work in the thorax but small enough to avoid complete collapse of the lung and therefore to avoid densification of the parenchyma during the image acquisitions. The parameters of our DynaCT protocol were as follows: 0.5° projection angle increment, 512 × 512 matrix, 211° of circular trajectory for 8 seconds, a system dose of 0.36 mGy per frame and a total of 419 projections. Acquired images were transferred to a commercially available dedicated workstation (MMWP station, Siemens Healthcare). DynaCT images were reconstructed with 1-mm section thickness in axial, coronal, and sagittal planes.

After the DynaCT acquisitions, volume DynaCT images allowed us to locate precisely the lesion. Afterwards, a 3D description of the lesion was created using a segmentation method. Our software was then able to create a projection of the representation of the nodule depending on the position of the surgical table, during usual fluoroscopic acquisitions, without any manual or semi-automatic registration.

In a second time, thanks to fluoroscopic guidance, the endoscopic forceps were placed next to the representation of the lesion overlaid on the fluoroscopic image. To improve the precision of the localization, another orthogonal fluoroscopic acquisition was done to place

a second forceps under the projection of the lesion.

Thanks to this positioning of the forceps, the nodule was then resected with surgical stapling system through the VATS trocar.

Results

A total of 5 patients underwent the DynaCT acquisitions, fluoroscopic localisation with augmented reality and the resection. Each patient presented one nodule only.

The first challenge of this work was to assess the feasibility to detect centimetric lesions on deflated lungs thanks to the DynaCT during the time of the surgery. We succeeded in locating the nodule in all the cases on the DynaCT acquisitions (figure 1). The density of the lesion was between -20 to 250 HU (Hounsfield Unit). The mean size of the lesion was of 17 mm (+/-10 mm). The mean depth of the nodules was of 20 mm (+/- 16 mm). We didn't find any significant difficulties to locate the lesion whether it was deep or superficial. Elsewhere, the histological nature of the nodule didn't influence its ability to be detected.

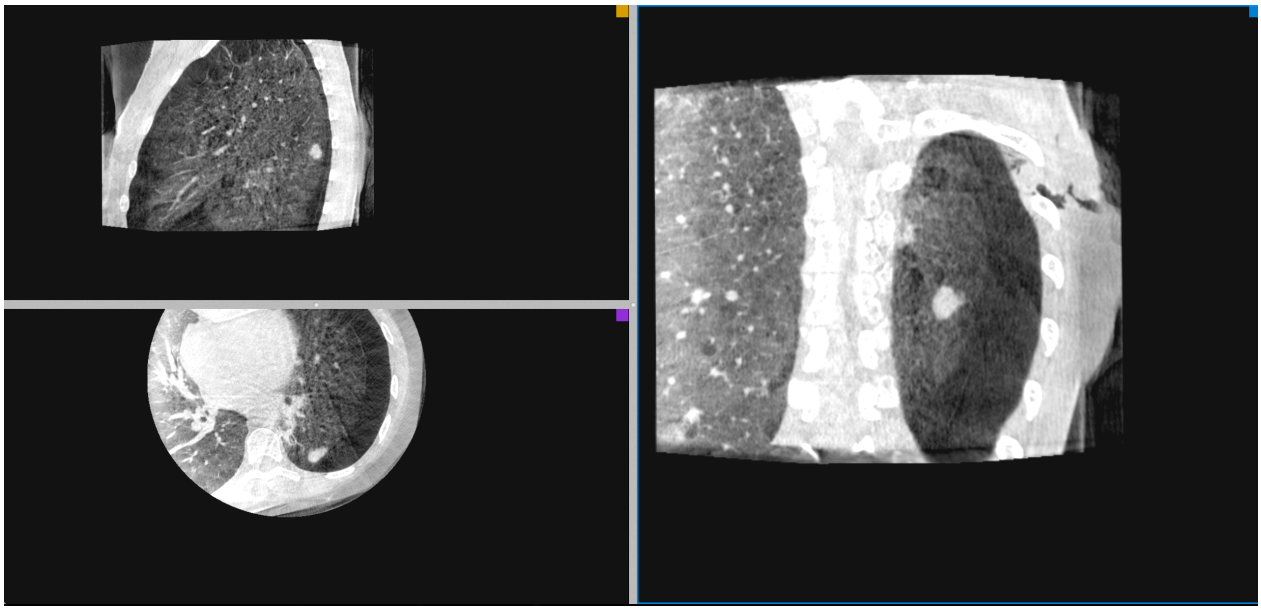

Figure 1: Example of DynaCT acquisition after multi-planar reconstruction

The main purpose of our study was to detect efficiently the lesion with augmented

fluoroscopy during the VATS (figure 2). We have been able to detect the lesion in all the cases. The mean duration to find the lesion was below 1 minute. In fact, the first positioning of the endoscopic forceps was in the projection of the lesion at the first attempt with one fluoroscopic incidence only for 80% of the cases, allowing the detection of the lesion. Only one patient required 2 incidences to obtain an accurate positioning of the surgical tools. The accuracy of the location was verified by digital palpation of the lesion. Because of its non invasive pattern, we did not experience any complication due to this localization method.

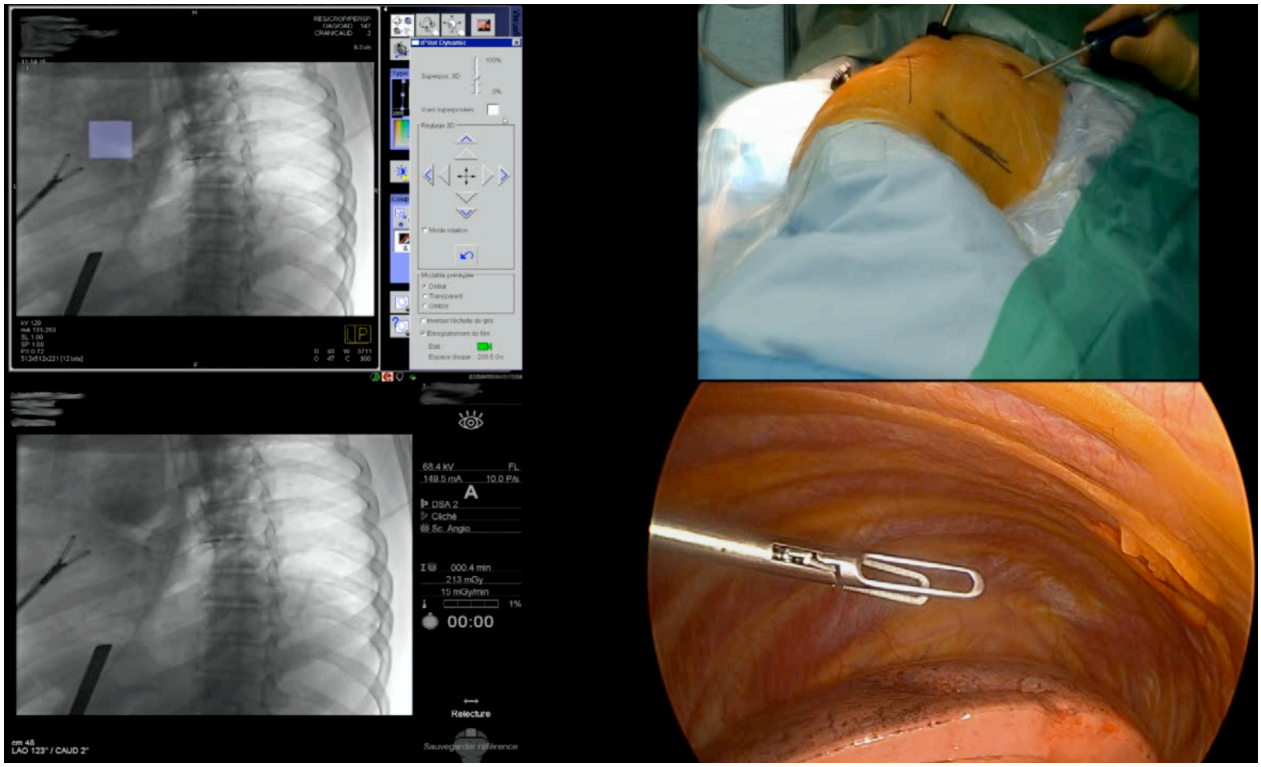

Figure 2: VATS procedure (right images) associated with augmented reality fluoroscopic acquisitions (top left image)

Conclusion

The intraoperative CBCT is an efficient tool to detect small pulmonary nodule in VATS. Associated with augmented reality, it offers a significant advance to VATS resection of subpalpable lung nodules. This initial experience highlights the potential of the proposed

approach to improve the perception of targeted tumor during VATS. Nevertheless, next challenges will be to make the fusion between videoscopic and fluoroscopic images to guide the localization of the lesion, with objective evaluation of the lesion localisation precision.

Acknowledgement

This work has been partially conducted in the experimental platform TherA-Image (Rennes, France) supported by Europe FEDER.
This work was partly supported by the French ANR within the Investissements d'Avenir program (Labex CAMI) under reference ANR-11-LABX-0004.

Bibliography

[1] Survival of cancer patients in Europe: the EUROCARE 2 study. Lyon, France: IARC scientific publications 1999: 1–572.
[2] Patz EF, Rossi S, Harpole DH, Herndon JE, Goodman PC. Correlation of tumor size and survival in patients with stage Ia non- small cell lung cancer. *Chest* 2000, 117: 1568–71.
[3] The National Lung Screening Trial Research Team. Aberle DR, Adams AM, Berg CD, Aberle DR, Adams AM, Berg CD et al. Reduced lung- cancer mortality with low-dose computed tomographic screening. N Engl J Med 2011;365:395–409.
[4] K. Mikita *et al.*, "Growth rate of lung cancer recognized as small solid nodule on initial CT findings," Eur. J. Radiol. 81(4), e548–e553 (2012)
[5] Zaman M, Bilal H, Woo CY, Tang A. In patients undergoing video-assisted thoracoscopic surgery excision, what is the best way to locate a subcentimetre solitary pulmonary nodule in order to achieve successful excision? Interact Cardiovasc Thorac Surg. 2012 Aug;15(2):266-72

COMPUTER-HUMAN INTERACTION

Haptic and visuo-haptic feedback for guiding laparoscopic surgery gestures

Thomas Howard[(1)] and Jérôme Szewczyk[(2)]

(1) Thomas Howard is with
Sorbonne Universités,
UPMC Univ Paris 06, UMR 7222, ISIR,
CNRS, UMR 7222, ISIR,
INSERM, U1150, Agathe-ISIR,
F-75005, Paris, France
Contact : howard@isir.upmc.fr

(2) Jérôme Szewczyk is with
Sorbonne Universités,
UPMC Univ Paris 06, UMR 7222, ISIR,
CNRS, UMR 7222, ISIR,
INSERM, U1150, Agathe-ISIR,
F-75005, Paris, France
Contact : sz@isir.upmc.fr

Due mainly to drastically shortened recovery times, lower overall cost and better patient outcomes, minimally invasive surgery (MIS) is growing standard for many surgical interventions. However, the characteristics of MIS incur severe perceptual and motor limitations, such as partial loss of visual depth perception, difficult hand-eye coordination and distorted haptic sensation. These limitations, in turn, have been shown to affect surgical performance – resulting in some cases in increased complication rates and intra-operative injuries when compared to the corresponding open surgery procedures.

We hypothesize that the perceptual limitations inherent to MIS settings may be overcome at least in part by providing additional information on the state of the surgical instrument and its interaction with manipulated organs to the surgeon during the operation. Using forms of augmented reality, we thereby hope to bring the quality surgical gesture performance in MIS back on par with that in open surgery.

Our initial experiments focus on the problem of assisting the surgeon in precisely guiding a surgical instrument tip within the patient's abdomen. The idea is to acquire the position of the instrument tip in space using sensors mounted on the instrument and to feed back the minimum amount of information relevant to the surgical task in order for the surgeon to not deviate further from a target trajectory in MIS than he would in a comparable open surgery setting.

In the following exploratory experiment, we aim to evaluate the respective contributions of haptic feedback (tactile and kinesthetic), visual feedback, and their combinations in guiding a user's tool towards a predefined 3-D target plane during a trajectory following task in said plane. In the context of a laparoscopic hepatectomy, the surgeon must delineate a plane crossing the liver along which the organ is then to be resected. The clinical quality of a hepatectomy is judged among other things by the fact that as little healthy tissue as possible is resected while all pathological tissue is removed. This supposes correct navigation of the instrument tip towards the defined plane while cutting, which can be a tricky task even for experienced surgeons due to the limited quality of the available visual feedback. This has motivated the choice of our experimental set-up for these first experiments.

23 healthy subjects with no previous laparoscopic experience carried out trajectory following tasks within a plane under provision of 9 different combinations of visual and haptic guidance feedback. The target plane was materialized by the tip of three pegs placed within a laparoscopic trainer (Endosim LaproTrain®, see fig.1 center).
Subjects were instructed to follow the trajectory while staying as close as possible to the target plane, while their secondary objective was to complete the task as fast as possible without compromising precision.
Evaluated forms of haptic feedback encompassed both tactile and kinesthetic feedback. Tactile feedback was provided by off-the-shelf eccentric rotating mass (ERM) vibration motors placed within the hand of the subjects (see fig.1 left). Kinesthetic feedback was implemented as soft guidance virtual fixtures using a Haption Virtuose 6D haptic interface co-manipulating the surgical tool along with the subject (see fig.1 right).

The selection of tactile feedback technology was based on the wide availability and low cost of ERM motors, making them most appropriate in view of potential future development of disposable medical devices, as well as promising results from their application to various other fields (e.g. notification, personal and vehicle navigation, etc.). The selection of haptic device for kinesthetic feedback was based on the relatively large required workspace and force range for effective co-manipulation of the laparoscopic grasper as well as previous experience within our research team regarding the application of Haption Virtuose devices to surgical co-manipulation tasks.

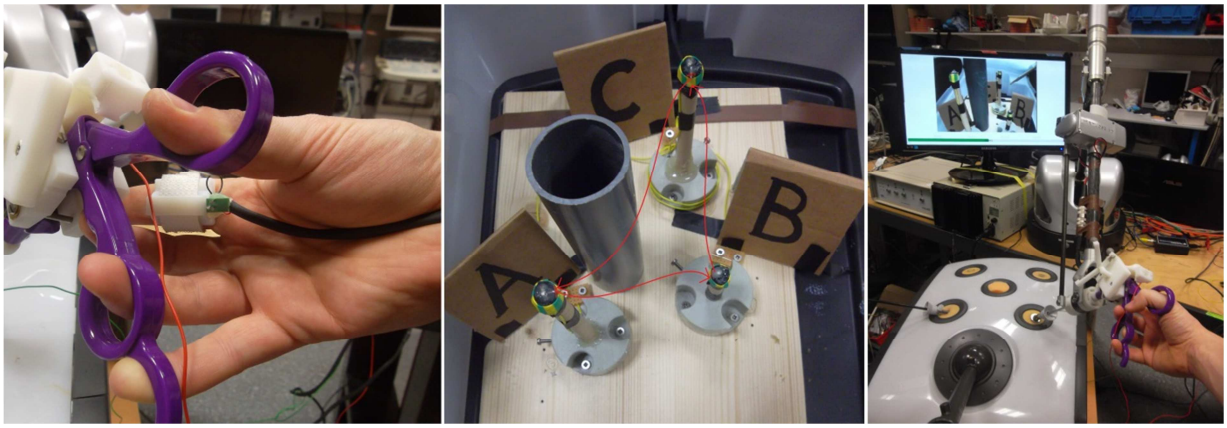

Figure 1 - Experimental setup, from left to right: Vibrotactile feedback via ERM motor attached to the subject's hand; View of the inside of the laparoscopic trainer and example of a trajectory; Combined kinesthetic and visual feedback using a 6DoF haptic interface.

Results show clear superiority of soft guidance virtual fixtures over other forms of feedback, leading to performance levels above those obtained as references in the open surgery setting (condition RC-O in fig.2). However, promising results for the use of cutaneous vibrotactile feedback are also obtained, with potential for integration in MIS tool handles.

Soft guidance virtual fixtures (conditions VT-VF and VT-VFV in fig.2 denote virtual fixtures without and with added visual feedback respectively) lead to highest performances in that both precision and times to complete task (TCT) are improved when compared to reference conditions where no feedback was provided. Precision was measured both through analysis of the time spent on target and of the deviation amplitudes. Under provision of kinesthetic feedback, percentage of time spent on target increased from 24% in the reference laparoscopic condition with no feedback (condition RC-L in fig.2) to 48%. Mean deviation amplitudes were similarly reduced from 28mm to below 10mm. This improved precision was also coupled with significantly reduced TCT, dropping from 50s to 30s in the mean.

Vibrotactile feedback (conditions VT-C and VT-CV in fig.2 denote vibrotactile feedback without and with added visual feedback respectively) shows promising results in that an effective feedback scheme only slightly increased TCT while significantly improving precision. In our experiment, while precision criteria did not reach the levels obtained in the reference open surgery setting, they did not either deviate significantly from these, while they did show significant improvement over precision in the reference laparoscopic condition. This lets us hope that refining the tactile feedback and optimizing it may actually lead to comparable performance levels between the laparoscopic condition with cutaneous vibrotactile feedback and the reference open surgery condition.

Simple visual feedback (condition RC-LV in fig.2) performs worse that vibrotactile feedback in that TCTs were generally longer when compared to those of simple vibrotactile feedback (condition VT-C in fig.2). Also precision criteria show a greater improvement of time spent on target when

vibrotactile feedback is provided, whereas deviation amplitudes are almost identical for simple visual feedback and simple vibrotactile feedback.
Also, the addition of visual feedback complementing vibrotactile (condition RC-CV in fig.2) or kinesthetic feedback (condition RC-VFV in fig.2) has little significant impact on performance, although users report that it increases their comfort when using kinesthetic feedback in that it acts as a confirmation of the sometimes ambiguous kinesthetic cues.
This confirms our hypothesis that the visual modality is already quite overloaded in laparoscopic settings, complicating the task of transmitting useful information to the user via this modality.

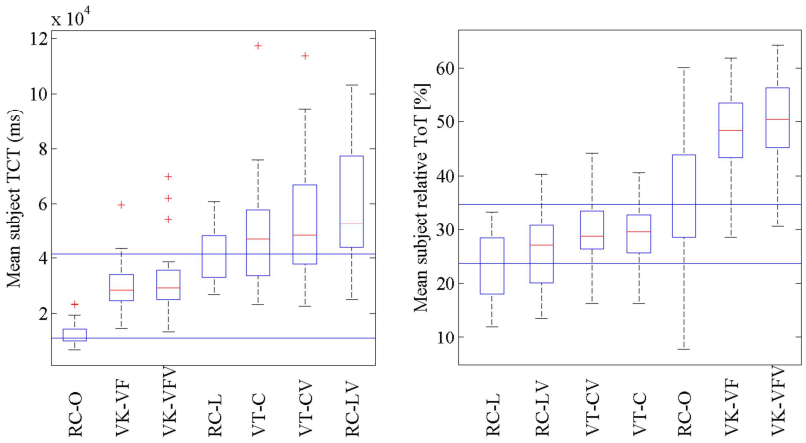

Fig. 2 – Mean subject times to complete task (TCT) vs. Mean subject relative time on target (ToT) for all conditions. TCTs are given in [ms], lower values indicating better performance. Relative ToT represents the percentage of TCT at deviations <1mm from the target plane, higher values indicating better performance.

Following these promising results, future work will focus on refining the tactile feedback in order to communicate more complex guidance information (i.e. guidance for 2D or 3D trajectories) in a more ergonomic fashion. A further important open question to be addressed will be that of the functionality of this haptic feedback for trained surgeons who would naturally be less prone to deviate from a given trajectory.

This work was supported by French state funds managed by the ANR within the Investissements d'Avenir programme (Labex CAMI) under reference ANR-11-LABX-0004.

A novel contactless human-machine interface for laparoscopic telesurgery

Fabien Despinoy[1,2,3], Alonso Sanchez[1], Nabil Zemiti[1], Pierre Jannin[2,3] and Philippe Poignet[1]

1: LIRMM - CNRS, UMR 5506, University of Montpellier 2, Montpellier, F-34000, France
2: LTSI, University of Rennes 1, Rennes, F-35000, France
3: INSERM, UMR 1099, Rennes, F-35000, France

Keywords: Infrared stereoscopic camera, human-machine interface, teleoperation, laparoscopic surgery, hand tracking.

Purpose

During the last three decades, the field of laparoscopic surgery has constantly been subject to technological advances looking to offer better healthcare in terms of safety, patient outcome, medical staff coordination and comfort [1]. Through the increasing availability of teleoperation systems for robot-assisted surgery, such as the *Da Vinci* (Intuitive Surgical Inc.), we have also seen an evolution of human-machine interfaces (HMIs) used to control these robots. Although their first function is to recover kinematic information from the surgeon's hands, they do have a direct impact on the overall performance of the system. This impact can be evaluated by means of multiple features which measure capacities of the HMI such as dexterity, bimanual exchanges, intuitiveness, comfort and precision, for instance.

In this paper, we present a continuation of a previous work [2] concerning a first experimental study to control a teleoperation system using a novel optical HMI, in the context of robot-assisted laparoscopic training.

Materials and Methods

The Raven-II system [3] (Applied Dexterity) is a bimanual robot composed of two 7 degrees of freedom (DoF) surgical manipulators dedicated to collaborative research in surgical robotics. This open platform was designed on a real-time controller using the Robot Operating System (ROS) framework. The robot control is ensured by a Cartesian position control based on a PID joint position control loop running at 1kHz. Connected through UDP, a master station allows kinematic exchanges with the robot controller.

To handle this robot, a new optical device named Leap Motion (Leap Motion Inc.) was plugged to the master station (Figure 1). Composed of 3 infrared (IR) lights and 2 monochromatic IR cameras, this device is able to track user's hands in a large field of view to control robot motions.

From the Leap Motion sensor information, a 7-DoF hand model was created using 3 particular tracking points which are the thumb, the index and the palm center of the hand. The position and orientation of the robot tooltips are controlled by the pose of the thumbs, whereas the grasping motions are handled by the angle between the thumb and the index of each hand.

Tremor filtering is applied on the hand models using an autoregressive moving-average (ARMA) low-pass filter, with an attenuation of 25dB at 2Hz [4]. Moreover, due to the optical nature of the device, special cares have been taken when tracking is lost and recovered afterwards so as to avoid bumps or unusual movements, ensuring safe and stable robot control.

Based on this model, every user can completely manipulate two robotized surgical instruments using only two fingers by instrument.

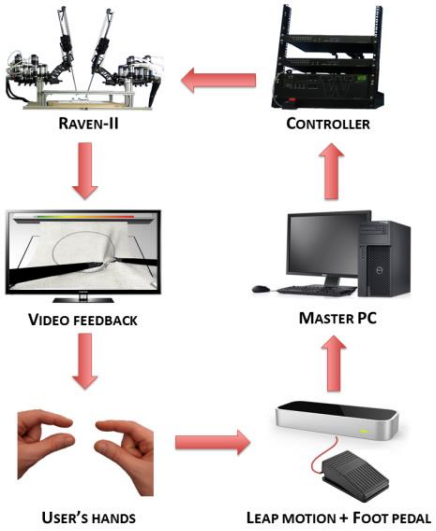

Fig.1. The teleoperation setup with the Leap Motion device, the master station, the Raven-II robot and a 3D camera for video feedback.

A preliminary performance evaluation of this new HMI was led on a population of ten researchers from the LIRMM lab. To carry out this experiment, we compared the Leap Motion device with the well-known Sigma 7 haptic interface (Force Dimension), used here as a reference for teleoperation control tasks.

The evaluation task consisted in the execution of a peg transfer scenario provided by the Fundamentals of Laparoscopic Surgery (FLS) exercises. The sequence was defined as follow: (a) Pick the first peg with the left tool and insert it in the leftmost target, (b) Pick the second peg with the right tool and insert it in the rightmost target, (c) Pick the last peg with the left hand, go to the center of the board and transfer it from the left to the right tool and then insert in the uppermost pin. From these experimentations, 30 trials were acquired (3 by candidates), including endoscopic videos and robot trajectories. Additionally, subjective information about the manipulation task were captured using an evaluation questionnaire at the end of the session.

Results

Recorded data were analyzed using JMP 11 software (SAS Institute Inc.) and Microsoft Excel 2010. On the one hand, we measured objective metrics such as completion time, percentage of success and clutching (number of activation/deactivation for repositioning) during the execution of the teleoperated task. From these first results, the leap Motion seems to perform as well as the Sigma 7 regarding the “duration” score (Figure 2a: +14s over a reference time of 101s) and “success” (Figure 2b: +12% over a reference score of 82%). However, considering the “clutching” score (Figure 2c), the Sigma 7 completely outperforms the Leap Motion. Note that this score has to be carefully considered because non-expected clutches appeared due to occlusions or tracking fails during the procedure which led to clutch in order to run again the robot.

On the other hand, we asked candidates to answer an evaluation questionnaire at the end of the session for a subjective evaluation. Here, five metrics were considered: reactivity, precision, intuitiveness, robustness and comfort (Figure 2d). The Leap Motion seemed to be well appreciated and easy to use relatively to the “reactivity”, “intuitiveness” and “comfort” subjective scores. However, the “robustness” and “precision” indexes indicate that some improvements need to be

considered. But generally, this new device obtained scores above the average rate which confirm that future large-scale experimentations should be considered for robot-assisted laparoscopic gestures, including other standard devices as well as a deeper analysis of the provided data (i.e. using video and kinematic data).

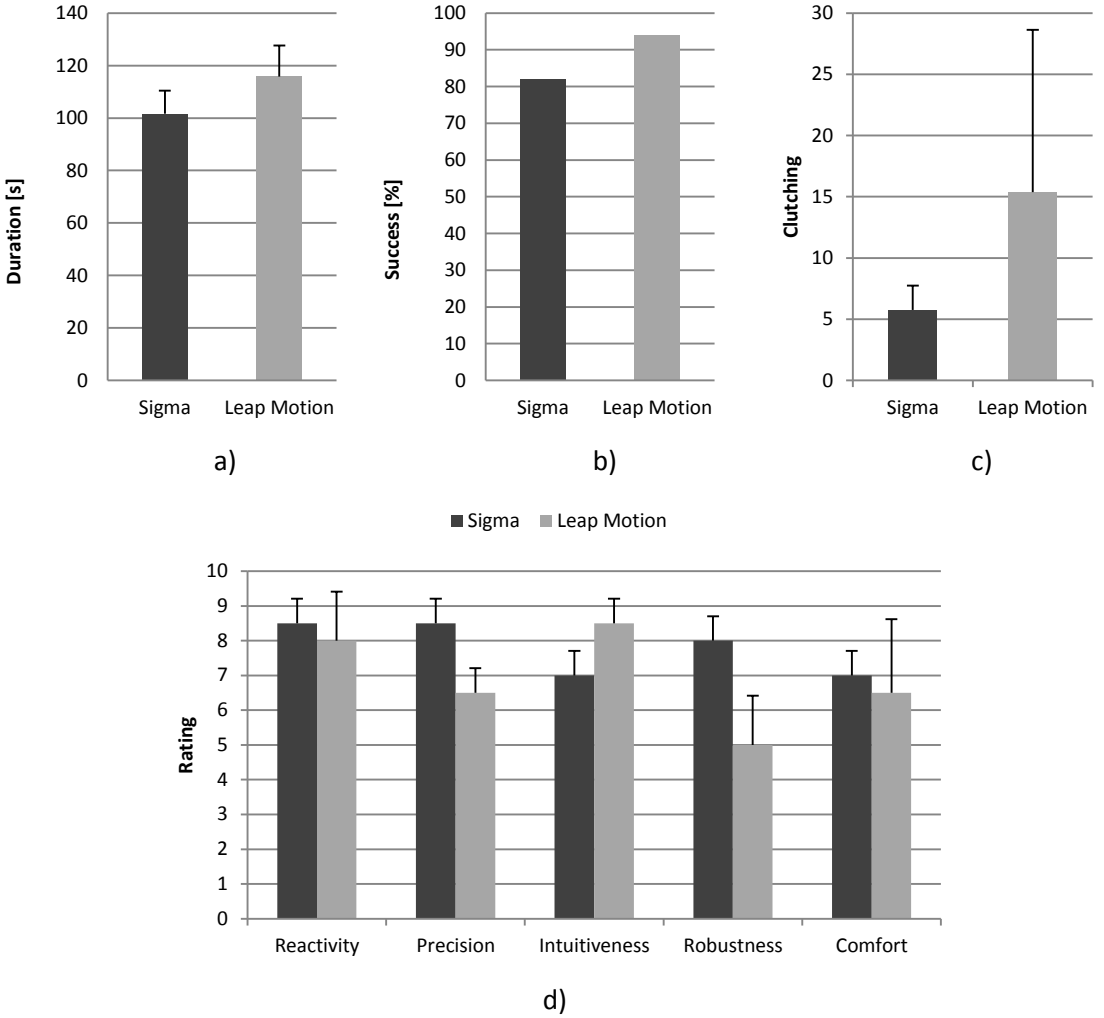

Fig.2. Comparison of the Leap Motion device by means of multiple metrics a) Completion time, b) Success of the execution, c) Number of clutching, d) Subjective metrics. Scores are represented by the mean value and the standard deviation from all candidates.

Discussion and conclusion

This work aims to evaluate a novel optical human-machine interface, namely the Leap Motion, for the execution of a laparoscopic training task. Connected to an open platform dedicated to research in robotics field, this HMI was evaluated and compared with the Sigma 7 interface by means of multiple metrics. From this preliminary evaluation, some draws can be concluded.

First of all, evaluation scores intend the leap Motion to be relevant alternative compared to standard mechanical HMIs due to small differences in terms of execution. Nevertheless real improvements need to be done with respect to user's opinions and technical issues, especially concerning occlusion and tracking fails, which could lead to better results for a larger evaluation campaign.

Moreover, some important features have to be also taken into account for the evaluation of HMI dedicated to teleoperated surgery. Two of them are the capacity to preserve asepsis during manipulation and the cost of the provided system.
In the first case, the Leap Motion device seems to be convenient for the integration in surgical teleoperation system due to its natural capacity to preserve hygiene with a contactless control. It simply avoids cleaning, waste of time to change gloves or necessary requirement to use plastic sheets and lead to an easier use in the operating room.
In the second case, a simple comparison between these two devices can be done: you can have access to more than 1,500 units of Leap Motion devices for the same price than two Sigma 7 (for bimanual teleoperation). Although the price of the last device is mainly justified by the embedded force feedback technology, a more convenient comparison should be done using Phantom Omni or similar "positioning" interfaces.
In any case, this preliminary assessment suggests that promising perspectives can be seen in the development of next-generation of human-machine interfaces in order to improve the efficiency and quality of computer-assisted surgeries.

Perspectives

Future works such as improvement of the occlusion management, integration of clinical experts and extension to other FLS tasks will be considered. Moreover, an advanced analysis on robot trajectories will be led for a quantitative evaluation of the HMI based on surgical gestures.

Acknowledgements

This work was partly supported by the French ANR within the Investissements d'Avenir program (Labex CAMI) under reference ANR-11-LABX-0004.

Supplementary Material

A short video presenting material and experiments is available here.

References

[1] Sanchez, A., Poignet, P., Dombre, E., Menciassi, A., Dario, P.: *A design framework for surgical robots: example of the ARAKNES robot controller*. Journal of Robotics and Autonomous Systems, special issue on Intelligent Autonomous Systems. Lee, S., Lee, J.M. and Menegatti, E., editors. Elsevier (2014)

[2] Despinoy, F., Sanchez, A., Zemiti, N., Jannin, P., Poignet, P.: *Comparative Assessment of a Novel Optical Human-Machine Interface for Laparoscopic Telesurgery*. Information Processing in Computer-Assisted Interventions, 8498, 21-30 (2014)

[3] Hannaford, B., Rosen, J., Friedman, D.W., King, H., Roan, P., Cheng, L., Glozman, D., Ma, J., Kosari, S.N., White, L.: *Raven-II: An Open Platform for Surgical Robotics Research*. IEEE Transactions on Biomedical Engineering, 60(4), 954-959 (2013)

[4] Bo, A.P.L., Poignet, P., Geny, C.: *Pathological Tremor and Voluntary Motion Modeling and Online Estimation for Active Compensation*. IEEE Transactions on Neural Systems and Rehabilitation Engineering, 19(2), 177-185 (2011)

Surgetica 2014

EVALUATION OF A NEW ROBOTIZED NEEDLE-HOLDER ON ERGONOMICS AND SKILLS

Authors:

Thierry Bensignor[1,2,3], Brice Gayet [1,2,3,4] and Guillaume Morel[1,2,3]

1. Sorbonne Universités, UPMC Univ Paris 06, UMR 7222, ISIR, F-75005, Paris, France
2. INSERM, U1150, AGATHE-ISIR, F-75005, Paris, France
3. CNRS, UMR 7222, ISIR, F-75005, Paris, France
4. Institut Mutualiste Montsouris, Digestive Surgery Department

Background. Laparoscopic surgery causes technical and ergonomics problems that do not exist in open surgery, due to the limited degrees of freedom (DOF) of instruments (1). Basics gestures, such as sutures, become difficult and vicious positions taken by the surgeon induces muscolo-skeletal pain (2). We have developed, in partnership with the Endocontrol Company®, a 5mm robotized needle-holder, Jaimy®, to overcome those issues. Jaimy® has 2 intracorporeal DOF, controlled by a joystick (3–5) (Figure 1). The tip of the instrument bends from 0° to 80° and its jaws can rotate with a modularly speed. The aim of this study was to evaluate the effect of a robotized needle-holder on surgical skills and ergonomics.

Figure 1. Description of the robotized needle holder Jaimy®; Left: handle design; Right: intracorporeal degrees of freedom

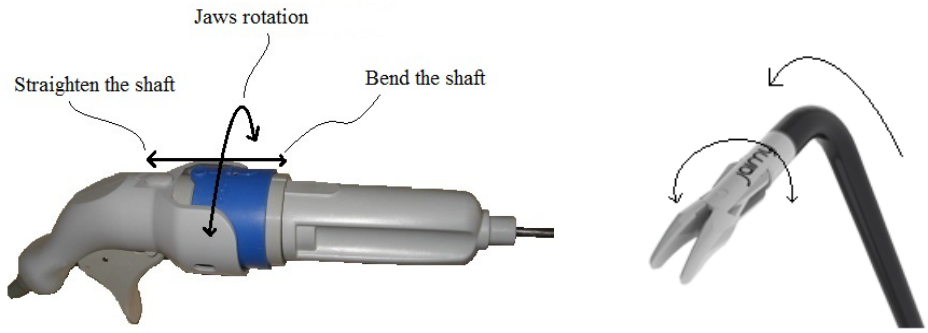

Methods Fourteen surgeons (8 surgeons, 6 residents) were cross-over randomized and stratified on their expertise. Surgeon had to performed a set of 3 limited time tasks selected among classic evaluation skills tasks, whether with Jaimy® and then with a standard needle-holder (NH) or in the reverse order. To evaluate surgical performance, the scoring system developed by Menhadji & al was used (6). Tasks were evaluated by a global score that was the product of a quantitative score and a qualitative score.

1. Pegboard task: composed of 2 pegboard and 6 pegs. Pegs were transferred from one pegboard to another. This was then reversed. We measured the number of peg transferred and the number of fallen peg.

2. Hexagonal suture: a running suture around a hexagonal pattern was made. The suture has to go through entrance and exit dots. We measured the quantity of stitches and the precision of entry and exit of each stitch.

3. Frontal suture: one stitch was made through an entry and an exit dots on a frontal axis and then a surgical knot was realized. We measured the distance between the exit of the stitch and the dot and the quantity and quality of the knot.

Postural ergonomic of the dominant arm was evaluated by motion capture and an ergonomic score for the dominant arm, called RULA score (7). It takes into account the

angles between the segments of the arm and is summarized in Table 1. It ranges from 4 to 15 and increases when ergonomics decreases. Five motion capture markers were positioned on the subject: hand, forearm, arm, acromion and sternum, together with one marker on the instrument and a reference marker on the pelvitrainer. The Polaris system® and the NDI ToolWiever® software are used to record markers positions with a 15Hz frequency. The centers of joints are obtained using a spherefit algorithm. Upper limb segments are then reconstructed between successive joint centers and angles values can be obtained by geometrical calculation. The RULA score for each task and the mean RULA score of 3 tasks are computed on MatLab®.

In addition, muscular ergonomics was evaluated with EMG and the measurement of the Cumulative Muscular Workload (CMW) of 6 muscular groups of the dominant arm: flexor carpi, extensor carpi, biceps, triceps, deltoid and trapezes. Raw EMG data was collected with TeleMyoDTS® and MyoResearch® software with a 1000 Hz frequency. EMG data's were full wave rectified and filtered using a Butterworth low-pass filter on Matlab®. The maximal voluntary contraction (MVC) of each muscle was recorded and used to normalize every recording as a percentage of this MVC. Finally the area under the curve of the EMG signal over the time was calculated and can be translated as the CMW.

Surgical skills were evaluated with two validated independent measures obtained thanks to motion capture: the length travel by the tip of the instrument that corresponds to the sum of the paths made the tip of the instrument and the number of movement during the task that is equal of the number of time when speed crosses zero (8).

Results The mean RULA score of the 3 tasks was statistically lower with Jaimy® than with NH with respective scores of 8.67 ± 1.05 versus 10.09 ± 1.44 ($p<0.001$). Therefore the postural ergonomic was increased with Jaimy®. The RULA score was statistically lower with Jaimy for the 2 sutures tasks: 8.58 ± 1.27 versus 9.98 ± 1.49 ($p<0.001$) for the hexagonal suture and 8.16 ± 1.1 versus 9.93 ± 1.67 ($p<0.001$) for the frontal suture. For the pegboard, the score was lower with Jaimy without statistical significance: 9.13 ± 1.48 versus 9.68 ± 1.45 ($p=0.056$).

For 4 muscular groups (extensor carpi, biceps, deltoid and trapezes), there was no difference for the CMW. However, the CMW on all tasks was in favor of NH with respectively for Jaimy® and NH: 15.96 ± 7.06 vs 9.85 ± 2.74 ($p<0.001$) for the flexor carpi and 18.72 ± 9 vs 11.93 ± 8.55 ($p=0.026$) for the triceps.

There was no statistical difference in the total number of movement on the 3 exercises between Jaimy® and NH with a respectively 343.1 ± 57 movements versus 322.9 ± 31

(p=0.88). Meanwhile, the path length of the tip of the instrument was shorter with Jaimy® 926.52cm ± 189.38 versus 1131.5cm ± 224.9 (p=0.006).

The pegboard task score was in favor of NH (22.5 ± 9.31 versus 34.5 ± 9.77; p=0.002), with a difference on the quantity score but none on the quality score. There was no statistical difference for the hexagonal suture (18 ± 7.46 versus 16 6 ± 6.08; p=0.13). The quality score was higher with Jaimy® (3 ± 0.55 vs 2 ± 0.47; p=0.003) when the quantity score was higher with NH (6 ± 2 vs 8 ± 2.14; p=0.034). The score of the frontal suture was increased with Jaimy® (26 ± 7.97 versus 15 ± 5.86 (p<0.001)), with superiority in both qualitative and quantitative score.

Table 1 RULA-score

Upper-arm score	*Arm elevation angle*
	(0° when arm down)
1	0 – 45°
3	45 – 90°
5	>90°
+1	If shoulder is raised by > 10mm
Forearm score	*Elbow flexion angle*
	(0° when arm and forearm aligned)
1	60 – 100°
2	<60° or >100°
+1	If hand crosses body midline or is out to side
Wrist posture score	*Wrist flexion angle*
	(0° when forearm and hand aligned)
1	-5 – +5°
2	-15 – -5° ou 5 – 15°
3	<-15° ou >15°
+1	If wrist deviation angle > 5°
Wrist twist score	*Forearm rotation angle*
1	-45 – 45°
2	<-45° or >45°

Discussion Our study shows that Jaimy® increases the postural ergonomics of the surgeon and the quality of difficult sutures. Furthermore all the surgeons (but one) had experience with conventional instruments but none with Jaimy. This suggests that surgeon

can realized better sutures in a better posture after a short learning curve.

This study brought out two minors technical problems that explained most of unfavorable results. First, the stiffness of the trigger that controls the jaws was set with a too high stiffness that explains the increased CMW of the flexor carpi. That issue was easily modified. Secondly the global score of the hexagonal suture was not different, but a higher quantity of suture was made with the classic instrument. The suture itself was quicker and more precise with Jaimy® thanks to the rotation of the jaws. But the correct introduction of the needle between the jaws takes time. Indeed the needle has to be perfectly perpendicular to the jaws to avoid making a cone during the suture. This will be improved with a new design of the jaws. At last, the result for the pegboard was not superior with Jaimy®. After careful observations, it was noticed that surgeons tried to use every robotized features of Jaimy®, even when it was unnecessary and so they lose time "playing" instead of focusing on the task.

Conclusion This study proves that the use of Jaimy® increases postural ergonomics and performance. This type of study also allowed identifying technical problems and transferring them back to the industrials in order to optimize the instrument.

Acknowledgement*: This work was partially supported by French state funds managed by the ANR within the Investissements d'Avenir programme (Labex CAMI) under reference ANR-11-LABX-0004 and through the FUI Fluoromis project.*

References

1. Berguer R. Surgery and Ergonomics. Arch Surg. 1999;134:1011–6.
2. Berguer R, Forkey DL, Smith WD. Ergonomic problems associated with laparoscopic surgery. Surg Endosc. 1999 May;13(5):466–8.
3. Herman B, Zahraee a. H, Szewczyk J, Morel G, Bourdin C, Vercher J-L, et al. Ergonomic and gesture performance of robotized instruments for laparoscopic surgery. 2011 IEEE/RSJ Int Conf Intell Robot Syst. Ieee; 2011 Sep;1333–8.
4. Zahraee AH, Paik JK, Szewcyzk J, Morel G. Towards the Development of a Hand-Held Surgical Robot for Laparoscopy. IEEE/ASME Trans Mechatronics. 2010;15(6):853–61.
5. Zahraee AH, Paik JK. Robotic Hand-Held Surgical Device : Evaluation of End-Effector ' s Kinematics and Developpement of Proof-of-Concept Prototypes. MICCAI 2010, 13th Int Conf Med Image Comput Comput Assist Interv. 2010;432–9.

6. Menhadji A, Abdelshehid C, Osann K, Alipanah R, Lusch A, Graversen J, et al. Tracking and assessment of technical skills acquisition among urology residents for open, laparoscopic, and robotic skills over 4 years: is there a trend? J Endourol. 2013 Jun;27(6):783–9.

7. Person JG, Hodgson a J, Nagy a G. Automated high-frequency posture sampling for ergonomic assessment of laparoscopic surgery. Surg Endosc. 2001 Sep;15(9):997–1003.

8. Mason JD, Ansell J, Warren N, Torkington J. Is motion analysis a valid tool for assessing laparoscopic skill? Surg Endosc. 2012 Dec 12;27(5):1468–77.

ROBOTICS

Towards clinical application of continuum active micro-endoscope robot based on EAP actuation

Mohamed Taha Chikhaoui, Kanty Rabenorosoa and Nicolas Andreff
AS2M Department, FEMTO-ST Institute, Besançon, France.
mohamed.chikhaoui@femto-st.fr, kanty.rabenorosoa@femto-st.fr, and nicolas.andreff@femto-st.fr

Keywords: continuum robots – surgical robotics – electro-active polymers – workspace analysis.

Introduction

Continuum robots have shown astounding abilities in the medical field as numerous robotized devices have emerged. For instance, colonoscopes, arthroscopes, catheters, endoscopes, and other medical tools have been developed [1]. Their ability to navigate through complex anatomy and narrow spaces represent the attractive features of continuum robots. We foresee to improve their usefulness for Minimally Invasive Surgery (MIS) and Natural Orifice Transluminal Endoscopic Surgery (NOTES). These robots may be downscaled depending on the target application, e.g., from endoscopy to neurosurgery. Shorter hospital stay, less pain and scarring, and quicker recovery might then be provided to the patient. Recently, active cannulas have been used for endonasal skull base surgery for pituitary gland cancer [2] as depicted in Figure 1a, transurethral laser prostate surgery [3], laser surgery [4], beating heart surgery [5], and neurosurgery [6]. Thus, we are interested in developing a micro-endoscope whether for diagnosis or laser surgery.

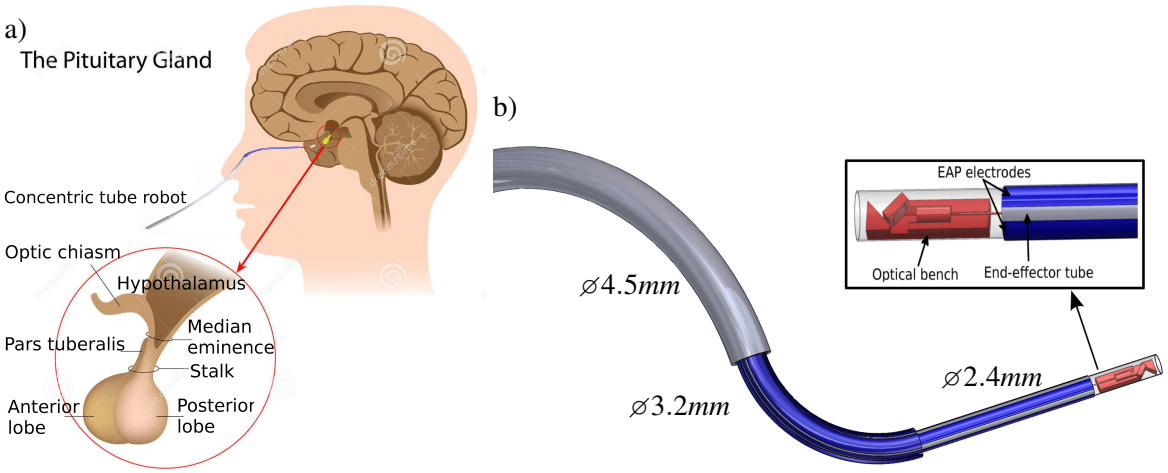

Figure 1: Concept of an EAP actuated concentric tube robot with: a) whole body reaching inserted in the nasal cavity to reach the pituitary gland detailed in the inset. b) CAD design of the robot. The inset shows the end-effector holding a laser tool.

Contribution

Our main idea is to add one or several degrees of freedom (DoF) to concentric tube robots by controlling the curvature of each tube. Doing so, we aim to compensate for the reduced mobility and dexterity of the usual concentric tube robots. Providing the extra DoF is possible through integrating embedded actuation using Electro-Active Polymers (EAP) [7]. In fact, coating thin EAP electrodes (about $10\mu m$) around the tube has demonstrated significant results [8]. One promising EAP material is the Polypyrrole (PPy). Adding to its biocompatibility, lightweight, and small size, this smart material requires very low activation voltages (less than one Volt) without any additional heating, in contrast with Shape Memory Alloys and piezoelectric materials. A curvature responding linearly to the applied voltage is the principal feature of PPy actuators [7] such as $\kappa = C_{PPy}V$, where κ is the curvature, V is the applied voltage and C_{PPy} is the PPy constant depending on tube and electrode geometry and material, and other empirical constants. Figure 1b shows the concept of an active cannula end-effector with embedded actuation.

Modeling and results

Modeling continuum robots is slightly more challenging than that of standard robots as there are no rigid links to determine the position and orientation of the tip. Instead, beam theory and constant curvature assumption are employed [9]. The robot final shape is divided into several sections, depending on the number and the shape of the overlapping tubes. For instance, the kinematic structure presented in this paper consists of 3 totally curved telescoping tubes (Figure 1b). With it, one can obtain 3 sections that can be automatically controlled to follow the trajectory defined by the surgeon through an appropriately ergonomic interface. The control-oriented modeling is based on a three-space decomposition: (i) the actuator space contains the actuation components, (ii) the configuration space holds the arc parameters of each section j, and (iii) the task space comprises the pose of the robot.

The kinematic improvement we propose relies principally on the comparison of specific Jacobian matrices J_{spec_j} of the j links depending on the actuator component derivatives. For the concentric tube robot, as only two components are available, J_{spec_j} is a 3 by 2 matrix. It leads to a non-holonomic behavior. This prompts a number of velocity directions to become unfeasible in a given state. Thanks to the proposed PPy actuation, the actuator space is broadened with a variable curvature yielding a square matrix 3 by 3 in equation 1. Matrix components and full computation are detailed in [10].

$$\begin{bmatrix} \dot{\kappa}_j \\ \dot{\phi}_j \\ \dot{\ell}_j \end{bmatrix} = \underbrace{\begin{bmatrix} J_{1,1} & J_{1,2} & 0 \\ J_{2,1} & J_{2,2} & 0 \\ 0 & 0 & 1 \end{bmatrix}}_{J_{spec_j}} \begin{bmatrix} \dot{\kappa}_{in,j} \\ \dot{\theta}_{in,j} \\ \dot{\rho}_j \end{bmatrix} \tag{1}$$

This square matrix restores a holonomic behavior: all the velocity directions are accessible again. Therefore, for diagnosis purpose, the imaging tool (camera or OCT probe) can be swept linearly while bypassing an obstacle (robot is in bent position). In the same way, in a surgical goal, the practitioner may realize either linear or curved movements with a laser or a scalpel. Besides, using three tubes with embedded actuation induces redundancy. This is highly recommended in surgical robotics. Indeed, several actuation scenarios are available to the surgeon in order to achieve a task safely.

Moreover, embedded actuation enhances the workspace with two major contributions. On the one hand, Figure 2a displays that the covered area increases towards either straight or extremely curved configurations. This is obtained with merely in-plane middle tube curvature change, which is consistent with the ranges achieved in [7]. Different possibilities are thus available such as (i) reaching further parts of the anatomy, (ii) better apprehending a specific organ, and (iii) bypassing obstacles. For instance, skull base surgery suffers a limited dexterity of current instrumentation. Figure 1a shows the possibility to

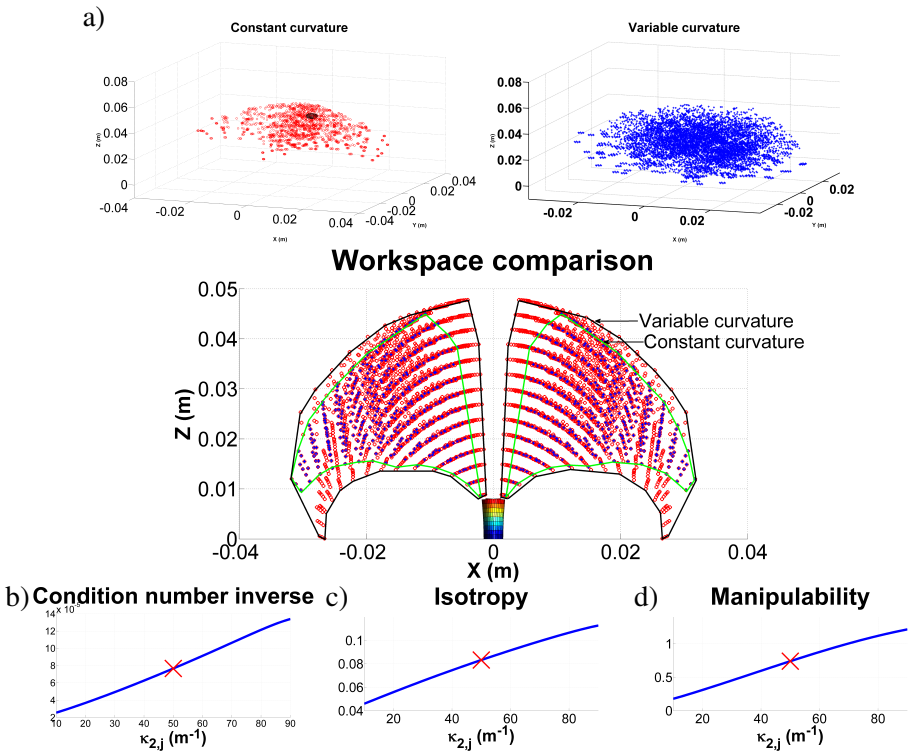

Figure 2: Workspace qualitative and quantitative analysis with a curvature sampling of $20m^{-1}$: a) the two upper insets show a 3D representation of the workspaces, the central figure displays a cross-section in the $x-z$ plane, b) Condition number inverse, c) Isotropy, and d) Manipulability versus second tube curvature.

reach a potential pituitary adenoma. For a malignant tumor, the cancer can spread to nearby tissue and structures. Such a device is then able to avoid the lobes (Figure 1a) or apprehend them in different poses.

On the other hand, the three most significant performance indices are slightly improved with embedded actuation. This means that the workspace is reached in a better manner when the middle tube bends beyond $54m^{-1}$ (the curvature used in [11]). Higher curvatures imply that the Jacobian kinematic matrix is better conditioned and isotropy increases, as depicted in Figures 2b,c. Hence velocities get more homogeneous in all directions. This provides the practitioner with a supplementary ease to control the concentric tube robot with embedded actuation when several orientations are required. Figure 2d shows the increasing system manipulability, which shifts the system further from singular positions. Thus, losing one or several velocity directions is prevented and a safe level of control of the surgical tool is ensured. In the pituitary gland area, the safety provided is critical as the optic nerves are close structures.

Conclusions

This paper highlights the benefits of adding a variable curvatures to concentric tube robots by the means of EAP. This embedded actuation should provide holonomy to the system and enhance its safety. Moreover, our theoretical analysis demonstrates that our proposal improves the kinematics of the system and enlarges the workspace both qualitatively and quantitatively. Hence it provides the practitioner better controllability and dexterity. A prototype is currently under construction to validate these theoretical results. Future work will concentrate on the technology in order to provide each tube with bending

capacities in two directions.

Acknowledgement

This work has been supported by the LabEx ACTION project (contract ANR-11-LABX-0001-01) and by μRALP, the EC FP7 ICT Collaborative Project no. 288663.

References

[1] R. J. Webster III and B. A. Jones, "Design and kinematic modeling of constant curvature continuum robots: A review," *The International Journal of Robotics Research*, vol. 29, no. 13, pp. 1661–1683, 2010.

[2] J. Burgner, P. Swaney, D. Rucker, H. Gilbert, S. Nill, P. Russell, K. Weaver, and R. J. Webster III, "A bimanual teleoperated system for endonasal skull base surgery," in *Intelligent Robots and Systems, IEEE/RSJ International Conference on*, pp. 2517–2523, Sept 2011.

[3] R. J. Hendrick, S. D. Herrell, and R. J. Webster III, "A multi-arm hand-held robotic system for transurethral laser prostate surgery," in *IEEE International Conference on Robotics and Automation*, 2014.

[4] D. C. Rucker, J. M. Croom, and R. J. Webster III, "Aiming a surgical laser with an active cannula," *Journal of Medical Devices*, vol. 3, no. 2, p. 027506, 2009.

[5] P. Dupont, A. Gosline, N. Vasilyev, J. Lock, E. Butler, C. Folk, A. Cohen, R. Chen, G. Schmitz, H. Ren, *et al.*, "Concentric tube robots for minimally invasive surgery," in *Hamlyn Symposium on Medical Robotics*, vol. 7, p. 8, 2012.

[6] E. J. Butler, R. Hammond-Oakley, S. Chawarski, A. H. Gosline, P. Codd, T. Anor, J. R. Madsen, P. E. Dupont, and J. Lock, "Robotic neuro-endoscope with concentric tube augmentation," in *Intelligent Robots and Systems, IEEE/RSJ International Conference on*, pp. 2941–2946, IEEE, 2012.

[7] T. Shoa, J. Madden, N. Fekri, N. Munce, and V. X. Yang, "Conducting polymer based active catheter for minimally invasive interventions inside arteries," in *Engineering in Medicine and Biology Society. 30th Annual International Conference of the IEEE*, pp. 2063–2066, Aug 2008.

[8] T. Shoa, N. R. Munce, V. Yang, and J. D. Madden, "Conducting polymer actuator driven catheter: overview and applications," 2009.

[9] R. J. Webster III, A. M. Okamura, and N. J. Cowan, "Toward active cannulas: Miniature snake-like surgical robots," in *Intelligent Robots and Systems, IEEE/RSJ International Conference on*, pp. 2857–2863, Oct 2006.

[10] M. T. Chikhaoui, K. Rabenorosoa, and N. Andreff, "Kinematic modeling of an eap actuated continuum robot for active micro-endoscopy," in *Advances in Robot Kinematics* (J. Lenarčič and O. Khatib, eds.), pp. 457–465, Springer International Publishing, 2014.

[11] R. J. Webster III, J. P. Swensen, J. M. Romano, and N. J. Cowan, "Closed-form differential kinematics for concentric-tube continuum robots with application to visual servoing," in *Experimental Robotics* (O. Khatib, V. Kumar, and G. Pappas, eds.), vol. 54 of *Springer Tracts in Advanced Robotics*, pp. 485–494, Springer Berlin Heidelberg, 2009.

Real-time FEM based control of soft surgical robots

F. Largilliere[1], E. Coevoet[2], L. Grisoni[3], C. Duriez[2]

[1] LIFL - University of Lille 1, France
[2] INRIA - University of Lille 1, France
[3] University of Lille 1, CNRS/INRIA, France

1 Introduction

Surgical robots, such as the Da Vinci©, interact with delicate biological structures such as blood vessels or internal organs. However, they are made of rigid materials that limit their ability of moving through confined spaces without inducing excessive contact pressures and stress concentrations which could create new injuries. An alternative solution, potentially easier to produce and suitable for interventions where the highest precision (less than a few millimeters) is not necessary, is growing in the scientific community with the development of robots made of soft materials [1]. This type of robots allows for a safer contact with internal organs and displacement among them at the cost of an increase in the complexity of control. Indeed, soft robots can dissipate the energy of collision and comply with the shape of their environment through their internal deformation. However, their infinite number of degrees of freedom does not allow to compute inverse kinematics easily. Also, the idea of using a large number of actuators to simplify the control is countered by the fact that these actuators are coupled together through the whole deformation of the robot.

Although soft, these robots could still be used in situations where medical instruments need to stay in a fixed position, by rigidifying a robot filled with particles jammed through vacuum actuation [2] .

To address the problem of controlling these robots, traditional robotic methods cannot be used because the coupling between actuators and effectors is constantly modified through the deformation of the robot. This is why it is necessary to know the influence of applied forces on the structure while controlling it. In this purpose, we have developed a new method of control [3] based on the real-time inverse simulation with internal deformation computed through the use of Finite Element Method (FEM). It was coded in SOFA, an open-source framework that contains fast implementations of FEM as well as optimization methods for collision response and mechanical interactions with haptic feedback. This work has demonstrated its first proofs on various numerical examples but also on a real deformable robot made of silicone and actuated through cables.

2 Method

To model the large non-linear deformations undergone by the soft structure, a corotational volume FEM formulation [4] is used in this work. At each step i of the real-time simulation, the internal forces are linearized as follows:

$$\mathbf{f}(\mathbf{x_i}) \approx \mathbf{f}(\mathbf{x_{i-1}}) + \mathbf{K}(\mathbf{x_{i-1}})d\mathbf{x} \tag{1}$$

where $\mathbf{f}$ represents the volumetric internal stiffness forces at a given position $\mathbf{x}$ of the nodes, $\mathbf{K}(\mathbf{x})$ is the tangent stiffness matrix that depends on the actual position of the nodes and $d\mathbf{x}$ is the displacement of nodes between two steps $d\mathbf{x} = \mathbf{x_i} - \mathbf{x_{i-1}}$.

In a first approach, we want the model to be in static equilibrium state regarding internal and external forces, which is acceptable for quasi-static motions i.e for low velocities. The following equation has then to be solved:

$$-\mathbf{K}(\mathbf{x_{i-1}})d\mathbf{x} = \mathbf{p} + \mathbf{f}(\mathbf{x_{i-1}}) + \mathbf{J}^T\boldsymbol{\lambda}. \tag{2}$$

where $\mathbf{p}$ represents the external forces (e.g. gravity) and $\mathbf{J}^T\boldsymbol{\lambda}$ gathers the contributions of the actuators through a product between $\mathbf{J}^T$ and $\boldsymbol{\lambda}$ that are respectively the direction of the forces and their unknown intensities.

Then, we use the following algorithm :

- First, a free configuration is found by solving the previous equation with $\boldsymbol{\lambda} = 0$. We can then compute the violation of the desired positions before the appropriate actuation.
- Secondly, the following projection into constraint space is used :

$$\boldsymbol{\delta} = \underbrace{\left[\mathbf{J}\mathbf{K}^{-1}\mathbf{J}^T\right]}_{\mathbf{W}}\boldsymbol{\lambda} + \boldsymbol{\delta}^{\text{free}} \tag{3}$$

  where $\boldsymbol{\delta}^{\text{free}}$ and $\boldsymbol{\delta}$ are respectively the violations before actuation and the one after actuation i.e to be minimized by the control. A Gauss-Seidel iterative solver is used to find a solution for the couple ($\boldsymbol{\lambda}$,$\boldsymbol{\delta}$)
- Finally, the free configuration of the robot is updated according to the influence of the forces $\mathbf{J}^T\boldsymbol{\lambda}$ previously calculated to obtain the configuration under actuation.

The constraint on the terminal actuator is set by assigning its three directions of displacement (x, y and z) and forcing $\boldsymbol{\lambda}$ at zero, as a non-directly actuated point. This formulation of the problem allows for various actuators to be modeled by taking into account their physical characteristics (directional of actuation, unilateral (e.g pulling cable)/bilateral actuation, limited stroke) through the use of bilateral or unilateral constraints. Pneumatic actuation can also be used via normal constraint applied to selected faces of the deformable cavity.

3 Coupling with soft-tissue models

When using FEM, it is usual to impose the load and get the displacements (or deformations), which could be considered as a direct mechanical model in robotics. On the contrary, what the algorithm presented here does is a novel use of FEM to obtain an inverse mechanical model. However, taking into account all degrees of freedom of the model would be too much expensive for the algorithm to be real-time. This is why a compliance matrix **W** condensed in the constraint space is used. This matrix holds only the modeling of the mechanical coupling between each actuator and effector (or other actuators) so that it can be used in the inverse algorithm computed fast enough to be efficient.

With very small changes in the algorithms, [5] uses the method for parametrization of soft-tissue models by inverse simulation. It is applied to semi-automatic registration for adaptive radiotherapy. Indeed, the same condensation strategy is used to find the parameters and the boundary conditions (physics-based external loads) that provide the displacements that are observed on the images. This strategy is very important in the context of the navigation of a surgical soft robot interacting with the soft-tissue environment of the patient (see figure 1)

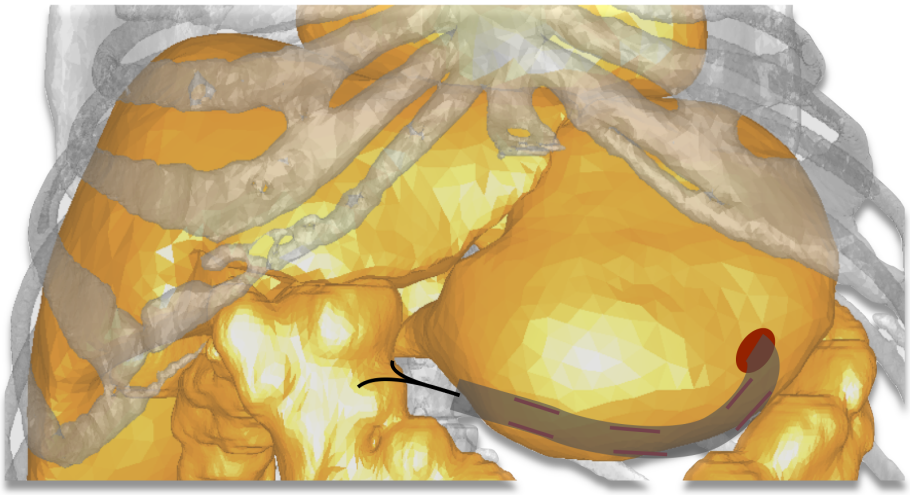

Fig. 1. The concept of a soft laparoscopic robot. Thanks to its flexibility, the robot can access difficult areas, while preventing hard contact stress with the wall of the soft tissues. Both patient anatomy deformations and soft robot would require FEM inverse method

The presentation will show how we envision to couple this inverse FEM method to provide online both control of the robot and registration of a physics-based model of the patient.

4 Conclusion

This work presents the use of a FEM inverse model, computed in real-time to control the motion of the soft robot. We also show that this inverse model strategy can be used to parametrize the modeling of the soft tissues of a patient by registration of the deformations. From these works, we can consider the development of a real-time simulation that could be used during a surgical intervention to control a soft robot that could navigate among organs whose positions and properties would be updated and taken in consideration while choosing how to plan the movements of the robot and how to actuate it. Another possible application is the control of soft robotic organs for realistic surgery training.

References

1. Majidi C., *Soft robotics: A perspective - Current trends and prospects for the future*, in Soft Robotics journal, Volume 1, pages 5-11, 2014.
2. Jiang A., Althoefer K., Dasgupta P. and Nanayakkara T., *The Core-Snake, the variable stiffness laparoscopic camera* in The Hamlyn Symposium on Medical Robotics, London, United Kingdom, 2013.
3. Duriez C., *Control of Elastic Soft Robots based on Real-Time Finite Element Method*, in Proceedings of ICRA (& Patent application WO 2014122134 A1), 2013.
4. Felippa C., *A systematic approach to the element-independent corotational dynamics of finite elements*, in Technical Report, Center for Aerospace Structures, 2000.
5. Coevoet E., Reynaert N., Lartigau E., Schiappacasse L., Dequidt J. and Duriez C., *Introducing interactive inverse FEM simulation and its application for adaptive radiotherapy*, in Medical Image Computing and Computer-Assisted Intervention (MICCAI), 2014.

Achieving high precision in prostate biopsy thanks to robot closed loop control based on 3D ultrasound imaging

Cecile Poquet [*] [†] [‡], Marie-Aude Vitrani[*] [†] [‡],
Pierre Mozer [*] [†] [‡] [§] and Guillaume Morel[*] [†] [‡]

Context

Prostate biopsy is the only examination that enables urologists to diagnose prostate cancer. It consists in taking off samples of the gland using a biopsy needle that slides in a needle-guide rigidly attached to a transrectal ultrasound probe. In clinical routine twelve systematic biopsies are distributed in the prostate volume and additional targeted samples can be taken in a given zone of interest (that has been detected earlier on an MRI image or during a previous biopsies session).

To perform prostate biopsies, the urologist uses the two-dimensional image as the only source of information while the patient is under local anaesthesia and the prostate experiences significant motions and deformations. Thus this gesture is difficult to perform but is also of the utmost importance as it constitutes the ground for therapeutic decisions making.

One key aspect of the procedure is the precision with which the needle aims at the desired biopsy location: the more accurate the needle placement is, the more accurate the diagnosis will be. An increase in the needle positioning process could also lead the way to focal treatments, that are known to present less side-effects

[*]Sorbonne Universités, UPMC Univ Paris 06, UMR 7222, ISIR, F-75005, Paris, France
[†]INSERM, U1150, AGATHE-ISIR, F-75005, Paris, France
[‡]CNRS, UMR 7222, ISIR, F-75005, Paris, France
[§]La Pitié Salpêtrière Hospital, Urology Dpt., F-75013, France.

than global ones.

Because of its crucial importance in terms of public health, robotic assistance to needle placement in the prostate has been the object of interest for the robotics community in the past years. A recent exhaustive overview of these systems can be found in [1].

Proposed system

A robot named Apollo which is aimed at assisting prostate biopsies through comanipulation has been developed. Its installation in a routine-like setting is shown on figure 1. Apollo, is an anthropomorphic arm that exhibits six degrees of freedom and a great transparency [2]. The first three axes (which constitute the shoulder and elbow) are equipped with motors, brakes are mounted on the three others that form the wrist.

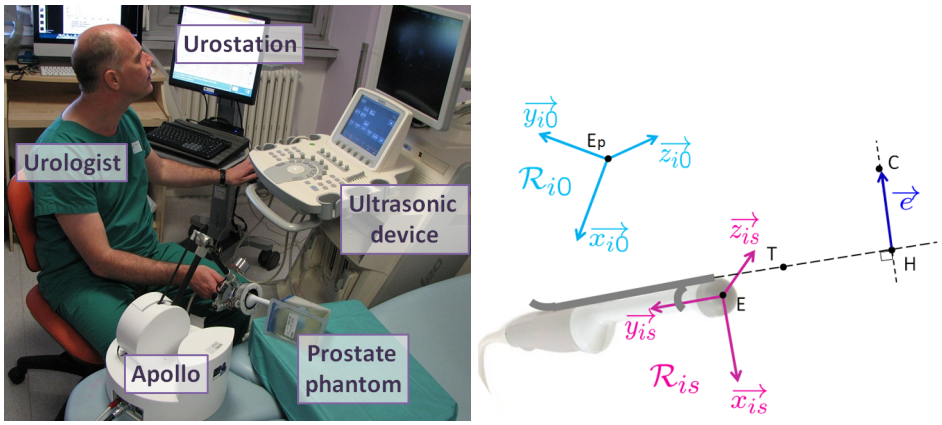

Figure 1: Proposed system in clinical-like setting and task modeling.

Two control modes have been developed: a free mode and a locked mode. In the first the surgeon controls the probe motion without interferences from the robot; in the second Apollo maintains the probe at its position precisely while exhibiting a low stiffness, which is important to ensure the patient safety. Apollo and its two control modes have been detailed in [2].

Although this system has been designed to be able to comanipulate the ultrasound probe together with the surgeon, it can be used to perform an automatic positioning of the probe, thanks to the 3 actuated joints. This is the object of the present paper.

The basic idea is to iteratively modify the position of the robot from an estimation of the error between the current target location and the desired target location in the prostate. In this closed-loop paradigm, a key issue is to measure the current target with respect to the prostate. This is achieved thanks to the Urostation, a device commercialized by KOELIS that performs registration between 3D ultrasonic images [3]. More precisely, the urologist first records an initial 3D image of the prostate (while the robot holds the probe in a locked mode), thus building a reference 3D volume. Through an interface, the urologist defines in this volume a target where the biopsy must be done. Then, using the robot in free mode, he/she moves the probe towards this target. When roughly positioned, the urologist switches to the locked mode. A new 3D image is then acquired and the positioning error can be computed thanks to the Urostation technology which registers the current 3D volume with respect to the reference 3D volume [4].

Robot control

In order to be able of controlling the robot, an interaction matrix between the robot displacements and the target error displacements shall be established. Our robot Apollo is able of actively controlling the position of point C, which corresponds to the wrist robot center, while the objective of the controller is to correct the position of the target point T. Point T belongs to the needle axis and is placed a few centimeters in front of the probe extremity; it corresponds to the center of the biopsy sample core and its location is the reference volume can be measured thanks to the Urostation. The wrist brakes being unlocked, when point C moves, a displacement of point T is described thanks to a lever model which fulcrum corresponds to the patient's anus.

Since the depth of the biopsy is controlled by the urologist in the ultrasound image, only the direction of the needle is seroved to the desired orientation. This means that only the two degrees of freedom of points C and T perpendicular to the needle axis are considered. As a result, the 2×2 interaction matrix between a small displacement δ_C of point C and the error variation δ_{ε_T} of point T, both

considered perpendicularly to the needle axis, writes:

$$\delta_{\varepsilon_T} \approx \begin{pmatrix} \alpha & 0 \\ 0 & \alpha \end{pmatrix} \delta_C \tag{1}$$

The control law uses an inverse of this estimated interaction matrix to compute a finite displacement d_C of point C to be sent to the robot from a measure of the error ε_T at point T:

$$d_c = \lambda \begin{pmatrix} \hat{\alpha}^{-1} & 0 \\ 0 & \hat{\alpha}^{-1} \end{pmatrix} \varepsilon_T \tag{2}$$

where λ is a correction gain and $\hat{\alpha}$ is an estimate of α.

Results

A first experimental result validating the approach is proposed in this paper. The experimental set-up is describe on figure 1. The probe extremity is inserted in a phantom that reproduces both the mechanical and echogenecity of a prostate and neighbouring tissues, including the anus and rectum.

A urologist first records the reference image and then engages the locked mode and releases the probe. A first set of movements is made in open loop, for which the point C displacement is imposed while point T displacement is measured. This allows to obtain an estimate for α (in this case: $\hat{\alpha} = 0.7$). Meanwhile λ is experimentally set to 0.5.

The desired target is then defined 5 *mm* away from the needle axis along the x image direction. Figure 2 shows the successive positions of point T and the needle axis in the reference image frame during an automatic adjustment experiment. Within six iterations, the pointing error reached 0.7 *mm*, which is a satisfactory precision.

It can be observed that the convergence is not smooth. It is hypothesized that deformations and movements of the prostate phantom lead to unexpected variations of the error. However, thanks to the closed loop approach and an appropriate selection of gain λ, a final convergence if obtained.

Conclusion

We have been able to generate automatic small motions of the ultrasound probe that allows a satisfactory alignment of the needle axis with a biopsy target defined

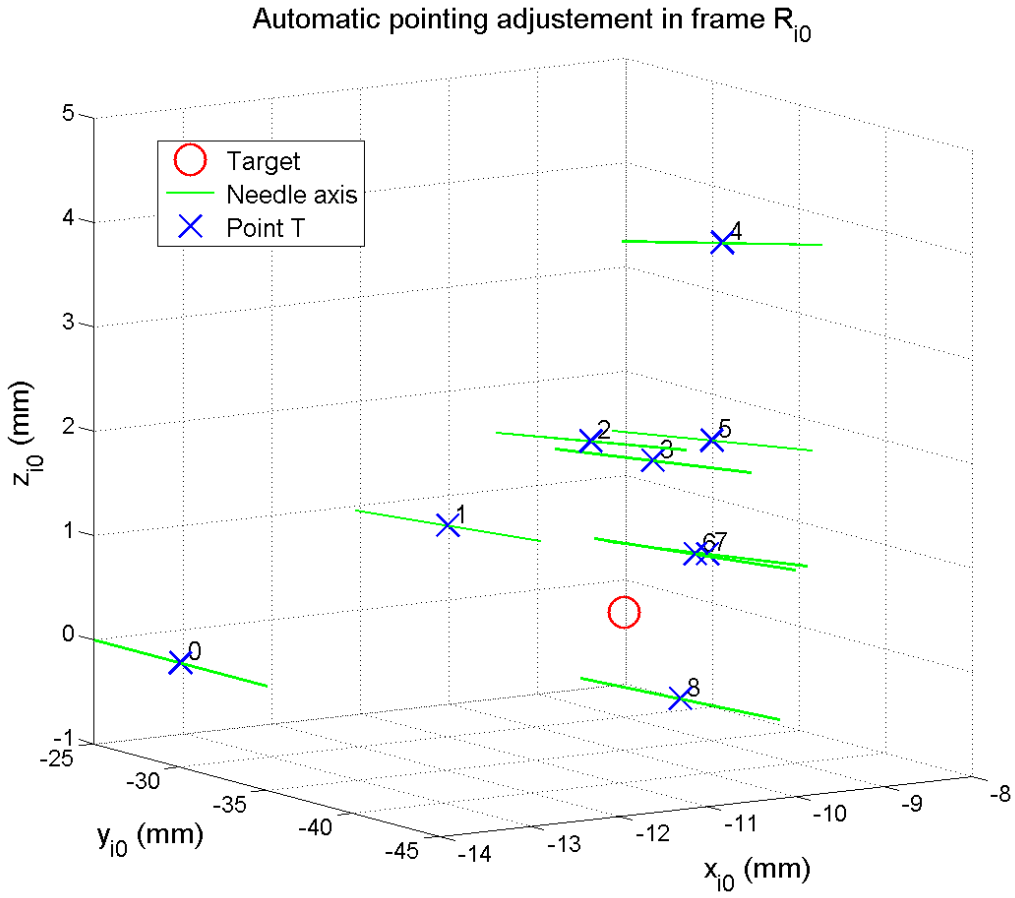

Figure 2: Successive positions of point T and the needle axis in the reference image frame during an automatic adjustment experiment.

with respect to the prostate, which is a moving and deformable organ.

This first proof of concept must now be further developed. Future work will include verification of the forces applied to the patient anus by the probe during automatic small adjustment motions and design of a more robust control.

Acknowledgment

This work was partially supported by French state funds managed by the ANR within the Investissements d'Avenir programme (Labex CAMI) under reference ANR-11-LABX-0004 and through the PROSBOT project under reference ANR-11-TECS-0017.

References

[1] N. Hungr, M. Baumann, J. Long, and J. Troccaz, "A 3-d ultrasound robotic prostate brachytherapy system with prostate motion tracking," *IEEE Transactions on Robotics*, vol. 28, no. 6, pp. 1382–1397, Dec. 2012.

[2] C. Poquet, P. Mozer, M.-A. Vitrani, and G. Morel, "An endorectal ultrasound probe comanipulator with hybrid actuation combining brakes and motors," *IEEE Transactions on Mechatronics (TMECH)*, 2013.

[3] "Koelis." [Online]. Available: http://www.koelis.fr

[4] M. Baumann, P. Mozer, V. Daanen, and J. Troccaz, "Prostate biopsy tracking with deformation estimation," *Medical Image Analysis*, vol. 16, no. 3, pp. 562 – 576, 2012.

TASK MODELLING OR MONITORING

OntoSPM: a core ontology of surgical procedure models

Bernard Gibaud[1,2], Cédric Penet[1,2] and Pierre Jannin[1,2]

[1]INSERM, UMR 1099, Rennes, F-35043, France
[2]Université de Rennes 1, LTSI, Rennes, F-35043, France

Context and objectives

Surgical procedure modeling receives growing interest in the Computer Assisted Medical Interventions (CAMI) community, due to important potential applications such as: development of new generations of surgical equipment (image-guided and information-guided surgery systems [1,2,3], context-aware visualization systems [4,5]), education and skill assessment of medical professionals, quality control, technology assessment etc. The interest of an ontological approach is now well-documented in the literature, especially related to clarifying, formalizing and standardizing the conceptual entities within a domain of discourse [6]. As for the surgical domain, such ontological modeling leads to practical implementation for storing/sharing [2], and reasoning about surgery-related entities [5].

The work presented here aims at designing a generic ontological model of the surgical procedure models' domain (core ontology called OntoSPM), suitable to be easily extended to cover the many sub-domains of CAMI, thus facilitating the design of such application ontologies in the future, and their implementation in surgical assistance equipment and data management systems.

Methods

The general approach used to design this ontology follows the general principles described in the Ontology Summit 2013 Communiqué [7], highlighting the need of ontology evaluation throughout the whole design process, especially through the documentation of use cases and competency questions.

The OntoSPM generic model is inspired by previous modeling work [1,2,3], complemented with the analysis of two detailed application domains (surgery of brain tumors, cataract surgery by phacoemulsification) initially documented as structured descriptions based on [1,2], and available as Excel sheets. Common entities and relationships were first identified, then modeled as generic OntoSPM entities. As much as possible, existing well-recognized ontological sources were reused. In particular, BFO (Basic Formal Ontology) [8] was used as a common ontological foundation, thus providing most of the basic entities (continuants, roles, occurrents, processes, etc.) and relationships (e.g. partinomy, inherence of qualities, participation in processes, realization of roles, etc).

Results

Our OntoSPM ontology puts emphasis on processes involved in surgical procedures, at various levels of granularity, from the complete procedure down to elementary actions performed by human or automated system actors (e.g. software). Currently, our efforts were primarily focused on modeling elementary actions, distinguishing physical actions affecting physical objects from conceptual actions and interactions (e.g. language acts). A particular attention was devoted to the modeling of roles, e.g. to distinguish: *human actor* (e.g. scrub nurse, surgeon or assistant surgeon), denoting the participation of a human in some process, *instrument effector*, denoting the instrument role played by

some physical object (e.g. scalpel, scissors) and *human effector*, featuring which precise part of an human is actually involved (e.g. right hand of the surgeon). Roles were modeled by specializing the role entity of BFO (*bfo:role*), as well as the relation connecting this role with some process realizing this role (*bfo:realized-in*), knowing that in BFO a role is modeled as a realizable entity.
OntoSPM currently contains 191 classes and 55 relations. It is represented in OWL 2 [9], the major ontology language of the web.

Discussion
This work allowed representing most conceptual entities involved in our two exemplary use cases (brain tumor surgery, cataract surgery). Many interesting modeling issues were raised. One of them deals with finding a reasonable tradeoff in characterizing actions and procedure steps to which they contribute: indeed such characterization enrich their description but might compromise reuse due to potential local variations.
The major current limitations of the proposed model are the following. Firstly, the model describes *performed* procedures, according to a simple class - instance model (instances actually represent procedures that occurred in real life, and classes model their common properties). Therefore, the model is not suitable for representing *plans* of future procedures, which might yet be needed, e.g. for surgery planning or during surgery. Secondly, the model currently adopts a simplistic modularization scheme, with a single OntoSPM module, imported by multiple more specialized application ontology modules (e.g. for cataract or brain tumors surgery domains). It is quite clear that, for example, anatomy-related entities should be gathered in a dedicated module, extracted from some reference ontology such as the Foundational Model of Anatomy (FMA).

Conclusion and perspectives
OntoSPM provides an interesting starting point for projects aiming at : (1) designing application ontologies dedicated to specific surgical procedures, (2) designing database schemas for storing detailed procedure descriptions, (3) or implement generic software for recording such procedures (e.g. from video recordings). The next steps of the project will first fill the gaps previously mentioned, e.g. regarding interaction between human actors and software actors. Another important extension will concern procedure plans and their relations with performed procedures.

Acknowledgements
This work is part of the S3PM project and has received a French government support granted to the CominLabs excellence laboratory and managed by the National Research Agency in the "Investing for the Future" program under reference ANR-10-LABX-07-01.
The authors warmly thank Charles Garraud (B-com, Cesson-Sévigné) for interesting feedback on early versions of the ontology and Guy Cazuguel and coll. (Inserm LATIM, Brest) for providing detailed documentation about the cataract surgery use case.

References
[1] P. Jannin, M. Raimbault, X. Morandi, L. Riffaud and B. Gibaud. Models of surgical procedures for multimodal image-guided neurosurgery. *Journal of Computer Assisted Surgery* (2003) 8(2) 98-106.
[2] P. Jannin and X. Morandi. Surgical models for computer-assisted neurosurgery. *Neuroimage* 37 (2007) 783-791.

[3] R. Mudunuri, O. Burgert and T. Neumuth. Ontological Modelling of Surgical Knowledge. In proceeding of: Informatik 2009: Im Focus das Leben, Beiträge der 39. Jahrestagung der Gesellschaft für Informatik e.V. (GI), Lübeck.
[4] N. Padoy, T. Blum, S.A. Ahmadi, H. Feussner, M.O. Berger and N. Navab. Statistical modeling and recognition of surgical workflow. *Medical Image Analysis* 16 (2012) 632-641.
[5] D. Katic, A.L. Wekerle, J. Görtler, P. Spengler, S. Bodenstedt, S. Röhl, S. Suwelack, H.G. Kenngott, M. Wagner, B. Müller-Stich, R. Dillmann and S. Speidel. Context-aware augmented reality in laparoscopic surgery. *Computerized Medical Imaging and Graphics* 37 (2013) 174-182.
[6] I. Horrocks. Ontologies and the semantic web. *Communications of the ACM*, (2008), 51(12), 58-67.
[7] F. Neuhaus, A. Vizedom *et al*. Ontology Summit 2013 Communiqué: Towards ontology evaluation across the life cycle. *Applied ontology* (2013) 8(3) 179-194.
[8] P. Grenon and B. Smith. SNAP and SPAN: Towards Dynamic Spatial Ontology, *Spatial Cognition and Computation* (2004), 4(1), 69-103.
[9] P. Hitzler, M. Krötzsch, B. Parsia, P.F. Patel-Schneider and S. Rudolph (editors). OWL 2 Web Ontology Language Primer (Second edition) http://www.w3.org/TR/owl2-primer/

Analysis of dose monitoring uncertainties for prostate adaptive radiation therapy using a FEM-based pelvic numerical phantom

M. Nassef [1,2], A. Simon [1,2], G. Cazoulat [1,2], C. Lafond [3], O. Acosta [1,2], J. Balosso [4], Renaud de Crevoisier [1,2,3], P. Haigron[1, 2]

[1] Université de Rennes 1, LTSI, Rennes, F-35000, France.

[2] INSERM U 1099, Rennes, F-35000, France.

[3] Department of Radiotherapy, Centre Eugène Marquis, Rennes, F-35000, France.

[4] Department of Radiation Oncology, Grenoble University Hospital, Grenoble, F-3800 France

Context

A radiation therapy (RT) treatment is classically planned using a unique planning Computed Tomography (CT) image and delivered in several treatment sessions, called fractions. In case of prostate cancer treatment, several anatomical variations such as prostate displacement and bladder or rectum deformations occur during the course of treatment. The well optimized Intensity Modulated RT (IMRT) planned dose may therefore not correspond to the actual delivered dose, with a potential clinical impact. Image-guided radiotherapy (IGRT) devices, such as the cone-beam CT (CBCT), offer the possibility of visualizing the pelvic anatomical structures at each fraction, enabling prostate repositioning and improving therefore prostate coverage. The consideration of organ at risk (OAR) deformations is however a lot more complex. Based on the non-rigid registration of the CBCT images with the planning CT, some dose monitoring methods have been proposed to estimate/monitor the cumulated dose actually received in these structures. The cumulated dose could be therefore compared to the planned dose and be used to guide an adaptive radiotherapy strategy[1]. The dose accumulation accuracy relies on the ability to precisely estimate local (i.e. voxel by voxel) anatomical correspondences in the context of large deformations using the low-contrasted CBCT images. The objective of this work was to quantify the dose monitoring uncertainties for prostate adaptive radiation therapy. Due to the difficulty to precisely measure the dose locally accumulated in deformable structures, this is a non-trivial task. We used a pelvic numerical phantom to provide a reference in terms of locally accumulated dose.

Method

- *Numerical phantom*

A finite element method (FEM)-based numerical phantom has been developed, providing a set of synthetic CT images simulating plausible deformations of the main male pelvic organs[2]. This included the prostate, seminal vesicles and the two main OARs surrounding the prostate bladder and rectum. Based on organ delineations from a typical patient with empty bladder and rectum, the structures were modeled in ANSYS Design Modeler®. Mechanical properties were assigned to each organ based on the literature. Different contact properties were defined between each organ and its neighborhood as bounded, frictionless, or no separation. Boundary conditions were based on clinician observations and simulation studies (see Figure1). To obtain a realistic behavior of the whole pelvis, different elastic supports have been added in order to simulate the tissues surrounding the main organs: on the inferio-anterior part of the bladder; to the first centimeter of the rectal wall which is surrounded by muscle fibers; in the posterior part of the rectum to limit its expansion in the direction of the spine. The parameter values of these conditions were adjusted to obtain a typical behavior, particularly for an anterior-posterior displacement of the prostate to up to 9mm. Based on previous study, the OAR internal pressure was modified, with values ranging from 0 to 5kPa and 0 to 2kPa for the bladder and rectum, respectively, to obtain classical variations of the bladder and rectum volumes (ranging from 97.1cm^3 to 294.0cm^3 and 52.4cm^3 to 84.0cm^3, respectively). From the FEM phantom model, 16 synthetic CT scan were constructed to simulate a data set composed of one planning and 15 per-treatment CT. Since Deformable Image Registration (DIR) accuracy may depend on the planning CT's organ configuration, each image was successively considered as the planning CT. The reference deformation fields, establishing the simulated anatomical correspondences between all 16 CT images, were provided by the numerical simulation.

Philips Pinnacle® Treatment Planning System (TPS) Version 9.2 was used to generate a step–and-shoot IMRT treatment plan giving the Planned Dose Distribution (PDD) based on synthetic CT images of the numerical phantom (see Figure2). The dose at each fraction was approximated by the PDD shifted to the prostate isocenter. A reference cumulated dose distribution (RCDD) was calculated by applying the known deformation fields given by the numerical simulation to each per-treatment dose distribution.

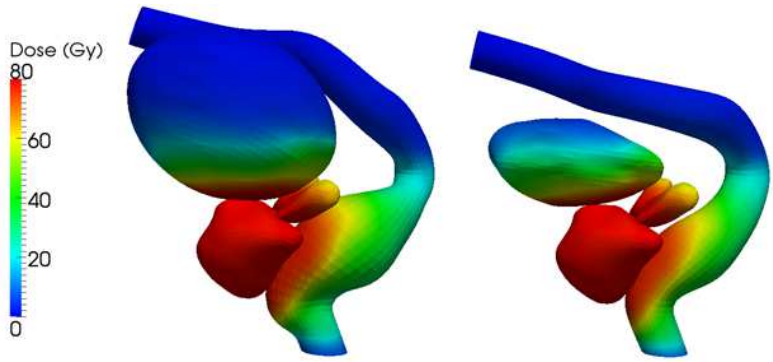

Figure 1: Representation of the organ surfaces of the pelvic finite element method-based numerical phantom at two different simulated fractions, with the associated dose for a given treatment plan

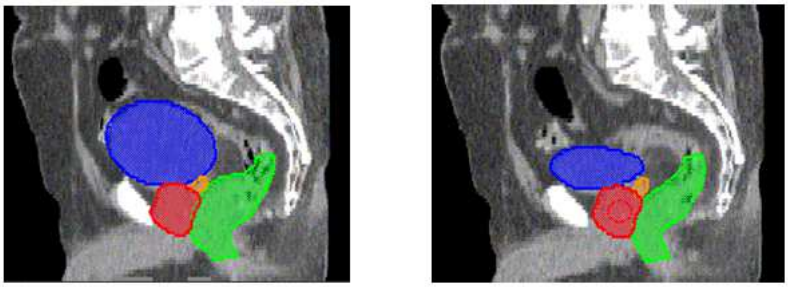

Figure 2: Representation of the synthetic CT images of the pelvic finite element method-based numerical phantom at two different simulated fractions.

- *Evaluated dose monitoring method*

Based on the planning CT with the associated PDD and the per-treatments images associated with their dose distribution, the goal of the dose accumulation process was to estimate the cumulative dose distribution (ECDD) in the planning anatomy. The dose accumulation method relies on the DIR of the per-treatment images toward the planning CT scan[3]. The DIR method was the demons registration algorithm method using the contours of the structures of interest (prostate, rectum, and bladder). A signed distance map, representing for each voxel the Euclidian distance to the considered organ, was generated for all organs of interest. The distance maps of each organ were registered to the corresponding distance maps obtained for the planning CT. The Dice score of the registered OARs were calculated. Deformations fields obtained with DIR were applied to each per-treatment dose distribution using trilinear interpolation for resampling dose distribution. The ECDD could be calculated on the planning CT by adding each deformed dose distribution

Results

The Dice scores following DIR were 0.97±0.01 and 0.98±0.01 for the bladder and rectum, respectively. The Dose Difference (DD) was defined as the differences between PDD and ECDD. The dose accumulation uncertainty (DAU) was defined by the differences between the RCDD and the ECDD. Dose Volume Histogram (DVH, i.e the percentage of organ's volume receiving at least a given dose) points were analyzed, especially the points used to optimize the plan as defined by the RTOG (Radiation Therapy Oncology Group).

For mean dose to the bladder, DD was 10Gy (16.7Gy maximum) with a DAU of 1.3Gy. For the rectum, DD was 2.8Gy (4.5Gy maximum) with a DAU of 1.4Gy. Volume differences along the whole dose-volume histogram between PDD and ECDD ranged from +19.8% to -23.5% and +12.4% to -9.7% for the bladder and rectum, respectively. The dispersion of the DAU ranged from +5.1 % to -12.7% for the bladder, and from +7.1 % to -5.5% for the rectum.

Conclusion

Our study quantified dose accumulation uncertainty using a pelvic numerical phantom. The DAU calculated were smaller than the observed DD. These findings support the interest and the capability of monitoring the cumulative dose in the bladder and rectum during prostate IMRT-IGRT treatment to guide adaptive radiotherapy strategy within a dose-guided framework. The quantified uncertainties will be compared to dose differences (between planned and accumulated dose distributions) computed on real patients.

Acknowledgment

This work was partly supported by the French ANR within the Investissement d'Avenir program (Labex CAMI) under reference ANR-11-LABX-0004

References

[1] Cazoulat G, Lesaunier M, Simon A, Haigron P, Acosta O, Louvel G, Lafond C, Chajon E, Leseur J, de Crevoisier R. From image-guided radiotherapy to dose-guided radiotherapy. Cancer/Radiothérapie. 2011; 15(8):691-8.

[2] Rubeaux M, Cazoulat G, Duménil A, Lafond C, Acosta O, De Crevoisier R, Simon A, Haigron P. Numerical Phantom Generation to Evaluate Non-Rigid CT/CBCT Registration Algorithms for Prostate Cancer Radiotherapy. MICCAI - workshop on Image-Guidance and Multimodal Dose Planning in Radiation Therapy; 2012; p. 74-81.

[3] Cazoulat G, Simon A, Dumenil A, et al. Surface-Constrained Nonrigid Registration for Dose Monitoring in Prostate Cancer Radiotherapy. IEEE Trans Med Imaging 2014.

DEVICES

Bidimensional Localization of Active Ultrasound Markers

Guillaume Custillon[1], Sandrine Voros[1], Philippe Cinquin[1], An Nguyen-Dinh[2], Alexandre Moreau-Gaudry[1]

[1]Université Joseph Fourier-Grenoble 1, CNRS, INSERM CIT803, TIMC-IMAG, UMR 5525, Grenoble, France

[2]VERMON, 180 rue Général Renault, BP3813, 37038 Tours Cedex, France

Introduction

During laparoscopic surgeries, the structures targeted by the surgical intervention appear as the surgeon goes along the dissection and can be hidden beneath organs surfaces. Such "hidden" structures can be visualized thanks to the ultrasound (US) modality. Fusing the laparoscopic and ultrasound modalities during a laparoscopy could help the surgeon in the intra-operative planning of his surgical intervention, by improving the visualization of interesting structures.

Such a fusion is based on the ability to identify reference points in both modalities, which is very challenging. To facilitate this identification, we focus in this paper on presenting an innovative ultrasound marker that can be localized with respect to a custom-designed trans-urethral ultrasound probe. Such a marker can be used during a prostatectomy as depicted in Fig. 1.

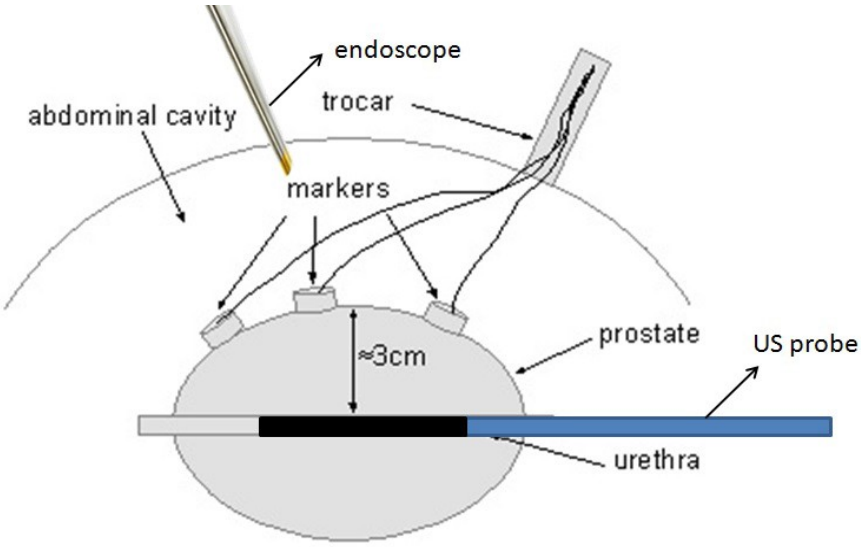

Fig. 1. Drawing of a prostatectomy where US markers, localized by the probe, are seen by an endoscope.

Material

We used an Ultrasonix SonixTouch ultrasound scanner. The main advantage of this system is its ability to design custom applications where all the parameters of the piezoelements of a probe can be controlled (e.g. trigger of the ultrasound wave, delay…).

This machine is used to control an innovative trans-urethral ultrasound probe. This probe is composed of 124 elements, is 25.42 mm long and works at a central frequency of 7.66 MHz, with a

-6dB bandwidth of 5.58 MHz.

The active marker is a small cylinder of 5 mm in height and 5 mm in diameter, containing a piezoelectric monoelement whose diameter is 200 μm. The central frequency of the marker is 5 MHz, with a -3dB attenuation bandwidth of 1 MHz, and its field of emission is a 60° cone. Used as a pure acoustic transmitter, its isotropic behavior makes it suitable for localization, whatever its position relative to the probe. The marker is directly plugged-in to the connector of the probe.

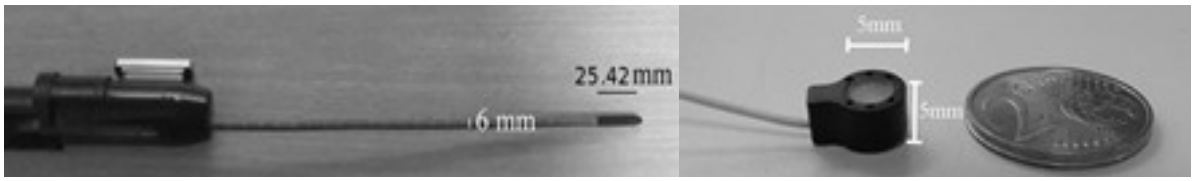

Fig. 2. Left: ultrasound probe. Right: ultrasound marker

Methodology

The marker is used as a "pure acoustic transmitter", and the probe as a "pure acoustic receiver". The localization of the marker is based on the measure of the time of flight of the US signal between the marker and the probe. The US characteristics of the marker and the probe are compatible with the expected distance of the marker and the probe in a prostatectomy configuration: typically less than 5 cm.

By assuming this localization can be real-time, we can switch the probe mode from "receiver", to perform a localization, to "emitter / receiver" for the creation of a standard image of the prostate. If the marker is switched-off during this imaging phase, it will be invisible in the resulting image.

By using a 2D probe, we can only retrieve two coordinates of the marker. Consequently, the marker can only be localized in the US plane of the probe. To localize the marker in 3D, we have to orient the US plane in the direction of the marker (the orientation corresponds to the third coordinate) and to compute the coordinates of the marker in the plane.

The marker emits ultrasound pulses, and each element of the probe detects parts of the wave emitted by the marker. The further the marker is from an element, the longer the time of flight of the ultrasound waves is. By comparing the time of flight between each element of the probe, we can compute the 2D marker coordinates. This technique is similar to the GPS localization.

Experiment and Results

The active marker and the ultrasound probe were placed in a water tank, facing each other. We localized the marker within the probe's plane; for this, we rotated manually the probe around its axis until we obtained a maximal intensity in the ultrasound image.

The marker was displaced in the probe's plane thanks to an XY micrometric platform. For each position of the marker, the emitted signals were recorded by the probe and the marker's coordinates were computed.

To compute the error made with our localization method, we recorded regularly-spaced (1 mm in each direction) positions of the marker with the micrometric platforms. We obtained the coordinates of the marker expressed in the frame of reference of the probe (the result of the measure) and the micrometric platform (the values read on the micrometers). Then we performed a rigid registration between these two frames of reference to compare the measures with the micrometric ground truth. The distance between each corresponding points was computed to estimate the root-mean-square (RMS) error over our measures.

As a result, we obtained an average RMS localization error of 232 μm ± 127 μm on the whole measure set (60 measurements).

Discussion and Conclusion

This experiment demonstrates the possibility to localize an active ultrasound marker in 2D in ideal conditions, *ie* when the marker faces the probe. However the reality is more complex: in a 3D world, the marker is not necessarily in the image plane of the ultrasound probe. This case was described previously: a rotation of the probe around its axis to find the maximal energy detected will enable the placement of the marker in the image plane.

The marker presented in this work has two advantages: it allows a decoupling of the marker's localization and the imaging of the scene (the marker's signal doesn't pollute the image and vice-versa); it can emit ultrasound waves over a large section of space (60°). It makes the marker's detection possible even if it is not directly in front of the probe. Its size make it compatible with laparoscopic surgery since it can be inserted through trocars. The marker's cables could be bothering during surgery, however the registration could be performed at specific moments of the procedure. The integration to the workflow will need to be studied.

The localization precision is comparable to other localization techniques developed by [1, 2] which are 230 µm ±110 µm and 360 µm ±160 µm.

Finally our localization method can be computed in less than one second, and thus allows near real-time localization. This is essential for a per-operative application: the surgeon does not have to wait for the results and can work in optimal conditions. In future work, with a motorized ultrasound probe, we should be able to localize several markers in three dimensions. The time required for the 3D localization will depend on the rotation of the probe. 3D localization will enable these markers to be used as identifiable points in ultrasound and video imagery, allowing the virtual reconstruction of the prostate.

Acknowledgment

This work was partly supported by the French ANR within the Investissements d'Avenir program (Labex CAMI) under reference ANR-11-LABX-0004.

Bibliography

1. Merdes, C.L., Wolf, P.D.: Locating a catheter transducer in a three-dimensional ultrasound imaging field. IEEE Trans. Biomed. Eng. 48, 1444–1452 (2001).
2. Mung, J., Vignon, F., Jain, A.: A Non-disruptive Technology for Robust 3D Tool Tracking for Ultrasound-Guided Interventions. In: Fichtinger, G., Martel, A., and Peters, T. (eds.) Medical Image Computing and Computer-Assisted Intervention – MICCAI 2011. pp. 153–160. Springer Berlin Heidelberg, Berlin, Heidelberg (2011).

Dental implant stability assessment using quantitative ultrasound

Romain Vayron, Guillaume Haiat
CNRS, Laboratoire MSME UMR CNRS 8208, 94010 Creteil

I) Introduction

Dental implants are widely used clinically and have allowed considerable progresses in oral and maxillofacial surgery, to restore missing teeth. However, implant failures, which may have dramatic consequences, still occur and remain difficult to anticipate [1].
Accurate measurements of implants biomechanical stability are of interest since they could be used to improve the surgical strategy by adapting the choice of the healing period to each patient. Empirical methods based on palpation and patient sensation are still used by dental surgeons to determine when the implant should be loaded with the prosthesis because it remains difficult to monitor bone healing in vivo [2]. Accurate noninvasive quantitative methods capable of assessing implant stability could be used to guide the surgeons and hence to reduce the risk of failure. The implant stability is determined by the quantity and biomechanical quality of bone tissue around the implant. Assessing the implant stability is a difficult multiscale problem due to the complex heterogeneous nature of bone and to remodeling phenomena.
Different approaches have been suggested in the past to assess the implant stability in vivo: X-ray radiography, µCT, or magnetic resonance imaging (MRI), but these techniques are not adapted due to diffraction phenomena (presence of titanium). Biomechanical methods have been developed, their main advantage consisting in the absence of ionizing radiation, inexpensiveness, portability and noninvasiveness, Periotest (Bensheim, Germany) and Osstell (Gothenburg, Sweden) for example. The most commonly used biomechanical technique is the resonance frequency analysis (RFA), which consists in measuring the first bending resonance frequency. However, the RFA cannot be used to identify directly the bone-implant interface characteristics.
The use of quantitative ultrasound (QUS) as an alternative method to assess the implant biomechanical stability has been suggested. The principle of the measurement relies on the dependence of ultrasonic propagation within the implant on its boundary conditions, which are related to the bone-implant interface biomechanical properties [3]. An in vitro preliminary study was carried out by our group with a prototype titanium cylinder shaped implant inserted in bone tissue, showing the feasibility of the approach [3], [4].

The objective of this study is to investigate the potentiality of a quantitative ultrasound method to assess the biomechanical stability of a dental implant. The measurement consists in using a 10 MHz contact transducer located at the implant extremity, as shown in Fig. 1. For each ultrasound measurement, a quantitative indicator I is derived based on the time variation of the amplitude of the *rf* signal. Three experiments were realized to validate the proof of concept.

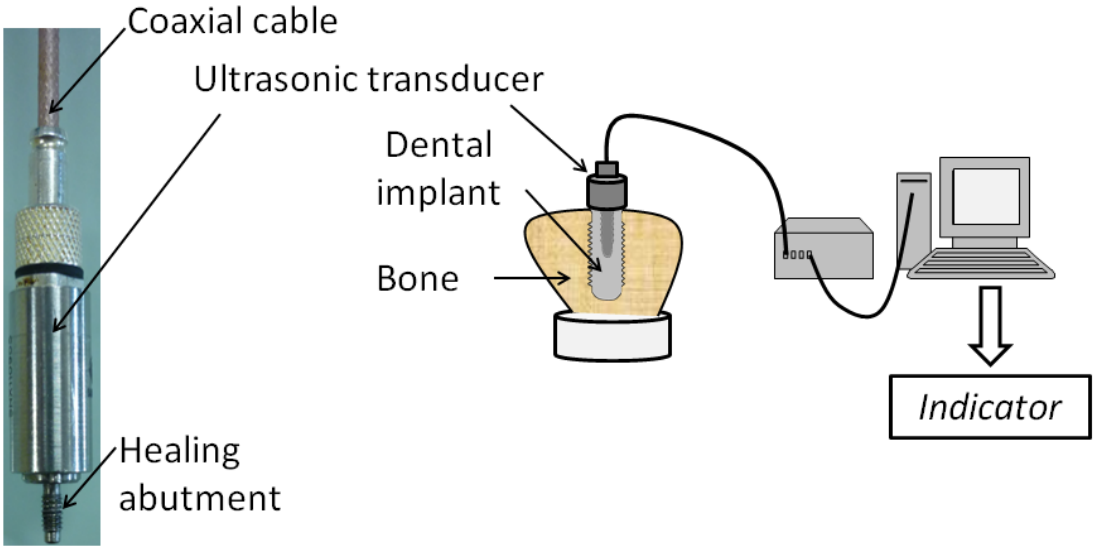

Fig. 1 Schematic description of the ultrasonic experimental set-up with the use of handy torque gauge. The ultrasonic transducer is screwed into the implant. The dental implant is completely inserted in the bone sample.

II) Influence of cyclic loading on the ultrasonic response of an implant inserted in a biomaterial

The use of tricalcium silicate-based cement (TSBC) as bone substitute material for implant stabilization is promising. However, its mechanical behavior under fatigue loading in presence of a dental implant was not reported so far because of the difficulty of measuring TSBC properties around a dental implant in a non destructive manner. The aim of this study is to investigate the evolution of the 10 MHz ultrasonic response of a dental implant embedded in TSBC versus fatigue time. Seven implants were embedded in TSBC following the same experimental protocol used in clinical situations in order to assess the reproducibility of the measurements. A torque gauge was used to control the torque used to screw the transducer into the implant. One implant was left without any mechanical solicitation after its insertion in TSBC. The ultrasonic response of all implants was measured during 24 hours using a dedicated device. An indicator I based on the temporal variation of the signal amplitude was derived and its variation as a function of fatigue time was determined. The indicator is related to the integral of the amplitude of the envelop of the rf signal. The results show no significant variation of I as a function of time without mechanical solicitation for the sample considered (), while the indicator significantly increases ($p<10^{-5}$, $F=199.1$) at an average rate of 2.2 h^{-1} as a function of fatigue time. The increase of the indicator is due to the degradation of the Biodentine-implant interface, which induces an increase of the impedance gap at the implant surface [5].

III) Influence of bone quantity in contact with the implant surface

The objective of this study is to investigate whether quantitative ultrasound (QUS) technique can be used to assess the amount of bone in contact with dental implants.

Ten implants are initially completely inserted in the proximal part of a bovine humeral bone sample. The 10 MHz ultrasonic response of the implants is then measured and an indicator I is

derived based on the amplitude of the *rf* signal obtained. Then, the implants are unscrewed by 2π radians and the measurement is realized again. The procedure is repeated and the indicator I is derived after each rotation of the implants. Analysis of variance (ANOVA) ($p<10^{-5}$) tests revealed a significant effect of the amount of bone in contact with the implant on the distribution of the values of I. The results show the feasibility of QUS techniques to assess implant primary stability in vitro [6].

IV) Effect of osseointegration on the implant ultrasonic response

The 10 MHz ultrasonic response of the implant was measured just after the implantation using the same device positioned at the emerging surface of the dental implant. The measurements were realized again before the sacrifice of the rabbits with the same device. An indicator $\widetilde{I}$ was derived based on the amplitude of the *rf* signal obtained for each configuration. The average value of the relative variation of the indicator $\widetilde{I}$ obtained after initial surgery and after the corresponding healing period varies between 7 and 40%. A Kruskal-Wallis test ($p<0.01$) revealed a significant decrease of the value of the indicator $\widetilde{I}$ as function of healing time. The results show that the ultrasonic response of a dental implant varies significantly as a function of healing time. The indicator $\widetilde{I}$ was significantly correlated ($R^2=0.45$) with the bone-implant contact ratio measured with histology [7]. The results show that the ultrasonic response of a dental implant varies significantly as a function of healing time [8-10].

Acknowledgements

This work has been supported by French National Research Agency (ANR) through EMERGENCE program (project WaveImplant n°ANR-11-EMMA-039) and through the PRTS program (project OsseoWave ANR-13-PRTS-0015).

References

[1]G. Haiat, et al., *Annu Rev Biomed Eng.*, **11**; pp. 187-213, 2014.
[2]V. Mathieu, et al., *J. Biomech.* , **47**, pp. 3-13, 2014.
[3]V. Mathieu, et al., *UMB*, **37**, pp. 262-270, 2011.
[4]V. Mathieu, et al., *JASA*, **129**, pp. 4062-4072, 2011.
[5]R. Vayron, et al., *J. Biomech.* , **46**, pp. 1162-1168, 2013.
[6]R. Vayron, et al., *Ultrasound Med Biol*, in press.
[7]R. Vayron, et al., *J Biomech*, in press
[8]V. Mathieu, et al., *J Biomech Eng-T Asme*, **133**, pp. 021006-6, 2011.
[9]R. Vayron, et al., *J Biomech eng*, **134**, pp. 021007, 2012.
[10]R. Vayron, et al., *Phys Med Biol.*, **59**, pp.1389-406.

An innovative NiTi based stent as an emergency treatment for acute urinary retention in case of benign prostatic hyperplasia

G.Antherieu[a,*], Y. Payan[a], D. Favier[a], N. Connesson[a], P. Mozer[b]

[a] *Laboratoire TIMC/IMAG, UMR CNRS 5525, Faculté de Médecine Domaine de la Merci, La Tronche, France*
[b] *ISIR/service d'urologie, hôpital de la Pitié Salpêtrière, 37, boulevard de l'Hôpital, 75013 Paris, France*

1. Introduction

As life expectancy is increasing, population is getting older. Ageing diseases are thus becoming more and more numerous. Benign Prostatic Hyperplasia (BPH) is a pathology mostly striking elder men : 40% of men over 50 years old show evidences of BPH [1]. BPH consists in an anarchic proliferation of prostatic stromal and epithelial tissues [2], resulting in an increase of the prostate volume. Since the prostatic urethra is surrounded by the prostate, BPH may eventually obstruct it, leading to Acute Urinary Retention (AUR). AUR is one of the most problematic complications of BPH, and requires an emergency treatment. Today, the first line treatment of AUR consists in catheterization. However, this procedure comes with various drawbacks :

- it is uncomfortable, and often painful,
- it reduces the patient autonomy and social life (due to the catheter and drainage bag),
- it may lead to Nosocomial Urinary Tract Infection (NUTI).

Urinary infection is a key issue, since catheterization is responsible for 80% of NUTI [3]. It is worth noting that infection risk increases by 3% to 10% each passing day [4]. Patients presenting AUR due to BPH are often old, polypathologic, and thus more likely to develop complications due to NUTI. Beyond the medical concern, NUTI is also responsible for a dramatic increase of the treatment costs.

To circumference these issues, an innovative NiTi based stent has been developped as an alternative to catheterization.

2. Urethral stenting and shape memory alloys

First intra urethral stentings began around 1985, notably with the *Prostakath*® prosthesis [5]. Various urethral stents have been developped ever since. Urethral stenting enables to treat AUR, with a minimized infection risk and discomfort. However, due to their complex and time-consuming implantation mechanism (for instance *Memokath*® stent requires sterile hot/cold water for its expansion/removal), existing conventional stents are inconvenient as an emergency treatment, and thus remain scarcely used.

The aim of the work introduced is this paper is to provide a suitable solution for the emergency treatment of AUR. In order to fulfil the clinical needs, this stent presents different innovative features :

- at least two distinct shape memories triggered successively by increasing its temperature : (1) an extension phase to release the urethra, and (2) a contraction phase to easily remove the stent,
- a bio-compatible silicone coating. This coating prevents the stent, heated using Joule effect, from damaging surrounding tissues,
- a global implantation procedure suitable for emergency treatment.

Double shape memory effect is achieved using NiTi shape memory alloy (SMA). SMA show interesting properties, as a rough description [6] :

- Through thermal treatments, SMA is given a transition temperature (T_{trans}), associated to the "set shape" of the alloy.

∗. Corresponding author
Email address: gabriel.antherieu@imag.fr (G.Antherieu)

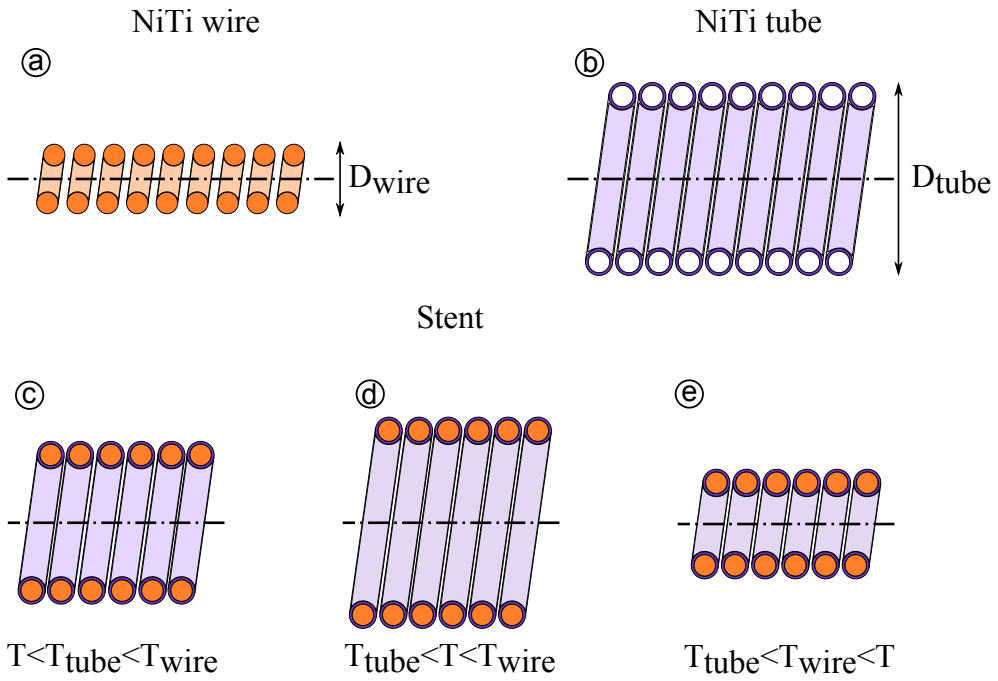

FIGURE 1: The double shape memory stent : an helical wire (a) inserted into an helical tube (b) ; and its various configurations (c,d,e)

- For $T < T_{trans}$, SMA is in martensitic state, and can be easily pseudo plastically deformed (SAM shows pseudo-plasticity around 1% strain).
- For $T > T_{trans}$, SMA austenitic state is triggered and presents super elasticity (up to 12%).
- When heated above T_{trans}, an initially deformed sample almost instantly recovers its set shape, if its shape is unconstrained : this is the shape memory effect.

3. Stent design

To achieve a two shape memory stent, a specific design was developed. (1) A NiTi wire, diameter 0.5mm, was given for shape memory an helical shape at diameter D_{wire}, and a $T_{trans} = T_{wire}$ (Fig 1,a). (2) A NiTi tube, inner diameter=0.5mm and wall thickness=0.05mm, was given for shape memory an helical shape at diameter $D_{tube} > D_{wire}$, and a $T_{trans} = T_{tube} < T_{wire}$ (Fig 1,b). The wire was then inserted inside the tube.

The stent obtained this way shows three different behaviours and shapes, according to its temperature T :

- For $T < T_{tube} < T_{wire}$, both wire (1) and tube (2) are in martensitic state. The stent can be easily deformed (Fig 1,c). Notably, the stent can easily be rolled around a specific insertion catheter.
- For $T_{tube} < T < T_{wire}$, the tube (2) shape memory is triggered while the wire (1) remains in martensitic state. The stent is thus expanded, and releases the urethra (Fig 1,d). The patient is then able to return home during HBP treatment, without discomfort or NUTI risk.
- For $T_{tube} < T_{wire} < T$, the wire (1) shape memory is triggered. The stent collapses, allowing an easy removal (Fig 1,e).

An alternative solution to obtain a double shape memory is to use a single wire, with two distinct set shapes associated to two distinct T_{trans}. This can be achieved using local thermal treatment, such as laser treatment for example.

To ensure that the stent is suitable for emergency use, the activation ($T > T_{tube}$) will be made using Joule effect, a custom made insertion catheter enabling electrical contact between the stent and the power supply. In fact, currently available urethral stents are mostly activated using hot water. Consequently, the clinical staff has to heat sterilized water and then to inject it inside the stent to expand it. It is understandable that this type of activation prevents the stent from being used in emergency. Using Joule effect allows to activate the stent fastly (less than 10s), without any specific

procedure. To ensure that the urethral tissues are not burnt during activation, the stent is coated with a biocompatible silicone layer. A preliminary axis-symmetric thermal simulation provided the duration of the release operation $t_{activation} = 8s$, and the maximum temperature of the urethra $T^{max}_{urethra} = 57^{\circ}C$. This temperature can easily be reduced by increasing the thickness of the silicone coating, knowing that for the simulation the coating thickness was $0.25mm$.

4. Conclusion

A innovative NiTi based stent has been developped. This stent is meant to be used as an emergency treatment for AUR due to BPH as an alternative to catheterization. Thanks to its double shape memory effect, the stent can be easily expanded, and removed, without hurting surrounding tissues. As a consequence, this stent will reduce the risk of NUTI and associated morbidity.

5. Acknowledgement

This work was supported by French state funds managed by the ANR within the Investissements d'Avenir programme (Labex CAMI) under reference ANR-11-LABX-0004.

6. References

[1] Tom McNicholas and Daniel Swallow. Benign prostatic hyperplasia. *Surgery (Oxford)*, 29(6) :282–286, June 2011.
[2] Tom McNicholas and Stephen Mitchell. Benign prostatic hyperplasia. *The Lancet*, 361(9366) :1359–1367, April 2003.
[3] R Plowman, N Graves, J Esquivel, and J a Roberts. An economic model to assess the cost and benefits of the routine use of silver alloy coated urinary catheters to reduce the risk of urinary tract infections in catheterized patients. *The Journal of hospital infection*, 48(1) :33–42, May 2001.
[4] S Alfandari. Prévention des infections urinaires nosocomiales : effets de lâinfection urinaire nosocomiale sur la durée de séjour, le coût et la mortalité. *Médecine et Maladies Infectieuses*, 33 :247–254, September 2003.
[5] Daniel Yachia. *Stenting the urinary system*. Isis Medical Media, Oxford, 1998.
[6] K. Otsuka and X. Ren. Physical metallurgy of TiâNi-based shape memory alloys. *Progress in Materials Science*, 50(5) :511–678, July 2005.

POSTERS

Patient Specific Guides For Total Knee Arthroplasty. A Cadaveric Study.

Severine Dao Lena, Philippe Merloz

Univ Dept of Orthopaedic Surgery, Grenoble

CIC-IT, Grenoble;

Lab TIMC – IMAG, (Univ. Joseph Fourier - CNRS UMR 5525), Pavillon Taillefer - Faculté de Médecine - 38706 La Tronche cedex - France

Keywords: Total Knee Arthroplasty, Specific Guides, Coronal Alignment, Cadavers

Introduction: Coronal alignment in total knee arthroplasty (TKA), regarding the literature, seems to be a major factor in the survivorship of the components and in the functional outcome. The Patient Specific Guides (PSG), based on 3 D imaging, had been introduced in surgical process in order to improve accuracy in TKA, and to reach post operative neutral mechanical alignment. Most of the papers in the literature are based on TKA proceeded by well-experienced surgeons. In this study, all TKA have been proceeded by a resident in orthopaedic surgery in last year of training.

Objectives: Compared with standard instrumentation (SI), PSG can improve the coronal alignment of the TKA and decrease the operative time, despite the low experience of the surgeon.

Methods: Thirty-three lower limbs (from femoral head to foot) have been taken from seventeen cadavers. A pre operative CT scan of each lower limb has been realized in order to measure: HKA (hip-knee-ankle) angle, MFA (mechanical femoral angle) and MTA (mechanical tibial angle), and to plan the TKA for shaping the PSG.
17 TKAs have been implanted with PSG, 16 with SI. 54% (18/33) knees presented osteoarthritis at least on one of the three compartments. Post operatively, a further CT scan has been used to make the measures to compare the two groups. Per operatively, operative time and positioning of PSG have been recorded.

Results: Pre operatively, 66,7% (22/33) of the lower limbs were in varus, 27,3% (9/33) were in valgus and 6% (2/33) were in neutral alignment, there was no significant difference between the groups. Post operatively, the overall mechanical alignment was between 177° and 183° for 81,25% (13/16) in SI group, and 76,47% (13/17) in PSG group. The mean HKA in SI was 179,1° (±2,45), and 178° (±2,18) in PSG group, there was no significant difference between the group (p-Value: 0,17). Concerning the MFA, the percentage of outliers 90° +/- 2° was 31,25% in SI group and 35,3% in PSG group. For the MTA, the percentage of outliers was 31,35% in SI group and 17,65% in PSG group. Only the operative time was significantly lower in PSG group with a median of 43 minutes [35-47] relative to the SI group with a median of 50 minutes [43-62,5] (p-Value: 0,041).

Conclusions: In our study, PSG used by a low-experience surgeon did not demonstrate a superiority regarding the coronal mechanical alignment comparing with SI in TKA. But the use of PSG process can reduce the operative time.

3D MRI/CT NON-RIGID REGISTRATION FOR IMAGE-GUIDED PROSTATE BRACHYTHERAPY

Iyas Hamdan[a], Julien Bert[a,b], Chafiaa Hamitouche[a,b], Guillaume Dardenne[a], Dimitris Visvikis[a,b]

[a] Institut de Recherche Technologique b<>com, Rennes, France
[b] Laboratoire de Traitement de l'Information Médicale, INSERM UMR 1101, Brest, France

I. INTRODUCTION

Low dose rate brachytherapy is an intra-operative radiotherapy technique for irradiating tumors. The radiation is delivered by placing radioactive sources in close proximity to tumors under the guidance of transrectal ultrasonography (TRUS). In brachytherapy, dose distribution is routinely calculated with the TG43 formalism which considers patients as water boxes. A personalization of patient dose planning that considers tissues heterogeneity has been recently developed using Monte Carlo simulations based on pre-operative 3D computed tomography (CT) images [1]. Therefore, optimal positions of radioactive sources are expressed in CT reference, while the insertion is done under TRUS guidance. To transfer this information between the two modalities, a registration between 3D ultrasound (3D-US) and CT is necessary. However, a robust and direct registration between those modalities is hardly possible since they both provide low contrast for soft tissues.

Recently, [2] proposed an efficient registration between magnetic resonance imaging (MRI) and 3D-US since MRI offers better characterization of soft tissues than CT. Therefore, introducing MRI as an additional modality could facilitate the 3D-US/CT registration. Moreover, it would help clinicians during the procedure since segmentation (of prostate and organs at risk) and accurate seeds placement are required. Within this context, a 3D MRI/CT registration is needed.
Generally, CT and MRI are not acquired simultaneously (in our case, images were acquired 3 months apart). Because of this interval, the prostate suffers from deformations caused by the evolution in size, different filling of the bladder and rectum as well as patient movements [3]. To overcome this problem, a non-rigid registration is necessary.

Only few studies are dedicated to prostate brachytherapy, most of them are based on rigid-body registration and require manual segmentation or visual identification of landmarks [4]. Other studies propose non-rigid registration based on monomodal or multimodal imaging but with modalities other than MRI/CT [5,6].

In this study, we propose a 3D MRI/CT registration for image-guided prostate brachytherapy where no manual segmentation is required. The proposed method uses a first rigid registration to initialize a second non-rigid one. In order to improve the robustness and the computation time as well as prevent unwanted objects present in the image from affecting the process, the registration was constrained to a region of interest (ROI).

II. MATERIALS AND METHODS

A. Determination of ROI

A first step consisted in manually choosing a slice from the axial view where the prostate and different bone structures (femurs, ischium and pubic symphysis) can be visualized. Then, CT voxels' values in Hounsfield Units were used to extract the bone structures by thresholding the image at the corresponding value (700 HU) [7].
The next step was to automatically define the ROI from this binary image. First, morphological operations and connected-component labelling were applied to detect and identify different regions in the image. Afterwards, a bounding box was drawn around pelvic structures in the image, which fulfill the rigid-body hypothesis (since pelvis doesn't deform between the two acquisition), defining the pelvic ROI for the rigid registration. Another box was drawn around the prostate only defining the prostate ROI for the non-rigid registration.

B. MRI/CT registration

Considering that images are from different modalities, an intensity-based registration is considered with the mutual information as similarity measure [8]. The transformation between MRI and CT was found iteratively using a regular step gradient descent optimizer in order to reach the maximum of the mutual information.

For the initial rigid registration, we used the pelvic ROI and we chose an affine model; i.e. rigid plus scaling and shearing. Afterwards, the transformation we found was applied on the CT image, and was used as an initialization for the non-rigid registration which was restricted to the prostate ROI. Concerning the non-rigid registration, a cubic B-Spline function was used. B-Spline computes deformation values of some control points located on a grid called B-Spline grid. Then, by interpolating these values to every point of the image, we get the deformation field that spatially relates the two images.

The final transformation was found iteratively using the same optimizer as before, and then it was applied on the deformed CT image leading to the final registration images.

III. EVALUATION STUDY

The proposed method was validated using one set of clinical patient data. CT and MRI (T1-weighted) pelvic images were pre-operatively acquired with 3 months in between. The CT data size was 512x512x150 voxels of 0.78x0.78x2 mm^3, while MRI was 640x640x44 voxels of 0.47x0.47x5.95 mm^3. After some experiments, we found that 8 control points for the B-Spline grid provided the best result for the non-rigid registration.

Considering that a ground truth for the registration was not accessible, the assessment was done using a segmentation approach. A contour around the prostate was made by a physician on both MRI and CT images after the rigid registration alone and after the final registration (rigid+non-rigid). These contours were used to find the oriented bounding box (OBB) within which the prostate lies in both images. OBBs in both images were compared leading to a quantitative evaluation criterion.

IV. RESULTS

The prostate boundaries overlap between images before and after the non-rigid registration is illustrated in Fig.1 showing a good correspondence and a continuity of the prostate contour in the final registration images. This visual assessment demonstrates that the proposed method was able to register MRI and CT images in a prostate imaging context.

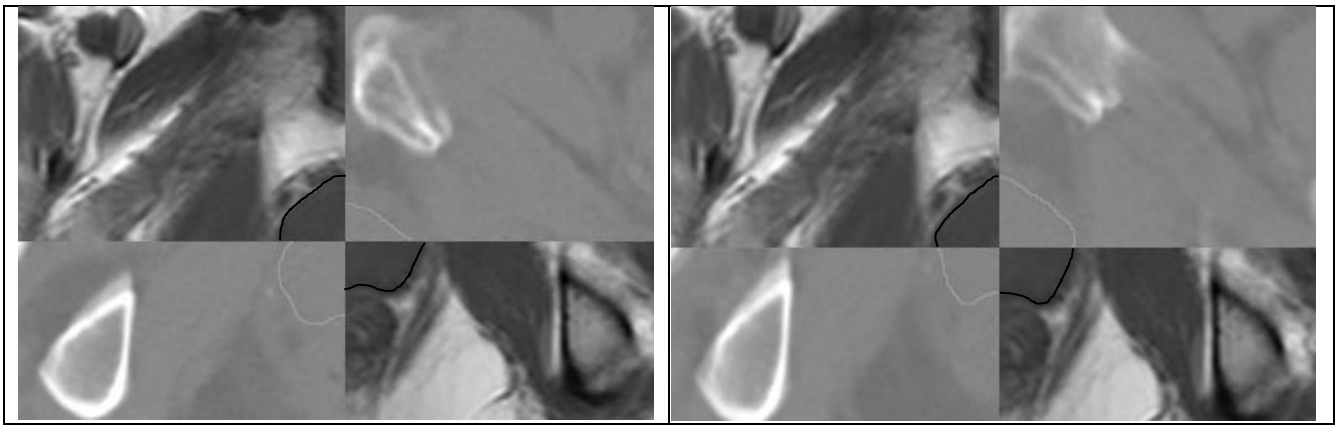

Fig.1: Prostate boundaries overlap; (left) after rigid only and (right) after final (rigid+non-rigid) registration

OOBs were found in final registration images, a comparison between their quantitative measurements in Tab. 1 shows that their characteristics were very similar with an error of 1.15% in the volume value.

	MRI	**CT**
Volume (cc)	32.92	32.54
Centroid (voxels)	[315.2, 354.6, 15]	[316, 354, 14.9]
Orientation (relative to vertical axis)	1.7°	1.62°
OOB size (voxels)	[99, 87, 6]	[98, 83, 6]

Tab.1: 3D OOB

These results ensure the accuracy of the registration considering errors introduced by the manual segmentation.

V. CONCLUSION

We presented a registration method between pre-operative MRI and CT images dedicated to prostate brachytherapy. This method did not require any manual segmentation or visual identification of landmarks. The assessment of the proposed method demonstrated its ability to register those images. A complete evaluation study considering several clinical data sets will be planned in order to estimate the accuracy and the robustness of this registration method. Further work will combine the proposed registration with 3D-US/MRI registration so that the image-guide brachytherapy procedure would be complete.

REFERENCES

1. Lemaréchal et al. “Monte Carlo Simulations on GPU for Brachytherapy Applications”. *IEEE NSS-MIC.* 2013.

2. Baumann et al. “Prostate biopsy tracking with deformation estimation”. *Medical Image Analysis*. 2012;16:562-576.

3. Herk et al. “Quantification of organ motion during conformal radiotherapy of the prostate by 3D image registration”. *International Journal of Radiation Oncology Biology Physics*. 1995;33:1311-1320.

4. Parker et al. “Magnetic resonance imaging in the radiation treatment planning of localized prostate cancer using intra-prostatic fiducial markers for computed tomography co-registration”. *Radiotherapy and Oncology*. 2003;66: 217–224.

5. Fei et al. “A comparative study of warping and rigid body registration for the prostate and pelvic MR volumes”. *Computerized Medical Imaging and Graphics*. 2003;27:267-281.

6. Crouch et al. “Automated Finite-Element Analysis for Deformable Registration of Prostate Images”. *IEEE TMI*. 2007;26:1379-1390.

7. Huang et al. “Efficient Segmentation Algorithm for 3D Bone Models Construction on Medical Images”. *Journal of Medical and Biological Engineering.* 2010;31:375-386.

8. Viola et al. “Alignment by Maximization of Mutual Information”. *International Journal of Computer Vision*. 1997;24:137-154.

Robust point matching and outlier handling for minimally invasive Computer Aided Orthopedic Surgery (CAOS)

Oussama Haddad[1, 2, 3], Julien Leboucher[1,4], Jocelyne Troccaz[3], Eric Stindel[1, 2, 4]

[1]Laboratoire de Traitement de l'Information Médicale, INSERM UMR 1101, 29609 Brest, France

[2]Université de Bretagne Occidentale, Brest, France

[3]Techniques de l'Ingénierie Médicale et de la Complexité - Informatique, Mathématiques et Applications, 38706 Grenoble, France

[4] Centre Hospitalier Régional et Universitaire de Brest, Service Orthopédie Traumatologie, Brest, France

Abstract:

The use of a calibrated ultrasound probe during the intervention in order to localize bones and guide surgeons has been proposed for minimally invasive CAOS. We propose a registration method that works well even with a rough segmentation of bones in the intra-operative ultrasound acquisitions. The proposed method outperforms the widely used registration algorithm for CAOS purposes (ICP).

I] Introduction:

In order to guide surgeons during the intervention, computers localize bones using a calibrated ultrasound probes. We propose a rigid registration scheme to match intra-operative 3D ultrasound bones to pre-operative segmented CT. We use the approach [1] and adapt it for minimally invasive CAOS purposes where a real time scheme is required and the mean registration error must be lesser than 2 mm. Our technique is based on two concepts. Both were proposed in [1] for the purpose of an elastic registration scheme and to our knowledge, they were not tested in the CAOS context in a single scheme. The first concept is the Softassign and it is adapted with the determination of an optimal number of destination points to use in order to find a better match for each source point instead of the use of all destination points in [1] which affects the runtime and introduces error. The second concept is an outliers rejection technique that is adapted with the use of a threshold that determines outliers instead of relying on the proposed technique in [1]. In order to adapt the algorithm for CAOS use, the determination of the optimal values of the parameters is done on 3D ultrasound acquisitions and CT scans of sawbones.

II] Softassign:

We aim to rigidly register bones in ultrasound and CT/MRI/ultrasound data. In either monomodal or multimodal registration the following difficulty is encountered: the two point clouds to register are not necessarily acquired neither processed in the same way. This implies that a given point in the source does not necessarily find its exact counterpart in the destination. Thus, a binary registration does not necessarily provide the best results. The basic idea of the Softassign is to relax the binary correspondence. For each point of the source, several points of the destination can participate to create its counterpart (a barycenter weighted by the probability of matches). This allows the point to "look" further to find a potentially better match, this fuzziness allows a better behavior for the energy function [2] because the correspondences are improving on a more rich space which contains the destination point cloud and the barycenters and this also helps to avoid falling into local minima [3].

For these reasons, we chose to use the Softassign and to introduce changes adapted to our needs. Let $X = \{X_1, \ldots, X_N\}$ and $Y = \{Y_1, \ldots, Y_L\}$ be the source and destination point sets. Each source point X_i uses its nearest $\mathbf{N_v}$ destination points $\{Y_{1Xi}, \ldots, Y_{NvXi}\}$ to create its counterpart Y_{Xi} as follows: where M(i,k) is the probability match between X_i and Y_{kXi}

$$Y_{X_i} = \frac{\sum_{k=1}^{N_v} M(i,k) Y_{k_{X_i}}}{\sum_{k=1}^{N_v} M(i,k)} \quad (1)$$

III] Outliers rejection:

To detect outliers in the source, an imaginary point (Outlier Cluster) in the destination is created in order to grab them. Since we have no a priori information on the location of the outliers in the source, the outlier cluster is placed at the center of the destination point cloud [1].

There is a relatively large uncertainty in the first iterations of the registration, but gradually as the two clouds of points are registered, the degree of uncertainty decreases. Therefore, in the beginning of the registration, we accept all source points to be inliers and participate in the registration. Thus, all points (and outlier cluster) initially begin with the same power of attraction (T_0). Then we iteratively reduce the attractiveness of all points while keeping constant that of the outlier cluster.

IV] Proposed scheme:

We first calculate the match coefficients $M(i,j)$: With $D(i,j)$ the Euclidean distance between the source point i to the destination point j ($j \leq L$). "Temperature" T represents the power of attraction.

$$M(i,j) = \frac{T}{D(i,j)+\varepsilon} \quad (2)$$

$$M(i, L+1) = \frac{T_0}{D(i,L+1)+\varepsilon} \quad (3)$$

T_0 is the temperature for the outlier cluster, it is set to the distance initially separating the two furthest homologous points [1] and it is kept constant. T is the temperature for all the rest of points, it starts with T_0 and it decreases at each iteration i: $T_{i+1} = 0.93 * T_i$ [1]. A normalization [4] step is applied on the match coefficients providing match probabilities. In order to decide for each source point if it is going to be considered as an outlier, we studied the effect of a threshold applied on the correspondence probabilities to the outlier cluster (Th_{Out}). In order to choose the best values of Th_{Out} and N_V, we tested several combinations of (N_v, Th_{Out}) on several tests. We used Target Registration Error [5] applied on the unit sphere:

$$Transformation_{Error} = Max_{\|U\|=1} \|M_{GT}{}^{-1} M_R U - U\| \quad (4)$$

Where: M_{GT} is the searched transformation (Ground truth) and M_R is given by the registration process.

V] Results:

We used CT and ultrasound acquisitions of different femurs to create 16 tests. The number of points in the source point clouds used in the tests vary from 100 to 300000. The Table.1 shows the results:

Table.1 studying the behavior of the proposed scheme according to (N_v, Th_{Out})

N_v	Th_{Out}	Mean Error (mm)	Variance	Average Runtime (seconds)
ICP		**4,97**	**29.58**	**0.23**
1	0,1	30.12	434.78	4.41
	0,2	12.05	134.35	7.22
	0,3	1.68	5.39	9.07
	0,4	0.76	0.49	10.68
	0,5	**0.72**	**0.20**	**11.77**
2	0,1	17.23	234.04	7.41
	0,2	0.79	0.58	13.41
	0,3	0.63	0.15	13.53
	0,4	0.71	0.17	13.61
	0,5	0.73	0.17	14.66
3	0,1	1.68	5.03	12.51
	0,2	**0.56**	**0.06**	**15.21**
	0,3	0.70	0.15	15.53
	0,4	0.69	0.10	15.58
	0,5	0.72	0.11	17.26
4	0,1	1.09	1.65	12.57
	0,2	**0.55**	**0.06**	**17.53**
	0,3	0.63	0.06	18.06
	0,4	0.64	0.08	16.47
	0,5	0.71	0.08	18.60
5	0,1	0.88	0.66	15.64
	0,2	**0.57**	**0.07**	**18.58**
	0,3	0.70	0.05	21.68
	0,4	0.70	0.05	20.09
	0,5	0.73	0.05	20.16

Table.1 shows that the best mean errors were found for (N_V, Th_{Out}) = (3-5, 0.2). It shows also the added value of the Softassign itself when we see that the registration error is improving with $\mathbf{N_v}$ more than 1. When $\mathbf{N_V}$=1, our proposed scheme is equivalent to ICP but we add the outliers rejection step. The best mean error 0.72 mm we had is when Th_{Out} =0.5. The mean error for the ICP algorithm applied on our 16 tests is 4.97 mm. Outperforming ICP when $\mathbf{N_V}$=1, proves the added value of the outliers detection step. As it presents the best compromise between error and running time, we recommend the use N_V =3 and Th_{Out} =0.2 for further investigations.

We present one example using CT data for the source point cloud that generates the destination point cloud first by applying the transformation (Ground truth), adding noise to the destination, changing the distribution of the points and cropping a part of it. For this example, the transformation error after the gross alignment (Based on the ObbTrees [6]: It provides in real time the smallest box that encompasses the entire cloud. The data are aligned by aligning the axes of their boxes.) is 6.18 mm, our registration runtime was 0.75s, and the source point cloud has 294 points. The resulting transformation error is 0.25 mm and for the ICP it is 4.53mm.

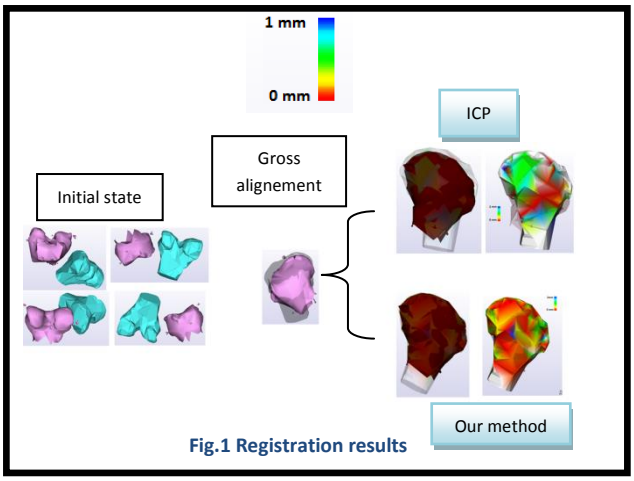

Fig.1 Registration results

Conclusion:

This preliminary study shows the ability of adapted robust point matching and outliers detection to work under minimally invasive CAOS requirements. A further validation step is required in order to make the proposed scheme applicable in the operating rooms.

Acknowledgment: This work was partly supported by the French ANR within the Investissements d'Avenir program (Labex CAMI) under reference ANR-11-LABX-0004.

References:

[1] Haili Chui and Anand Rangarajan (2003). A new point matching algorithm for non-rigid registration. Computer Vision and Image Understanding **89** 114–141.

[2] A. L. Yuille and J. J. Kosowsky (1994). Statistical physics algorithms that converge. Neural Computation, 6(3):341–356.

[3] A. Rangarajan, H. Chui, and J. Duncan (1999). Rigid point feature registration using mutual information. Medical Image Analysis.

[4] Winter, S., Brendel, B., Pechlivanis, I., Schmieder, K., Igel, C (2008). Registration of CT and Intraoperative 3-D Ultrasound Images of the Spine Using Evolutionary and Gradient-Based Methods. IEEE Transactions on Evolutionary Computation 12(3), 284–296.

[5] Dean C. Barratt, Graeme P. Penney, Carolyn S. K. Chan, Mike Slomczykowski, Timothy J. Carter (2006). Self-Calibrating 3D-Ultrasound-Based Bone Registration for Minimally Invasive Orthopedic Surgery. IEEE TRANSACTIONS ON MEDICAL IMAGING, VOL. 25.

[6] S. Gottschalk M. C. Liny D. Manocha. OBBTree: A Hierarchical Structure for Rapid Interference Detection. Proc. of ACM Siggraph,1996

Input : $X=\{x_1,..,x_n\}$, $Y=\{y_1,..,y_m\}$

Alignement: OBBTrees → $Y_p=\{y_{p1},..,y_{pm}\}$

Registration:

Initialization $T_0 = Max(Dist_{Paired-Points}), T_{end} = 1\ \{1\ mm\ is\ a\ clinically\ accepted\ RMS\},\ T = T_0$

Repeat

- *Find for each x_i the nearst N_v points in Y_p $\{Y_{i1},..,Y_{iNv}\}$: KdTrees*
- *Calculate Probability Match for the N_v points and for the Outlier cluster using (4) then normalize using [10].*
- *Apply Threshold Outliers*
- *For each inlier x_t calculate* $Y_{X_t} = \frac{\sum_{k=1}^{N_v} M(t,k) Y_{tk}}{\sum_{k=1}^{N_v} M(t,k)}$
- *Find the optimal transformation* $\Omega_{Opt} = Argmin\{Error = \sum_t \left\| x_t - Y_{x_t} \right\|^2\}$
- *$Y_p = \Omega_{Opt}\ (Y_p)$*
- $T = R * T$ *(R=0.93)*

Until (Error<1 mm{$Error_{acceptable}$ }) or ($T \leq T_{end}$)

Registration using wavelet coefficients in spectral domain for OCT images

Mouloud Ourak, Brahim Tamadazte and Nicolas Andreff
FEMTO-ST Institute, AS2M department
Franche-Comté University/CNRS/ENSMM/UTBM
24, rue Alain Savary, 25000 Besançon, France.
firstname.lastname@femto-st.fr

Abstract

This abstract presents a rigid registration of OCT images based on the wavelet transform. The validation tests show that beside non-stationary and highly inhomogeneous OCT images, the wavelet-based registration demonstrates very interesting results.

1 Introduction

A biopsy is a medical intervention usually performed by a clinician who takes, from the body, a sample of a suspect tissue for an *ex-situ* examination [1]. The latter is performed using usually a microscope to detect signs of damage or disease. Biopsies can be performed on all parts of the human body even in the brain. Thus, there are various types of biopsy processes: needle biopsy, endoscopic biopsy, surgical biopsy, etc. Most of these methods are invasive procedures even minimally and generally follow four essential steps: sampling, transfer, histological analysis, and then diagnostic. This takes time, requires a short hospitalization of the patient, a general or local anesthesia, and especially can cause infections in the tissue collection [2].

Furthermore, a biopsy may be performed in another way using specific medical imaging systems. This is usually known as *optical biopsy* and consists of an in-situ and real-time optical analysis of the suspect tissue without any removal. To perform an optical biopsy, it requires miniature and high resolution imaging systems as an optical endomicroscopic device. Doubtless, the two most popular techniques used in optical biopsy are confocal microscopy [3] and OCT [4]. Over the past two decades, OCT has emerged as the most suitable technique for carrying optical biopsies. This is mainly due to a better compromise between resolution and depth of penetration of tissues compared to the confocal microscopy technique.

This paper deals with the use of OCT images as a means for an *in-situ* chronological monitoring diagnosis of suspect tissues by taking several optical biopsies of the same tissues at time intervals specified by the oncologist. To be able to compare the different optical biopsies and detect the evolution of the suspect tissue, it is necessary to represent all the biopsies in the same reference. This amounts to perform a registration between successive OCT images [5]. To ensure an accurate registration of the high resolution OCT images, we provide a novel method based on wavelet representation in the spectral domain of the OCT signals.

2 Wavelet Transform

The wavelet transform allows to represent a 1D or 2D indeed 3D signal by orthonormal series [6]. The wavelet is widely used for the study of non-stationary and highly inhomogeneous signals in both time and frequency domains. It decomposes the signal into a set of elementary waveforms called *wavelets* defined by the wavelet coefficients (1).

$$\mathbf{WI}(b,a,\phi) \simeq \int_{-\infty}^{+\infty} \mathbf{I}(\mathbf{x})\overline{\psi\left(\frac{\mathbf{r}_{-\phi}\,(\mathbf{x}-\mathbf{b})}{a}\right)}d^2\mathbf{x}, \tag{1}$$

where $\mathbf{WI}$ are the wavelet coefficients, ψ is the mother wavelet, $\mathbf{I}(\mathbf{x}) \in \mathbb{R}^2$ is an image, $a \in \mathbb{R}_*^+$ is the scale parameter of the wavelet, $\mathbf{b} \in \mathbb{R}^2$ translation parameters along x and y, respectively, and $\mathbf{r}$ is the 3×3 rotation matrix carried by the angle ϕ. Thereby, $\mathbf{r}$ is given by

$$\mathbf{r} = \begin{pmatrix} \cos(\phi) & -\sin(\phi) & 0 \\ \sin(\phi) & \cos(\phi) & 0 \\ 0 & 0 & 1 \end{pmatrix} \tag{2}$$

In order to maintain the continuity of the signal $\mathbf{I}$, we choose ψ as the mother complex oriented *Morlet wavelet* [7] defined in the spatial domain by considering the correction exponential term $e^{-\frac{1}{2}k_\psi^2}$ as follows:

$$\psi(x,y) = \left(e^{ik_\psi x} - e^{-\frac{1}{2}k_\psi^2}\right) e^{-\frac{1}{2}\left(x^2+y^2\right)} \tag{3}$$

where k_ψ is the wavenumber associate to the *Morlet wavelet*.

3 Wavelet-based Registration

The registration defined as the process to align current image $\mathbf{I}_c$ with reference image $\mathbf{I}_r$. This returns to find the minimum of the cost-function defined by:

$$\widehat{\mathbf{T}} = arg\min[\mathbf{WI}_r, \mathbf{WI}_c] \tag{4}$$

where $\widehat{\mathbf{T}} \in (SE(2) \times SO(1))$ is the estimated rigid transformation and $\mathbf{WI}_r$ and $\mathbf{WI}_c$ are the wavelet coefficients of $\mathbf{I}_r$ and $\mathbf{I}_c$ respectively.

Therefore, using a *log-polar* phase correlation method [8] yield to represent the cost-function between two images to be registered by the convex shape curve shown in Figure 1. Note that the minimum of this cost-function is well defined and can be easily computed by a simple gradient-based optimization algorithm.

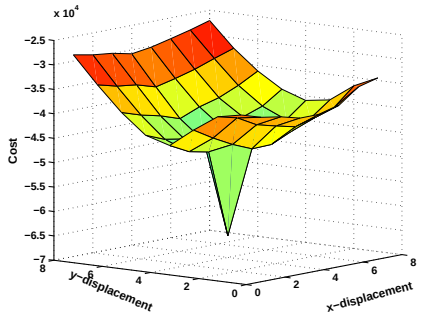

Figure 1: Illustration of the cost-function used in the developed registration method.

The developed wavelet-based registration method can be summarized by the algorithm given in Figure 2.

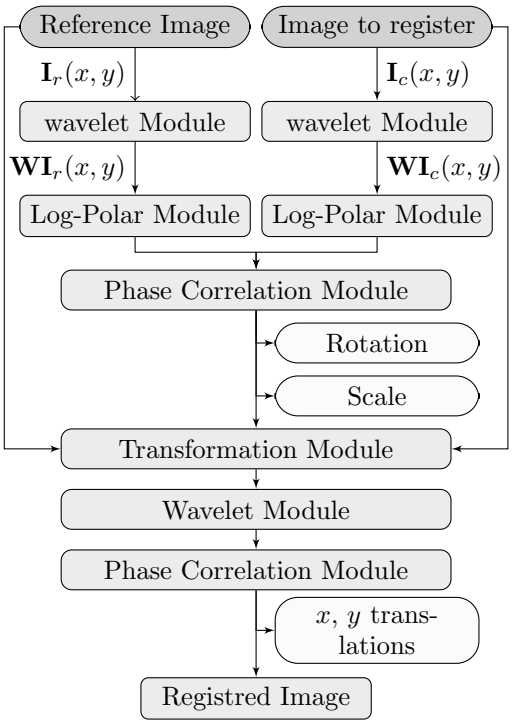

Figure 2: Overview of the registration algorithm.

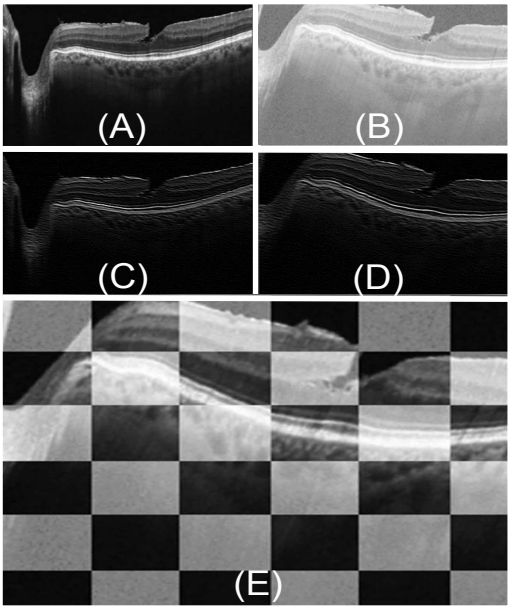

Figure 3: Registration results: (A) OCT reference image, (B) OCT image to be registered, (C) and (D) the corresponding wavelet coefficients, respectively, and (E) the result of the registration process.

4 Experimental Validation

Having not yet experimental set-up for a physical registration, we opted for a 4 Degrees Of Freedom (DOF) (x, y, z, and θ) numerical registration. To ensure this, we consider a first OCT image $\mathbf{I}_r$ (reference image shown in Figure 3(A)) taken under nominal conditions (first point of view) and a second image $\mathbf{I}_c$ (image to register shown in Figure 3(B)) taken using another point of view (different with the first one) and under extreme conditions of saturation. The choice of the images Figure 3(A) and 3(B) will evaluate the precision of the algorithm on long and short point of view distance and the robustness to the image variations. Figure 3(C) and 3(D) represent the corresponding wavelet coefficients computed for fixe mother wavelet parameters (a, ϕ) of $\mathbf{I}_r$ and $\mathbf{I}_c$, respectively. The registration result is illustrated in Figure 3(E). Indeed, this image combines $\mathbf{I}_c$ and $\mathbf{I}_r$ after transformation in order to compare the results visually. Thus, the image 3(E) combine one on two square of image $\mathbf{I}_c$, and one on two square of the image $\mathbf{I}_r$ after transformation. By analyzing the image result, it can be highlighted the high accuracy of the proposed registration method despite the high difference between $\mathbf{I}_r$ and $\mathbf{I}_c$. The registration process takes only 130 milliseconds for image of 256×256 pixels, this using a 3.5 GHz PC.

5 Conclusion

In this paper, it was shown the initial results using a wavelet-based registration method in the case of OCT images. Despite of the large difference between the OCT images to be registered (i.e., nominal acquisition conditions *vs.* saturation acquisition conditions), the proposed method was illustrated that the wavelet-based registration algorithm remains efficient with high level of accuracy of convergence.

The next stages of this work will involve the implementation of the developed method in an experimental set-up (including a multiple DOF) in order to achieve a physical registration during repetitive optical biopsies. Then, compare our algorithm with the existing ones (sum square difference, normalized cross-correlation, mutual information, etc.).

Acknowledgment

This work was supported by the French ANR Labex-ACTION no ANR-11-LABX-0001-01

References

[1] D. Zerbino, "Biopsy: its history, current and future outlook," *Likars'ka sprava/Ministerstvo okhorony zdorov'ia Ukrainy*, no. 3-4, pp. 1–9, 1993.

[2] M. Greco, R. Agresti, N. Cascinelli, P. Casalini, R. Giovanazzi, A. Maucione, G. Tomasic, C. Ferraris, M. Ammatuna, S. Pilotti *et al.*, "Breast cancer patients treated without axillary surgery: clinical implications and biologic analysis," *Annals of surgery*, vol. 232, no. 1, p. 1, 2000.

[3] J. Pawley, *Handbook of biological confocal microscopy*. Springer, 2010.

[4] D. Huang, E. A. Swanson, C. P. Lin, J. S. Schuman, W. G. Stinson, W. Chang, M. R. Hee, T. Flotte, K. Gregory, C. A. Puliafito *et al.*, "Optical coherence tomography," *Science*, vol. 254, no. 5035, pp. 1178–1181, 1991.

[5] B. Zitová and J. Flusser, "Image registration methods: a survey," *Image and Vision Computing*, vol. 21, no. 11, pp. 977 – 1000, 2003.

[6] S. Mallat, *A wavelet tour of signal processing*. Academic press, 1999.

[7] L. G. Weiss, "Wavelets and wideband correlation processing," *Signal Processing Magazine, IEEE*, vol. 11, no. 1, pp. 13–32, 1994.

[8] B. Reddy and B. N. Chatterji, "An fft-based technique for translation, rotation, and scale-invariant image registration," *Image Processing, IEEE Transactions on*, vol. 5, no. 8, pp. 1266–1271, Aug 1996.

TRUS/T2 MRI 3D prostate elastic registration for HIFU thermal therapy

Ke Wu[a,b,c], Carole Garnier[a], Huazhong Shu[b,c] Jean-Louis Dillenseger[a,c]

[a] INSERM, U1099, Rennes, F-35000, France; Université de Rennes 1, LTSI, Rennes, F-35000, France;
[b] Laboratory of Image Science and Technology, School of Computer Science and Engineering, Southeast University, Nanjing, China;
[c] Centre de Recherche en Information Biomédicale sino-français, Laboratoire International Associé, Inserm, Université de Rennes 1, France, Southeast University, Nanjing, China.

The work presented in this paper is focused on image guided focal therapy of prostate cancer by High Intensity Focused Ultrasound (HIFU). The principle of a HIFU prostate therapy is to insert a specific ultrasound (US) probe within the rectum. This device focuses ultrasound waves to the tissues to be ablated or destroyed through the rectal wall. In more detail, a 2D ultrasound imaging system is available in the middle of the therapeutic probe. The first step of the therapy is to acquire a 3D US image of the prostate by translating the probe. This volume is used to define semi automatically the therapy planning (the prostate shape to be heated). The device then performs automatically the thermal therapy under the supervision of the urologist.

The development of new probes allowed such a gain in spatial precision that a focal tumor treatment may be considered instead of a total prostate destruction [1]. But in this case the treatment planning and image guidance have to be modified according to the imaging capabilities. An US imaging system is not able to locate the tumor within the prostate. So at contrary to the whole prostate treatment, the focal tumor therapy under US imaging guidance is not directly possible. So far, only MRI can be used to describe the prostate, its different zones and the tumor with sufficient contrast and resolution. The main idea for the therapy guidance in our project is to use a clinical preoperative T2 MRI volume to locate the tumor within the prostate and then to use this information within the US guided therapy. This fusion of information can be performed by registering the preoperative T2 MRI volume to the per-operative ultrasound images.

The choice of the registration scheme is directly related to the data to merge. In our case, the prostate undergoes deformations between the several imaging steps due to the bladder and rectum filling and moreover to the endorectal coil (if any) and endorectal therapeutic probe. So an **elastic** registration scheme must be considered. Transrectal ultrasound (TRUS) and T2 MRI share little common information. TRUS images have a low structure information, except the external prostate surface and partially the urethra. T2 MRI allows to recover rich internal features (prostate zones, tumors) but the external surface (the capsule) presents a hyposignal and is consequently badly defined. However, due to the US image characteristics, only the prostate surface is a common information between both modalities. Hence we chose a **surface to surface registration** technique. The registration scheme is then the following:

- 3D surface segmentation on TRUS image. We used a semi-automatic surface segmentation method based on Optimal Surface Detection method [2]. In this method, the radiologist or urologist defines interactively 6 points (base, apex and 4 points in a mid slice) and then the 3D prostate surface is extracted as a mesh. We intentionally used a semi-automatic method in order to incorporate the medical expertise in the apex and base zones generally badly defined on the US volume.
- 3D surface segmentation on T2-MRI. As said previously, on T2 MRI, the capsule presents a hyposignal sometimes similar to the surrounding organs as rectum and bladder wall; This lead to a bad surface estimation with some leakage to the surrounding organs. We used a semi-automatic multi-organs surface segmentation method based on OSD method [3]. As for the US images, the radiologist or urologist defines interactively 6 points on the prostate surface and 4 more points on the rectum. The multi-objects OSD segments then concurrently the prostate, the bladder and the rectum in order to better estimate the prostate surface. The result of this segmentation step is a 3D mesh of the MR prostate surface.

- Rigid registration. For the rigid registration, we applied the Iterative Closest Point algorithm [4] on the nodes of the surface meshes in both modalities. This allows to align globally the MRI volume to the TRUS volume
- Elastic registration. The main purpose of our registration scheme is not simply fitting surfaces, but more finding a 3D deformation field to deform the surface and also the inside of the prostate volume. From this constraint, we have to choose a 3D elastic volume registration scheme which uses surface information. The demons algorithm [5] is able to perform this type of registration. Moreover, in order to recover the inner deformation field we applied the demons algorithm on only the surface information (binary volume), or, as suggested in [6], on normalized distance maps of the two prostate surfaces instead of the binary volumes.
- Information propagation. The rigid transformation matrix and the 3D deformation field estimated by the elastic registration method are then used to propagate the information provided in the preoperative T2 MRI (prostate zones, tumor location, etc. delineated manually or automatically) into the per-operative 3D US volume.

In order to validate the feasibility of the proposed framework, we applied it on a set of 10 patients treated by an Ablatherm device [7]. For each patient we had a preoperative T2 MRI volume and a peroperative TRUS volume recorded on the Ablatherm device during the treatment planning. We tested the registration process to the whole dataset of the 10 different patients, and we deformed the MRI volumes to the US images (see the results of one patient on the Figure 1).

With our method (segmentation and registration), we were able to register all the ten couple of clinical data. The overall method seems to be robust. However, because we had no possibility to evaluate the final accuracy of registration, only some qualitative preliminary conclusions can be assert based on the visual examination of our results as for example the influence of the demon grid deformation model (Figure 2).

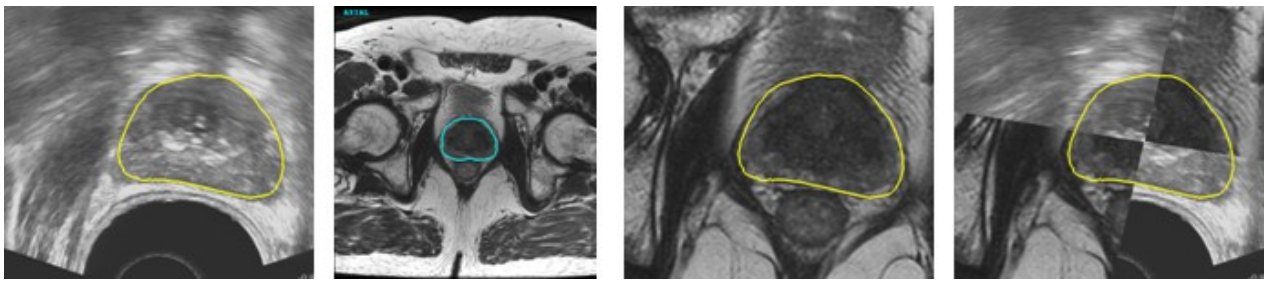

TRUS with segmented contour | T2 MRI with segmented contour | T2 MRI after registration | TRUS /T2 MR fusion

Figure 1: Registration and fusion result on one patient.

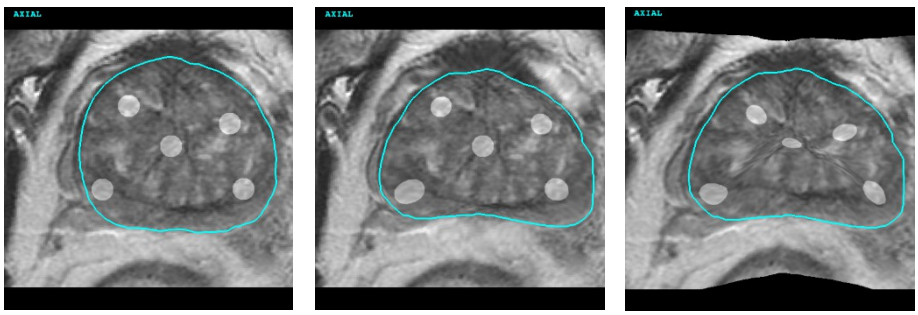

(a) (b) (c)

Figure 2: Comparison between different demon grid deformation models: (a) T2 MR image after rigid registration with circular areas simulating some region of interest; (b) Elastic registration result with binary model; (c) Elastic registration result with normalized distance map model

References

[1] Mari J.-M., et al. “Study of a dual-mode array integrated in a multi-element transducer for imaging and therapy of prostate cancer”, IRBM, 34(2), 2013, pp. 147-158

[2] Garnier, C., et al. "Prostate segmentation in HIFU therapy." IEEE trans. Medical Imaging, 30(3), 2011, pp. 792-803.

[3] Wu K., et al. “Adaptation and evaluation of the multiple organs OSD for T2 MRI prostate segmentation” IEEE EMBS conf, Chicago, 2014, pp. 4687-4690.

[4] Besl P. J., McKay N. D., "A method for Registration of 3-D Shapes", IEEE trans. PAMI, 14(2), 1992, pp. 239-256.

[5] Thirion, J.-P. "Image matching as a diffusion process: an analogy with Maxwell's demons" Medical Image Analysis 2(3): 1998, pp. 243-260.

[6] Dréan, G., et al. “Inter-individual organ-driven CT registration for dose mapping in prostate cancer radiotherapy” ISBI, 2012.

[7] http://www.edap-tms.com/products-services/ablatherm-hifu

Acknowledgments

This work was supported by the French ANR TecSan MULTIP project (ANR-09-TCS-011-04). It was performed in a laboratory partner of the CAMI LABEX (ANR-11-LABX-0004).

Real-time simulation of soft tissue deformations for the childbirth related models using HEML

Zhuo-Wei Chen — François Goulette

Mines ParisTech, PSL Research University, Centre de Robotique, 60 Bd St Michel 75006 Paris, France

Abstract

Virtual surgery simulators show a lot of advantages in the world of surgery training, where they allow to improve the quality of formalization of surgeons' gesture. We are interested in constructing a childbirth simulator taking into account the morphology of women to improve medical trainings for the obstetricians and midwives. For such kind of simulator, one of the current major technical difficulties is the possibility to realize a real-time computation of soft tissue deformation by considering the accurate modeling of their mechanical properties. However today, most existing methods are still time costly or lack of realism. Mass-spring model [1] has been widely used due to its simplicity of implementation and its low computation complexity properties, however, it suffers from a lack of realism. Mass-tensor model [2] is as efficient as mass-spring model and can handle large deformations and large displacements with the Saint Venant-Kirchhoff constitutive law. However, it is limited only to this specific material. Marchesseau et al. [3] proposed Multiplicative Jacobien Energy Decomposition (MJED) method for discretizing hyperelastic materials on linear tetrahedral meshes which leads to faster matrix assembly than the standard Finite Element Method. It is not limited to one specific hyperelastic material but cannot reach the ideal 25 frames per second needed for the real-time simulation. For these reasons, we try to find a compromise between biomechanical accuracy and computational efficiency to realize a real-time simulator. We present in this abstract the real-time simulation of complex biomechanical models using a new method that we call 'HEML' (HyperElastic Mass Links), which is particularly fast, derived from the finite element method, can handle hyperelastic and large deformation modeling [4].

This method is extremely fast to calculate the force field, and is only applicable for the tetrahedral mesh due to the specific characteristic of constant deformation gradient tensor **F** over a given tetrahedron for P1 element which will be used in our method. As it is based on the finite element method by using the strain energy density function W which is a scale function of one of the strain tensors, it can handle the nonlinear and large deformation problems. HEML is not limited to only one hyperelastic material. In the "P1 approximation" of finite elements, mesh elements are tetrahedral; the approximation states that the deformation gradient tensor **F** is constant over a given tetrahedron T_k, it is also the same case for the right Cauchy-Green deformation tensor **C** (**C**=$\mathbf{F}^T\mathbf{F}$). It can be demonstrated that, under the P1 approximation, the value of **C** depends linearly on the vector **l** (edge square lengths), in other word, it depends only on the vertices positions.

Instead of computing the force using the first derivative of the energy with respect to **C** (leading to the second Piola-Kirchhoff stress tensor **S**), we compute it directly by deriving the energy with respect to the nodal position. Combining with the fact that W is a function of the vector **l**, we can express the force as:

$$f_{i,k} = \frac{\partial W_k(\mathbf{l}_k)}{\partial x_i} = \frac{\partial W_k}{\partial \mathbf{l}_k}\frac{\partial \mathbf{l}_k}{\partial x_i} \tag{1}$$

We have used this approach (Eq. 1) to derive elastic forces for various specific isotropic hyperelastic materials: Saint Venant-Kirchhoff, Neo-Hookean and Mooney-Rivlin. Saint Venant-Kirchhoff model is a

hyperelastic material model which is an extension of the linear elastic material model to the nonlinear regime. The volumetric energy function is usually formulated with the Green-Lagrange tensor **E**, and the Lame coefficients λ and μ. Neo-Hookean and Mooney-Rivlin are popular hyperelastic material models that can be used for predicting the nonlinear stress-strain behavior of rubber or biomechanical materials undergoing large deformations [5, 6]. For each type of hyperelastic model, the energy density is a function of the three invariants I_1, I_2, I_3, and we express it by the edge square lengths **l**.

This algorithm has been implemented into a computer, with the Visual C++ developing environment under Windows 7. The computer was an Intel Core at 3.40 GHz, 8.00 Go RAM. Two biomechanical models have been considered in our work: a model of fetus with 4430 tetrahedral elements and 1128 nodes (fig. 1a), a model of abdomen of the parturient woman with 21436 tetrahedral elements and 5591 nodes (fig. 1b). The two mesh models are provided by the SAARA Team of LIRIS of University of Lyon 1 as described in [7]. The Neo-Hookean model and the material parameters have been chosen the same as in the article. The average computation times per iteration for the elastic force field are given in the table 1. It is noticeable that, for the abdomen model, containing as many as 21436 tetrahedrons, the computation is feasible and can reach an average time of 3.75 ms.

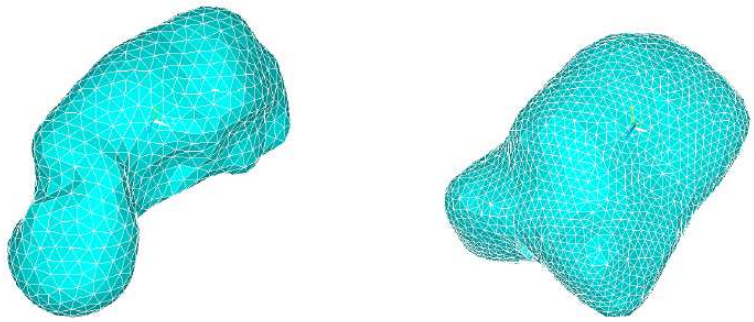

a b

Figure 1. Mesh of the fetus and the abdomen of the parturient woman

Table 1: Computation time per iteration for the two models in millisecond

	Fetus (4430 elements)	Abdomen (21436 elements)
Computation time (ms)	0.62	3.75

Bibliographies

[1] P. Meseure and C. Chaillou. A deformable body model for surgical simulation. J Visual Comput Animat, 11(4):197–208, 2000.

[2] S. Cotin, H. Delingette, and N. Ayache. A hybrid elastic model allowing real-time cutting, deformations and force-feedback for surgery training and simulation. Vis Comput, 16(8):437–452, 2000.

[3] S. Marchesseau, T. Heimann, S. Chatelin, R. Willinger, and H. Delingette. Fast porous visco-hyperelastic soft tissue model for surgery simulation: Application to liver surgery. Prog Biophys Mol Biol, 103:185–196, 2010.

[4] F. Goulette and S. Chendeb. A framework for fast computation of hyper-elastic materials deformations in real-time simulation of surgery. Computational Biomechanics for Medicine (CBM) Workshop of the Medical Image Computing and Computer Assisted Intervention (MICCAI) Conference, Copenhagen, Denmark, 2006.

[5] G.Venugopala Rao, C. Rubod, M. Brieu, N. Bhatnagar and M. Cosson. Experiment and finite element modelling for the study of prolapse in the pelvic floor system. Comp. Methods in Biomechanics and Biomedical engineering, 73:317–330, 2008.

[6] S. Majumder, A. Roychowdhury, and S. Pal. Effects of trochanteric soft tissue thickness and hip impact velocity on hip fracture in sideways fall through 3d finite element simulations. Journal of Biomechanics, 41:2834–2842, 2008.

[7] R. Buttin, F. Zara, B. Shariat, T. Redarce and G. Grangé. Biomechanical simulation of the fetal descent without imposed theoretical trajectory. Comput Meth Programs Biomed 111:389-401, 2013.

Biopsym : a virtual reality simulator integrating a learning environment for image-guided prostate biopsy

Sonia-Yuki Selmi[a,*], Gaelle Fiard[b], Emmanuel Promayon[a], Lucile Vadcard[c], Jocelyne Troccaz[a,b]

[a] *UJF-Grenoble 1 / CNRS / TIMC-IMAG UMR 5525, Grenoble, F-38041, France*
[b] *Grenoble University Hospital, Department of Urology, Grenoble, France*
[c] *LSE, UPMF, Grenoble, France*

1. Introduction

Last few years, new technology in imaging and virtual reality allowed the development of medical training simulators. That rapid growing is more motivated by the educational needs and by the low cost of such training tools. Current teaching methods in medecine, based on apprenticeship, expose the patients to the students' learning curve and depend on the apprentice-mentor relationship. The integration of simulator into the medical education can lead to the patient safety. Surgical simulators, which represents a small proportion of available simulators, allow teaching complex procedures and working on specific gesture [1]. In the field of urology, most of them are dedicated to laparoscopic skills. Few devices dedicated to the simulation of prostate biopsy are reported in the literature. Xuan et al. [2] and Zeng et al. [3] developed 3D simulation models and Chalasani et al. [4] designed a validated Virtual Reality TransRectal UltraSound (TRUS) guided prostate biopsy simulator, with a limited teaching environment. We designed a virtual reality simulator dedicated to TRUS prostate biopsy, enhanced by a learning environment.

2. Context

Prostate cancer is the second most common cancer worldwide for males [5]. Prostate biopsy procedures are performed in order to obtain prostate tissue and prove the presence of cancerous cells. Conventional biopsies are performed under TRUS guidance and the operator has to perform a biopsy by positioning the samples only using information from the visualized ultrasound images. In clinical practice, a 12-core biopsy protocol is usually performed, using an end-fire probe. To obtain a complete and accurate cancer diagnosis, these 12 samples have to be well-distributed and located in 12 different 3D anatomical zones of the prostate. The procedure is challenging because it requires a good understanding of

*I am corresponding author
Email address: sonia-yuki.selmi@imag.fr (Sonia-Yuki Selmi)

ultrasound and a good 3D mental representation to reconstruct 3D data from 2D views and a good eye-hand coordination, the prostate being a small organ, almost spherical (about 4 cm in diameter). The initial diagnosis of cancer and the treatment strategy depend mainly on the quality of a prostate biopsy procedure. Previous work showed that a visual feedback about the real location of performed biopsy distribution [6] helps clinicians to improve biopsy distributions. Moreover, recent progress in Magnetic Resonance Imaging (MRI) allowed the performance of targeted biopsies on suspicious areas and created a new need in terms of learning for this specific task of mental fusion between two modalities.

3. Biopsym simulator

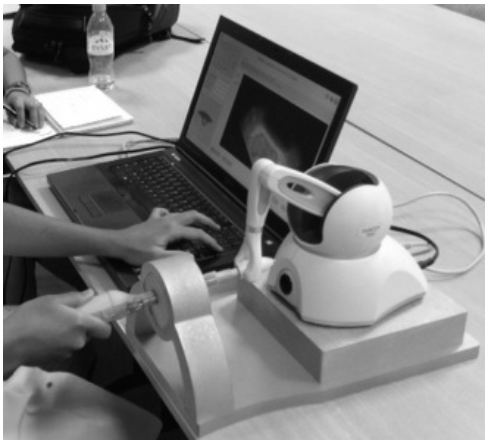

Figure 1: BiopSym simulator

3.1. Educational content

A didactical study was performed to evaluate the training needs [7] in order to develop well adapted activities and to transpose reference situations into a simulator. According to this study, the learning environment of BiopSym includes a teaching session, an initiation for first usage, a complete biopsy procedure simulation, seven specific exercises and a learning pathway. The exercises target different aspects of the surgical gesture, such as TRUS image reading, prostate volume measurement, prostate cancer risk estimation, sector or area targeting, and MRI-TRUS mental fusion. Each exercise can be performed with or without assistance. The assistance consists in displaying a 3D representation of the prostate with the current probe plane position in addition to the usual 2D TRUS image. Users can perform biopsy procedure with different levels of difficulty. Each exercise provides the users with both a visual feedback (3D visualization) and a numerical feedback (biopsy score). The implemented learning pathway is a decision-making system which automatically provides a set of exercises depending on previous results of the user.

3.2. Description of the simulator

We developed a virtual-reality learning environment dedicated to prostate biopsies [8]. The simulator is composed of a laptop computer and an haptic device (Phantom Omni, Sensable Devices Inc., MA, France), enhanced by a probe mock-up and a silicon-made rectum, see Fig. 1. A clinical case database was integrated into the simulator to offer both real clinical data and 3D ultrasound volumes. Patient data was collected and anonymized from the UroStation system (Koelis, France).

Users perform virtual biopsy procedure, taking 12 samples, guided by the 2D TRUS image plane, see Fig. 2a. The simulator also offers the possibility to perform three targeted biopsies, based on a target displayed on an associated MRI. Then, a biopsy feedback is displayed by visualizing sample positions relatively to the 3D image of the prostate, see Fig. 2b.

4. Experimental results

Development of learning simulators requires validation study to affirm their appropriateness and clinical benefit. Validation of such simulators is based on various criteria [9] : (1) reliability (reproducibility and precision), (2) validity (whether the simulator is actually teaching what it is intended to teach).

A first validation of the BiopSym simulator was performed [10]. The aim of the study was to validate reliability, face (the simulator represents what it is supposed to represent), content (the simulator teaches what it is supposed to teach) and construct (the simulator is able to distinguish between experienced and inexperienced users) of the simulator. The results of this first study, on one hand, proved the reliability and validated the face and content and on other hand showed that the realism and scoring score have to be improved to validate the construct.

After the study, the scoring system was adapted to be more accurate : the prostate is now divided into 12 anatomical zones with the same volumes and the score takes into account the length of sample inside the targeted zone.

5. Conclusion

The designed virtual reality simulator allows students practicing in prostate biopsy procedure. We focused on the training needs, particularly on targeted biopsies using the fusion. Evaluating the educational value is a complex task, we performed a validation which proved versatility and reliability, face and content validity. The recent integration of tissue deformation added realism and first tests was satisfactory. Future work consists in a complete evaluation, including evaluation of the last improvements and the transfer of the acquired skills to an actual patient.

(a)

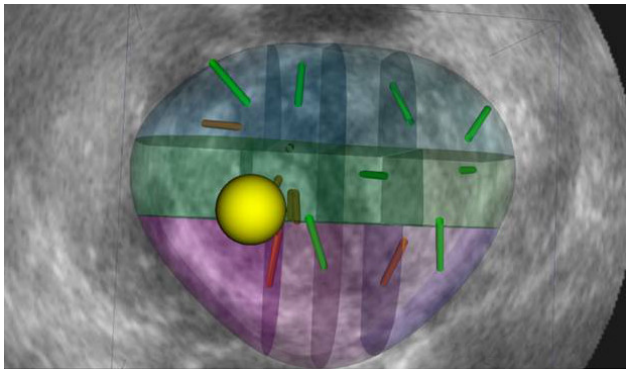

(b)

Figure 2: (a) Interface of the BiopSym simulator (b) Visual feedback of a performed virtual biopsy

6. Acknowledgments

This work was supported by French state funds managed by the ANR within the PROSBOT project and the Investissements d'Avenir programme (Labex CAMI) under reference ANR-11-LABX-0004 and by INSERM CHRT (grant J. Troccaz).

References

[1] H. A. de Sante, Etat de l'art (national et international) en matiere de pratiques de simulation dans le domaine de la sante, Rapport de mission.

[2] J. Xuan, Y. Wang, I. Sesterhenn, J. W. Moul, S. Mun, 3D model supported prostate biopsy simulation and evaluation, Notes Comput Sci 1496 (1998) 358–367.

[3] J. Zeng, J. Bauer, W. Zhang, I. Sesterhenn, R. Connelly, J. Lynch, J. Moul, S. K. Mun, Prostate biopsy protocols: 3D visualization-based evaluation and clinical correlation, Comput. Aided Surg. 6 (1) (2001) 14–21.

[4] V. Chalasani, D. Cool, S. Sherebrin, A. Fenster, J. Chin, J. Izawa, Development and validation of a virtual reality transrectal ultrasound guided prostatic biopsy simulator, Canadian Urology Association Journal 5 (1) (2011) 19–26. doi:10.5489/cuaj.09159.

[5] P. D. Baade, D. R. Youlden, L. Krnjacki, International epidemiology of prostate cancer: geographical distribution and secular trends, Mol Nutr Food Res 53 (2) (2009) 171–184.

[6] P. Mozer, M. Baumann, G. Chevreau, A. Moreau-Gaudry, S. Bart, R. Renard-Penna, E. Comperat, P. Conort, M.-O. Bitker, E. Chartier-Kastler, F. Richard, J. Troccaz, Mapping of transrectal ultrasonographic prostate biopsies: quality control and learning curve assessment by image processing, J Ultrasound Med 28 (4) (2009) 455–460.

[7] C. Meurger, Caractrisation didactique d'un simulateur pour la formation mdico-chirurgicale (in French), Master's thesis, Pierre Mendes France University, Grenoble, France (2009).

[8] S. Selmi, G. Fiard, E. Promayon, L. Vadcard, J. Troccaz, A virtual reality simulator combining a learning environment and clinical case database for image-guided prostate biopsy, in: 26th IEEE International Symposium on Computer-Based Medical Systems, Porto, Portugal, 2013. doi:10.1109/CBMS.2013.6627785.

[9] E. M. McDougall, Validation of surgical simulators, Journal of Endourology 21 (3). doi:0.1089/end.2007.9985.

[10] G. Fiard, S. Selmi, E. Promayon, L. Vadcard, J.-L. Descotes, J. Troccaz, Initial validation of a virtual-reality learning environment for prostate biopsies: realism matters!, Journal of endourology 28 (4) (2014) 453–458.

Toward an MR-compatible needle holder with adaptive compliance using an active tensegrity mechanism

Quentin BOEHLER*[1], Marc VEDRINES[1], Salih ABDELAZIZ[2], Philippe POIGNET[2], and Pierre RENAUD[1]

[1]ICube, Université de Strasbourg, CNRS, INSA Strasbourg,France
[2]LIRMM, Université de Montpellier II, CNRS, France

1 Introduction

The field of MR imaging has extended from diagnosis to guidance and control in a wide variety of interventional procedures [1]. Due to the lack of space and manipulability within the MRI scanner, there is an ongoing interest for robotic assistance in MR-guided interventions. Numerous MR-compatible robots have been proposed, especially for needle manipulation.

For needle insertion in the liver, patient-mounted robots are particularly interesting for the provided partial compensation of the breathing motion. The needle holder must however still fulfill two contradictory requirements: it needs to be stiff during the insertion and compliant afterwards, in order to avoid organ lacerations [2]. This led to the development of needle grasping systems that allow the needle to move freely between two insertion phases [3].

In this paper, an alternate approach is considered: a needle manipulation system with adaptive compliance is proposed that is based on so-called tensegrity mechanisms. Numerous challenges related to MR-compatibility and compliance control could be overcome thanks to this recent class of robots, as outlined in the following through the design of a first device for needle orientation control.

2 Toward a needle holder using tensegrity mechanisms

2.1 Tensegrity mechanisms

Tensegrity mechanisms are derived from tensegrity structures. These structures are self-stressed systems comprising a set of compressed bars in a set of tensioned cables [4]. In tensegrity mechanisms, cables are replaced by springs and some components, either bars or springs, are actuated to control the mechanism configuration.

The components of a tensegrity mechanism are only axially loaded, so they can be lightweight as well as the system. In addition, tensegrity mechanisms can exhibit high workspace to size ratio, as demonstrated by their use in different deployable systems. They can be remotely actuated using cables so as to ensure MRI compatibility. Previous MR-compatible systems using cable-driven robots have shown the interest of this approach [5, 6]. Since tensegrity mechanisms are prestressed systems, their compliance can be adjusted through the control of the spring prestress without changing their configuration. Moreover, the stiffness variation can be achieved even when using linear springs [7]. Tensegrity mechanisms constitute therefore an interesting class of mechanisms for the design of compact and lightweight needle holder devices with adaptive compliance. Such a use is original to the best of our knowledge.

The position of the needle entry point can be computed in a preoperative period and registered through the position of the device on the patient skin before the insertion. The control of the needle orientation before and during the insertion is on the contrary challenging. As a consequence, we focus here our attention on the design of a device with two degrees of freedom in orientation.

*quentin.boehler@icube.unistra.fr

2.2 Design of a 2-DOF needle holder

In this application, four variables have to be controlled, namely the two DOF in rotation of the needle and the two angular compliances with respect to the rotation axes. For ease of use, a device with a Remote Center of Motion (RCM) is considered.

The kinematics of the proposed system are featured Fig. 1(a). The device is based on two perpendicular planar parallelogram linkages connected by a cylindrical joint. Each linkage controls one DOF in rotation of the needle, with a decoupling of the two DOF for an easy control.

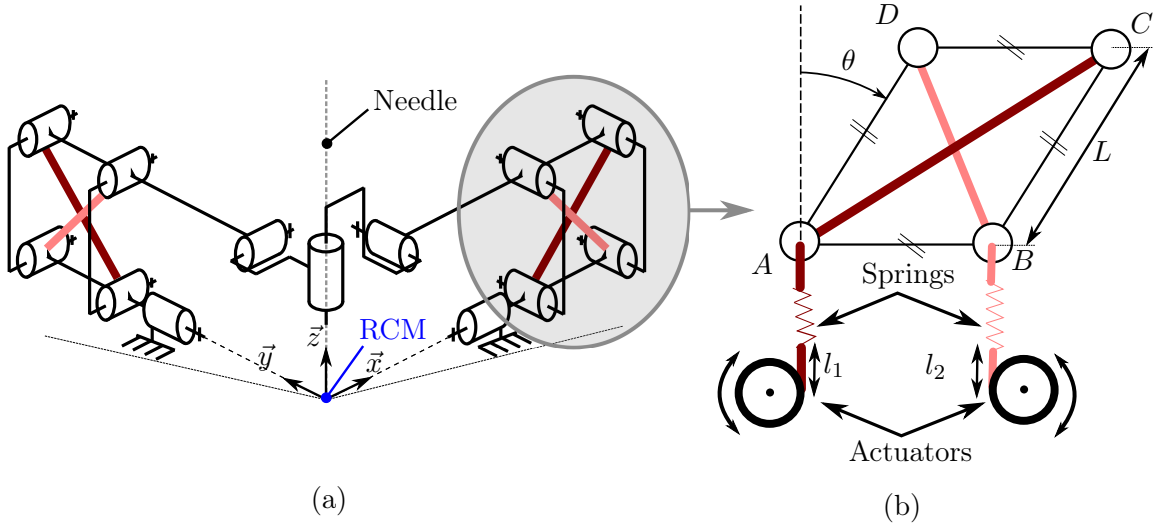

Figure 1: (a) RCM-based needle holder architecture, (b) Planar tensegrity mechanism based on parallelogram linkage.

As described in Fig. 1(b), each parallelogram linkage is a planar tensegrity mechanism articulated with cables connected in series with springs along the diagonals AC and BD. The configuration of the parallelogram, represented by the angle θ, is remotely controlled by changing the lengths (l_1, l_2) of the two cables. As two cables are used, the angle θ of the parallelogram is controlled together with the angular compliance through the springs prestress. In [8], an extreme case of this parallelogram mechanism is assessed using zero free length springs thus exhibiting a zero stiffness behavior.

In total, four cables are actuated providing four controllable variables for the entire device. The device is remotely actuated to ensure MRI compatibility.

The device geometry is being defined using an iterative design process. The length L is chosen equal to 70 mm in order to keep the device compact. The angular range is equal to $\pm 45°$. As a first step, only standard commercial linear springs are considered for the integration. The maximum compliance variation range is investigated by considering the maximum and minimum tensions in the springs for nominal working conditions.

3 Results and discussion

First simulation results show that a simultaneous control of the orientation and the compliance of the needle is feasible for the two DOF. Using standard commercial linear springs, the needle can be oriented on $\pm 45°$ along two directions, while modifying by more than 25% the level of compliance of the needle axis.

Such a compliance variation remains limited for the context. In order to improve the compliance range, an identification of adequate spring behavior is performed. Using non linear springs, the compliance variation range can be enlarged up to 300% for the given angular range. Several works exist on the design of such non linear springs (see [9] and references therein). The next step will now concern the design of efficient compliant elements for further implementation, and afterwards the design of an insertion DOF.

Acknowledgements

This work was supported by French state funds managed by the ANR within the Investissements d'Avenir programme (Labex CAMI) under reference ANR-11-LABX-0004 and by the Région Alsace.

References

[1] S.G. Hushek, A.J. Martin, M. Steckner, E. Bosak, J. Debbins, and W. Kucharzyk. MR systems for MRI-guided interventions. *J Magn Reson Imaging*, 27(2):253–266, 2008.

[2] D. Sun, C. Willingham, A. Durrani, P. King, K. Cleary, and B. Wood. A novel end-effector design for robotics in image-guided needle procedures. *Int J Med Robot.*, 2(1):91–97, 2006.

[3] O. Piccin, N. Kumar, L. Meylheuc, L. Barbé, and B. Bayle. Design, development and preliminary assessment of grasping devices for robotized medical applications. In *ASME 2012 IDETC/CIE*, pages 65–73, 2012.

[4] R. Motro. *Tensegrity: Structural Systems for the Future*. Butterworth-Heinemann, June 2003.

[5] S. Abdelaziz, L. Esteveny, L. Barbé, P. Renaud, B. Bayle, and M. De Mathelin. Design of an MRI-compatible cable-driven manipulator with original instrumentation and synthesis methods. *J Mech Des*, May 2014.

[6] I. Bricault, E. Jauniaux, N. Zemiti, C. Fouard, E. Taillant, F. Dorandeu, and P. Cinquin. LPR: A Light Puncture Robot for CT and MRI Interventions. *IEEE Eng Med Biol Mag*, 27(3):42–50, May 2008.

[7] S.D. Guest. The stiffness of tensegrity structures. *IMA J Appl Math*, 76(1):57–66, January 2011.

[8] J. L. Herder. *Energy-free systems: theory, conception, and design of statically balanced spring mechanisms*. PhD thesis, November 2001.

[9] S.A. Migliore, E.A. Brown, and S.P. DeWeerth. Biologically inspired joint stiffness control. In *Proceedings of the 2005 IEEE Int Conf Robot Autom*, pages 4508–4513, April 2005.

Robotized needle steering with 3D ultrasound feedback for prostate brachytherapy

Paul Mignon[a,b], Philippe Poignet[b], Jocelyne Troccaz[a].

[a] *University J. Fourier, TIMC Laboratory, Domaine de la Merci, 38706 La Tronche, France*

[b] *University Montpellier II, LIRMM, 161 rue Ada, 34095 Montpellier, France*

1 Introduction

Needle-based surgical interventions like brachytherapy aim at guiding the needle tip to a precise location in 3D space. Unfortunately some issues such as tissue deformation, presence of critical areas in needle path or unintentional needle bending prevent clinicians to reach high precision.

In this context needle insertion robot has proved to be a helpful solution to increase clinicians precision. A source of significant improvement could be the control of needle bending during insertion, which is called needle steering. However an essential difficulty for needle steering lies on needle visual detection used as feedback.

A well-known method to reach needle shape reconstruction is to use medical imaging. One of the most widely used imaging device in interventional procedures is the ultrasound (US) imaging. It is relatively easy to implement, inexpensive and safe for patient but suffers from lack of definition and presence of artifact due to acoustic properties. Needle detection therefore needs strong image processing.

2 Needle steering approach

2.1 Related work

Robotic needle steering devices are very promising for clinical interventions. Thus many studies deal with needle steering problematic but only two main approaches emerge. One of them use the force and moment applied on the needle base to guide the tip in the tissue. The other approach use the force acting on an asymmetrical beveled needle tip during the insertion to bend the needle (see Figure 1).

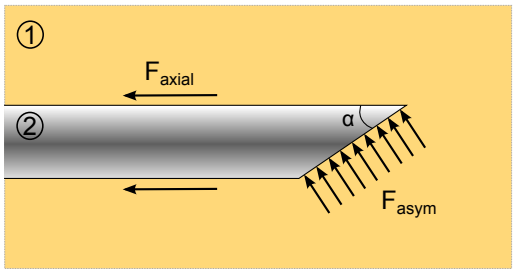

Figure 1: Illustration of the asymmetrical forces F_{asym} applied on beveled needle tip, and axial forces applied on all the needle during insertion. Note that 1 represent tissue or phantom, 2 needle material and α needle bevel angle.

The second approach led to a number of robotic steering devices and some of them add real-time path replanning to increase efficiency[1]. Another work led by Wood et al. [2] uses duty-cycle rotation during needle insertion in order to modify the needle curvature and allows more paths to be done.

2.2 Experimental setup

This work is included in the PROSPER project in Grenoble. A percutaneous-needle-insertion robot for brachytherapy intervention has been developed and is associated with non-rigid prostate registration [3]. This robot could insert straight needle precisely with specific angle and has already raised seed insertion precision up to 75 % compared to an insertion device without prostate registration. The needle can also rotate during the insertion and allows duty-cycle rotation to be performed. The aim of this work is to increase significantly the precision of this previously designed robotic device by reducing the off-needle-axis error using needle steering.

3 Needle shape detection in 3D US volume

3.1 Related Work

In ultrasound image, needle's voxels are usually brighter than those of the medium, for this reason detection algorithms generally use image threshold as a first segmentation step.

Two main methods are then used : projection of the volume on several planes or direct 3D algorithm. After projecting the volume using various algorithm, lines or curves in 2D images are detected using classical algorithms or other novel methods [4]. 3D direct needle reconstruction avoid projection which can save computational time. A 3D technique which shows good results to detect shape in a noisy medium is the Random Sample Consensus (RANSAC) [5]. This algorithm use randomization to find a curve which fit best needle's voxels and reject noise.

3.2 Experimental setup

A RANSAC algorithm inspired by [6] has been implanted on a C++ program and could detect needle shape using a

Bezier curve of any order (see figure 2).

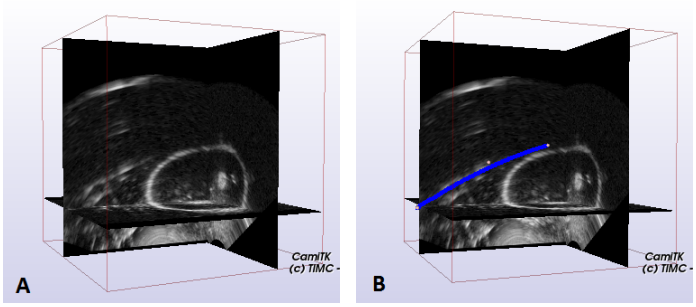

Figure 2: Illustration of the needle segmentation using 3D RANSAC algorithm. (A) US volume before segmentation. (B) US volume after segmentation

This program is associated with an Ultrasonix Sonix RP Device and 4DEC9-5/10 Ultrasonix probe. Another program was developed on the Sonix RP device to acquire 3D ultrasound volume. The association of these two programs thanks to CamiTK framework allows volume to be acquired and needle shape to be detected in the same application.

3.3 Results

Thanks to the detection program, needle can be segmented using a Bezier curve shape in a lapse of time of 1 or 2 s. This result is obtained by reducing the volume interest with a prior knowledge of the needle location given by the robot and a rigid registration between robot frame is ultrasound frame. This shape is displayed on screen and can by modified at any time by the clinician by moving Bezier curve control points coordinates. This adds safety to the system by preventing needle false detection.

4 Future work

Further experiments will be done to quantify detection algorithm precision, and check influence of parameters such as threshold value. The needle insertion will be performed step by step, so that previous detections could be used to improve future detection by adding a Kalman filter as in [6].

The asymmetrical beveled needle tip approach will be performed and associated with 3D US needle shape detection, adding a visual feedback in order to control needle path during the insertion. The insertion will be performed by the PROSPER robot, using its capability to rotate the needle to modify needle curvature during the insertion. A real time path planner inspired by the work of M.Bernardes[1] will be implanted and will allow automatic or semi-automatic needle insertion to be performed.

Needles used in brachytherapy have significant diameters (up to 1 mm or more). However the needle unicycle model uses the hypothesis that the forces exerted by the needle on the tissue are not insignificant which is not verified with brachytherapy needles. In order to add precision to our path planning we will propose a novel needle-tissue interaction based on virtual springs. This model will help to predict needle bending and to choose correct parameters for insertion.

5 Conclusion

An image processing algorithm has been implemented to detect needle shape in noisy medium such as US volume. It directly uses 3D RANSAC algorithm to find an approximate shape. A needle steering approach based on the force acting on the needle tip during insertion will allow needle tip to be guided in the tissue. The needle shape detection will be used as feedback for needle steering.

6 Acknowledgment

This work was partly supported by the French ANR within the Investissements d'Avenir program (Labex CAMI) under reference ANR-11-LABX-0004.

References

[1] M.C. Bernardes, B.V. Adorno, P. Poignet, and G.A. Borges. Semi-automatic needle steering system with robotic manipulator. In *Robotics and Automation (ICRA), 2012 IEEE International Conference on*, pages 1595–1600, 2012.

[2] Nathan A Wood, Khaled Shahrour, Michael C Ost, and Cameron N Riviere. Needle steering system using duty-cycled rotation for percutaneous kidney access. In *Engineering in Medicine and Biology Society (EMBC), 2010 Annual International Conference of the IEEE*, pages 5432–5435. IEEE, 2010.

[3] N. Hungr, M. Baumann, J.-A. Long, and J. Troccaz. A 3-d ultrasound robotic prostate brachytherapy system with prostate motion tracking. *Robotics, IEEE Transactions on*, 28(6):1382–1397, 2012.

[4] Stephen H. Okazawa, Richelle Ebrahimi, Jason Chuang, Robert N. Rohling, and Septimiu E. Salcudean. Methods for segmenting curved needles in ultrasound images. *Medical Image Analysis*, 10:330 – 342, 2006.

[5] Martin A Fischler and Robert C Bolles. Random sample consensus: a paradigm for model fitting with applications to image analysis and automated cartography. *Communications of the ACM*, 24(6):381–395, 1981.

[6] Alexandre Krupa Pierre Chatelain and Maud Marchal. Real-time needle detection and tracking using a visually servoed 3d ultrasound probe. *Conference ICRA 2013*, 2013.

3D Ultrasound Probe Calibration Using Robotic Arm and Image Registration

Johan Sarrazin *[1,2], Emmanuel Promayon[2], Michael Baumann[1] and Jocelyne Troccaz[2]

[1]KOELIS SAS, 5. av. du Grand Sablon, La Tronche, F-38700,France
[2]UJF-Grenoble 1 / CNRS / TIMC-IMAG UMR 5525, Grenoble, F-38041, France

October 31, 2014

Keywords *- Hand-Eye Calibration, 3D Ultrasound*

Providing accurate localization data in UltraSound (US) robotized image guided interventions can greatly assist the surgeon to puncture specific areas. To precisely locate the targets, it is necessary to perform a calibration step before the intervention. We present a calibration method based on both 3D US image registration and robot kinematic model or localizer.

1 Introduction

3D US imaging is a widely valuable technique used in many clinical applications. Ultrasound imaging provides a good compromise between the image quality, the acquisition time, the convenience and the ease of use when other modalities, such as MRI or CT scan, are difficult to set-up and to use during interventions. In image guided intervention, the use of a US probe held by a robot enables the surgeons to have a better accuracy when they puncture a clinical target [1] by providing localization data. It can also help to efficiently follow up medical targets in space. But a calibration of the probe with the robot is necessary. A lot of methods have been developed, during the last decade, to perform fast and robust 3D robot probe calibration. These methods, generally require adding external equipment such as tracking devices, planar calibration rigs or large phantoms [2, 3]. The lack of space or the sterilization standards in the operating room can prevent the use of such a technique.

Based on this observation, we propose a method to calibrate an US probe held by a robot by only using the registration of 3D US images and data generated by the robot kinematic model. This calibration method can be performed either on the image reference frame or with a virtual reference frame directly based on the transducers. The latter one avoids the computation of a new extrinsic calibration each time a US imaging parameter is modified (e.g, probe depth or the scale). The use of a tracker is not needed as the calibration can be performed without any external equipment.

*johan.sarrazin@imag.fr

2 Proposed Method

The calibration process is based on the hand-eye calibration algorithm, see Fig.1, developed by [5] and adapted for our own use. The principles of the method, presented here, are to acquire a dataset of robot movements and the corresponding image registrations computed from the acquired 3D US images. These data are then used to solve the equation $AX = XB$.

As it is shown in Fig.1, A_i corresponds to the transformation matrices from the reference space to each robot position (i.e., a virtual reference on the arm that holds the probe). These A are provided by the robot kinematic model at each position. B_i are the transformation matrices from each image frame to the reference image space. B are provided by an image registration algorithm. X is the resultant matrix. It mathematically binds the robot space to the image space by giving a homogeneous transformation matrix.

By solving this equation, the image spaces and the robot positions can be expressed in the same reference space. Thus, any further images could be expressed in the same space, by means of the X matrix and the A and B matrices of the current acquisition, allowing the system to follow-up or to target clinical areas.

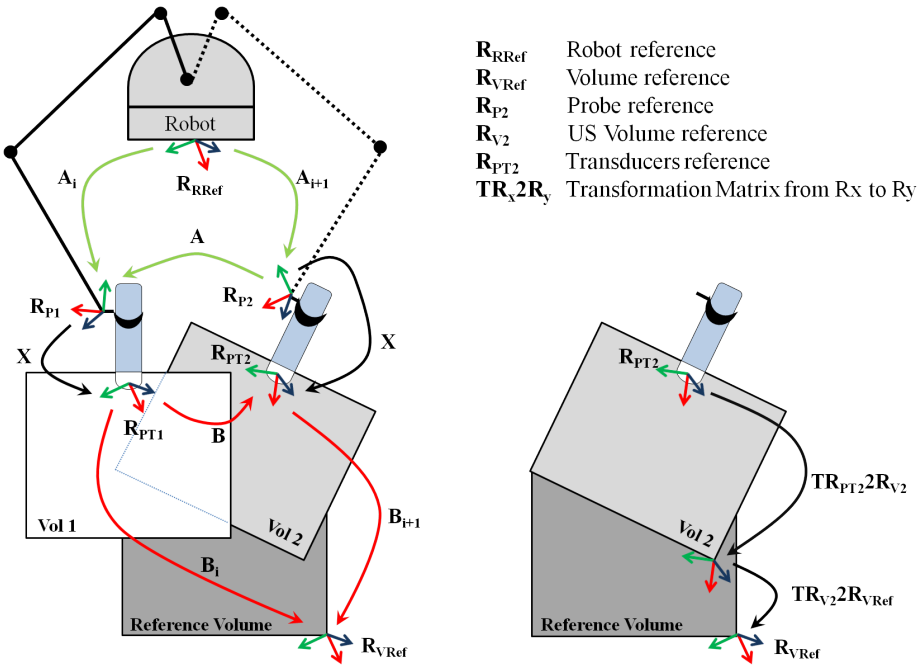

Figure 1: Schema of the Hand-eye Calibration problem in our context. On the left, the general schema is shown. On the right, the calibration with transducers is drawn.

To improve the robustness of our method, the calibration is done by computing for each image an affine frame directly positioned at the probe transducers.

To insert the probe transducers frame as an input of our method, we have to consider the B matrices as: $B_i = TR_{Vi}2R_{VRef}.TR_{PTi}2R_{Vi}$, where $TR_{PTi}2R_{Vi}$ is the transformation matrix from the probe transducers affine frame (R_{PTi}) to the image frame (R_{Vi}). $TR_{V2}2R_{VRef}$ is the transformation matrix from the current acquired volume to the reference volume, i.e., $P_{(VRef)} = TR_{Vi}2R_{VRef}.P_{(Vi)}$.

3 Experiment and Results

The work presented here is tested with a 3D transrectal ultrasound (TRUS) probe, a localizer [6] and a small phantom (16x12x9cm) designed for this purpose, see Fig 2. A rigid polyvinyl chloride (PVC) mixture and a standard one have been used to construct the phantom [4]. The particularity of these PVC are the speed of sound which is approximately the same as human tissue. It is approximately $1540m\backslash s$ for the human tissues and respectively $1580m\backslash s$ and $1440m\backslash s$ for the two mixtures used.

The phantom is composed of a prostate, including beads, and shapes in order to facilitate registration between the images. Beads and shapes are used to estimate the calibration accuracy. The prostate was segmented in a real patient MRI. A PVC model was made from the resulting geometry to obtain a real anatomic shape.

We used an optical localizer to simulate the robot to have preliminary results. A rigid-body is fixed on the probe to track its positions during the calibration. The system localizer/rigid-body can be used to replace the robot system. Both of the systems give, at each acquisition, a reference frame allowing the process of calibration. As far as the acquired image is sufficient to compute a good registration, any kind of data can be used to calibrate the robot-probe system and no extra equipment is required.

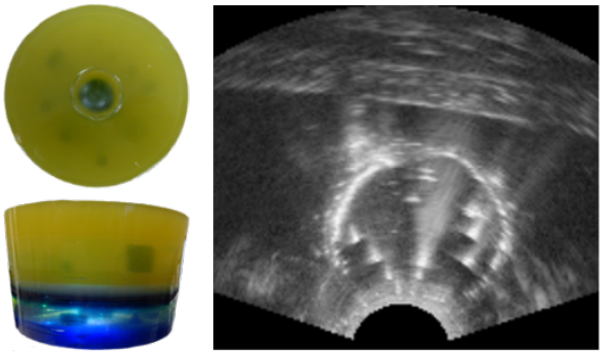

Figure 2: From left to right: the top view and the profile view of the phantom and a resulting US slice.

A first test has been performed and gives a Root Mean Square distance error (RMSe) of 2.27mm for the image reference frame calibration. The calibration with the transducers virtual reference frame gives an RMSe of 2.33mm. To compute this error, 8 beads have been segmented in 7 of the 9 image spaces used

in the calibration, and re-projected in the localizer reference frame thanks to the calibration. Thus, we can observe bead positioning errors. The calculation represents the ability to exactly compute the position of targets, found in the image space, in the reference space or in another one.

4 Conclusion

We presented a method to calibrate a robot-US probe system without using extra equipment. As a first test, we used an optical localizer to simulate the robot in order to check the viability of the calibration. The results are encouraging but they have to be improved by enhancing the segmentation and the robustness of the experimentation. This method is robust as the calibration can be performed on an affine frame representing the probe transducers. As a result, the calibration is not image dependent anymore. This leads to eliminate the error induced by changing the acquisition parameters such as depth, frequency, etc. These parameters have an influence on image reconstruction and give misleading results if they changed during or after the procedure with a calibration based only on the image spaces.

Acknowledgements-This work is supported by Koelis, ANRT and ANR grants (PROSBOT project ANR-11-TECS-0017 and CAMI labex ANR-11-LBX-0004). We also would like to thank Voros, S., and Agustinos, A. for their help.

References

[1] Kim, C., Chang, D. Petrisor, D., Chirikjian, G., Han, M., Stoianovici, D.: Ultrasound Probe and Needle-Guide Calibration for Robotic Ultrasound Scanning and Needle Targeting. IEEE Transactions on Biomedical Engineering, vol 60, no 6, 1728–1734 (2009)

[2] Bergmeir, C., Seitel, M., Frank, C., De Simone, R., Meinzer, H-P., Wolf, I.: Comparing calibration approaches for 3D ultrasound probes. International journal of computer assisted radiology and surgery 4, 203–213 (2009)

[3] Baumann, M., Daanen, V., Leroy, A., Troccaz, J.: 3-D Ultrasound Probe Calibration for Computer-Guided Diagnosis and Therapy. Proceedings of CVAMIA'06 4241, 248–259 (2006)

[4] Hungr, N., Long, J-A., Beix, V., Troccaz, J.: A realistic deformable prostate phantom for multimodal imaging and needle-insertion procedures. Medical Physics 39, 2031–2044 (2012)

[5] Zhao, Z.: Hand-Eye Calibration Using Convex Optimization. IEEE International Conference on Robotics and Automation, 2947–2952 (2011)

[6] Poquet, C., Mozer, P., Vitrani, M.A., Morel, G.: An Endorectal Ultrasound Probe Comanipulator With Hybrid Actuation Combining Brakes and Motors. Mechatronics, IEEE/ASME Transactions on, 1–11 (2014)

Feature Comparison for Unsupervised Laparoscopic Video Retrieval

Andru Putra Twinanda, Michel De Mathelin, and Nicolas Padoy

ICube, University of Strasbourg, CNRS, IHU Strasbourg, France
{twinanda,demathelin,npadoy}@unistra.fr

Keywords: laparoscopic videos, visual features, task retrieval, HOG, SIFT.

Along with the improvement of camera technology, the volume of multimedia data, i.e. images and videos, has been growing exponentially in the last decade. Such improvement also affects the domain of medicine, especially in minimally invasive surgery (MIS). By introducing an endoscope to the procedure, MIS allows the recording of large amount of videos. These videos contain invaluable information regarding the execution of procedures in various patient-specific conditions. The information, for instance surgeons' techniques in performing specific tasks, can later on be exploited for teaching purposes, assistance during difficult cases, and quality evaluations. Up to this point, such information can only be obtained by manually browsing the videos one by one. In order to facilitate the access to this information, semantic annotations can be attached to the videos. However, as the laparoscopic videos build up to an overflowing amount, performing the semantic annotation manually is rendered impractical and expensive.

In summary, it is required to have a system that: (1) allows the access to the afore-mentioned information in the laparoscopic video database, and (2) works with limited supervision so that the need for manual annotation can be reduced. In particular, we are interested in the problem of finding the time boundaries (the beginning and ending) of a task T in surgical videos by providing a single video snippet of task T. With such system, fellow surgeons can study the execution of a particular task in various patient conditions. In addition, the system can also give boundary candidates to aid the process of semantic annotation.

One possible solution to this retrieval problem was proposed by Chu et. al. in [1]. Within an unsupervised framework, they introduced the temporal commonality discoveries (TCD) method, which is an approach to find the time boundaries of the common events happening in two videos. The method ensures global optimality by carrying out the boundary search through a branch and bound (B&B) optimization with histogram encoding and l_1/χ^2 bounding distance.

Another solution was presented in [2] by Twinanda et. al. who argued that the global optimality of TCD comes at the cost of a suitable similarity measure. Namely, TCD enforces the use of histogram encoding. In addition, [2] also argued that despite the optimization, the B&B still carries out too many evaluations, thus taking a long time to find the task boundaries for one video. As a solution, a greedy coarse-to-fine approach combined with the Fisher Kernel (FK) encoding was proposed. With such approach, the method improved the performance and

the speed of the task retrieval. It was also shown that the similarity measures on FK encoding are better suited to this problem than the ubiquitous similarity measure *dynamic time warping* (DTW) [3]. We refer to this method as Single-FK since only histogram of gradients (HOG) feature was used.

Inspired by the success of Single-FK, we would like to investigate the effect of feature combination on the performance of the coarse-to-fine approach. In this work, we propose to extend the approach by performing similarity measures on multiple features, by using the combination of SIFT (scale-invariant feature transform) and HOG features. In addition, we also incorporated the usage of multiple greedy initializations into the approach in order to obtain better initialization of the boundary candidates. We name this method Multi-FK.

To observe the performance of Multi-FK, we tested the method on the same dataset as in [2], which is explained in detail in Table 1. The dataset consists of 4 tasks: intestine stitching (IStitch), intestine stapling (IStaple), fat stitching (FStitch), and mesh placing (MPlace). Specifically, the distribution of the tasks is as follows: 2 tasks in 49 bypass videos, 1 task in 45 bypass videos, and 1 task in 23 hernia videos. To check the robustness of the method, we also carried out 1 cross-surgery task retrieval between 49 bypass and 7 sleeve gastrectomy videos. In total, the dataset contains 79 surgeries performed by 8 surgeons. The experiments were carried out similarly to the ones of [2]: by taking 4 random video snippets for each task and retrieving their time boundaries in the remaining videos. This process was repeated 5 times. In addition, we keep the same underlying assumption that the task was present in every target video.

For comparison, we put the results of Multi-FK alongside with other methods in Table 2. As expected, Multi-FK takes longer time to find the task time boundaries than Single-FK, but still takes shorter time than TCD. However, it can be seen that a very significant improvement can be achieved by Multi-FK, with increasing precisions and recalls up to 15% and 13% respectively. Thus, we can conclude that the combination of features and the multiple initialization scheme significantly improve the performance of the coarse-to-fine approach.

Acknowledgements

This work was supported by the French ANR within the Investissements d'Avenir program under references ANR-11-LABX-0004 (Labex CAMI), ANR-10-IDEX-0002-02 (IdEx Unistra), and ANR-10-IAHU-02 (IHU Strasbourg).

References

1. Chu, W.S., Zhou, F., De la Torre, F.: Unsupervised temporal commonality discovery. In: ECCV. (2012)
2. Twinanda, A.P., Mathelin, M.D., Padoy, N.: Fisher kernel based task boundary retrieval in laparoscopic database with single video query. In: MICCAI. (2014)
3. Sakoe, H.: Dynamic programming algorithm optimization for spoken word recognition. IEEE Trans. on Acoustics, Speech, and Signal Processing **26** (1978) 43–49

Task	Surgery Type	#Surg.	Avg. Len. (min.)	
			Task	Surgery
IStitch	Bypass	49	14 ± 5	111 ± 27
	Sleeve Gast.	7	25 ± 8	109 ± 16
FStitch	Bypass	49	6 ± 2	111 ± 27
IStaple	Bypass	45	7 ± 5	114 ± 26
MPlace	Hernia	23	4 ± 2	50 ± 25

Table 1. The details of the tasks and surgeries: the number of surgeries containing the task, the length of task and videos in minutes (mean ± std).

Task	Q→T	TCD [1]			DTW [3]		
		Prec (%)	Rec (%)	Time (s)	Prec (%)	Rec (%)	Time (s)
IStitch	B→B	70.91	78.26	33 ± 21	40.91	41.83	2.7 ± 1.7
	B→S	58.57	**22.14**	45 ± 24	35	8.5	2.3 ± 1.5
FStitch	B→B	37.44	38.19	21 ± 12	20.51	16.73	0.9 ± 0.5
IStaple	B→B	10.02	12.44	26 ± 17	9.55	9.44	1.6 ± 1.5
MPlace	H→H	19.47	18.52	9 ± 8.2	11.3	10.86	0.5 ± 0.3

Task	Q→T	Single-FK [2]			Multi-FK		
		Prec (%)	Rec (%)	Time (s)	Prec (%)	Rec (%)	Time (s)
IStitch	B→B	78.57	77.85	4.4 ± 3.3	**87.24**	**85.40**	17 ± 15
	B→S	59.28	19.28	1.9 ± 0.5	**67.86**	20.00	24 ± 18
FStitch	B→B	53.51	45.61	0.3 ± 0.2	**61.83**	**54.49**	7.3 ± 4.9
IStaple	B→B	23.44	26	2.4 ± 1.2	**38.78**	**39.22**	20 ± 17
MPlace	H→H	38.04	31.95	2.2 ± 1.2	**38.48**	**34.35**	4.3 ± 3.0

Table 2. Comparison of precision, recall, and execution time (mean ± std) between TCD, DTW, Single-FK, and Multi-FK. Q and T respectively stand for query and target. We use the first letter of the surgery to identify them, thus B, S, and H respectively represents bypass, sleeve gastrectomy, and hernia. For instance, B→S means searching the task in sleeve gastrectomy videos with a video query taken from bypass videos.

Surgical Process Model of laparoscopic rectopexy

A. Huaulmé[1], S. Voros[1], F. Reche[2], J.L. Faucheron[2], P. Jannin[3,4], A. Moreau-Gaudry[1,5].
[1]UJF-Grenoble1 / CNRS / INSERM, TIMC-IMAG UMR 5525, Grenoble, F-38041, France
[2]Surgery Department, CHU Grenoble, Grenoble, France
[3]INSERM, UMR 1099, Rennes, F-35000, France
[4]Université de Rennes 1, LTSI, Rennes, F-35000, France
[5]UJF-Grenoble1 / CHU Grenoble / INSERM, Centre d'Investigation Clinique - Innovation Technologique, CIT803, Grenoble, F-38041, France

1. State of the art and objectives

a. Main objective

Surgical process modeling (SPM), was introduced in laparoscopy[1] and neurosurgery [2] for the purpose of:

1) Formalizing surgical knowledge,
2) Evaluating surgical skills and systems,
3) Better assisting the surgeon during the intervention.

However, this type of model do not exist, to the best of our knowledge, for laparoscopic rectopexy, although it is a standardized surgery. The majority of works on evaluation of rectopexy focused on surgical outcome based on preoperative data and without taking into account the course of the surgical intervention [3], [4]. However, this intraoperative description may potentially help the surgeon to better compare his technique to the model with, as consequences, the possibility of avoiding some complications.

The main objective of this study is to model the "typical" rectopexy by the Orr-Loygue's technique [5] using SPM methodology. Its principle consists in fixing the anterolateral rectum to the anterior vertebral ligament with 2 meshes body to correct rectal prolapse. The Orr-Loygue's technique has some variations across surgical teams, but we chose to focus on the Grenoble's technique. This "proof-of-concept" methodology and model could then be extended to other techniques.

b. Second objective

Surgical process models will be used for studying deviations that may happen during surgery. We focus on two types of deviations that can occur in a surgical process. Deviations caused by the patient's anatomical particularities (AP) and deviations caused by the surgeon's gestures (SG).

The first type of deviation can generate the second type of deviation, for example the section of micro-vessel during an adhesiolysis can only occur if the patient has adhesions.

According to the French National Authority for Health (HAS) [6] the deviations caused by AP are part of deep causes (*"circumstance, act or element susceptible to have participated in the birth or in the arisen of an incident or to have increased the risk of serious adverse event"*). The involuntary SG deviations are part of immediate causes (*"objective cause more immediately linked in the arisen of*

adverse event"). The HAS also defines an adverse event as *"a situation which moves away from procedures or from expected results in a usual situation, and which is or which would be potentially a source of damage"*.

2. Method

In order to model a "typical" rectopexy and the deviations from this "ideal" surgery, we need to acquire the surgical terminology, the sequence of events involved in a rectopexy, the deviations from the "typical" surgery and their causes. For this, we chose to use cognitive task analysis (CTA) [7], [8]. Although more than 100 types of CTA methods were identified, most of them use a five-stage process:

1) Collect preliminary knowledge,
2) Identify knowledge representations,
3) Apply focused knowledge elicitation methods,
4) Analyze and verify data acquired,
5) Format result for the intended application.

This five-stage process is an iterative process, with a loop between stages three and four until the data is considered complete.

a. Stages of CTA

The first stage is performed so the analyst can become familiar with the knowledge domain, and allows to identify experts of the field. We used three common techniques: documents analysis, unstructured interviews and unobtrusive observations. We also identified three experts, two for the elicitation process (stages 3 and 4) and one for the validation (stage 4).

For the knowledge representations, we chose an ontology still under development by P. Jannin *et. al.* inspired by is work in [2]. This ontology based on three main concepts: phase, step and activity.

For the third stage (ongoing work) we use two elicitation methods: semi-structured interviews and observations. Elicitation is the process which leads an expert to clarify his automated procedural knowledge, i.e. the knowledge which became an automatism with years of practice.

The fourth stage also uses interviews to validate the result of the elicitation process with the experts.

In the fifth stage, the results of the elicitation process are incorporated in the knowledge representations chosen in step 2.

b. Interviews

Unstructured interviews are used in the first stage of the CTA where the expert is asked to explain the reasons for a rectopexy and its principle. Semi-structured interviews are used in the elicitation process. They allow 1) catching the medical vocabulary describing the sequence of events involved in a "typical" rectopexy and 2) catching the immediate causes of adverse events that result in deviations of

this “typical” surgery. Finally the model validation (step 4) is performed through semi-structured interviews.

c. Observations

Unobtrusive observations are used in stage 1 of the CTA: the elicitor observes the surgical intervention without interaction with the medical staff or equipment. The purpose of this type of observation is to understand the global environment of the surgery.

In the third stage, observations are based on laparoscopic videos. The observation is performed with or without a surgeon explaining what happened in the video. It allows better understanding of the sequence of events performed, or the identification of some information extracted from the interviews.

3. Results and perspectives

Thanks to this preliminary work, we were able to describe the “typical” rectopexy with medical vocabulary on the granularity of phases and steps. We identified three phases and eighteen steps, but they must still be validated.

Our next stages will be to describe this surgery at a lower level of granularity (the activities) and identify the immediate causes, and if possible adverse events.

Acknowledgment: This work was partly supported by the French ANR within the Investissements d'Avenir program (Labex CAMI) under reference ANR-11-LABX-0004.

4. Bibliography

[1] N. Padoy, T. Blum, S.-A. Ahmadi, H. Feussner, M.-O. Berger, and N. Navab, “Statistical modeling and recognition of surgical workflow,” *Med. Image Anal.*, vol. 16, no. 3, pp. 632–641, avril 2012.

[2] P. Jannin and X. Morandi, “Surgical models for computer-assisted neurosurgery,” *NeuroImage*, vol. 37, no. 3, pp. 783–791, Sep. 2007.

[3] J. L. Faucheron, D. Voirin, F. Reche, and A. Dubreuil, “Résultats techniques de la rectopexie au promontoire par voie cŒlioscopique pour prolapsus total du rectum : Evaluation prospective chez 100 patients consécutifs,” *J. Coelio-Chir.*, no. 63, pp. 40–43, Sep. 2007.

[4] C. B. Samaranayake, C. Luo, A. W. Plank, A. E. H. Merrie, L. D. Plank, and I. P. Bissett, “Systematic review on ventral rectopexy for rectal prolapse and intussusception,” *Colorectal Dis.*, vol. 12, no. 6, pp. 504–512, 2010.

[5] D. Lechaux, “Traitement des prolapsus du rectum par abord laparoscopique,” *EMC - Tech. Chir. - Appar. Dig.*, vol. 2, no. 1, pp. 1–7, Jan. 2007.

[6] “Haute Autorité de Santé.” [Online]. Available: www.has-sante.fr. [Accessed: 11-Jun-2014].

[7] R. E. Clark, D. Feldon, J. J. van Merriënboer, K. Yates, and S. Early, “Cognitive task analysis,” *Handb. Res. Educ. Commun. Technol.*, vol. 3, pp. 577–593, 2008.

[8] D. H. Jonassen, M. Tessmer, and W. H. Hannum, *Task analysis methods for instructional design*. Psychology Press, 1999.

An Ontology-based Software Suite for the Analysis of Surgical Process Model

Charles Garraud[1], Bernard Gibaud[1,2,3], Cedric Penet[2,3], Guy Cazuguel[1,4,5], Guillaume Dardenne[1], and Pierre Jannin[1,2,3]

[1]Institut de Recherche Technologique b-com, Rennes, F-35000, France
[2]INSERM, UMR1099, Rennes, F-35000, France
[3]Université de Rennes 1, LTSI, Rennes, F-35000, France
[4]Inserm, LATIM UMR1101, Brest, F-29200, France
[5]Institut Mines-Telecom; Telecom Bretagne; UEB; Dpt ITI, Brest, F-29200, France

October 14, 2014

1 Purpose

Todays surgical routines are constantly evolving and adapting to new technological innovations. However, most innovative systems lack flexibility and do not properly fit specific surgical needs. As a result, surgery actors in the operating room (OR) are being faced with ever-increasing process complexity. The field of surgical process model (SPM) has recently emerged and aims at better understanding OR activities in order to accurately meet specific procedure requirements [1]. SPMs are used to describe surgical interventions in a formal way for further analysis or visualization. Software applications have been developed recently to support acquisition of SPMs pre and post-operatively [3]. Our objective is to introduce an ontology-based software suite capable of building and post-processing such SPMs in a robust and reproducible way.

2 Method

The software system consists of a main application built upon task-oriented modules. All subsystems are based on a common framework.

2.1 Common Framework

The formal description of surgical activities can be challenging and rely on procedure dependent notions. Our approach to represent these domain-specific concepts is based on the ontological knowledge representation formalism : "In computer science, an ontology is an engineering artifact, usually a model of (some aspect of) the world; it introduces vocabulary describing various aspects of the domain being modeled and provides an explicit specification of the intended meaning of that vocabulary" [4]. The common framework implemented in C++ relies on such ontologies in two ways a) The model layer used to represent SPMs fits the base concepts defined in a core ontology (OntoSPM [5]) b) The data access layer queries a database built manually from domain-specific ontologies to load taxonomy and rules related to a given procedure.

2.2 Observation Module

The module aims at building SPMs by recording surgical activities of any actors involved in a specific procedure. Recording SPMs can be performed either intra-operatively (live mode) or post-operatively (offline mode) with the support of external media (video of the procedure). Emphasis was placed onto a) *Robustness* to ensure safety and reproducibility b) *Ergonomics* to maximize efficiency and comfort during recording. Robustness was achieved through the use of state machines to control the module workflow. One key feature of the module is the ergonomics-driven implementation. Dynamic and adaptable graphical user interfaces (GUIs) were designed by domain experts. Furthermore, the runtime loading of procedure-specific taxonomy and rules helps configuring these GUIs with only the necessary and sufficient information.

2.3 Analysis Module

The module provides tools to make a time-based analysis of a set of SPMs. The main results are displayed graphically while an in-depth processing of the SPMs can be performed by exporting detailed metrics in CSV format.

3 Conclusion

The need for specific tools to better apprehend surgical routines arises from the increasing complexity in the OR due to the use of many heterogeneous medical devices. A formalized way of representing the information is required to achieve a thorough understanding of surgical procedures. In our software suite, the ontological knowledge representation formalism assists in implementing a dual strategy of completeness and accuracy to describe surgical processes. The first requirement was achieved through the conceptual match with a core ontology while the precision aspect was reached by using domain-oriented inherited ontologies.

References

[1] Lalys, F., Jannin, P. *Surgical process modelling: a review*, International Journal of Computer Assisted Radiology and Surgery, (2014), 495-511.

[2] Jannin, P., Raimbault, M., Morandi, X., Riffaud, L., Gibaud, B. *Models of Surgical Procedures for Multimodal Image-Guided Neurosurgery*, Journal of Computer Aided Surgery, (2003), 98-106.

[3] Neumuth, T., Mudunuri, R., Jannin, P., Meixensberger, J., Burgert, O. *SWAN-Suite: The tool landscape for surgical workflow analysis*, Computer Assisted Medical and Surgical Interventions (SURGETICA), (2007), 199-204.

[4] Horrocks, I. *Ontologies and the semantic web*, Commun. ACM, (2008), 58-67.

[5] Gibaud, B. et al *OntoSPM: a core ontology of surgical procedure models*, SURGETICA, (2014).

Reconstruction of 3D dose distribution in external beam radiotherapy using portal imaging

Laurence Autret[1], Julien Bert[1], Saadia Benhalouche[1], Laurent Desbat[2], Dimitris Visvikis[1]

[1] UMR1101 INSERM LaTIM, Brest
[2] TIMC-IMAG, CNRS and Université Joseph Fourier (UMR5525) Pavillon Taillefer, Grenoble

The verification of the dose delivered to a patient during radiation therapy is a particularly important step for ensuring treatment quality. This step, known as *in vivo dosimetry* can be realized using punctual dosimeters. However, for most current state of the art irradiation techniques such as IMRT (Intensity Modulation Radiation Therapy) or VMAT (Volumetric Modulated Arc Therapy), these dosimeters do not represent sufficiently the dose distribution inside the patient. An alternative approach, named *transit in vivo dosimetry* and based on portal imaging, represents an extension of *in vivo dosimetry* to those techniques. An EPID (Electronic Portal Imaging Device) placed behind receives the dose through the patient, giving a 2D dose map of the transmitted dose. The acquisitions of such 2D dose maps around the patient can allow the calculation of a 3D dose distribution delivered to the patient. The aim of my work is to develop a real-time patient specific 3D dose reconstruction, for the latest irradiation techniques such as VMAT, based on Monte Carlo simulations accounting for both physical and geometrical distortions.

Several methods of 3D dose reconstruction are described in the literature. Some of them are based on the back projection through the voxelized patient of the primary contribution of the dose, extracted from the 2D EPID images. The dose deposited in each voxel may then be calculated by convolving the primary signal entering the voxel with a dose deposition kernel [1] or using a Monte Carlo dose calculation algorithm [2]. In a more recently proposed 3D dose reconstruction approach [3], patient and EPID response impulse functions are supposed linear; during an irradiation, the cumulative dose in the EPID and in the phantom/patient plane are related by a linear system. As the dose signal acquired by the EPID is known for an irradiation, the resolution of the linear system simply relies on patient and EPID impulse response function estimations. This resolution leads to a 2D dose reconstruction in the considered phantom/patient slice. A 3D dose distribution may then be obtained by repeating this resolution step for each patient slice. In this work, Monte Carlo simulations are used to estimate these response functions. All physical phenomena are taken into account and included in impulse response function estimations. However, the computational time required for solving the proposed linear system, leading to the patient dose calculation, cannot be realized in clinical practice considering the size of the necessary impulse response matrices. The aim of my work is to adapt and to improve this method in order to reconstruct in *real-time* the 3D dose distribution inside the patient.

In the initial implementation of the proposed method [4], a mid-plane dose reconstruction in a homogeneous RW3 phantom (Octavius, PTW Freiburg Germany) and for a particular beam angle was obtained. In this reconstruction, an impulse signal, also called *beamlet*, is defined as a mm^2 squared field describing a mm^2 squared field in the intensity plane (Multileaf Collimator MLC plane). The measured and reconstructed dose distributions in the mid-plane phantom are presented and compared, using the gamma index test, on the following figures:

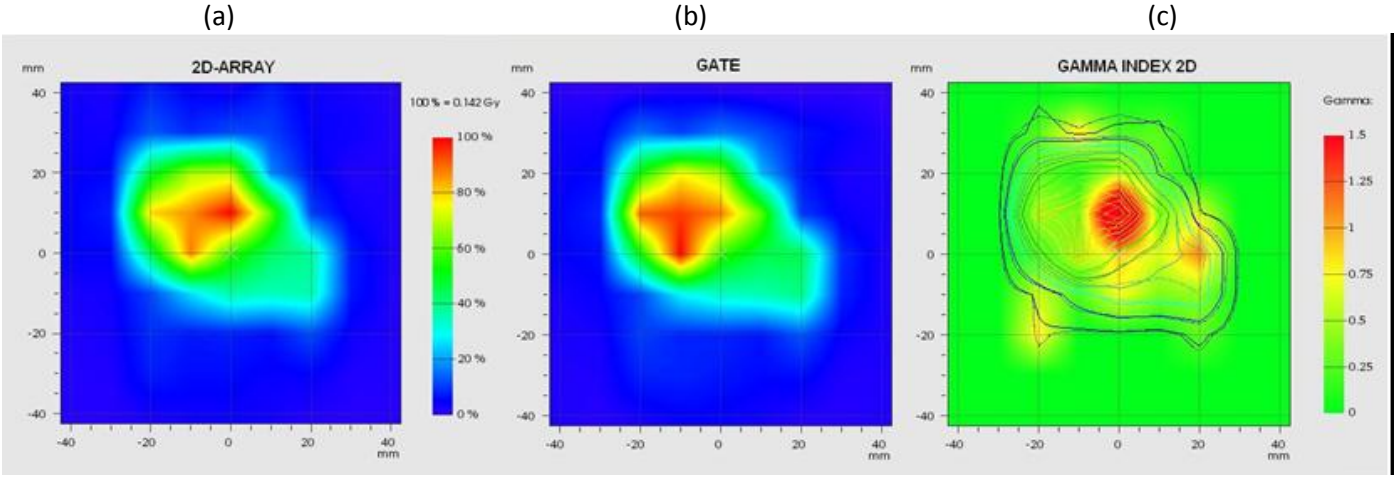

Figure 1: (a) Dose profiles measured with the 2D-Array matrix of ionization chamber in the plane of the Octavius phantom located at 99.6 cm from the source for an IMRT clinical field, (b) dose profiles reconstructed for the same opening field. (c) Gamma Index map for the 3% Dose difference and 3 mm Distance-To-Agreement.

The gamma index allows the comparison between the measured dose distribution which is the reference and the reconstructed dose distribution. For the acceptance criteria, an agreement distance limit of 3 mm and a maximal dose difference of 3 % were considered. A gamma index greater than 1 indicates the points which failed the test of acceptance criteria. 92% of the reconstructed dose points passed the gamma index test.

This 2D dose reconstruction was realized with impulse response matrices of small size. However, IMRT fields are frequently larger and such a reconstruction method requires the storage of large impulse response matrices.

A part of my work has therefore been dedicated to the study of impulse response matrix properties. The estimation of EPID and phantom impulse response functions were obtained using GATE, a Monte Carlo-based simulation platform [5].

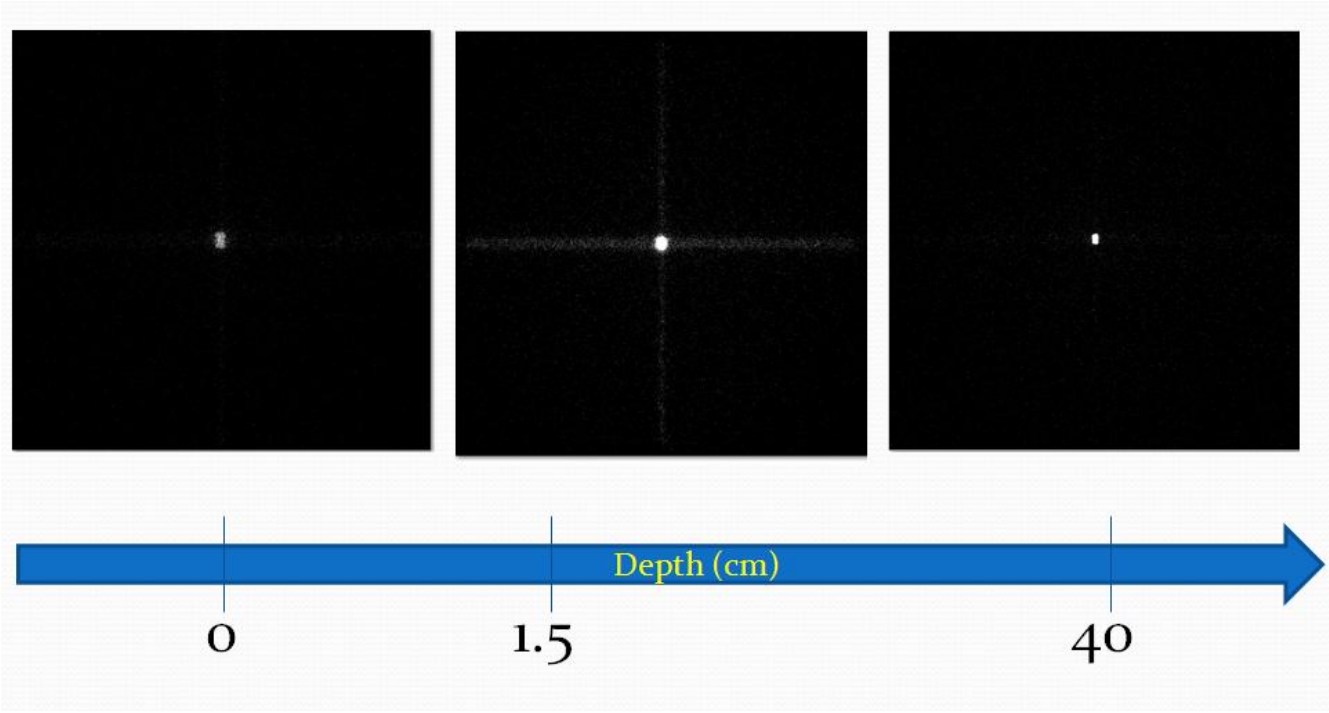

Figure 2: Dose impulse response functions to an impulse signal at different depths (GATE, Water Box).

Considering a homogeneous water medium, this study showed that dose impulse response matrices were large and sparse. This property is of interesting as far as operations needed for the calculation of the patient dose could be

done in a compressed domain, decreasing computational time and data-set dimensions. In order to provide a 3D dose distribution at the end of an irradiation fraction, impulse response matrices will be pre-calculated on Graphics Processing Units (GPU) during the treatment planning. Future work will explore different compression schemes for the dose impulse response matrices as well as the exploitation of Graphics Processing Units for the necessary Monte Carlo simulations.

This work was partly supported by the French ANR within the Investissements d'Avenir program (Labex CAMI) under reference ANR-11-LABX-0004.

[1] McNutt and al., Modeling dose distributions from portal dose images using the convolution/ superposition method, Med Phys 1996, 23(8)

[2] Jarry and Verhaegen, Patient-Specific dosimetry of conventional and intensity modulated radiation therapy using a novel full MC phase space reconstruction method, Phys. Med. Biol., 2007, 52(8)

[3] IJ Yeo and al., Dose reconstruction for intensity-modulated radiation therapy using a non-iterative method and portal dose image, Phys. Med. Biol., 2009, 54(17)

[4] Saadia Benhalouche, Julien Bert, Nicolas Boussion, Awen Autret, Olivier Pradier and Dimitris Visvikis: Imaging and Radiation Therapy: GATE Monte Carlo Simulation of a 6 MV photon beam LINAC and its MV-CBCT Flat Panel for IMRT applications. MCW 2014 Quebec.

[5] Jan and al., GATE: a simulation toolkit for PET and SPECT, Phys. Med. Biol., 2004, 49(19)

Observations of Lightly Flexible Needle Deflection in 3D CT/MRI*

E. Dorileo[1], N. Zemiti[1], P. Poignet[1], N. Hungr[2], I. Bricault[2], C. Fouard[2]

Research supported by ANR (National Research Agency – France): TECSAN project ROBACUS (ANR-11-TECS-020-01) and LABEX CAMI - Computer Assisted Medical Interventions (ANR-11-LABX-0004).

[1]E.D., N.Z. and P.P. authors are with LIRMM – Robotic Department, University Montpellier II, France.
e-mails: {Ederson.Dorileo, Nabil.Zemiti, Philippe.Poignet} @lirmm.fr.
[2]N.H., I.B. and C.F. authors are with TIMC-IMAG, University Joseph Fourrier, La Tronche, Grenoble, France
e-mails: {Nikolai.Hungr, Ivan.Bricault, Celine.Fouard} @image.fr.

Abstract— Singular challenges associated to ARCS (Abdomino-pelvic Robotic-driven lightly flexible needle insertion performed in CT/MRI-guided Scenario), make difficult to incorporate most of the existing needle deflection modeling approaches, not originally conceived to this context. This paper addresses the issue by proposing observation and study of percutaneous insertion experiments under a robotic platform compatible to ARCS. Study and observations of 3D reconstructions obtained from experiments of percutaneous insertion in soft tissues are presented in this work. Design of experiment setup allowed the building of a procedure´s database which is an important step to the compatible characterization of percutaneous procedures into ARCS.

Introduction. Numerous models for needle deflection prediction were proposed in the last years. Most of them were committed to improve the efficiency and consistency of needle path planning and steering, considering the several existent interventional robotic platforms [1] [2]. ARCS has special challenges associated to the bore size, radiation and ferromagnetic compatibility. Moreover, 3D real-time (RT) feedback isn't feasible in most standard CT/MR scanners today. All these issues limit the use of RT systems and conventional force sensors. It makes more difficult the application of most of the existing needle deflection modeling approaches not originally conceived for this particular scenario. Currently, 6-DoF LPR is the only robotic teleoperation platform that can perform needle translation, rotation and needle insertion in CT/MRI [3] [4] [5]. Generalist models conceived to other contexts and platforms don't fit directly to the ARCS' constraints [6] [7] [8] [9]. Meanwhile, more relevant efforts need to be committed to provide a compatible model that could be used in this complex context. This paper addresses the issue by proposing to create insertion experiments database involving this platform. The pilot database will be important to the design of a simulation model that could be compared to the results obtained in real case. First, we start presenting experiment setup, procedure and test samples. Then, we present and discuss result of the experiments committed to characterize 3D needle deflection inserted in soft tissues. Thirdly, we also tested mechanical properties of PVC and ex-vivo pork. Finally, we provide conclusions and recommendations for future works.

Methods. Experiments of robot-driven lightly flexible needle interacting with (10x10x13cm) PVC (100% soft plastisol) and ~(8x8x10cm) ex-vivo pork (1.5kg, supported by a plastic canister) tissues were performed using a LPR. A 6-DoF force-torque sensor (nano43 / SI-36-0.5 / ATI Industrial Automation) was mounted below the phantom and was used to track the resulting forces and torques on the phantom body. The force data were used to enrich the system's study and observations. They were not considered as input in the modeling. A framework support was built to fix the robot using two rigid plastic walls attached to a wood base (Figure 1A). The force sensor was fixed in this base, while an additional wood base was attached on the force sensor using screws (Figure 1B). The tissues were

placed on this extra rigid surface (Figure 1C). The Figure 1D shows the robot's grippers (G1 and G2) holding the needle.

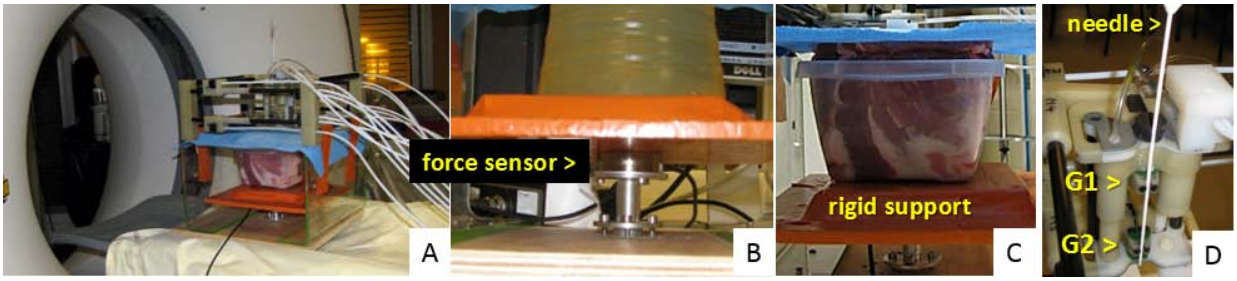

Figure 1. Experiment setup. A. Customized support framework. B. Force sensor C. Ex-vivo tissue pork. D. LPR´s grippers (G1 and G2) and needle.

Insertions were performed progressively into different tissues (100% soft synthetic PVC and in ex-vivo pork). The images were acquired using a Siemens Somaton Sensation 16 CT scanner at the CHU-Grenoble. They have dimensions of (512x512) (~200 slices/sequence) and voxel resolutions of (0.6x0.3x0.3mm). A database with 36 CT image sequences was created, related to thirteen insertion procedures and tests of the tissue properties scanned progressively. Vertical insertions as well as insertions inclined by 10 degrees in various directions were performed using a long (20 cm), 17 degrees bevel-tip spinal needles.

Results and Discussion. The setup's design presented in the previous section was motivated by the clinical challenges of ARCS. The experiment setup allowed the observation of 3D CT reconstructions and fiducials points (Figure 2A), obtained under submillimetric precision. Measurements of the axial and orthogonal needle deflection, as well as tissue deformation were performed. They will be used as ground truth for subsequent modeling and simulations. Deflections of the needle orthogonal to the insertion direction were observed in the range of 3-6 mm in both tissues for insertion depths of nearly 5-8 cm (Figure 2B). The tissue (stiffness) parameters (*Kt*) were obtained pre-operatively at surface level by axial compression tests as in ref [7], having the coefficients *Kt*(Homog)=490 N/m, Kt(2Layers)=115 N/m and Kt(4Layers)=130 N/m.

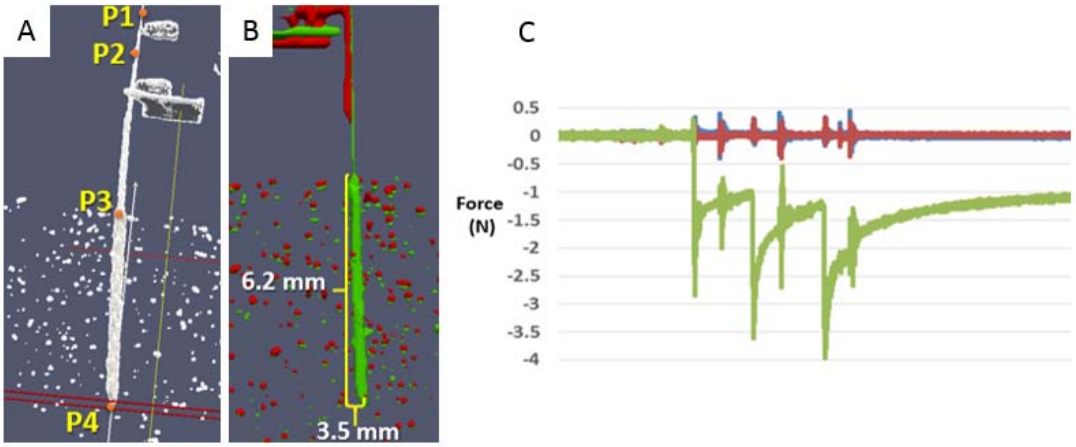

Figure 2. A: Fiducial points. B: Needle deflection sample. C: Transverse and axial force measurements into a insertion sample.

The force data (Figure 2C) shows the three insertion steps of a full insertion. It reveals occurrence of tissue relaxation. For the several samples, the relaxation stability was reached at nearly 1N, after some rest time between insertions. The observations and studies of the described experiments and database information gathered in this work provided a better comprehension of the mechanics of the lightly flexible needle inserted into soft medium. The information collected will be worthy in the implementation of a 3D model compatible with the unique constraints of this scenario and platform. Additionally, the experiment setup could be reapplied to gather more insertion samples to support a future validation approach.

REFERENCES

[1] M. Abayazid, M. Kemp and S. Misra, "3D flexible needle steering in soft-tissue phantoms using fiber bragg grating sensors," *In Proc. of ICRA - IEEE Int. Conf. on Rob. and Autom.,* pp. 5843-5849, 2013.

[2] H. Su, M. Zervas, G. Cole, C. Furlong and G. Fischer, "Real-time MRI-guided needle placement robot with integrated fiber optic force sensing," in *ICRA - IEEE Int. Conf. on Robt. and Autom.*, Shangai, 2011.

[3] E. A. Dorileo, N. Hungr, N. Zemiti, C. Fouard and P. Poignet, "A modular CT/MRI-guided teleoperation platform for robot assisted punctures planning," in *28th CARS - Computer Assisted Radiology and Surgery*, Fukuoka, 2014 (to appear in).

[4] N. Zemiti, I. Bricault, C. Fouard, B. Sanchez and P. Cinquin, "LPR: A CT and MR-Compatible Puncture Robot to Enhance Accuracy and Safety of Image-Guided Interventions," *IEEE/ASME Transactions on Mechatronics,* vol. 13, no. 3, pp. 306-315, 2008.

[5] N. Hungr, C. Fouard, A. Robert, I. Bricault and P. Cinquin, "Interventional Radiology Robot for CT and MRI Guided Percutaneous Interventions," in *MICCAI*, Toronto, 2011.

[6] R. J. Webster, N. J. Cowwan, G. S. Chirikjian and A. M. Okamura, "Nonholonomic modeling of needle steering," *Int. Journal of Robotic Research,* vol. 25, pp. 509-525, 2006.

[7] D. Glozman and M. Shoham, "Image-Guided Robotic Flexible Needle Steering," in *IEEE Transactions on Robotics, Vol 23, N.03*, 2007.

[8] S. P. DiMaio and S. E. Salcudean, "Needle Steering and Motion Palling in Soft Tissues," 2004.

[9] R. Alterovitz, K. Goldberg and A. Okamura, "Planning for Steerable Bevel-Tip Needle Insertion through 2D Soft Tissue with Obstacles," in *IEEE Intern Conf on Robotics and Automation*, 2005.

Calibration with DCC in tomography

Laurent Desbat, Benjamin Spencer
TIMC-IMAG, UMR 5525, Grenoble University
In3S, Faculté de Médecine, 38706 La Tronche, France

Many interventional x-ray systems, such as isocentric C-arms, need to be calibrated on-line. Calibration systems using markers and methods involving image processing may be used. Hybrid methods using external information for localizing the acquisition system are also used [7]. Recently, a method using consistency of the data has been proposed for pinhole x-ray system calibration [5]. This exploits the fact that an x-ray plane may be measured twice during the acquisition. In the following, we propose a 2D proof of concept of calibration based on the 2D parallel Data Consistency Conditions (DCC). The main advantage of such an approach would be avoiding the use of markers in the measured region and the radiographic data treatment for finding the marker projections.

DCC and calibration We consider the following 2D CT calibration problem. Let $\mu \in \mathbb{L}^1(\mathbb{R}^2)$ be the attenuation function of an organ measured by an x-ray system. We consider the parallel CT geometry, i.e.,

$$p(\phi, s) = \int_{\mathbb{R}} \mu(s\vec{\theta} + l\vec{\zeta})\mathrm{d}l \tag{1}$$

where $\vec{\theta} = (\cos\phi, \sin\phi)\,, \vec{\zeta} = (-\sin\phi, \cos\phi)\,, \phi \in [0, 2\pi)$ and an acquisition on an interval of length π is sufficient for the reconstruction.

Parallel projections are not independent. DCC on p (called Helgason-Ludwig conditions) are known to be necessary in order for p to be a measurement. Also, these conditions are even sufficient for a compactly supported projection [6].

Proposition 0.1 (Helgason Ludwig Conditions)**.**

$$\forall n \in \mathbb{N}, \int_{\mathbb{R}} s^n p(\phi, s)\mathrm{d}s = \pi_n(\cos\phi, \sin\phi) \tag{2}$$

where π_n is an homogeneous polynomial of degree n.

We now consider the following calibration problem. We suppose we have acquired the measurement m such that $m(\phi, s) \overset{\text{def}}{=} p\,(\phi, s - s_\phi)$ where s_ϕ are unknown shifts depending on ϕ. We suppose that the acquisition angle $\phi_i, i = 1, \ldots, P-1$ are known but that the shifts $s_i (= s_{\phi_i})$ must be identified i.e. calibrated. It can be easily shown that the DCC of order $n = 0$ do not depend on s_i ($\int m(\phi, s)\mathrm{d}s = \int p(\phi, s)\mathrm{d}s = v_\mu$ where $v_\mu = \int_{\mathbb{R}^2} \mu$). However, the DCC of order $n = 1$ from Eq. (2) yields:

$$s_i = \frac{\int_{\mathbb{R}} sm(\phi_i, s)\mathrm{d}s - (a\cos(\phi_i) + bsin(\phi_i))}{v_\mu} \tag{3}$$

where $v_\mu = \frac{1}{P}\sum_{i=0}^{P-1}\int m(\phi_i, s)\mathrm{d}s$ and $a \in \mathbb{R}, b \in \mathbb{R}$ are the coefficients of $\pi_1(\cos\phi, \sin\phi) = a\cos(\phi) + b\sin(\phi)$ to be identified. It is easy to see that fixing two projection shifts, say s_0 and $s_{P/2}$, is equivalent to choosing the origin, or center of rotation. For better stability we choose $\phi_0, \phi_{P/2}$ because $\phi_{P/2} = \phi_0 + \pi/2$ (for even P) and we compute (a, b) from:

$$\begin{bmatrix} \cos\phi_0 & \sin\phi_0 \\ \sin\phi_{P/2} & \sin\phi_{P/2} \end{bmatrix} \begin{bmatrix} a \\ b \end{bmatrix} = \begin{bmatrix} \int_{\mathbb{R}} sm(\phi_0, s)\mathrm{d}s - s_0 v_\mu \\ \int_{\mathbb{R}} sm(\phi_{P/2}, s)\mathrm{d}s - s_{P/2} v_\mu \end{bmatrix} \tag{4}$$

The other s_i are then computed from (3)

Numerical experiments We have simulated $P = 800$ projections of the Shepp-Logan phantom on $[0, \pi)$, each projection with 512 parallel rays, see Figure 1. The order 1 DCC have been computed (red points) and fit perfectly the theory (green curve). The 800 projections were randomly shifted with a standard deviation of 5 pixel shift and a maximum absolute shift of 15 pixels allowed in order stay within in the field of view. The corresponding order 1 DCC are far from a polynomial of the form π_1. Using Eq.(3),(4), we succeeded in estimating $(s_i)_{i=1\ldots,P-1,i\neq P/2}$ with a mean absolute error of 0.0745 pixels and a maximum absolute error is 0.3150 pixels. This estimation accuracy is sufficient for a large improvement in the reconstruction.

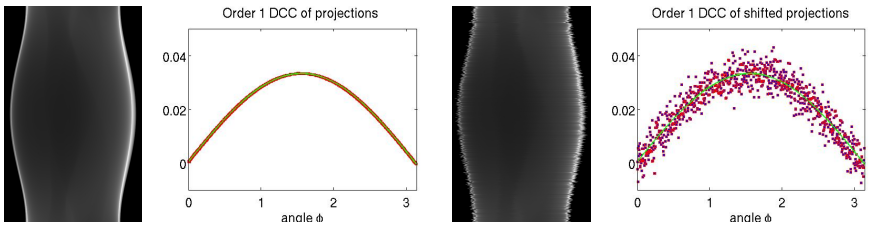

Figure 1: Projections of the Shepp-Logan phantom 800×512 and corresponding order 1 DCC of the Shepp and Logan projections (left); Randomly shifted projections and corresponding order 1 DCC (right);

Conclusion and future work The method is robust in the presence of noise. DCC of higher order could be used for estimating other calibration parameters. This confirms the results obtained in [2, 1] showing that both the unknown projection angles and shifts can be stably estimated from moments of order 0,1,2 and 3 when the number of projections is larger than 25. This work must be extended to 3D using for example [3] and following [4] in order to take into account data truncation.

Aknowledgments This work was partly supported by French state funds managed by the ANR within the Investissements d'Avenir program (Labex CAMI) under reference ANR-11-LABX-0004.

References

[1] S. Basu and Y. Bresler. Feasibility of tomography with unknown view angles. *IEEE Trans. Image Processing*, 9:1107–1122, 2000.

[2] S. Basu and Y. Bresler. Uniqueness of tomography with unknown view angles. *IEEE Trans. Image Processing*, 9:1094–1106, 2000.

[3] R. Clackdoyle and L. Desbat. Full data consistency conditions for cone-beam projections with sources on a plane. *Phys. Med. Biol.*, 58:8437–8456, 2013.

[4] R. Clackdoyle and L. Desbat. Data consistency conditions for 2d truncated parallel projections. In *nternational Conference on Image Formation in X-Ray Computed Tomography*, 2014. to appear.

[5] C. Debbeler, N. Maass, M. Elter, F. Dennerlein, and T. Buzug. A new ct raw-data redundancy measure applied to automated misalignment correction. In *Fully Three-Dimensional Image Reconstruction in Radiology and Nuclear Science*, pages 264–67, 2013.

[6] F. Natterer. *The Mathematics of Computerized Tomography*. Wiley, 1986.

[7] N. Navab, S-M. Heining, and J. Traub. Camera augmented mobile c-arm (camc): Calibration, accuracy study, and clinical applications. *IEEE Trans. Med. Imaging*, 2010.

Direct model based needle trajectory generation for ultrasound-guided regional anaesthesia

N. Morette, C. Novales, A. Housni, P. Vieyres (PRISME laboratory – Orleans University)
O. Hadjerci, A. Hafiane (PRISME laboratory – INSA CVL)

***Acknowledgement**: this work is being supported by the "Région Centre" within the DANIEAL 2013 project.*

Ultrasound-guided regional anaesthesia (UGRA)

Ultrasound-guided regional anaesthesia (UGRA) has rapidly become popular for performing RA blocks. Many anaesthetists lack experience with UGRA as it requires complex hands coordination: during the needle insertion, done with one hand, the anaesthetist has to position, with the other hand, the ultrasound probe in order to maintain the nerve position in the US image, to visualize the needle tip and to ensure the perineural spread pattern. Hence, UGRA requires new cognitive skills to (1) visualize a needle as the needle is being inserted, (2) maintain the needle in the US probe observation plane and (3) guide the needle tip to a target point by making needle trajectory adjustments as necessary and observing the distribution of local anaesthetic during injection.

This paper presents an interactive tool for the practitioner based on automatic nerve detection using ultrasound images, that offers a real-time needle trajectory based on direct model including vulnerable structures avoidance; the needle detection in the US image was not considered in this work.

Automatic nerve detection in the ultrasound image

Ultrasound (US) images segmentation and detection methods have been applied to various medical applications. Depending on the application, these methods require a choice of relevant features to detect the regions of interest. Texture information is an important clue for the nerve blocks detection. Although, several works have demonstrated useful proprieties based on texture to segment tissues in US images. Gabor filter **[Bovik 1990]** was often used to segment the US images, feature based Gabor filter was used to detect prostate **[Mohamed 2006]**, liver and cystic kidney **[Khanna 2012]**. However, very few works have studied the automatic nerve detection in the US images **[Thouin 2011]**.

The nerve region presents a particular pattern that can either be a hypoechoic or hyperechoic structure, depending on the nerve size, the probe frequency and the angle of the US beam **[Marhofer 2007]**. Based on Khanna's method **[Khanna 2012],** we have developed a two-step method to detect a nerve region. The first step consists in a segmentation of the hyperechoic foreground tissues to distinguish the hyperechoic tissues from non-useful information. The second phase extracts the nerve area in the foreground using support vector machine (SVM) and Gabor descriptor. 173 ultrasound images of the median nerve were used; the results showed that the bank Gabor descriptor achieves better accuracy than the other features. These results provide us an identified and relevant target used to develop the needle trajectory generation and the targets for the perineural spread (fig.1).

Fig. 1. Example of nerve detection in US image

Direct model for needle trajectory generation

Path planning and control of the needle tip advancement is a complex task due to the risk of nerve collision and the dynamic environment i.e. needle and tissues interactions. Research works on the actuation and control of the needle insertion mainly focused on pre-computed trajectory tracking suited for static environment (**[Wood 2010]**). However, in **[Bernardes 2012]**, a robotically assisted system combined with image feedback was proposed to control the current tip position and update the reference trajectory during the medical act, taking into account changes in the obstacles positions.

From our expertise applied for mobile robots evolving in complex and unknown environment **[Morette 2011]**, and in order to propose to the medical expert a safe and admissible trajectory to perform its LRA act, we have developed a direct model approach to predict the needle's motions in the operational space from the admissible control profiles in the articular space. These profiles correspond to different types of functions defined on a temporal horizon T_p, and parameterized by a chosen number of parameters varying continuously. In this approach, the needle used for LRA is considered stiff, and only the position of the tip of the needle is modelled; this restricts this approach to the case of soft tissues whose the resistance to deformations is considered negligible.

Direct model based trajectory method

The needle polar motions in the plan are composed of rotations and linear displacement around the insertion point into the patient skin. The needle control is parameterized through function defined by a set of continuous parameters and on a prediction horizon $[t_0, t_0+T_p]$. In order to provide by-pass trajectories, 2 parameters are chosen on each of the control component (linear and rotation). A set of these 4 parameters corresponds to a control function on the prediction horizon and generates a trajectory based upon the needle's geometric model.

In order to choose the parameters corresponding to the best trajectory, a cost function Z is defined to integrate environment constraints for a safe trajectory, planned path following constraints and constraints on the needle's kinematics. Hence, the set of parameters minimizing Z corresponds to the trajectory the nearest to the planned path. Generating this best needle's trajectory from t_0 to the prediction horizon T_p becomes an optimization process under constraints which is resolved using a real-time optimization algorithm. Every T_e the whole navigation issue is updated with data collected from the US image and an updated trajectory is computed.

Simulation results

Fig. 2. shows a generated trajectory for the tip of the needle in an US image resulting from automatic nerve detection. The corresponding controls of the needle respect the constraints on the needle's movements; these constraints, with the processed US image, correspond to the entry data of our method. Each small cross on the needle's trajectory corresponds to the sampling time T_e during when a new trajectory is generated. Finally, the method provides controls to follow this generated trajectory; it is adjustable to the US image dynamics by lowering or increasing T_e value.

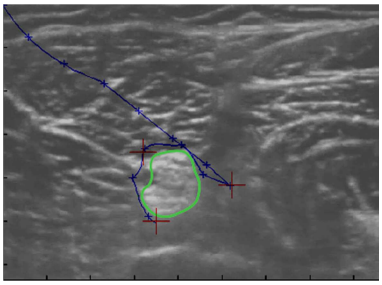

Fig. 2. Trajectory generation in the ultrasound image: the segmented nerve block (green line), red crosses represent the anaesthetic agent successive delivering targets.

Perspectives

These preliminary results validate the direct model needle trajectory generation for obstacle avoidance in soft tissues environments. This approach generates safe trajectories that fulfil the constraints on the needle kinematics and enable to bypass obstacles when needed, in order to deliver the anaesthetic agent on identified target points chosen by the medical expert in the US image. This method is adaptable to the environment dynamics by managing the prediction horizon and sampling times.

Currently the drawback of this method is that the full interaction of the needle trajectory with its immediate environment was not taken into account. Tissue distortion appears when the needle moves around the insertion point on the patient skin, and depends on the environment compliance properties. This distortion propriety is very useful when the anaesthetist wants to target a point behind a vulnerable structure or obstacles; it would be unreachable otherwise. The work in progress consists in taking into account the environment deformation according to the needle trajectory during the computation of the trajectory itself.

References

M. C. Bernardes, B. V. Adorno, P. Poignet, G. A. Borges, « Semi-automatic needle steering system with robotic manipulator", in Robotics and Automation (ICRA), 2012 IEEE Intern. Conference on, 2012, pp. 1595 – 1600

A. C. Bovik, M. Clark, and W. S. Geisler, "Multichannel Texture Analysis using Localized spatial filters," IEEE Transactions on Pattern Analysis and Machine Intelligence , vol. 12, no.1, pp. 55-73, 1990.

A.Khanna, M.Sood, and S.Devi, US Image Segmentation Based on Expectation Maximization and Gabor Filter, international Journal of Modelling and Optimization, Vol.2, No. 3, June 2012.

P. Marhofer, W. Vincent, and S. Chan. Ultrasound-guided regional anaesthesia: Current concepts and future trends. Journal of Clinical Anaesthesia, 105, 2007.

S. S. Mohamed, A.M.Youssef, E. F. El-Saadany and M. M. A. Salama, Prostate Tissue Characterization Using TRUS Image Spectral Features, Springer, Berlin and Heidelberg New York, 2006, pp. 589–601

N. Morette, C. Novales, L. Josserand, P. Vieyres, « Direct Model Navigation issue shifted in the continuous domain by a predictive control approach for mobile robots », Robotics and Automation (ICRA), 2011 IEEE International Conference on, 2011, pp. 2566 – 2573

E. Thouin, A. Hafiane, P. Vieyres, N. Xylourgos, G. Triantafyllidis. Nerve region segmentation for ultrasound guided local regional anaesthesia. Mediterranean Conf. on Information Systems 2011.

N. A. Wood, K. Shahrour, M. C. Ost, and C. N. Riviere, "Needle Steering System using Duty-Cycled Rotation for Percutaneous Kidney Access," in Proc. IEEE Annual Int. Conf. of the EMBS, 2010, pp.5432–5435.

Fusion on multi-modal data for Cardiac Resynchronization Therapy planification and guidance

S. Bruge[1,2], A. Simon[1,2], A. Hernandez[1,2], C. Leclercq[1,2,3], M. Garreau[1,2]

[1]INSERM, U1099,Rennes, F-35000 France
[2]Université de Rennes 1, LTSI, Rennes, F-35000 France.
[3]CHU Rennes, Service de cardiologie et maladies vasculaires, Rennes, F-35000 France

Introduction Cardiac insufficiency (CI) is a cardiovascular disease which affects 2-3% of the developed countries population, but 20 to 30% of the 70-80 years old people [2]. Among the concerned population, 30 to 40% of patients have a cardiac asynchronism. To improve patients' life and to reduce the associated short term mortality, Cardiac Resynchronisation Therapy (CRT) is considered as an efficient treatment. Indeed, CRT can reduce the cardiac asynchronism thanks to the implantation of a multi-sites cardiac stimulator, including a left ventricle (LV) lead inserted through the coronary venous network. However around one third of the patients treated with CRT do not show any response to the therapy. A way to optimize CRT is to characterize the best cardiac sites for stimulation and to guide the implantation. In previous works, a way to pre-operatively characterize the implantation sites through the fusion of multimodal images had been proposed [4] [1]. Now, we seek to provide the pre-operative analysis results in the operative room to guide the clinician during the implantation. In front of the short time between patients analysis and the stimulator implantation, a software had been implemented to treat rapidly each modality and to visualize the results efficiently.

1.Pre Operative Analysis

Patients pre operative exams contain several modalities, with very different characteristics: CT-Scan, Electro-Anatomical Mapping (EAM), Speckle Tracking Echocardiography (STE) and MRI data. Each modality provides some complementary descriptors in terms of anatomy, electrical and mechanical functions and tissular characterization.

First, the dynamic CT-scan, which is composed of 20 volumes acquired at each 5% of the cardiac cycle, provides the heart geometry during this cycle. As we are particularly interested in the LV, a pre-processing chain is applied on each volume to obtain a specific patient mesh model of the LV. As the CT-scan has the higher spatial resolution, it is used as the reference on which all the other information will be projected *(figure 1)*.

EAM provides the local electrical function of the myocardium thanks to the acquisition of electrograms (EGM). This is an invasive examination, in which a catheter is introduced in the LV. The LV cavity is reconstructed including all catheter positions. As the catheter not always reach the myocardium, the EAM surface being very different from the LV geometry making the registration between the both surfaces quite difficult. So, a semi-interactive registration method is used: after an initialization using an alignment of barycenters and principle inertia axes, the user is free to adjust the EAM surface position into the LV by additional rotations and translations. To analyze the electrical propagation, the EGM amplitude and Local Activation Times (LAT) can be computed. After the registration process, these descriptors can be displayed on the LV using a radial projection.

The mechanical function in response to the electrical stimulation can be quantified by Speckle Tracking Echocardiography (STE). In this examination, 2D contours of the LV are segmented by a cardiologist for each echocardiographic plane. Then, a fully automatic method to register STE segmented contours and LV mesh model for 2 and 4 chambers STE was developed [5]. It involves finding the CT plane corresponding to the echocardiographic plane. Strain amplitude and Global Electro Mechanic Delays (EMD) -delay between the global electrical stimulation, as measured by the ECG, and peak of strain- are extracted from STE to study the quality of the mechanical response. To better characterize the electro-mechanical coupling, local EMD -mechanical response to the local electrical stimulation- can be computed by considering also the EAM. As both exams are acquired at different times, a temporal matching between the corresponding ECG is needed to express the EGM peaks time in the STE temporal base and to compute the delay between EGM peak and each segment strain peak *(figure 1)*. To do this, after a normalization of the both signals, a dynamic time warping method is used to compute the temporal matching between the RR-cycles of this ECG's.

2. Venous network extraction

As the LV lead being implanted through the venous network, a preview of the venous network would be helpful to plan the implantation but also to register the pre-operative CT-scan with the per-operative angiography. First a Sato Filter [3] to enhance tubular structures is applied to the CT Volume. After this step, too many vessels are detected. Thus, a 2-steps region growing process is considered. First, a 3D region growing with a very restrictive threshold provides a list of points belonging to the vessel. Then, these points are defined as seed points to launch successive 2D region growing in each slice with a more permissive

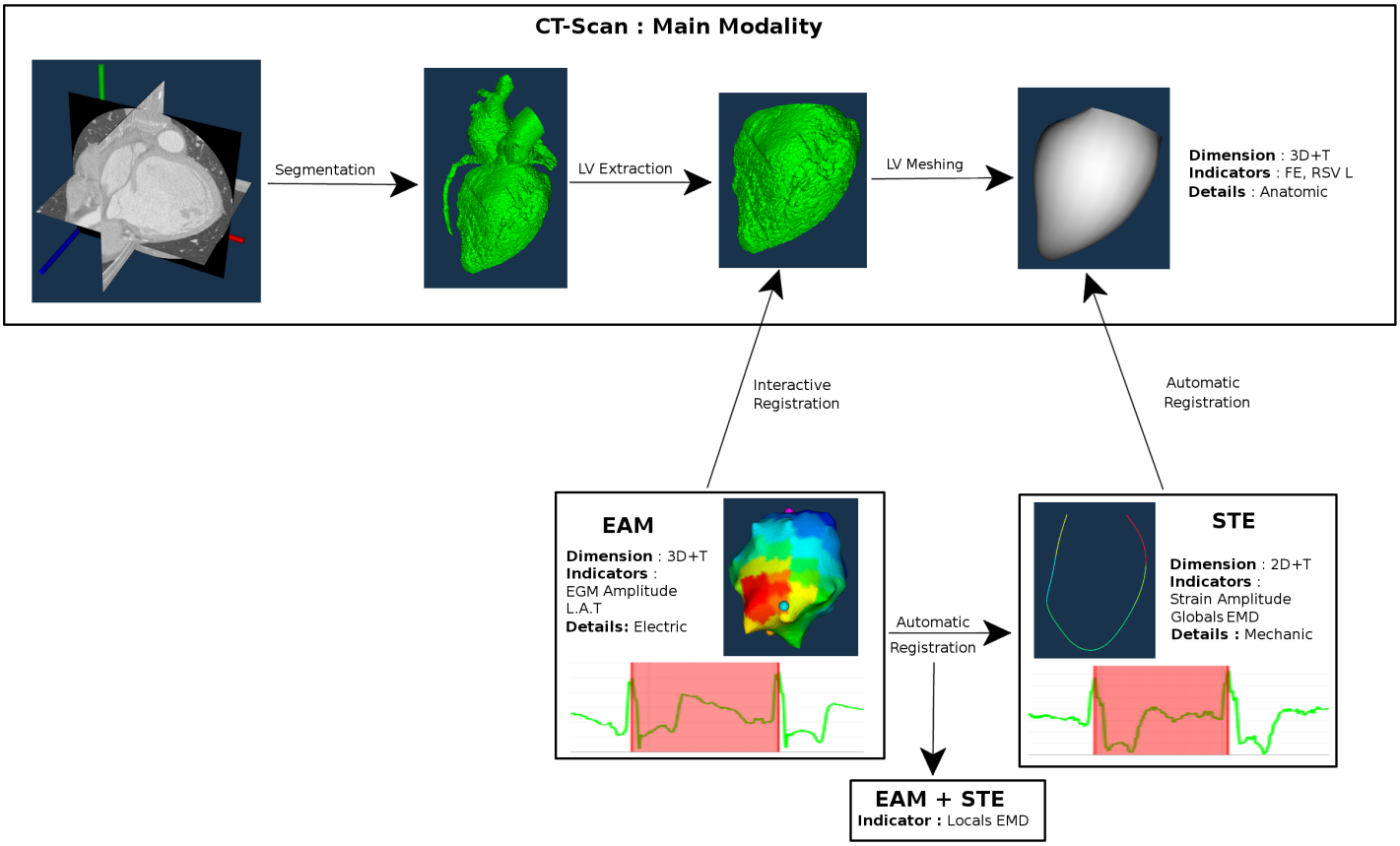

Figure 1: *Registration of multimodal images*

threshold. As we limit the segmentation dimension to 2, it keeps the center on the vessel and doesn't expand to the vessels network. In this way, we avoid a segmentation of too much vessels which will drive the cardiac sites accesses very confused.

3. Indicators visualization

The main income of this work was the development of a graphical user interface (GUI) to visualize pre-operative data and to help the clinician to select the best cardiac sites for implantation. As explain on the first part, a lot of cardiac descriptors are extracted among the different modalities. Indeed, the EAM contains several stimulation mode (sinusal, bi-ventricular...) in which two descriptors (LAT and EGM Amplitude) are computed. Furthermore, each stimulation is subjected to a registration with STE to add the Local EMD to the analysis. In front of this substantial number of available descriptors, the GUI had been organized as following *(figure 2)*:

1. Select the CT view for data representation: left heart, LV, LV mesh
2. Select an EAM stimulation mode and choose an available descriptor. This stimulation will be used to display the corresponding Local EMD.
3. Select the registered STE and a corresponding descriptor.
4. Adjust the EAM Bull Eye resolution.

An other question was the fusion between the 2D data bring by STE and the others 3D modalities. First, the electrical details are projected on the CT to build a 3D map. Then, 3D spheres with strain data are displayed along the intersection between the CT surface and the computed registration plane.

To avoid color confusion, the HSV color space had been split in two to separate EAM and strain data representation.

Some bull-eye representations, very used in clinical routine, are also displayed. The resolution (segments and layers) of the EAM bull-eye can be interactively adjusted. The segmented vessels can also be added to the global representation.

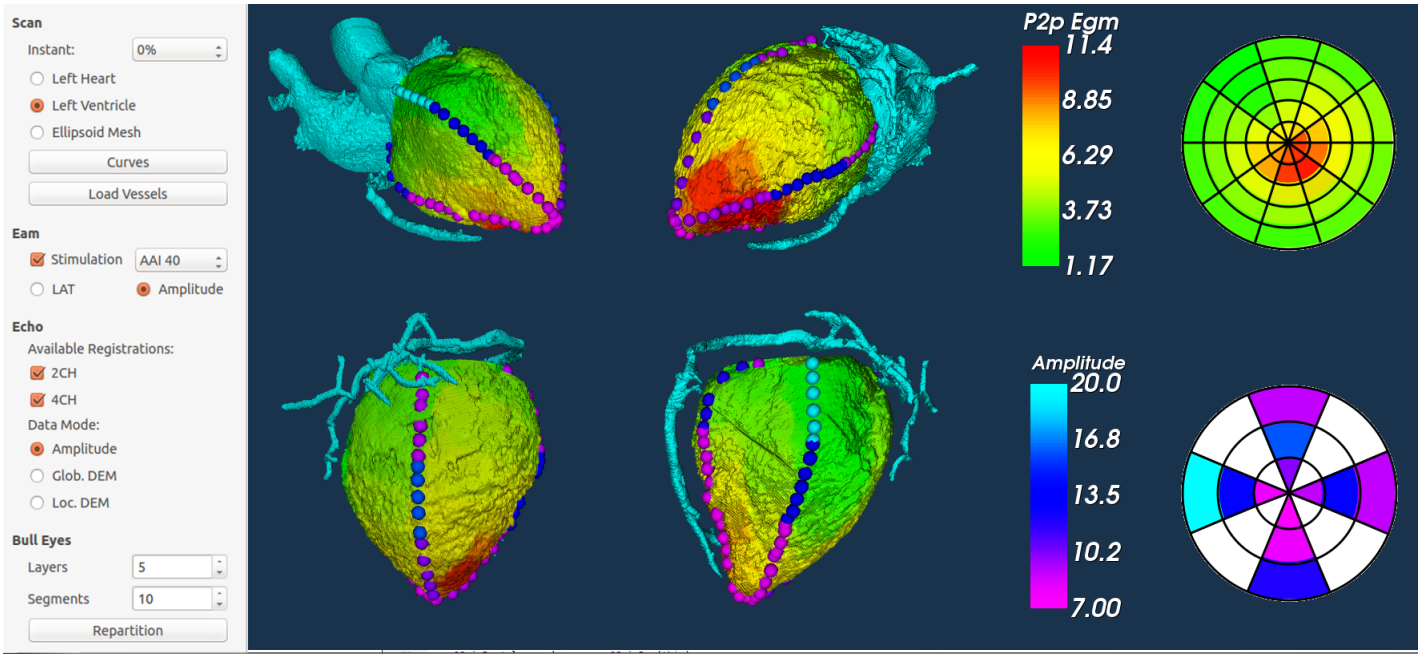

Figure 2: *3D representation of EGM Amplitude in sinusal stimulation and Strain Amplitude for 4 and 2 chambers STE and their corresponding bull eyes. Top: data fusion on the left heart. Bottom: data fusion on the left ventricle with segmented vessels display.*

Conclusion We have presented a method to integrate several pre-operative cardiac descriptors to characterize CI with their projection on the CT-scan. This multi-modal information has to be completed with tissue scar area determination from MRI [1] and with the characterization of best sites candidates for stimulation. Then, the registration of the CT-Scan segmented vessels and a per-operative angiography would allow to provide a stimulator implantation guiding system to reach these sites.

Acknowledgment

This work was supported by the French National Research Agency (ANR) in the framework of the Investissement d'Avenir Program through Labex CAMI (ANR-11-LABX-0004).

References

[1] Betancur J., Schnell F., Simon A., Tavard F., Donal E., Hernandez A., and Garreau M. Spatio-temporal registration of 2d us and 3d mr images for the characterization of hypertrophic cardiomyopathy, functional imaging and modeling of the heart. *Lecture Notes in Computer Science*, 7945:292–299, 2013.

[2] Harlan M Krumholz, Ya-Ting Chen, Yun Wang, Viola Vaccarino, Martha J Radford, and Ralph I Horwitz. Predictors of readmission among elderly survivors of admission with heart failure. *American heart journal*, 139(1):72–77, 2000.

[3] Yoshinobu Sato, Shin Nakajima, Nobuyuki Shiraga, Hideki Atsumi, Shigeyuki Yoshida, Thomas Koller, Guido Gerig, and Ron Kikinis. Three-dimensional multi-scale line filter for segmentation and visualization of curvilinear structures in medical images. *Medical image analysis*, 2(2):143–168, 1998.

[4] François Tavard. *Recalage et fusion d'informations multimodales pour l'optimisation de la thérapie de resynchronisation cardiaque*. PhD thesis, Université Rennes 1, 2012.

[5] François Tavard, Antoine Simon, Christophe Leclercq, Erwan Donal, Alfredo I Hernández, and Mireille Garreau. Multimodal registration and data fusion for cardiac resynchronization therapy optimization. *IEEE, Transactions on Medical Imaging*, 33(6):1363–1372, 2014.

Virtual fracture reduction of the acetabulum using a rigid body biomechanical model

M. Boudissa[1,2], M. Chabanas[1], H. Oliveri[1], J. Tonetti[2]

1. *TIMC-IMAG lab, Univ. Grenoble Alpes, CNRS UMR 5525, France.*
2. *Grenoble Hospital, dpt. of Orthopedic Surgery, Univ. Grenoble Alpes, France.*

Introduction

Acetabular fractures are a challenge in orthopedic surgery. Many fracture patterns occur [1], in a deep anatomical area surrounded by numerous vascular and nervous elements, generally in a polytraumatic context. A reduction with less than 2mm of incongruence is generally considered acceptable [2], to limit the post-operative osteoarthritis that could rapidly require total hip arthroplasty. Due to the long learning curve, this surgery is limited to large reference centers [3].
A full understanding of the fracture, based on CT images and 3D reconstructions, is required to specify the best planning, especially the surgical acces(es). Several preoperative planning tools have been proposed [4-6]. The different bone fragments are first segmented in the CT images, then mobilized in 3D to simulate the fracture reduction. This result can then be used to conform osteosynthesis plates to the patient anatomy, and define the number and length of fixation screws. These authors have reported a much better understanding and definition of the surgical strategy, which lead to a significant reduction of the per-operative duration. However, several key challenges remain to use such systems in clinical routine. After presenting our current strategy for the segmentation, the main contribution of this paper is an intuitive simulation of the fracture reduction using a mechanical model.

Material & Methods

A 3D model of the hip bones, including separated fragments, is first build out of the CT images. Semi-automatic segmentation procedures are usually performed using commercial software likes Mimics® or Amira® [4,5] or via the development of advanced methods to increase the automation of the process [7,8], which currently remains too time-consuming for a clinical routine use. In this study, we have used an existing non-commercial software (itksnap [9]), to perform automatic threshold, region growing with active contours and finally manual refinements. Models of adequate quality (figure 1), similar to other authors, could be built in less than 30 minutes in complex cases.
The next crucial step is the simulation of the fracture reduction. All authors in the literature propose geometrical repositioning of each bone fragment, with six degrees of freedom (translation + rotation). However, reducing the fracture in 3D through mouse interactions is difficult, quite non-intuitive and hardly guaranty non-penetration between fragments. [6] have thus proposed a virtual environment controlled with a haptic device reacting to collisions. One of the main drawback of all these methods is that their goal is simply to position the bone fragments so that the fracture is considered as reduced. However, even if this target position is *in fine* correct, the process to achieve does not correspond to the reality of the surgical procedure: fragments are moved freely

in 3D space, with few or no anatomical consideration, resulting to movements that may not be realized in real surgery.
A new paradigm is then to *simulate the procedure itself*, instead of the desired result. During surgery, bone fragments are repositioned using clamps, hooks or Schanz screws (figure 2). The fracture is then reduced via the application of *forces* by the physician. Moreover, the surgeon use the contacts between structures, e.g. lean the ischium on the femoral head, to produce the expected movements. To simulate such a procedure we have chosen to use a mechanical model of the hip joint bony elements, implemented within the non-commercial Artisynth framework [10]. Each bone fragment is considered as an independent rigid body. One of them is usually considered as fixed, e.g. the anterior or posterior column and/or the femoral head. Collisions are handled to ensure non-penetration between elements, with dry friction (Coulomb) response. The action of a clamp is simulated via a Hill muscle model which extremities are the clamp jaws positions on the bones. The interactive "contraction" of this model apply forces similarly to the real clamp action. In reality, the muscular system apply heavy constraints to the bones during their repositioning. While modeling this accurately is an extremely complex problem, moreover in a patient-specific context, a first approximation is to add a strong global damping to the all system. Even if preferred anatomical directions are not accounted for, this high resistance ensure the response to collisions and numerical instabilities are very low in comparison to the forces directly applied to the bones. When all these elements are set, the dynamic numerical system is solved using traditional methods (Euler implicit, Runge-Kutta…).

Results

Figure 2 present a clinical case with a "simple" transverse + posterior wall fracture of the acetabulum. The position of the clamps is chosen by the surgeon according to his knowledge of the surgical approach and the feasibility of the procedure. A fracture is the result of a non physiological displacement in a contraignant soft tissue area. The surgeon tries to reproduce, in the other way, the initial displacement to get a perfect reduction. The best reduction is obtained when the less of manipulations are made. We have simulated several ways of reduction and the best procedure is presented here. Each procedure tested was technically feasible in real surgery (the position of the clamps, the direction of the displacements, the strength on the bones, the motion of the bones).Two clamps are successively used, to close the gap between the ischium and ilium then to slide the ischium in its final reduced position. The user just has to set the clamps position and to control their activation, the simulation being run in real-time. The simulation is quite stable, and the moved fragments are clearly sliding over the fixed ones along with the clamp closing, according to the behavior expected during surgery. The final simulated reduction is qualitatively correct.

Conclusion

A new method has been proposed for virtual fracture reduction. Unlike unconstrained geometrical repositioning, the biomechanical model enables to easily and intuitively simulate the effects of real surgical procedures. Even if limits could be addressed, especially the soft tissue environment of the hip area, preliminary results are quite promising. This technique could be an effective planning tool for the surgeon to define

his best therapeutic strategy, mostly which surgical access to choose as well as how and in which order to reposition the bone fragments.

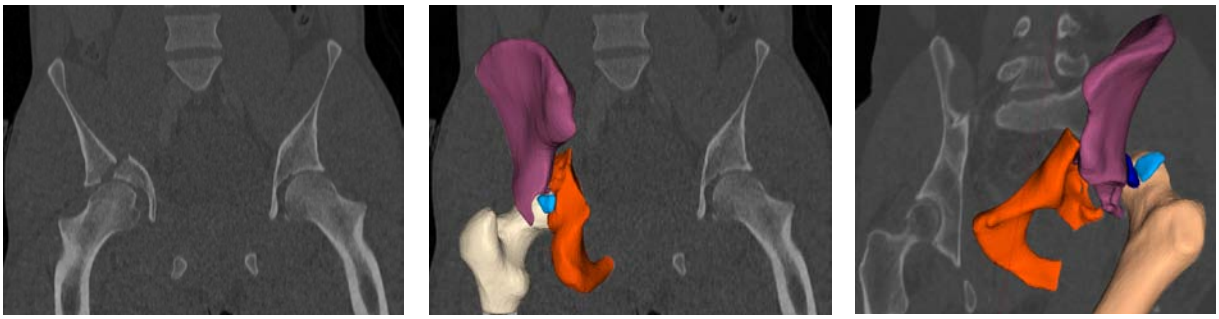

Figure 1 Example of transverse + posterior wall fracture of the acetabulum (left: CT image only; middle: along with the reconstructed 3D model). Right: a more complex case with two comminutive fragments and a dislocation of the femoral head.

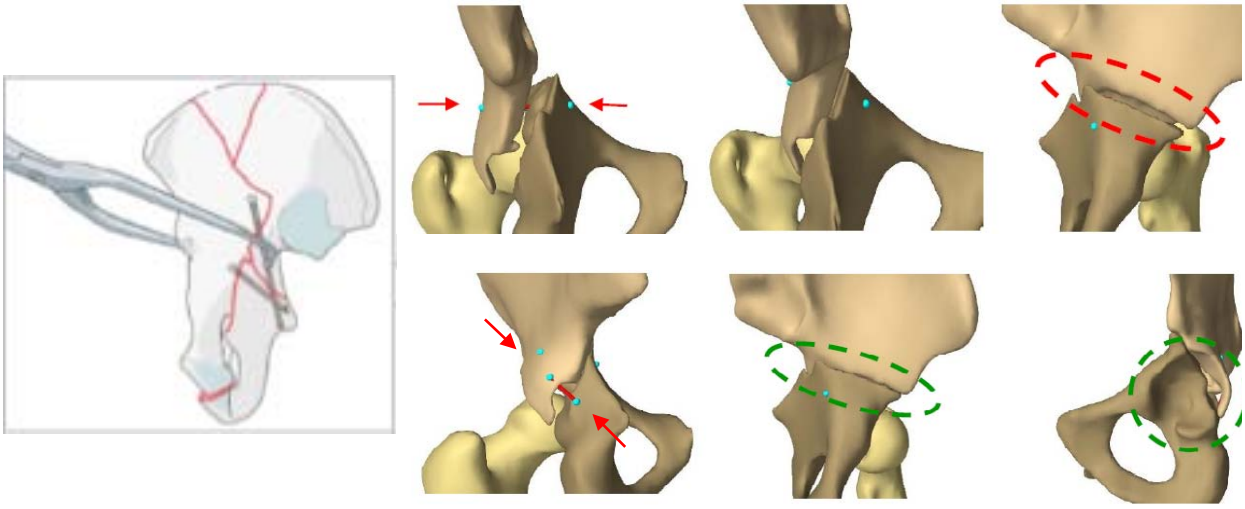

Figure 2 Left: examples of clamps and screws used to reduce a fracture. Top row: simulation of the first clamp action. Second raw: simulation of the second clamp. The fracture is finally reduced (a comminutive fragment is not display here).

This work was partly supported by the French ANR within the Investissements d'Avenir program (Labex CAMI) under reference ANR-11-LABX-0004.

References

[1] Judet R, Judet J, Letournel E. Fractures of the acetabulum: classification and surgical approaches for open reduction. Preliminary report. J Bone Joint Surg Am 1964.
[2] Matta JM, Merritt PO. Displaced acetabular fractures. Clin Orthop Relat Res 1988
[3] Tonetti J. Management of recent unstable fractures of the pelvic ring. An update conference supported by the Club Bassin Cotyle. (Pelvis-Acetabulum Club). Orthop Traumatol Surg Res. 2013 Feb; 99(1 Suppl): S77-86
[4] Cimerman M, Kristan A. Preoperative planning in pelvic and acetabular surgery : The value of advanced computerised planning modules. Injury 2007; 38: 442-449.
[5] Hu Y and al. Computer-assisted virtual surgical procedure for acetabular fractures based on real CT data. Injury 2011; 42: 1121-1124.
[6] Fornaro J and al. An interactive surgical planning tool for acetabular fractures : initial results. Journal of Orthopaedic Surgery and Research 2010.
[7] Fornaro J and al. Semi-automatic Segmentation of Fractured Pelvic Bones for Surgical Planning. F. Bello and S. Cotin (Eds) : ISBMS 2010, LNCS 5958, pp. 82-89, 2010
[8] Wu J and al. Fracture Detection in Traumatic Pelvic CT Images. International Journal of Biomedic. ID 327198, Volume 2012.

[9] Yushkevich P et al. User-guided 3D active contour segmentation of anatomical structures: Significantly improved efficiency and reliability. *Neuroimage* 2006 Jul 1; 31(3):1116-28. www.itksnap.org
[10] Loyd J, Stavness I and Fels S. ArtiSynth : A fast interactive biomechanical modeling toolkit combining multibody and finite element simulation. Soft Tissue Biomechanical Modeling for Computer Assisted Surgery, pp. 355-394, Springer, 2012. www.artisynth.org

TOWARDS A COMPUTER ASSISTED SYSTEM FOR DOSIMETRY OPTIMISATION OF INTRAPLEURAL PHOTODYNAMIC THERAPY FOR MALIGNANT PLEURAL MESOTHELIOMA

1. Munck C.[1,2,4]
2. Mordon S.[1,5]
3. Scherpereel A.[2,5]
4. Porte H.[1,3,5]
5. Dhalluin X.[1,2]
6. Betrouni N.[1,5]

[1] INSERM, U 703, Lille, France
[2] Department of Pulmonary and Thoracic Oncology, Calmette Hospital, Lille, France
[3] Department of Thoracic Surgery, Calmette Hospital, Lille, France
[4] University Paris XI, Paris, France
[5] University Lille 2, Lille, France

1- Background and rational

Malignant pleural mesothelioma (MPM) is an aggressive tumour of the pleura, caused by a professional exposure to asbestos fibres. MPM has a poor prognosis, partly due to ineffective treatments. When surgery is part of a multimodal treatment for MPM, it seems crucial to add a local adjuvant treatment to kill residual tumour cells. The tumouricidal action of photodynamic therapy results from the interaction of a photosensitizer, oxygen and light at a specific wavelength activating the photosensitizer. Recently, intrapleural photodynamic therapy (iPDT), after surgery, has emerged as a promising treatment in this goal, with a major impact on survival and minimum toxicity (1). Successful iPDT requires the most complete and uniform light delivery, all the more that the pleural cavity has a complex geometry. In clinical practice, a photosensitizer is administered to the patients 48 hours before a maximal surgical tumour resection. Then, a light device connected to a laser source (wavelength 635 nm) is moved inside the pleural cavity, to illuminate the cavity walls (the target), filled with dilute intralipid, until the light dose of 60 $J.cm^{-2}$ is obtained. Today, the light delivery monitoring is achieved by 7 isotropic probes placed at strategic locations in the thorax and connected to a dosimetry system (2). However, this method does not provide information about the light delivered between these 7 locations. This study aims at developing a better per operative dosimetry for iPDT, using a therapy administration system allowing complete, homogenous illumination with a visual display of the light distribution

2- Material and methods

The development of such a system requires:

- The characterization of the illumination profile of the light device
- The real time tracking of the device
- The spatial mapping and illustration of the delivered dose

2-1 Illumination Profile

The illumination device is composed of a cylindrical diffusing optical fibre attached to a stick. Two complementary methods were used to perform light dosimetry around the tip of the light device. It was fixed in a tank filled with dilute intralipid, used as a diffusing medium. First, an isotropic probe (Medlight®) was connected to a wattmeter (Newport® 841-PE) and measured the power delivered at 124 positions above the optical fibre, every 5 millimetres using a benchmark.

Secondly, a digital photography (pixel) of the light device gave a global spatial representation of the light delivery.

Applying the light diffusion theory stipulating that light propagation in a medium is defined by an effective attenuation coefficient (μ_{eff}) expressed as: $I=I_0.\exp(-\mu_{eff}.z)$, where I_0 and I are respectively, initial and at z medium depth light intensities, a correlation between this theoretical model and the experimental measurements from the isotropic probe was done. An error calculation and an optimal μ_{eff} were estimated.

2-2 Spatial monitoring of the delivered dose

To locate the light device inside the pleural cavity during surgery, a 3D electromagnetic tracking system (EMTS) (TrackSTAR®, Ascension Technology Corporation, USA) with a sensor of 4 mm was used.

Before treatment, a chest CT scan was realised to estimate the target surface. Fiducial markers were used to allow spatial transformation from the images space to the operating room space. At each position update, the light device position was matched to the 3D CT scan. It allowed a precision of 0.5 mm at the frequency of 10 Hz.

To optimize the per-operative dosimetry of iPDT, the idea was to combine the real time tracking of the light device with the illumination profile and to match it with CT images allowing, in this way, a real-time display of the cumulated dose.

2-3 Validation

In order to validate the global solution, a phantom was constructed. It consisted of a human-sized thorax, made of plaster, and moulded into a right-side intraoperative and post tumour resection pleural cavity. CT acquisition of the phantom was done and the thoracic cavity was segmented to calculate its surface. The validation protocol consisted in evaluating the feasibility of the approach on this phantom in obtaining a real time display of the delivered light dose.

3- Results

3-1 Diffusion Profile

The experimental measurements obtained with the isotropic probe allowed to define an effective attenuation coefficient $\mu_{eff}=0.705cm^{-1}$. This optimised value allows a mean error of 5.32% between the experimental and the theoretical values.

Associated with the spatial representation of the photography, an illumination profile of the light device was established. It showed an ellipse-shaped illumination and percentage of remaining light starting from the centre of the optical fibre (Figure 1). From this model, iso-dose lines combining surfaces (cm^2) and irradiance ($W.cm^{-2}$) were established. For instance, 80% of the light power delivered, with a laser output of 3W, is spread on a surface of 9,2cm^2, with a corresponding irradiance of 0,261$W.cm^{-2}$.

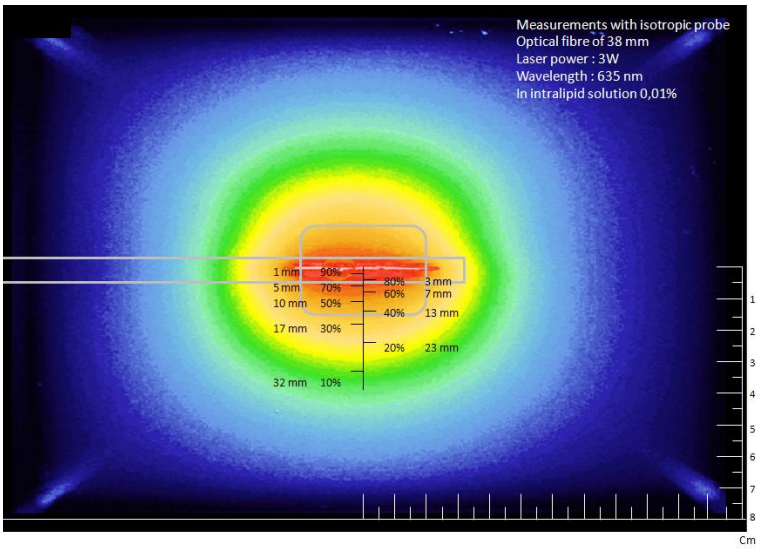

Figure 1: Illumination profile of the light wand with percentage of light from the optical fibre

3-2 Spatial monitoring of the delivered dose

The surface of the chest wall of the phantom was 1270 cm^2. With a laser emitting at 7 Watt, the complete treatment with 60 Joule at each square centimetre requires 10885 s.
Figure 2 depicts the real time display of the delivered dose. Thanks to this visual feedback, the surgeon guides the light wand towards the target.

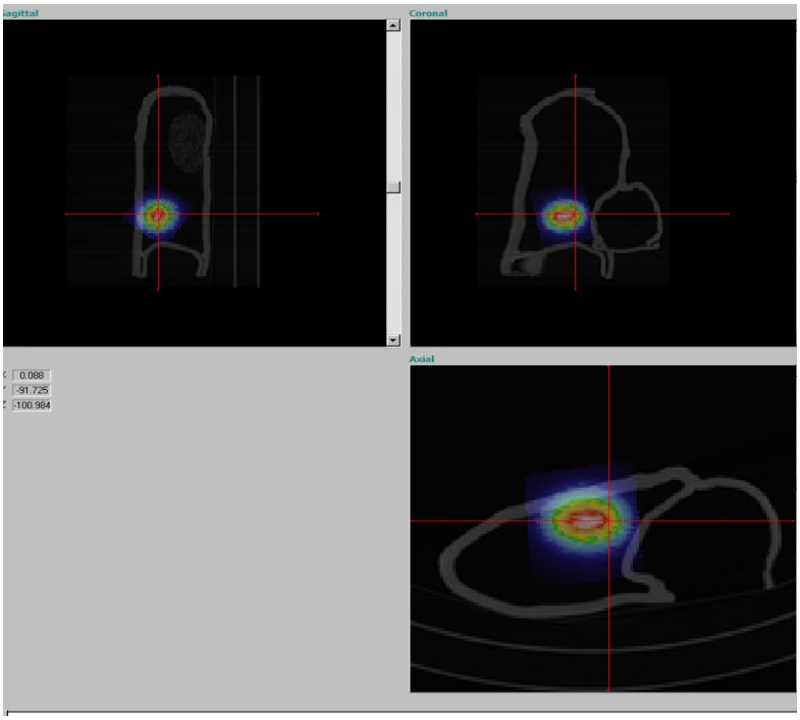

Figure 2: Real time tracking of the light wand matching and display of the delivered dose.

4. Conclusions and perspectives

A new dosimetry method was introduced based on a theoretical modelling of the illumination profile of a light device and combination with a spatial tracker, allowing a monitoring of the light source movement in real-time, in the pleural cavity of a thorax phantom. Preliminary study showed the feasibility of the approach. Further experiments, mainly to compare the computed dose to the punctual measurements collected by the 7 probes, are ongoing. Clinical validation of the method will conducted during the clinical trials starting soon at the Lille University Hospital.

In line with the main challenge of iPDT, this study suggests a future computer-assisted procedure for a more reproducible, complete and accurate light dosimetry for iPDT, and this for the treatment of MPM, as well as for other pleural malignancies.

REFERENCES

(1) Friedberg JS, Culligan MJ, Mick R et al. Radical Pleurectomy and Intraoperative Photodynamic Therapy for Malignant Pleural Mesothelioma. Ann Thorac Surg. 2012 May; 93(5):1658–67

(2) Dimofte A, Zhu T, Finlay J et al. In-vivo dosimetry for pleural PDT, Proc. of SPIE 2009 February, Vol. 7164

Evaluation of two Computed Assisted Medical Intervention (CAMI) systems in Forensic investigation

Grenier F*, Voros S***, Boutonnat J**, Scolan V*, Paysant F*, Moreau-Gaudry A****

* CHU Grenoble, Forensic department;
** CHU Grenoble, Cytology department;
***UJF-Grenoble 1 / CNRS / INSERM, TIMC-IMAG UMR 5525, Grenoble, F-38041, France;
****Centre d"Investigation Clinique - Innovation Technologique, INSERM, CHU de Grenoble, UJF-Grenoble 1, CIT803, Grenoble, F-38041, France;
UJF-Grenoble 1 / CNRS, TIMC-IMAG UMR 5525, Grenoble, F-38041, France.

Introduction Autopsy is extremely important in medical research, education, and professional development [1] but many studies show its decline in the second half of the 20th century, when there is no suspicion of criminal action. This can be explained by the difficulties to obtain the consent of the family and the advances in premortem diagnostic techniques [2]. Indeed, in the past 10 years, medical imaging techniques have been increasingly applied to forensic investigations but these techniques do not allow to obtain histological and toxicological information: in autopsies, tissue and liquid samples are required and "minimally invasive" tools offer interesting perspectives. Lots of methods were presented in the scientific literature associating imaging and robotic to perform biopsies, or navigation systems to guide biopsies using preoperative imaging [3-4]. In forensic sciences, the use of imaging systems to visualize a biopsy path (without navigation) is called virtual autopsies as opposed to traditional autopsies. Our aim is to demonstrate the feasibility of using two mini-invasive "Computer Assisted Medical Interventions" (CAMI) devices for mini-invasive exam of corpses with the underlying objective of using them in the daily activity of the forensic science department for non-criminal causes. The two studied Medical Devices were developed by TIMC-IMAG. Although both devices have already been validated on patients in interventional radiology and laparoscopic surgery they have not been evaluated in forensic conditions: the particularities of dead bodies (putrefaction, absence of blood circulation, some specificities in imaging) must be taken into account.

Materials and Methods: the two devices used were: a navigation system for the draining from multislide scan from the company Imactis® (http: // www.imactis.com)[5] (figure 1a) and a robotic endoscope manipulator ViKY® marketed by the EndoControl company® (http: // www.endocontrol-medical.com) [6] (figure 1b). One of the main challenges in using a navigation system like the Imactis system is the very frequent absence of CT Scans in the autopsy room. Thus, before investigating the precision of the system we must determine whether its use is compatible with the displacement of the corpse from the forensic institute to a scanner room in terms of internal organs mobility. We transported a corpse to the radiology room. An initial scan was performed, then, we realized 3 others scan after mobilization of the body like during a transport. We performed a rigid registration based on the manual pairing of a few salient anatomical parts (e.g. lumbar rachis) on the four scanners with the open source software MITK 3M3 Image Analysis, and compared them with the initial scan. On three corpses, we followed the following protocol for the evaluation of the CAMI devices:

- With the Imactis® station, we transported the corpses to the autopsy room after the CT-Scan. Then, under the navigation system, with a biopsy core needle (14 gauges by 250 mm) and a pistol device, biopsies programmed were: liver, kidneys, spleen, and puncture of the bladder and the gallbladder. All the samples were fixed in phosphate-buffered 4% paraformaldehyde and sent to the anatomopathologist for analysis and identification.
- With ViKY® robot, we put the camera and the robot endoscope manipulator 5 centimeter above the umbilicus. Four other trocars were placed in the iliac fossa left and right, and the hypochondrium left and right. We started to the ileo-caecal valvula and we explored the intestines in the centrifugal direction. Then we began the exploration and biopsies of the kidneys, pancreas, liver, and spleen; and punctures of gallbladder and stomach.

Results The rigid registration highlights an average mobility of 4.36 millimeters (with a standard deviation of 0.87mm). With the Imactis® system, the experimentation duration was between 1 and 3 hours with only 15 minutes of installation (showing an easy to pick up and play). Biopsies were performed to reach a predefined target in an organ, with an a posteriori verification by the anatomopathologist. Only the biopsies of big organs such as liver were successful in the first and second experimentation. The biopsies of small organs failed because of the errors of registration due to the transport and the mobility of the internal organs and the gas purification release in the abdominal cavity. In the third experimentation, all the organs were biopsied because of the absence of purification gazes, so it doesn't add to the errors of registration as the two first experimentations (table 1).

Concerning the ViKY® robot, the calibration of the vocal command of the robot requires some time (almost 30 minutes, performed only once per user). Our biggest difficulty came from the laparoscopic navigation because the learning curve seems important and specialization is required to use it correctly. All the peritoneum was explored. All the targets were biopsied and punctured by one investigator, without the assistance of a surgeon experimented in laparoscopy. The experimentation duration was 4 hours with 1 hour of calibration and installation. In this case, all the targets were successfully reached, but the manipulation of this device remains a specialty technique that could be challenging for unformed forensic doctors.

Conclusion/extension These two CAMI approaches require different learning curve and should be tailored to the specificities of forensic medicine to offer an important help in the non-homicidal autopsies via a minimally invasive approach. So, their adaptation for forensic medicine could be considered by a few adaptations (e.g. multiple localizations and MRI compatibility for Imactis, and a 3D reconstruction of the process using the ViKY robot). Despite some problems linked to the first use of those devices in this indication, the experimentation is very positive with the promise of better results and amelioration soon.

1 Burton JL, Underwood J. Clinical, educational, and epidemiological value of autopsy. Lancet. 2007 Apr28;369(9571):1471-80.
2 Leibovitz A, Blumenfl ed O, Baumoehl Y, Segal R, Habot B. Postmortem examinations in patients of a geriatric hospital. Aging Clin Exp Res 2001; 13: 406–09.
3 Thali MJ, Dirnhofer R, Vock P. The Virtopsy approach, 3D optical and reconstruction in forensic medicine. CRC Press, 2009.
4 Loughrey MB, McCluggage WG, Toner PG. The declining autopsy rate and clinicians' attitudes. Ulster Med J 2000; 69: 83–890.
5 imactis website http://www.imactis.com/index.php?module=produit&language=en_EN&PHPSESSID=c6cee5face9e89a0a462b1e5afe956d0 [consult 20/05/2014]
6 Voros S, Haber GP, Menudet JF, Long A, Cinquin P. ViKY Robotic Scope Holder: Initial Clinical Experience and Preliminary Results Using Instrument Tracking. IEEE/ASME Transactions on mechatronics 2010 dec ; 15 (6).
7 Rouvière H, Delmas. Anatomie humaine, descriptive, topographique, fonctionnelle. 12th edition . Masson, 1991.

Table 1: Results of different biopsies in each experimentation

Organs Targeted	Average size (7) (cm)	1st experimentation		2nd experimentation		3rd experimentation	
		Imactis ®	Viky ®	Imactis ®	Viky ®	Imactis ®	Viky ®
Liver	28*16*8	Ok	Ok	Ok	Ok	Ok	Ok
Spleen	12*8*4	Fail	Ok	Fail	Ok	Ok	Ok
kidneys	12*6*3	Fail	Ok	Fail	Ok	Ok	Ok
Gall bladder	Variable	Fail	Ok	Fail	Ok	Ok	Ok
Bladder	Variable	Ok	Ok	Ok	Ok	Ok	Ok

Ok: attempt validated by anatomopathologist exams
Fail: failed attempt or sample no validated by anatomopathologist exams

Figure 1:
a- The Navigation system Imactis b- The robotic endocope holder ViKY

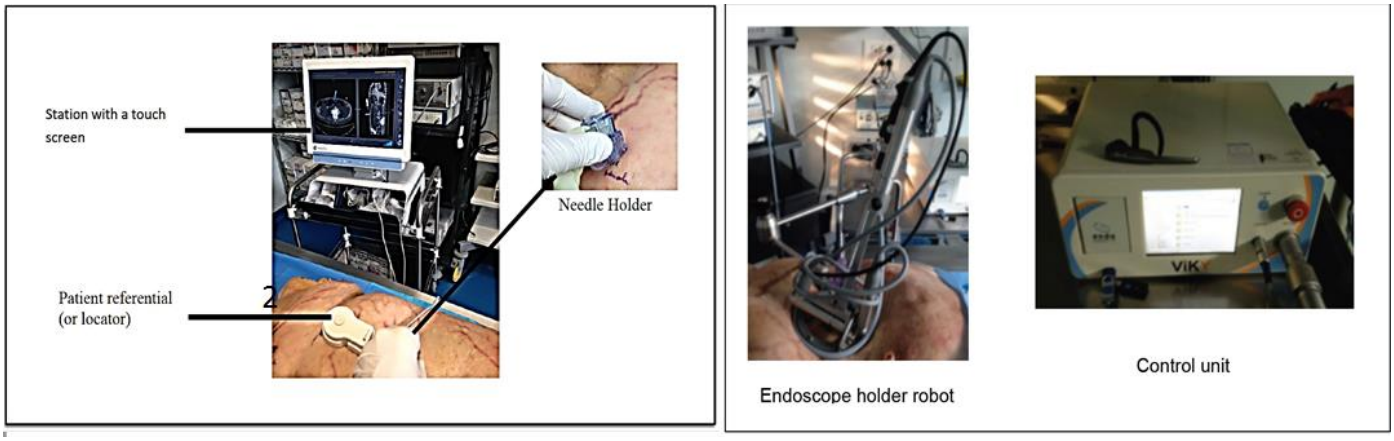

Acknowledgements: This work was partly supported by the French ANR within the Investissements d'Avenir program (Labex CAMI) under reference ANR-11-LABX-0004.

The CATANE project: a SMA-based approach of mini-invasive surgery

Jean-Baptiste Cazeneuve[1], Raphaël Blanc [2], Jérôme Szewczyk [3]

[1]Jean-Baptiste Cazeneuve is with Sorbonne Universités, UPMC Univ Paris 06, UMR 7222, ISIR, CNRS, UMR 7222, ISIR, INSERM, U1150, Agathe-ISIR, F-75005, Paris, France
cazeneuve@isir.upmc.fr

[2]Jérôme Szewczyk is with Sorbonne Universités, UPMC Univ Paris 06, UMR 7222, ISIR, CNRS, UMR 7222, ISIR, INSERM, U1150, Agathe-ISIR, F-75005, Paris, France
sz@isir.upmc.fr

[3]Raphaël Blanc is with Department of Interventional Neuroradiology, Rothschild Foundation Hospital, Paris, France.

Endovascular interventions impose the surgeon to control a catheter inside the vascular system, from the outside of the body and often involve travel through sharp turnings or delicate crossings. Due to their length and flexibility, conventional catheters show significant limitations in terms of maneuverability and stability, therefore operations require certain skills. In this context, there is a great need for intelligent catheters providing enhanced maneuverability and agility. .

Different forms of drivable active catheter have been proposed in the literature. For example, in [1], authors propose a magnetic navigation system. Deflection of the system is obtained by aligning a small magnet fixed at the tip of the catheter with a desired magnetic field vector created by the three large electromagnets placed next to the patient table. Each direction modification of the catheter tip deflection requires time and manipulation to reorient the magnetic field and therefore limits its use for navigation.

In [2], Dupont & al. propose a novel approach based on concentric tubes combinations. Tip deflection of the system is generated by rotation and extension of pre-curved elastic tubes with respect to each other. The system is substantially stiffer than conventional catheter and the current prototype presents a curvature radius of 10 cm. One major drawback of this system is that the minimum radius of curvature increases with the number of concentric tubes. Consequently a complex 3D curvature with thigh radii like the one that can be found in the vascular system can be difficult to achieve.

Cable actuated catheter like Sensei robotic system [3] or Fustar [4] manual systems present several limitations. Deflection occurs in a single plane and with a fixed radius which limits the freedom of movement of the device. The flexion range achieved by the tip of a cable driven catheter can be relatively large (>90°) but it is path dependent.

Active catheters featured with small Shape Memory Alloy (SMA) actuators constitute a promising approach to this issue. Compared to other solutions, the SMA approach shows advantages in terms of size, weight and strength. However it also presents some major drawbacks including short stroke and poor energy efficiency.

To address this concern we first developed a mathematical model aiming at thoroughly and accurately describing the multi-physics phenomenon underlying the SMA-based catheter actuation including the actuator-structure coupled behavior [5]. Based on this modeling and according to the actuator-structure characteristics, a method for dimensioning the main parameters of the SMA wires such as pre-strain, length and diameter has been proposed. The model gives a prediction of the

maximum bending angle that can be reached by the multi-degrees of freedom (dof) and multi-stages SMA-based active catheters.

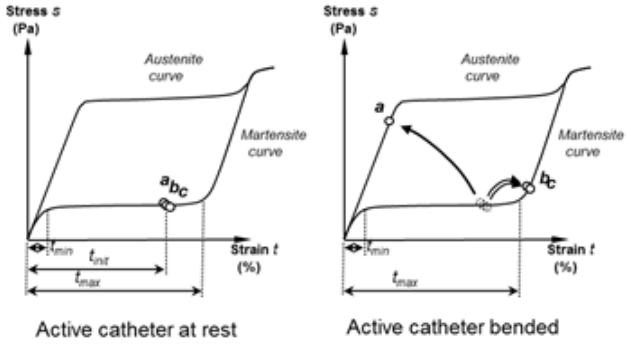

Figure 1 – Thermo mechanical behavior of the SMA actuators

The thermal impact of SMA actuation on the catheter environment has been investigated with numerical modeling (thermal and hydrodynamic) and experimental tests [6]. The catheter must be designed in order not to cause damage to biological tissues and fluids due to the rise of temperature during activation. An exact upper limit is difficult to quantify, depending of several factors. Based on literature, an upper limit of 49°C of the surface temperature of the active catheter has been chosen.

The assembly process for the prototypes relies on a cramping method described in a French patent application [7]. It does not require any soldering nor complex electrical connection and can be used on a wide range of catheter. Insulation with the environment is obtained by application of a flexible varnish coating without detrimental effect on performances.

Fig 2 - Prototypes of different diameters and controllable shape. From left to right, (a) 6-Fr multi-stage active catheter, (b) single stage active catheter, (c) Multi directional active guidewire, (d) single stage active guidewire, (e) active guidewire combined with an active catheter.

Various kinds of prototypes (see Fig 1) with different diameters and controllable shapes were realized with a lifetime greater than 25 activations and confirmed strong robustness of the manufacturing process.

Experiments showed good behavior of the system in terms of bending angle and radius of curvature. For example, a bending angle greater than 80° and a radius of curvature as low as 10 mm were obtained with 1 dof stage. A high level of maneuverability can be reached by combining several 1 dof stages and/or multidirectional flexion stages.

These active devices were tested by an expert surgeon in a realistic environment using a realistic 3D anatomical model. Different prototypes were used to pass through the aortic arch and enter the carotid artery (see Fig 2). Activation and relaxation time have been measured to be around 1 second which confirms the pertinence of using this device as a navigation system.

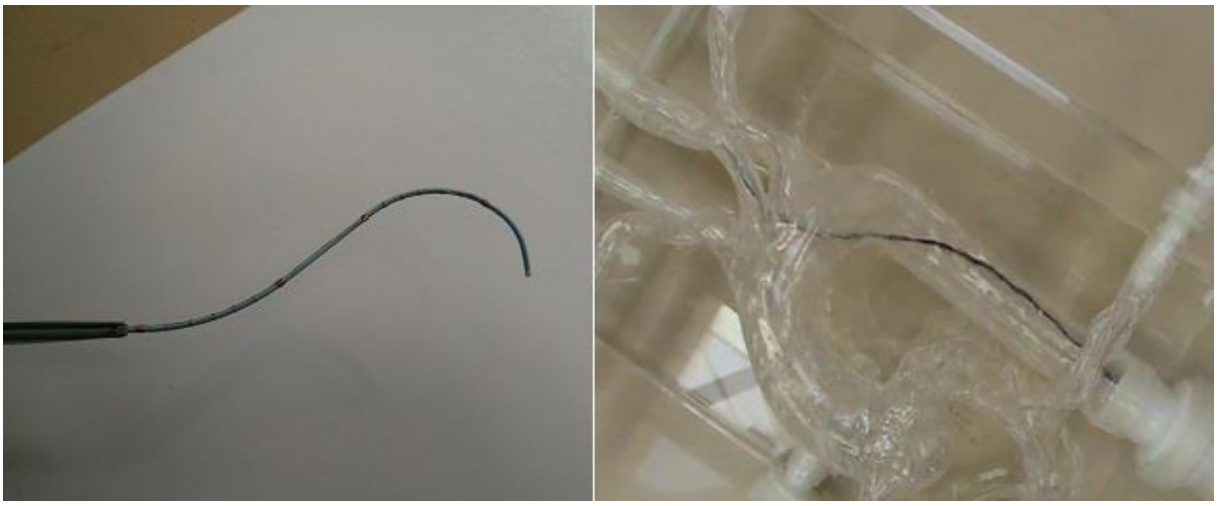

Fig 3 - 6-Fr prototype going through the carotid artery using multidirectional flexion stages.

First feedbacks by the surgeon concerning the maneuverability of the active catheter are promising. We intend now to create an intuitive control interface compatible with CT angiographic system and to build active catheters in series in order to prepare a large scale validation campaign and possibly launch a transfer to industry.

This work was supported by French state funds managed by the ANR within the Investissements d'Avenir programme (Labex CAMI) under reference ANR-11-LABX-0004.

[1] MN. Faddis, W. Blume, J. Finney, A. Hall, J. Rauch, J. Sell, KT. Bae, M. Talcott, B. Lindsay, *Novel, Magnetically Guided Catheter for Endocardial Mapping and Radiofrequency Catheter Ablation,* Journal of American Heart Association, 2002.

[2] P E. Dupont, J. Lock, B. Itkowitz, E. Butler, *Design and Control of Concentric-Tube Robots,* Robotics, IEEE Transactions on, Vol 26(2), pp 209 – 225, 2010.

[3] http://www.hansenmedical.com/

[4] Fustar steerable introducer from Lifetech Scientific (http://www.lifetechmed.com)

[5] J. Szewczyk, E. Marchandise, P. Flaud, L. Royon and R. Blanc, *Active Catheters for Neuroradiology*, Journal of Robotics and Mechatronics, Vol 23(1), pp 105-115, 2011.

[6] E. Marchandise, L. Royon, P. Flaud, J. Szewczyk and R. Blanc, *Thermal and hydrodynamic modeling of active catheters for interventional radiology*, Computer Methods in Biomechanics and Biomedical Engineering, Vol 14(7), pp 595-602, 2011.

[7] J. Szewczyk, *Méthode pour assemblage des cathéters / Méthode d'amélioration des courbures des cathéters et autres*, French patent application FR 10 52119, 2010

COMPUTER ASSISTED
MEDICAL INTERVENTIONS